Measurement of Event Shape Variables in Deep Inelastic *ep* Scattering with the ZEUS Detector at HERA and a Study of Power Corrections

DISSERTATION

zur Erlangung des Doktorgrades
am Fachbereich Physik
der Universität Hamburg

vorgelegt von

Ulrike Wollmer
aus Neumünster

Hamburg
September 1999

Gutachter der Dissertation: Prof. Dr. R. Klanner
Prof. Dr. R.-D. Heuer

Gutachter der Disputation: Prof. Dr. R. Klanner
Prof. Dr. B. Naroska

Datum der Disputation: 21.02.2000

Dekan des
Fachbereichs Physik und
Vorsitzender des
Promotionsausschusses: Prof. Dr. Fr.-W. Büßer

Abstract

A measurement of event shape variables has been made with the ZEUS detector at the HERA electron-proton collider using the 1996 and 1997 datasets, corresponding to an integrated luminosity of $35.4\,\mathrm{pb}^{-1}$.

The analysis is performed in the Breit frame of reference, which is convenient for comparisons with results from e^+e^- experiments. The differential distributions of Thrust, C-parameter, Jet Mass, Jet Broadening and their mean values are shown. The mean values are further analysed using the method of “power corrections” and the universality assumption of the power correction parameter $\overline{\alpha_0}$ is tested. The obtained values show a spread of ±4% which is within the theoretical uncertainty and is also in agreement with the results of e^+e^- experiments. Thus good supporting evidence for the applicability of this phenomenological model is found.

A value of α_s is extracted for each of the four event shape variables. A combined value of $\alpha_s = 0.1201 \pm 0.0006(stat)^{+0.0143}_{-0.0108}(tot)$. This is in good agreement with the current world average value.

Zusammenfassung

Mit dem ZEUS-Detektor, der am Elektron-Proton Speicherring HERA in Betrieb ist, wurde eine Messung von Ereignis-charakterisierenden Observablen (engl.: *event shapes*) durchgeführt. Hierzu wurden die Datensätze der Datennahmeperioden 1996 und 1997 verwendet, die sich auf eine Gesamtluminosität von $35.4\,\mathrm{pb}^{-1}$ belaufen.

Die Datenanalyse erfolgte im Breit-System, das einen einfachen Vergleich mit Ergebnissen von e^+e^- Experimenten ermöglicht. Es werden die differentiellen Verteilungen der Variablen Thrust, C-Parameter, Jet Masse und Jet Breite sowie die Mittelwerte dieser Verteilungen gezeigt. Die Mittelwerte werden dann verwendet, um die Methode der "power corrections" und vor allem die ihr zugrunde liegende Universalitätsannahme des Parameters $\overline{\alpha_0}$ zu testen. Die erhaltenen $\overline{\alpha_0}$ -Werte haben eine Streuung von ±4% und liegen damit innerhalb der theoretischen Unsicherheit. Ausserdem stimmen sie mit den von e^+e^- -Experimenten erhaltenen Werten überein. Diese Beobachtungen unterstützen die Anwendbarkeit des phenomenologischen Modells.

Für jede der vier Observablen wurde ein Wert für die starke Kopplungskonstante α_s extrahiert. Der gewichtete Mittelwert ist $\alpha_s = 0.1201 \pm 0.0006(stat)^{+0.0143}_{-0.0108}(tot)$. Er liegt in guter Übereinstimmung mit dem derzeitigen Weltmittelwert.

Acknowledgements

I would not have been able to start, work on and finish this thesis without the motivation, guidance and support of many people and institutions, so here is my big thank you to all of them.

I thank the DESY directorate for giving me generous financial support throughout my time at DESY.

I thank Prof. Erich Lohrmann for encouraging me to start working on a doctoral thesis. I thank my supervisor Prof. Robert Klanner for always having “open ears” and time for discussions. He has earned my special thanks for giving me the freedom to work on an analysis topic I have really enjoyed exploring.

My thanks go also to the Deutscher Akademischer Austauschdienst, DAAD, which gave me the financial support to spend six months at the University of Oxford during 1997. I profited greatly and in many different ways from this period. The stay would not have been possible without Prof. Lohrmann who encouraged me to apply for it and who introduced me to Prof. Roger Cashmore. I thank Roger in turn for inviting me over and giving me a warm welcome.

I would like to say that I have enjoyed working in the ZEUS collaboration. I found the friendly, international atmosphere very stimulating and enjoyable. During the years I had the opportunity to meet many people from many different countries, an experience I have certainly profited from. I would particularly like to thank Irmgard Harm and Birgit Breetzke for impressive organisation and efficiency.

I thank Prof. Robin Devenish heading the ZEUS group in Oxford as well as the group itself and the whole Nuclear and Particle Physics Department at Oxford for great hospitality during my stay. Everyone was very helpful and I greatly enjoyed my stay. The afternoons spent out on the cricket pitch were unforgettable …

Regarding my choice of analysis topic I thank Dr. habil Nicolai Pavel and Dr. Jutta Hartmann for helpful discussions, suggestions and enthusiasm. I have profited a lot from Dr. Anthony Doyle who was leading the analysis working group for analyses in the Breit frame while he was based in Hamburg and physics chairman.

Thank you to Rob and Gavin for good collaboration, for seeing things more relaxed than I am able to and for repeated reminders not to panic.

Another big thank you goes to Nicolai who initiated the idea of the DISTUPLE and got me involved in the project. Once everything was set up, thank you Andreas Ochs, doing analysis became fast and easy.

Thanks to Michael, Adrian and Stefan for letting me use CPU-time on their PCs for generating the DISENT runs.

Thanks to Ulli for sharing an office with me for so many years. Thanks for staying calm and friendly all the time, even when I was grrring at my terminal for whatever reason and thank you for keeping my plants alive while I was away!

Thanks to Mark for letting slip my escape plans. A shame we started the squash thing so late.

Thanks to Renate and Kirstin for being themselves and for sharing frustration, stories and laughter over coffee and lunch, which always made me a great deal more cheerful.

Thanks to Sabine and Adrian for reading the thesis and making corrections. A special thanks to Adrian for patiently brushing up my English and for encouraging me to bloody well get down to finishing this thesis.

Thanks to Christine and Harald for being such fun. A big thank you to Harald who built my computer with a Swiss Army knife and a gallon of Jever.

Thanks to Kia for making Matthesonstr. such an enjoyable and fun place to live.

Last – but not least – I owe an immense debt of thanks to my father for love, support and encouragement. Thank You!

Contents

List of Figures

List of Tables

Chapter 1

Introduction

The wish to understand what nature in general – and what matter in particular – is made of and which underlying forces govern its behaviour has stimulated generations of physicists. Research in the 20th century has led to a remarkable gain in the understanding of the fundamentals of our world, yet many open questions remain.

With ever-increasing resolution scattering experiments in the past have led to the subsequent discoveries of atoms, nuclei and nucleons. This chain of experiments culminated in the discovery of partonic substructure of the nucleons and thus gave birth to modern particle physics. This birth can be dated at around 1950 with the discovery of the pion and other mesons. The developmen tof high energy accelerators had started in the 1940's and consequently, further motivated by the discoveries, study of the substructure of nucleons became a vigorous field of activity. Experimentalists and theorists have since worked hand in hand in order to push the limits of our knowledge ever further – the former building ever more powerful machines for "seeing" the constituents of matter and the latter providing an ever more elegant and predictive theoretical understanding.

The process of building, refining and rejecting theoretical models has culminated in the formulation of the Standard Model, which, with the exception of gravity, embodies our present understanding of the microscopic physical world. Within the Standard Model the phenomena of the strong interaction are described by Quantum Chromodynamics (QCD), a renormalizable, non-abelian quantum field theory with the two striking features of asymptotic freedom and confinement. To date no significant deviation between QCD predictions and experimental results has been seen.

Matter is described as being built of pointlike quarks and gluons, and the gauge bosons which mediate the strong force between them. The strength of the coupling between the quarks and the gluons is denoted α_s. It is a "running coupling" in the sense that it changes its value with the process scale – i.e. the momentum transfer Q^2 in deep inelastic scattering or the centre of mass energy in e^+e^- annihilation. If the process scale is large enough the perturbation technique of calculating Feynman diagrams, well-known from QED, can be applied.

The functional dependence of the strength of the coupling α_s is predicted by the theory. However, the actual value at least at one scale must be determined experimentally. This is done by measuring a dimensionless observable F which has a perturbative expansion in terms of α_s: $F(Q^2) = A_0 + A_1\alpha_s(\mu^2) + A_2(Q^2/\mu^2)\alpha_s^2(\mu^2) + \ldots$ Here μ^2 denotes the renormalization scale. The coefficients A_i are calculable in the theory and α_s is extracted from the normalisation of the measurement result.

Event shape variables are a set of such dimensionless observables. They are defined as sums of particle momenta and are a means of describing the shape of the hadronic final state of an event, for example whether the distribution of particles is jet-like or more isotropic. They were first defined for e^+e^- annihilation and have proven useful for testing QCD predictions. In fact studies of event shapes provided the first indications that gluons are *vector* particles in accordance with QCD assumptions.

In addition to studies of event shape variables, α_s has been extracted from a wide range of experimentally-observable quantities such as jet production rates, the total e^+e^- cross section or scaling violations in deep inelastic scattering (DIS) and many other. These complementary methods give broadly consistent results and thus have provided a thorough test of QCD. The different results have been combined into a *world average* value, which is quoted at the mass of the Z^0 [Bet98]:

$$\alpha_s(M_Z^2) = 0.119 \pm 0.004$$

There is very good agreement between the values of α_s measured at different experiments. However, deviations are observed between certain measured quantities and the QCD predictions, that is the next-to-leading order calculations to be more precise. In the case of event shape variables, these deviations are very large – in the order of 20 % – and furthermore they vary with the inverse of the process scale Q. By contrast Monte Carlo programs incorporating phenomenological models of the hadronisation process succeed in describing the data well. Thus the deviations have been explained away as poorly-understood non-perturbative (long-distance) phenomena or *hadronisation corrections* and swallowed into the "black boxes" of event generators. Consequently, model-dependence has been found to be a source of large systematic errors.

A more satisfying explanation would be one obtained from a theoretical approach which makes use of well-established perturbative techniques. The QCD series is divergent and calculating QCD observables to next-to-leading order may neglect large contributions from higher orders. A particular set of Feynman diagrams, the so-called *bubble diagrams* (see Chapter 2), leads to sets of unsummable, factorially-divergent contributions which are identified as *infrared renormalons.* If the contributions from these diagrams are included in the calculations of various quantities, they give rise to $(1/Q)^p$-dependent corrections – and this offers the hope that they can explain the $(1/Q)$-dependent hadronisation corrections.

In order to make numerical predictions an additional universality assumption has to be made. It is assumed that a meaningful and universal coupling exists down to very low scales. Although the functional dependence of this coupling is unknown, it is sufficient to use its first moment in the calculations. The value of the first moment, $\overline{\alpha_0}$, is extracted from the measurement results together with the value of α_s.

The results of these new calculations are corrections to the next-to-leading order calculations of QCD observables. They have become known as *power corrections* and are available for various observables such as DIS structure functions [Da96, Li98], and both DIS and e^+e^- fragmentation functions [Da97b] and event shape variables (see the references in Chapter 2). Event shapes – both in DIS and in e^+e^- – may be regarded as the prime testing ground since the encountered hadronisation corrections are largest in this case. The goal of this thesis is thus to apply power correction fits to experimentally-obtained values of event shape variables. The extracted values of α_s and $\overline{\alpha_0}$ are then used to test the validity of this method. It is particularly compelling to investigate the usefulness of a universal low-energy effective coupling as a phenomenological concept. If valid, this would allow independence from hadronisation models tuned to experimental data.

The layout of this thesis is as follows. Some theoretical background is given in Chapter 2. The main concepts and features of QCD and the running coupling are recalled. The event shape variables under study are defined and the dispersive method leading to the calculation of the power corrections is explained. The HERA machine and the ZEUS detector are described in Chapter 3. Chapter 4 describes the selection of the data sample, followed by Chapter 5 with details on tracking, clustering and matching. Chapter 6 presents the measurement results of the event shape mean values and a study of systematic effects. In Chapter 7 the measurement results are analysed in terms of QCD and power corrections. Extracted values of α_s and the power correction parameter $\overline{\alpha_0}$ are presented. They are compared to the results from e^+e^- experiments. The question of whether the assumed universality of the power corrections actually holds is raised here. The main results are summarized in Chapter 8. An Appendix is provided which contains further items of relevance to the thesis, including the differential event shape distributions.

Chapter 2

Theoretical Background

This chapter provides the necessary theoretical background for the investigations made in this thesis. The main characteristics of QCD and deep inelastic scattering are summarised in Section 2.1 and Section 2.2. Definitions are given for the Breit frame of reference in which the analysis is performed (Section 2.3) and for the event shape variables under study (Section 2.4). Section 2.5 contains a discussion of α_s. In Section 2.6 information is given on the event generators which have been used in this analysis. The dispersive method leading to the formulation of *power corrections* to perturbative calculations of final state observables is explained in Section 2.7.

2.1 Quantum Chromodynamics

Quantum chromodynamics (QCD) [Ha84] is our current best theoretical model of the force acting between the constituents of baryons and mesons. Its formulation was triggered by the apparent violation of Pauli's principle in the Δ^{++} baryons. A new degree of freedom – *colour* – was introduced, and the fermions of the theory, the quarks, carry not only electromagnetic charge but also one of the three possible colour charges red, blue or green.

QCD is a renormalizable quantum field theory which was constructed in close analogy to quantum electrodynamics (QED), the extraordinarily successful theory of electromagnetic interactions.

The three-colour model of quarks has local SU(3) symmetry. Eight different *gluons* are the carriers of the strong force between the quarks. The gluons themselves also carry colour charge and can thus interact with each other – a feature of so-called *non-abelian* gauge theories. To lowest order, attractive forces are found for the qqq and the $q\overline{q}$ systems and repulsive forces for the qq system respectively.

Two significant properties of QCD are the phenomena of *asymptotic freedom* and *confinement*. The interaction strength α_s is asymptotically small at short distances – or equivalently *at large scale* since momentum transfer and spacial resolution are in reciprocal relation to each other, according to the uncertainty principle.

Thus short-distance interactions can be computed using the well-known *perturbative* techniques from QED. The interaction strength increases for larger distances, binding quarks

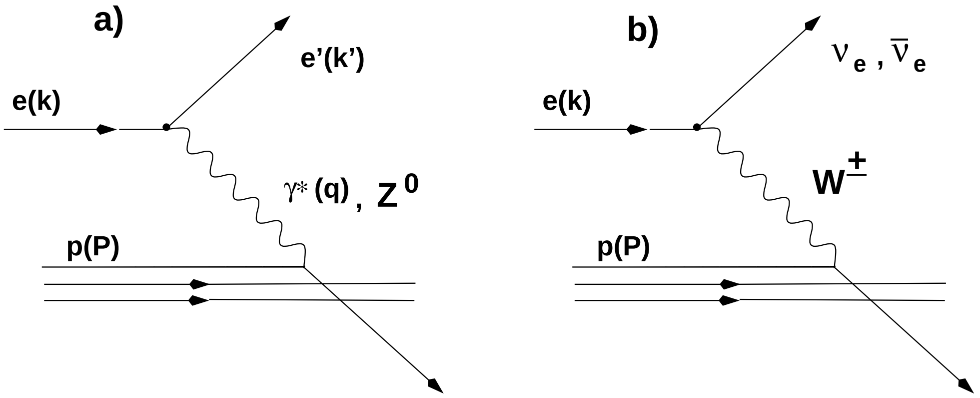

Figure 2.1: *The two leading Feynman diagrams for deep-inelastic electron-proton scattering: a) neutral current (NC), b) charged current (CC). Note that these diagrams are of zeroth order in* α_s .

and gluons together in colour-neutral objects. Unfortunately for experimenters, this confinement means that quarks and gluons are not observable as free particles.

2.2 Deep Inelastic Scattering

The term *deep inelastic scattering* (DIS) [El96] refers to lepton-nucleon scattering experiments where the (in general off-shell) momentum transfer from the lepton (e^+, e^-, ν, $\overline{\nu}$) to the nucleon (p, n) is sufficiently large that the nucleon fragments. The measured cross sections provide insight into the substructure of the nucleon.

The two leading order Feynman diagrams of deep inelastic electron-proton scattering are shown in Figure 2.1. Both the graph for neutral current (NC) and for charged current (CC) are shown. k and k' denote the four-momenta of the incoming and scattered electron/positron (neutrino/antineutrino) respectively, P denotes the four-momentum of the proton. In the neutral current process the momentum transfer from the electron to the proton is mediated via a virtual photon γ^* with four-momentum $q = k - k'$. If the momentum transfer Q^2 is large enough, the exchange of Z^0 or $W^\pm$ in charged current processes respectively is also important. The kinematics of the process is described by the variables Q^2, $x_{\rm bj}$ and y, which are derived from the four-momenta of the involved particles:

$$Q^2 = -q^2 \tag{2.1}$$

$$x_{bj} = \frac{Q^2}{2\nu} = \frac{Q^2}{2M(E-E')} \tag{2.2}$$

$$y = \frac{q \cdot P}{k \cdot P} = 1 - \frac{E'}{E} \tag{2.3}$$

where M is the proton mass, and E and E' are the energies of the incident and scattered electron respectively. Only two of the three variables Q^2, $x_{\rm bj}$ and y are independent since

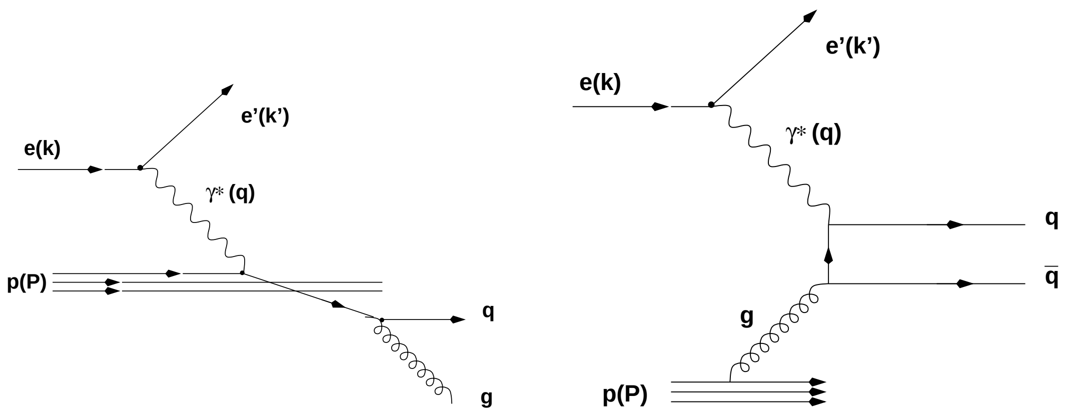

Figure 2.2: *Feynman diagrams for next-to-leading order DIS processes.* **left:** *QCD-compton process.* **right:** *Boson-gluon fusion.*

they are related to each other via the square of the centre-of-mass energy s of the electron-proton system:

$$Q^2 = x_{bj} \cdot y \cdot s \tag{2.4}$$

Figure 2.2 shows the two next-to-leading order Feynman diagrams for neutral current DIS. Shown is the diagram for gluon bremsstrahlung – the QCD-Compton process – and the diagram for boson-gluon fusion where the photon fluctuates into a quark-antiquark pair one of which then interacts with a gluon from the proton. Note that these processes are of first order in α_s ($\mathcal{O}(\alpha_s)$) since only one QCD vertex is involved.

Structure functions $F_i(x, Q^2)$ parametrize the structure of the target (as "seen" by the virtual photon). They represent the densities of partons in the nucleon, which are found at given values of x_{bj} and Q^2. They are used to formulate the double differential cross section:

$$\frac{d^2\sigma}{dx dQ^2} = \frac{4\pi\alpha^2}{Q^4}\left[[1 + (1 - y^2)]F_1 + \frac{(1-y)}{x}(F_2 - 2xF_1)\right] \tag{2.5}$$

In this equation the proton mass is neglected.

Early DIS experiments [SLAC] provided supporting evidence for QCD predictions. In particular it was discovered that only about 50% of the momentum fraction of the proton is carried by the charged partons. It was found that the remaining momentum fraction is carried by charge neutral, spin 1 partons, which were later identified with the gluons. The presence of gluons in the proton introduces a logarithmic dependence on Q^2 to $F_2(x, Q^2)$. This Q^2 dependence has become known as *scaling violation* and is predicted by QCD. Thus the original and still most powerful test of perturbative QCD is the experimental observation of the breaking of Bjorken scaling in deep inelastic lepton-hadron scattering.

2.3 The Breit frame

The Breit frame of reference [Fe72, St79] is defined to be the reference frame where the exchanged photon is completely space-like: the energy component of the photon is zero and

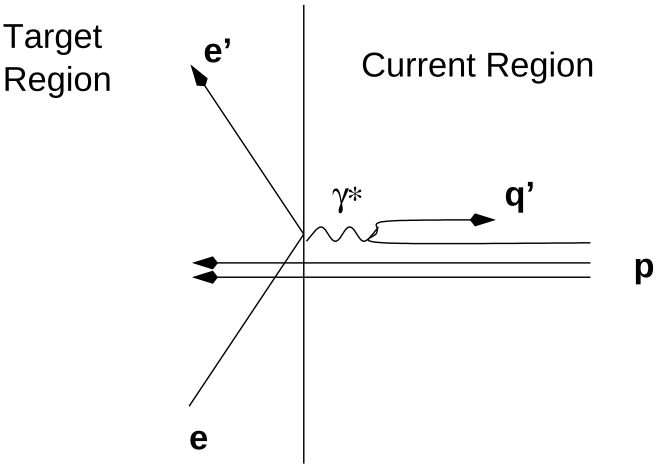

Figure 2.3: *The Breit frame of reference. One of the incoming quarks collides head-on with the exchanged – completely spacelike – photon and is scattered back by 180° . The direction of the exchanged photon divides the Breit frame into two hemispheres, the current hemisphere which contains the fragmentation products of the struck quark and the target hemisphere which contains the fragmentation products of the proton remnant.*

the momentum component is aligned along the negative z-direction: $q = (0, 0, 0, -Q/2)$. The exchanged photon collides head-on with one of the incoming quarks which carries the momentum fraction x of the proton momentum p. The struck quark in turn is scattered back by 180°, as is shown in Figure 2.3

The direction of the exchanged photon divides the Breit frame into two hemispheres. The hemisphere containing the scattered quark with momentum $p'_{\text{quark}} = -xP$ is known as the *current region* and the hemisphere containing the proton remnant with momentum $p'_{\text{remnant}} = (1-x)\,Q/2x$ is known as the *target region*. Particles are assigned to these regions according to their longitudinal momentum in the boosted frame: particles with $p'_z < 0$ are assigned to the current region, and particles with $p'_z > 0$ to the target region.

The current region of the Breit frame is similar to one of the hemispheres in e^+e^- annihilation. Thus the Breit frame is particularly convenient when comparing analysis results with results from e^+e^- experiments. However, the analogy is true only at leading order (which is zeroth order in α_s). At next-to-leading order (first order in α_s) there exists only gluon bremsstrahlung (QCD-Compton) in e^+e^-, whereas in DIS there is also the contribution from boson-gluon fusion.

At higher orders the invariant mass of the produced $q\overline{q}$ or qg pairs is no longer negligible. The incoming parton carries a fraction $p_p = \xi P$ of the protons momentum, and $\xi > x$ in order to allow for the emission of the parton pair. The cross-section for these $\mathcal{O}(\alpha_s)$ processes depends on five variables, x, Q^2, x_p, z_p and ϕ^*. The variable ϕ^* is the azimuthal angle of the jet plane with respect to the virtual photon in the γ^*-parton centre of mass system (CMS). The scaling variables x_p and z_p are given by:

$$x_p = \frac{Q^2}{2p_p \cdot q} = \frac{Q^2}{m^2 + Q^2} \qquad (x \geq x_p \geq 1)$$

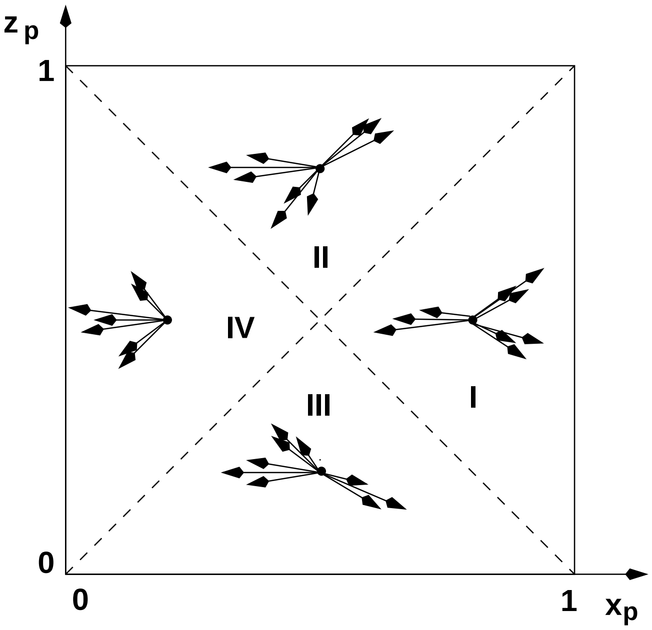

Figure 2.4: *Event topologies in the* (x_p, z_p) *plane. Region I shows two jets in the current region and one in the target region. In regions II and III there is one jet in the current region and two jets in the target region. In region IV the current region is depopulated and all three jets are in the target region.*

$$z_p = \frac{P \cdot p'_p}{P \cdot q} = \frac{1}{2}(1 - \cos\theta^*) \qquad (0 \geq z_p \geq 1)$$

where m is the invariant mass of the qg or $q\overline{q}$ system and p'_p is the momentum of the final state quark/gluon. Three different event topologies are observed which populate different regions in the (x_p, z_p) plane as shown in Figure 2.4.

The transformation from the HERA laboratory frame to the Breit frame is performed by a Lorentz boost followed by a rotation in order to align the virtual photon axis in the negative z' direction in the Breit frame. The Breit frame travels with velocity $\vec{\beta}c$ with respect to the laboratory frame. $\vec{\beta}$ is calculated from $q = (q_0, \vec{q})$ and $p = (p_0, \vec{p})$, the four-momenta of the virtual photon and the incident proton beam measured in the laboratory frame:

$$\vec{\beta} = \frac{\vec{q} + 2x\vec{p}}{q_0 + 2xp_0}. \tag{2.6}$$

$\vec{\beta}$ is used to derive $\gamma_{\rm boost}$: $\gamma_{\rm boost} = 1/\sqrt{1 - |\vec{\beta}|^2}$. When $\vec{\beta}$ and $\gamma_{\rm boost}$ have been determined, particles with energy E and momentum $\vec{P}$ in the laboratory frame may be boosted into the Breit frame according to the Lorentz transformation equations:

$$E' = \gamma_{\rm boost}(E - \vec{\beta} \cdot \vec{P}) \tag{2.7}$$

$$\vec{P}' = \gamma_{\rm boost}(\vec{P} - \vec{\beta}E) \tag{2.8}$$

2.4 Definitions of the Event Shape Variables

As the name suggests, event shape variables are a set of observables which describe the shape of the final state of an event. They are a means of measuring for example whether an event is more pencil-like or more isotropic. Event shapes were first defined for e^+e^- annihilation [El80, Ca92]. Due to the similarity between one hemisphere in e^+e^- and the current region of the Breit frame they are easily applicable in DIS as well [Da97a]. Actually the situation is a little simplified in DIS since the axis of the virtual photon in the Breit frame imposes a natural axis of reference. In e^+e^- the axis of reference, the *thrust axis* needs to be found first, which is defined as the axis $\vec{n}_T$ that maximises the Thrust T_c as defined as followes:

$$T_c = \max \frac{\sum_i |\vec{p}_i \cdot \vec{n}_T|}{\sum_i |\vec{p}_i|} \tag{2.9}$$

A particular characteristic of the event shape variables is *infrared safety*. That means that particle splitting of a particle p_i into two daughter particles $p_i \to p_j + p_k$ leaves the result virtually unchanged if one of the particles is *soft*, i.e. is emitted with only very small momentum perpendiular to the momentum direction of the particle p_i. Clearly it is the linear sums of particle momenta – as given in the definitions below – which guarantee infrared safety.

Four event shape variables are considered in this analysis. They are defined in the current region of the Breit frame as follows:

Thrust T_z with respect to the virtual photon axis $\vec{n}$:

$$T_z = \frac{\sum_i |\vec{p}_i \cdot \vec{n}|}{\sum_i |\vec{p}_i|} = \frac{\sum_i |\vec{p}_{z,i}|}{\sum_i |p_i|} \tag{2.10}$$

Note that $\tau_z = 1 - T_z$ is often used instead of T_z. **Jet broadening** J_b also with respect to the virtual photon axis $\vec{n}$:

$$J_b = \frac{\sum_i |\vec{p}_i \times \vec{n}|}{2\sum_i |\vec{p}_i|} = \frac{\sum_i |\vec{p}_{t,i}|}{2\sum_i |\vec{p}_i|} \tag{2.11}$$

Jet mass J_m:

$$J_m = \frac{M^2}{(2\sum_i E_i)^2} = \frac{(\sum_i E_i)^2 - |\sum_i \vec{p}_i|^2}{(2\sum_i E_i)^2} \tag{2.12}$$

and **C-parameter** C_p:

$$C_p = 3(\lambda_1\lambda_2 + \lambda_2\lambda_3 + \lambda_3\lambda_1) \tag{2.13}$$

where λ_i $(i = 1, 2, 3)$ are the eigenvalues of the momentum tensor $\theta^{\mu\nu}$ defined as

$$\theta^{\mu\nu} = \frac{\sum_i \vec{p}_i^{\,\mu}\, \vec{p}_i^{\,\nu} / |\vec{p}_i|}{\sum_i |\vec{p}_i|} \tag{2.14}$$

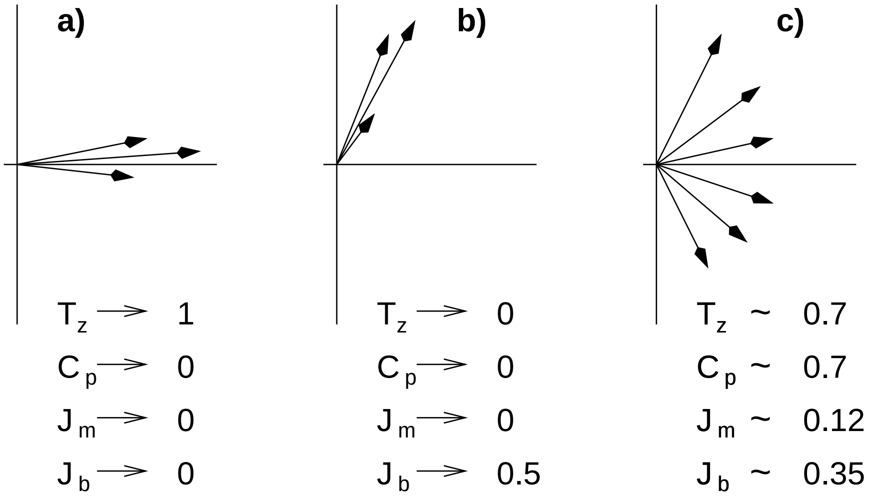

Figure 2.5: *Event shape values for different particle configurations in the current region of the Breit frame.* a): *collimated particles along the photon axis.* b): *event with a collimated jet which has large* p_T *with respect to the photon axis.* c): *more isotropically distributed particles.*

An alternative definition of the C-parameter is:

$$C_p = \frac{3}{2} \frac{1}{\left(\sum_i E_i\right)^2} \sum_{a,b \in CR} |\vec{p_a}|\,|\vec{p_b}| \sin^2 \theta_{ab} \tag{2.15}$$

where the sum over p_a and p_b extends over all combinations of particles in the current region (CR) (each pair of particles is counted twice) and θ_{ab} is the three-dimensional angle between particle a and particle b.

The range of possible values extends over the interval $[0, 1]$ for T_z and C_p, over $[0, 0.5]$ for J_b and over $[0, 0.25]$ for J_m respectively. The variables are undefined if the current region is depopulated. Figure 2.5 shows some examples of particle configurations in the current region and the corresponding values of the four variables.

Thrust T_z is a measure of how strongly the particles in the current region are collimated with respect to the virtual photon axis. It takes the maximal value of 1 for highly collimated events pointing in the photon direction (see Figure 2.5a). Events which are more isotropic, i.e. where the particles in a jet show a broader distribution, Figure 2.5c, take lower values. The lowest values of $T_z \rightarrow 0$ are taken for events with collimated jet almost perpendicular to the photon axis (2.5b). This in particular is different to e^+e^- annihilation where thrust is defined with respect to the thrust axis only and consequently takes values only between 0.5 and 1.

Analogously, *Jet broadening* as defined in Equation 2.11, is for DIS a measure of the transverse broadening of the particles with respect to the photon axis. Thus J_b takes values of $\rightarrow 0$ for events with particles collimated along the photon axis (Figure 2.5a). If the same collimated particles have a large angle to the photon axis (Figure 2.5b), J_b takes on its maximal values of $J_b \rightarrow 0.5$.

The calculation of *C-parameter* and *Jet mass* – both are measures of the broadening of particles – does not require an axis of reference. For events with collimated particles, regardless of their direction (compare (a) and (b)), both variables take very small values: C_p, $J_m \to 0$, increasing for less collimated particle configurations (c).

2.5 The Running Coupling α_s

The strength of the QCD coupling between quarks and gluons is denoted α_s. It is said to be a running coupling since it varies with the process scale Q. The functional dependence of α_s on the process scale Q is predicted by QCD. However the actual value, or normalisation, at at least one scale value must be determined experimentally.

As a consequence of the non-abelian character of QCD the value of α_s is large at small scales – i.e. large distances – and decreases for increasing values of the scale. In a region where α_s is sufficiently small, perturbation techniques may be applied for predicting measurement results. The perturbative domain extends down to values of $Q^2 \approx 4$ - $5\,\mathrm{GeV}^2$. Cross section measurements at HERA [ZEUS97] have shown that the perturbative predictions still hold for even lower values (down to around $1.5\,\mathrm{GeV}^2$), although the theoretical justification for such an extension remains unclear.

Since the functional dependence of α_s on Q is given by the theory, a measurement result obtained at any scale may be extrapolated to a reference scale value. It has become convention to use the mass of the Z^0 boson (91.2 GeV) for this purpose. Extrapolated to the Z^0 mass the results of different measurements are easily compared. Figure 2.6, taken from reference [Bet98], shows measurement results from a wide variety of processes. They combine to an average value of $\alpha_s(Z^0) = 0.119 \pm 0.004$. The broad agreement of the various values is strong supporting evidence for QCD.

The β function

The running of the coupling constant α_s with Q^2 is given by the renormalisation group equation:

$$Q^2 \frac{\partial \alpha_s}{\partial Q^2} = \beta(\alpha_s). \tag{2.16}$$

where the β function has the following perturbative expansion:

$$\beta(\alpha_s) = -b\alpha_s^2(1 + b^{'}\alpha_s + b^{''}\alpha_s^2 + \mathcal{O}(\alpha_s^3)) \tag{2.17}$$

and the coefficients b and b' are given as follows:

$$b = \frac{(11C_A - 2n_f)}{12\pi} = \frac{(33 - 2n_f)}{12\pi} \tag{2.18}$$

$$b^{'} = \frac{(17C_a^2 - 5C_A n_f - C_F n_f)}{2\pi(11C_A - 2n_f)} = \frac{(153 - 19n_f)}{2\pi(33 - 2n_f)} \tag{2.19}$$

where n_f denotes the number of active light flavours.
An alternative notation is:

$$\beta(\alpha_s) = -\alpha_s \sum_{n=0}^{\infty} \beta_n \left(\frac{\alpha_s}{4\pi}\right)^{n+1}$$

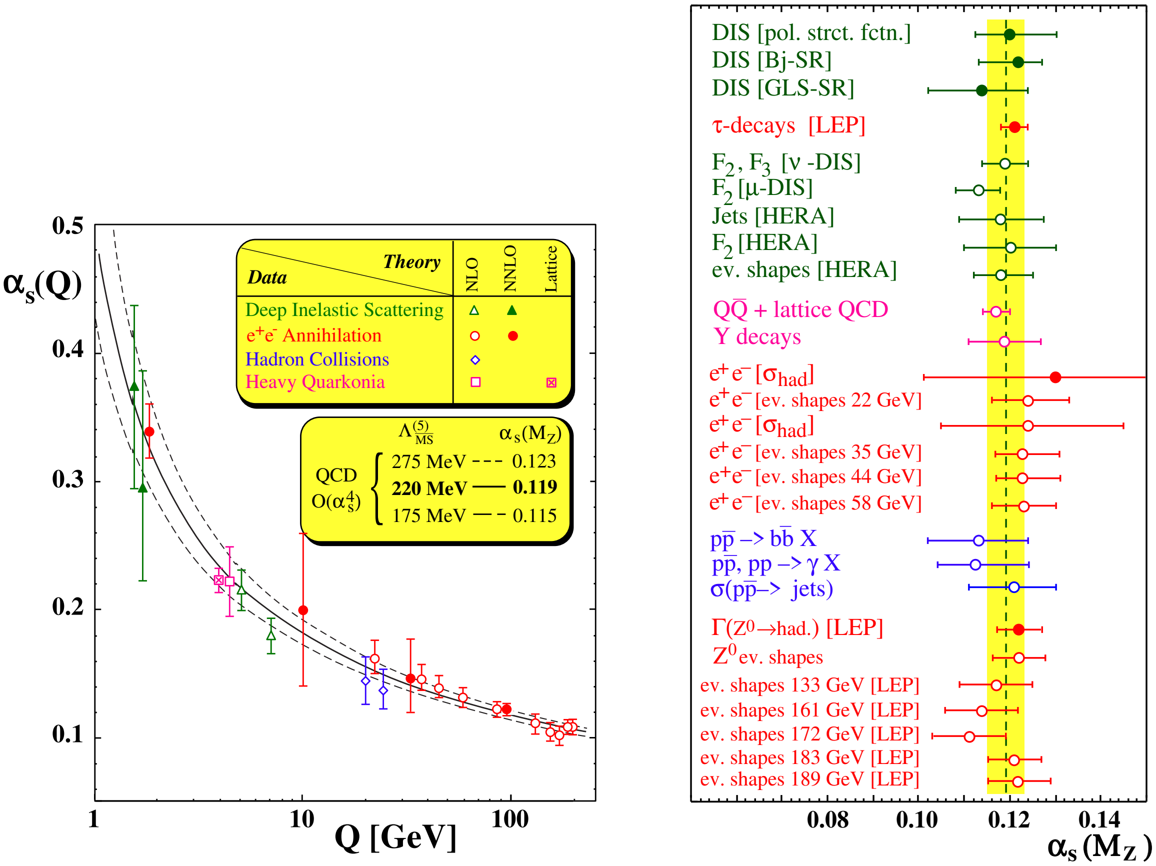

Figure 2.6: Overview of various α_s measurements. **left:** The functional dependence of α_s on Q. **right:** Comparison of the measurement results after extrapolation to the mass of the Z^0. The results are combined to an average values of $\alpha_s = 0.119 \pm 0.004$ as quoted in [Bet98].

$$\begin{aligned}\beta_0 &= 4\pi b = 11 - \frac{2}{3}n_f\\ \beta_1 &= 16\pi^2 bb' = 102 - \frac{38}{3}n_f\end{aligned}$$

The $\Lambda^{[4]}$ parameter

By convention a dimensionful parameter is used in the definition of $\alpha_s(Q^2)$. This parameter is called $\Lambda^{[4]}$ and is defined as the constant of integration over the β function:

$$\ln\frac{Q^2}{\Lambda^2} = -\int_{\alpha_s(Q^2)}^{\infty}\frac{dx}{\beta(x)} = \int_{\alpha_s(Q^2)}^{\infty}\frac{dx}{bx^2(1+b'x+\ldots)} \tag{2.20}$$

The value of $\Lambda^{[4]}$ lies in the neighbourhood of 200 MeV. It depends on the choice of renormalisation scale, the number of quarks included in the calculation and the assumed values for the masses of the heavy quarks. $\Lambda^{[4]}$ has the dimensions of energy squared and is regarded as the scale at which the coupling diverges if it is extrapolated towards the border of the perturbative domain. Within the perturbative region, α_s can be written in terms of $\Lambda^{[4]}$. At leading order (LO) solving of Equation 2.20 yields:

$$\alpha_s(Q^2) = \frac{1}{b\ln(Q^2/\Lambda^2)} \tag{2.21}$$

If the definition for $\Lambda^{[4]}$ is extended to next-to-leading order, the next coefficient in the β function is included in the integral and one obtains:

$$\frac{1}{\alpha_s(Q^2)} + b' \ln\left(\frac{b'\alpha_s(Q^2)}{1+b'\alpha_s(Q^2)}\right) = b\ln\left(\frac{Q^2}{\Lambda^2}\right) \tag{2.22}$$

Alternatively, one can approximate the solution of this equation in terms of inverse powers of $\ln(Q^2/\Lambda^2)$:

$$\alpha_s(Q^2) = \frac{1}{b\ln(Q^2/\Lambda^2)}\left[1 - \frac{b'}{b}\frac{\ln\ln(Q^2/\Lambda^2)}{\ln(Q^2/\Lambda^2)} + \ldots\right] \tag{2.23}$$

To this order, the two equivalent definitions presented in the Equations 2.22 and 2.23 differ by a constant factor, since the *true* expansion of $\alpha_s(Q^2)$ in inverse powers of $\ln(Q^2/\Lambda^2)$ would contain a term of order $k/\ln^2(Q^2/\Lambda^2)$ with a constant k.

2.6 Monte Carlo Event Generation

Three different generators were used in this analysis. Two of them, ARIADNE [Lo] and HERWIG [Ma91], were used for generating full events, which were then passed to a simulation of the detector response. DISENT [Ca96a, Ca97a] was used only for generating events at the hard process level. The results obtained with DISENT were used for the power correction fits described in Chapter 7.

Event generation may be divided into three steps. The first is the generation of the underlying hard process. This followed by modelling of parton showering, leading to what is referred to as the *parton level.* The third stage is the hadronisation of these partons into hadrons. At this point one is at the *hadron level.* Following this, the hadrons may be fed into a detector simulation program (see Section 3.2), at which point one is at the so-called *detector level.*

The hard process is calculable directly from scattering matrix elements derived from the underlying theory. The processes of parton showering and hadronisation are implementations of phenomenolgical models. They are in general based on the hypothesis of *local parton-hadron duality* [Az85] where it is assumed that the flow of momentum and quantum numbers at the hadron level tends to follow the flow established at the parton level. Brief descriptions of the string model (used in JETSET), the colour dipole model (used in ARIADNE) and the low-mass cluster model (used in HERWIG) are given below.

In the string model [Ar74, Bo81, An86, An83] the quark and antiquark from a produced $q\overline{q}$ pair separate in opposite directions, losing energy to the colour field, which is supposed to collapse into a stringlike configuration between them. The string has a uniform energy per unit length and later breaks up into hadron-sized pieces through spontaneous $q\overline{q}$ pair production in its intense colour field. The string may be broken up starting at either the quark or the antiquark end, or both simultaneously, and it proceeds iteratively by $q\overline{q}$ pair creation. The presence of gluons leads to the production of kinks on the string, each initially carrying localized energy and momentum equal to that of its parent gluon. Eventually all of the coloured partons are associated by strings into colour singlet states which do not have sufficient invariant mass to further break apart.

The string model is implemented in the JETSET simulation program [SJ86] for final-state parton showering as well as hadronisation. JETSET itself is an e^+e^- generator, but it is used by ARIADNE for the hadronisation. ARIADNE models the parton shower in terms of colour dipole splitting.

The colour dipole model CDM [Gu88] uses a slightly different approach. Here the combination of struck quark and the proton remnant is modelled as a colour dipole. When this dipole radiates a gluon, it splits into two radiating dipoles: one between the struck quark and the gluon and the other between the gluon and the proton remnant. This procedure is repeated and thus generates a chain of such dipoles. The proton remnant in this appoach must be treated as an extended object.

The program HERWIG uses a low-mass cluster hadronisation model in conjunction with initial- and final-state cascades. Colour-singlet clusters of partons are formed after the perturbative phase of jet development and then decay into the observed hadrons. The colour-singlet clusters form through splitting of gluons into $q\overline{q}$ pairs. Neighbouring colour-connected quarks and antiquarks can then combine into singlet clusters.

DISENT

The DISENT [Ca96a, Ca97a] program is a general-purpose Monte Carlo program for carrying out arbitrary QCD calculations for deep inelastic scattering in next-to-leading order accuracy. The program implements a generalised version of the subtraction algorithm [El81], which is an established method. The generalisation was made possible after new improved factorisation formulae, called *dipole factorisation formulae* were derived. Contrary to analytic calculations, only contributions giving rise to singularities are treated analytically, the remaining part is calculated using numerical integration techniques (Monte Carlo methods).

2.7 The Dispersive Method

α_s at a particular scale may be extracted from a measurement of the mean value F of an event shape distribution. In perturbation theory F can be expressed as an expansion in terms of α_s as follows. $F(Q^2) = A_0 + A_1\alpha_s(\mu_R^2) + A_2(Q^2/\mu_R^2)\alpha_s^2(\mu_R^2) + \ldots$ In this equation μ_R^2 denotes the renormalisation scale. The functional dependence of α_s on the scale and the coefficients A_i are predicted by the theory, but the actual value at least at one scale must be determined from the normalisation of the measurement result.

Perturbative calculations of event shapes are available at next-to-leading order accuracy. However, when the predictions are compared with experimental results, large deviations are observed between the two. Figure 2.7 shows measurement results for $<1-$ Thrust$>$ from several e^+e^- experiments at different centre-of-mass energies E_{CM} which is conveniently chosen to be the scale. The difference between the data points and the $\mathcal{O}(\alpha_s^2)$

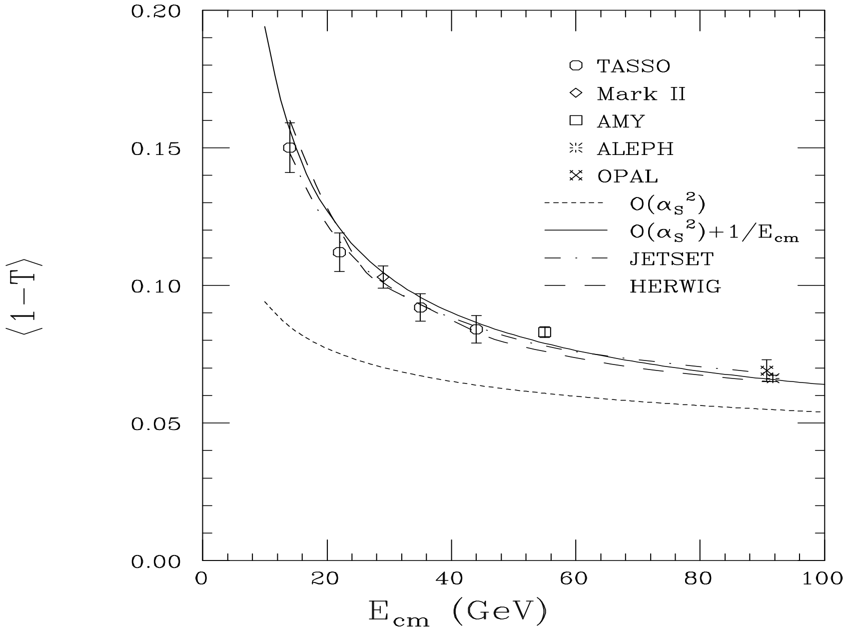

Figure 2.7: ⟨1− *Thrust*⟩ *measured by several* e^+e^- *experiments at different centre-of-mass energies* E_{CM}*, which is also taken to be the process scale. Substantial deviations are present between the data and* $\mathcal{O}(\alpha_s^2)$ *calculations. The Monte Carlo generators JETSET or HERWIG describe the data, as well as a fit of* $\mathcal{O}(\alpha_s^2) + A/E_{\mathrm{CM}}$*, where* A *is a constant. (The figure was taken from [Do97].)*

predictions is significant. Figure 2.7 also shows that a fit of $\mathcal{O}(\alpha_s^2) + A/E_{\mathrm{CM}}$ (where A is a constant) describes the data points well. It can thus be derived that deviations between data and NLO show a functional $1/E_{\mathrm{CM}}$ dependence.

Figure 2.7 also shows that the Monte Carlo generators JETSET and HERWIG succeed in describing the data. Thus the differences between the perturbative calculations and the data are named *hadronisation corrections*, which account for effects in the hadronisation process during which hadrons are formed from the underlying partons.

The Ansatz of the *dispersive method* [Do96] is an attempt to overcome this rather unsatisfying situation. It is based on renormalon theory, but in addition certain universality assumptions are made in order to make numerical predictions for specific observables. The existence of a universal coupling α_s^{DM} is postulated which is meaningful down to very low scales – in contrast to the perturbatve coupling α_s whose functional dependence diverges near the $\Lambda^{[4]}$ pole.

The Renormalon Background

During the search for a more satisfying explanation of the origin of the $1/Q$ deviations shown in Figure 2.7, theoreticians came across a certain set of Feynman diagrams – so-called *bubble diagrams* as shown in Figure 2.8. The bubble diagrams lead to singularities in the complex plane of Borel transformations [Za92, Mu92]. The singularities which lie on the integration contour of the Borel variable are identified as *renormalons*, which

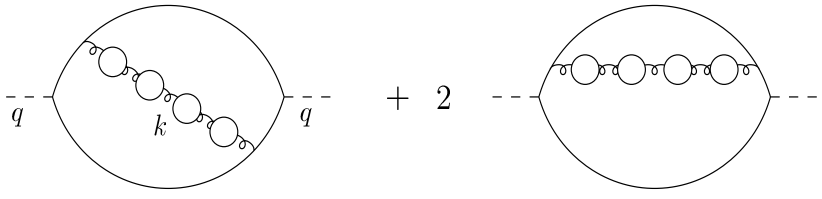

Figure 2.8: *Bubble Diagrams. Shown are two Feynman diagrams with chains of gluon loops which are identified as renormalons.*

give rise to terms proportional to $1/Q$ which are to be added to the result of the plain NLO calculation [Ko95, Ak96]. A very extensive description of all phenomena related to renormalons – history, theoretical explanation and comparison with experimental results – is presented in the habilitation thesis of M. Beneke [Bene99] and references therein.

Despite the exciting prospect that renormalons may account for the so-called "non-perturbative effects", it has to be said that without any further assumptions the renormalon answers are ambiguous [Bene99]. The universality assumption made in the dispersive method (see below) is just one of several possible assumptions. (For more, see Beneke's thesis.)

A Universal Coupling at Low Scales

One of the main features of the dispersive method is the assumed existence of a universal coupling $\alpha_s^{\mathrm{DM}}(\mu^2)$ which is defined down to arbitrarily low values of the (general) scale μ^2. In the following it is denoted $\alpha_s^{\mathrm{DM}}(\mu^2)$ in order to distinguish it from the perturbative QCD coupling $\alpha_s = \alpha_s^{\mathrm{PT}}(\mu^2)$.

For a perturbative calculation of α_s^{PT} carried out to second order in the $\overline{MS}$ renormalisation scheme with the renormalisation scale μ_R^2 one has the following functional description:

$$\alpha_s^{\mathrm{PT}}(\mu^2) = \alpha_s(\mu_R^2) + \left[b \ln\left(\frac{\mu_R^2}{\mu^2}\right) + k \right] \alpha_s^2(\mu_R^2) \tag{2.24}$$

$$\begin{aligned} \text{with} \quad b &= \frac{11C_A - 2N_f}{12\pi} && (2.25) \\ k &= \frac{(67 - 3\pi^2)C_A - 10N_f}{36\pi} && (2.26) \end{aligned}$$

where $C_A = 3$ and $C_F = 4/3$ are the colour factors for three active flavours, and b is the coefficient of the β function as described in Equation 2.17. The constant term k reflects a change of renormalisation scheme from the $\overline{MS}$ scheme for the perturbative calculation to the more physical CMW scheme where dispersive calculations are performed.

It is assumed to have reasonable analytic properties – in particular it is assumed that it has no singularities as $\mu^2 \to 0$ other than a cut along the negative real axis.

In the perturbative region at medium and large scales, α_s^{DM} is virtually identical to the perturbative description α_s^{PT} of the strong coupling. However at low scales the two may differ substantially from each other. The difference between the dispersive (and assumed to be true) coupling α_s^{DM} and the perturbative coupling α_s^{PT} is denoted $\delta\alpha_s$ or alternatively α_s^{NP} :

$$\delta\alpha_s(\mu^2) \simeq \alpha_s^{\mathrm{DM}}(\mu^2) - \alpha_s^{\mathrm{PT}}(\mu^2)$$

The running of the coupling may be written as a formal dispersion relation [Do96]:

$$\alpha_s^{\mathrm{DM}}(\mu^2) = -\int_0^\infty \frac{dm^2}{m^2+\mu^2}\rho_s(m^2) \tag{2.27}$$

where m denotes a finite gluon mass (see below), and the quantity $\rho_s(m^2)$ is the so-called *spectral function.* It represents the discontinuity of $\alpha_s^{\mathrm{DM}}(\mu^2)$ across the cut:

$$\begin{aligned}\rho_s(m^2) &= \frac{1}{2\pi i}\mathrm{Disc}\left\{\alpha_s(-m^2)\right\} \\ &\simeq \frac{2}{2\pi i}\left\{\alpha_s(m^2\mathrm{e}^{i\pi}) - \alpha_s(m^2\mathrm{e}^{-i\pi})\right\}\end{aligned} \tag{2.28}$$

The Characteristic Functions

In the following V denotes the mean value of an event shape variable. The power corrections are calculated from a *characteristic function* $\mathcal{F}$, which is process-dependent and specific to a given observable. It is derived using the technique of Feynman diagrams with a non-zero gluon mass m[1]. Illustratively the gluon mass can be understood as the virtuality of a gluon which then decays into two partons. As a consequence $\mathcal{F}$ is a function of the ratio $\epsilon = m^2/Q^2$. Numerical predictions are determined from the leading non-analytic term in the asymptotic behaviour of $\mathcal{F}$ as $\epsilon \to 0$ [Do98a].

The symbol $\mathcal{V}$ in the following refers to the contribution to V from one or two soft partons. $\mathcal{V}$ can be expressed as the integral over m^2 of the product of the characteristic function $\mathcal{F}$ and the spectral function $\rho_s(m^2)$:

$$\mathcal{V} = \int \frac{dm^2}{m^2}\rho_s(m^2)\mathcal{F}(\epsilon) \tag{2.29}$$

α_s and ρ_s are related according to Equation 2.28. The correction $\delta\alpha_s$ leads to a corresponding correction term in the spectral function:

$$\delta\rho_s(m^2) = \frac{1}{2\pi i}\mathrm{Disc}\left\{\delta\alpha_s(-m^2)\right\}. \tag{2.30}$$

Inserting Equation 2.30 into Equation 2.29 and changing the integration contour separately in the two terms of the discontinuity gives the non-perturbative contribution to $\mathcal{V}$:

$$\delta\mathcal{V} = \int_0^\infty \frac{dm^2}{m^2}\delta\alpha_s(m^2)\mathcal{G}(\epsilon) \tag{2.31}$$

---

[1] It should be pointed out that using a massive gluon in the calculations is not intended to imply that the gluon has in any sense a real effective mass, merely that the dispersive representation can be expressed in this way.

$$\mathcal{G}(\epsilon) = \frac{1}{2\pi i}\text{Disc}\,\{\mathcal{F}(-\epsilon)\} \tag{2.32}$$

From Equation 2.32 it follows that terms analytic in ϵ (i.e. linear functions of ϵ) cannot contribute to $\delta\mathcal{V}$. If the functional progression of the true coupling α_s were known, $\delta\mathcal{V}$ could be evaluated directly.

Moment Integrals

However for the calculations it is sufficient to use the moments $\mathcal{A}_q$ of the strong coupling correction $\delta\alpha_s$:

$$\mathcal{A}_q \equiv \frac{C_F}{2\pi}\int_0^\infty \frac{dm^2}{m^2} m^q \delta\alpha_s(m^2) \tag{2.33}$$

One may then write $\delta\mathcal{V}$ in the following way:

$$\delta\mathcal{V} = \frac{a_V}{\pi}\frac{\mathcal{A}_1}{Q} \tag{2.34}$$

Since α_s and α_s^{PT} are assumed to coincide at moderate and large momentum scale ($>$ 2 GeV has been suggested by theoreticians), it is expected that $\delta\alpha_s(\mu^2)$ tends to zero very rapidly with increasing μ^2. Thus the moment integrals can be truncated at a so-called *infrared matching scale* μ_I. Using Equation 2.24 one obtains:

$$\begin{aligned}
\mathcal{A}_1 &\simeq \frac{C_F}{\pi}\int_0^{\mu_I} dm \left(\alpha_s^{\mathrm{DM}}(m^2) - \alpha_s^{\mathrm{PT}}(\mu_R^2) - \left[b\ln\left(\frac{\mu_R^2}{m^2}\right) + k\right]\alpha_s^{\mathrm{PT}^2}(\mu_R^2)\right) && (2.35)\\
&= \frac{C_F}{\pi}\mu_I\left(\overline{\alpha_0}(\mu_I) - \alpha_s^{\mathrm{PT}}(\mu_R^2) - \left[b\ln\left(\frac{\mu_R^2}{\mu_I^2}\right) + k + 2b\right]\alpha_s^{\mathrm{PT}^2}(\mu_R^2)\right) && (2.36)
\end{aligned}$$

The parameter $\overline{\alpha_0}$, or "power correction parameter", is the integral from 0 to μ_I of the true, but unknown, coupling α_s. At present its numerical value cannot be calculated, and it has to be obtained by experiment.

$$\overline{\alpha_0} \equiv \frac{1}{\mu_I}\int_0^{\mu_I} \alpha_s^{\mathrm{DM}}(m^2)dm \tag{2.37}$$

As a consequnce of the assumption that α_s^{DM} is universal, $\overline{\alpha_0}$ should take on the same value for different observables (i.e. different event shape variables) and for different processes. The event shape analyses in e^+e^- experiments in particular should yield the same numerical value for $\overline{\alpha_0}$ as presented here, i.e. a DIS analysis. Providing a test of this universality assumption is one of the major goals of this thesis. The results of this test are shown and discussed in Chapter 7. The fitting method is also described there in detail.

The Milan factor

At first the calculations arising from the dispersive method were carried out with just 1-loop accuracy. However the 1-loop result generally suffers from ambiguities as was pointed out by Nason and Seymour in [Na95]. Some event shape variables were found in e^+e^- annihilation to be not sufficiently inclusive, i.e. the decay products of a gluon might go into two different hemispheres which would distort the result.

The calculations were then extended to 2 loops. The results have been published in [Do98a, Do98c] for e^+e^- and in [Da98] for DIS. In the 2-loop calculation an additional factor was needed, the so-called Milan factor. This is assumed to be universal. A change of scale is expected from $A \to A(1 + \mathcal{O}(\alpha_s/\pi))$. Higher order corrections are expected to be of the order of magnitude of $\approx 20\%$ [Sa98].

Chapter 3

The ZEUS Detector at the HERA Accelerator

This chapter introduces the ZEUS detector as one of the experiments at the HERA collider. The main characteristics of the HERA machine are listed below, wherever possible restricted to the performance during the years 1996 and 1997.

A detailed description of the ZEUS detector and its components can be found in the *Green Book* [ZEUS93a]. A general overview over the main components is presented here. More detailed information is provided about detector components used in this analysis, in particular about the inner tracking detector and the calorimeter. Components not relevant for the analysis are not discussed here.

3.1 The HERA Accelerator

The **H**adron **E**lectron **R**ing **A**ccelerator HERA situated at Deutsches Elektronen Synchrotron Laboratory, DESY at Hamburg, is the first electron-proton storage ring of its kind, allowing deeply-inelastic lepton proton scattering to be studied at much higher centre-of-mass energies than in previous fixed target experiments. The possible momentum transfer squared is raised by two orders of magnitude: an electron[1] beam energy of 27.5 GeV and a proton beam energy of (since 1998) 920 GeV allow observation of events at a centre-of-mass energy up to 320 GeV. The technical proposal for HERA was approved in April 1984, first collisions in the interaction regions were observed on Oct 19th 1991, and nominal data taking started in spring 1992 for the experiments H1 and ZEUS.

The HERA machine consists of two storage rings, for electrons and protons respectively. They both have a length of 6336 m and are situated at 15-30 m beneath the surface. Figure 3.1 shows the HERA ring and the accelerator complex on the DESY site. Older and smaller accelerators including the former e^+e^- storage ring PETRA are now being used as preaccelerators for HERA. Along the HERA ring are four experimental halls. The

---

[1] The term *electron* needs to be clarified: positrons were accelerated during the data taking periods 1994 - 1997 and electrons were accelerated in 1993, the beginning of the 1994 running period and since 1998. This thesis is based on the positron data taken in the running periods 1996 and 1997. The term *positrons* will be used wherever specification is necessary, the term *elctrons* will be used as general term refering to both electrons and positrons.

Figure 3.1: *The accelerator complex at Deutsches Electronen Synchrotron DESY in Hamburg. The left hand side shows a general overview of the HERA accelerator. The enlarged right hand side shows the preaccelerators on the DESY site.*

ZEUS detector is located in the DESY South Hall, the H1 detector opposite in the North Hall. H1 and ZEUS were designed as multi-purpose detectors for the precise measurement of deep inelastic ep scattering. They are built around two interaction regions where the electron and proton beams are conducted in one beam pipe towards a collision point in the centre of each experiment.

The remaining two experimental areas house two fixed-target experiments, HERMES and HERA-B. The HERMES collaboration [HERMES] is exploring the spin structure of nucleons using the (longitudinally) spin-polarised electron beam for inelastic scattering of polarised gas jet targets (hydrogen, deuterium or He^3). The HERA-B collaboration [HERAB] is studying CP-violation in the $B^0\overline{B^0}$ system. B^0 mesons are produced with wire targets in the halo of the HERA proton beam. HERMES started operation in 1995, HERA-B is expected to start taking physics data in spring 2000.

Positron Acceleration

Positrons with an energy of 500 MeV are filled from a linear accelerator into a small storage ring (PIA, positron intensity accumulator). The positrons are collected until one bunch corresponding to a current of about 60 mA has accumulated. This bunch is then transferred to DESY II, where the positrons are accelerated to 7 GeV before they are injected into PETRA. In PETRA 70 bunches are accumulated and accelerated to 14 GeV. At this energy the positron bunches are injected into HERA where they are accelerated to their final energy of 27.5 GeV. The maximum energy of the positron beam is limited by the radio frequency power needed to compensate for energy loss due to synchrotron radiation.

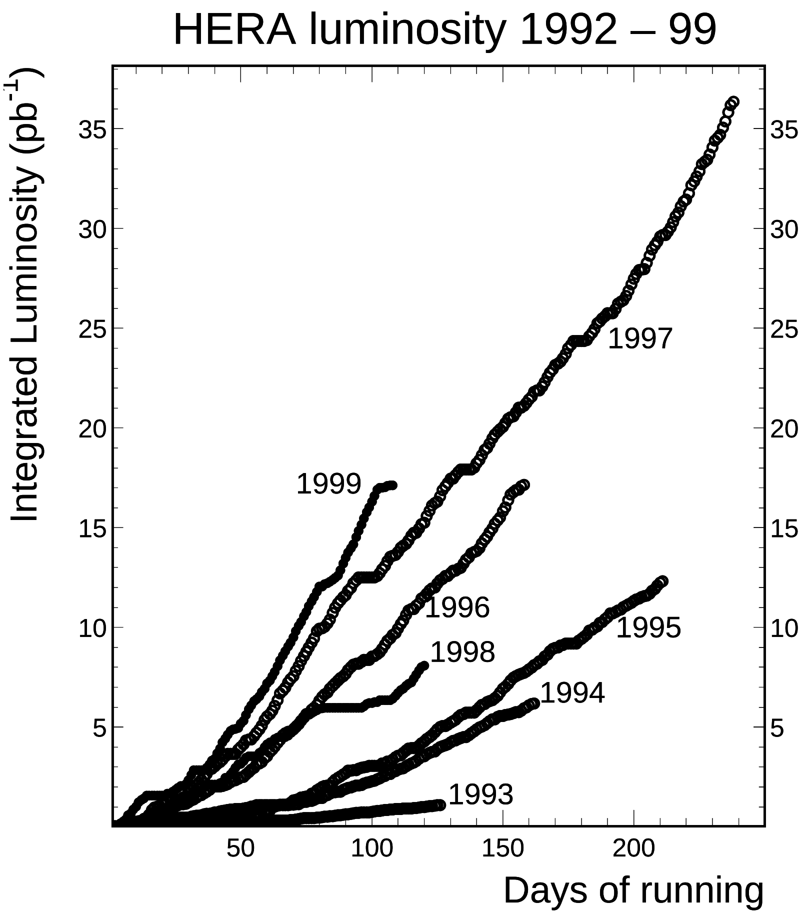

Figure 3.2: *Integrated luminosity delivered by the HERA machine in the years 1992 – 1999. The experience gained over the years is clearly reflected in the increased luminosity each year. The years 1998 and 1999 (electron running instead of positrons) are to be compared with the 1993 performance of electron operation.*

Proton Acceleration

Proton acceleration starts with a H^- 50 MeV linear accelerator. The H^- ions are stripped of their charge and are then injected into DESY III. 11 bunches with already the final spacing of 96 ns are collected and accelerated to 7.5 GeV. These bunches are filled into PETRA II, where up to 70 buches are collected and accelerated to 40 GeV. Then the proton bunches are injected into HERA where they are accelerated to their final energy of 820 GeV (1992-7) or 920 GeV (1998-9). In contrast to the electron ring where conventional magnets are used, the protons are accelerated in the HERA ring using superconducting magnets with liquid helium cooling.

Some of the design parameters for HERA are listed in Table 3.1 along with the running parameters actually achieved in the data taking periods 1996 and 1997. Over the years considerable experience in operating the HERA machine has been acquired. This is clearly reflected in the increase of integrated luminosity each year, as can be seen in Figure 3.2.

Figure 3.3: *Cross section of the ZEUS detector parallel to the beam axis.*

3.2 The ZEUS Detector

The ZEUS experiment was built as a general-purpose detector for studying *ep* scattering.

The ZEUS coordinate system is a right-handed orthogonal frame with its origin at the nominal interaction point (IP). The positive Z direction points in the proton direction, the positive X direction points towards the centre of HERA, resulting in the positive Y axis pointing upwards. The azimuthal angle ϕ is measured with respect to the positive X axis. The polar angle θ is measured with respect to the positive Z axis, leading to a polar angle of 0° for the proton beam and a polar angle of 180° for the electron beam directions. The positive Z direction is referred to as the *forward* direction and the negative Z direction as the *backward* direction.

Parameter	Design Values		Values of 1996		Values of 1997	
	$e^{\pm}$	p	e^+	p	e^+	p
Circumference (m)	6336					
Energy (GeV)	30	820	27.6	820.	27.6	821.2
Centre of mass energy (GeV)	314		300.9		301	
Current (mA)	58	160			36	78
Magnetic field (T)	0.165	4.65	0.165	4.65	0.165	4.65
Number of bunches	210	210	$174 + 15$	$174 + 6$	$174 + 15$	$174 + 6$
Bunch crossing time (ns)	96					
Integr. luminosity p.a. (pb^{-1})	35		17.2		36.5	
Instant. luminosity ($\mathrm{cm}^{-2}\mathrm{s}^{-1}$)	$1.5 \cdot 10^{31}$		$1.45 \cdot 10^{31}$		$1.45 \cdot 10^{31}$	

Table 3.1: *HERA design parameters and running performance during the data taking periods 1996 and 1997*

Figure 3.4: *Cross section of the ZEUS detector perpendicular to the beam axis.*

Figures 3.3 and 3.4 show cross sections of the ZEUS detector parallel and perpendicular to the beam axis. The design has a forward-backward asymmetry accounting for the large energy difference between the electron and the proton beam energies. As a consequence of this energy difference the *ep* centre-of-mass frame (CMS) is moving along the proton direction relative to the laboratory frame.

The general structure of the ZEUS detector shows the typical onion-skin structure of large collider experiments with several layers of subcomponents for different purposes. The innermost layer is a vertex detector surrounding the interaction point. The vertex detector (VXD) shown in Figures 3.3 and 3.4 was removed during the winter break 1995/96. A new microvertex detector is currently under construction.

Tracking detectors are used to reconstruct the path and thus the initial direction, the sign of the charge and the momentum of charged particles. The central tracking detector (CTD) of the ZEUS experiment is described in more detail below. It is surrounded by a superconductiong solenoid producing an axial magnetic field of 1.43 T. In addition to the CTD there is a forward tracking system (FDET) consisting of 3 forward tracking detectors (FTD) and two transition radiation detectors (TRD) sandwiched inbetween them. Another tracking detector, the rear tracking detector (RTD) is installed in the backward region.

One of the main purposes of the next layer – the calorimeter – is an energy measurement of the final state particles. The ZEUS uranium calorimeter is divided into a forward (FCAL), a rear (RCAL) and a central (BCAL) calorimeter. More details are given below.

The main calorimeter is surrounded by an iron yoke which serves as a return path for the

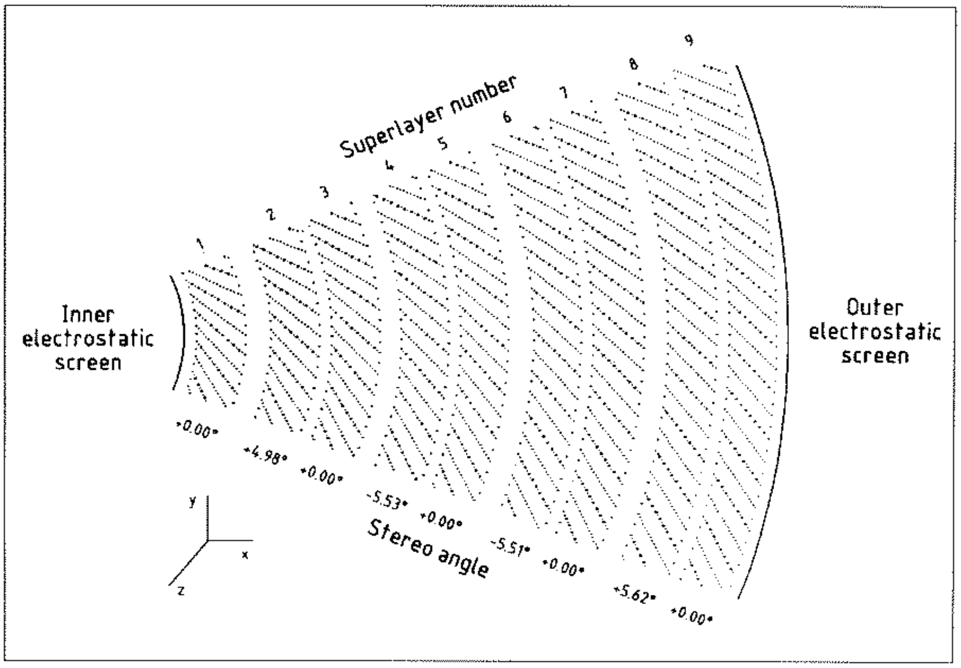

Figure 3.5: *Diagram of a CTD octant. The small points represent the sense wires, the large points represent the field shaping wires. and more text.*

solenoid magnetic flux. It is magnetized to 1.6 T. In addition it houses the backing calorimeter (BAC). The BAC consists of proportional chambers and is a device for measuring the energy of late showering or highly energetic particles.

The outermost layer of the detector consists of muon chambers in the forward direction (FMUON) and in the central section (BMUON). A veto wall is installed in the backward direction at $Z = -7.3\,\mathrm{m}$ and serves to suppress beam gas-induced background.

The Central Tracking Detector (CTD)

The central tracking detector, CTD [Fo94], is a cylindrical drift chamber surrounding the interaction point and the inner beam pipe. It measures the directions and momenta of charged particles with high precision, and is thus used to determine the position of the event vertex, with a resolution of approximately 1.5 mm in Z direction. In addition it is possible to use the CTD to provide an estimate of the energy loss dE/dx which can be used for particle identification.

The CTD is 205 cm long with an inner radius of 18.2 cm and an outer radius of 79.4 cm. The covered polar angle extends from $\theta = 15°$ to $164°$. The CTD is operated in a magnetic field with $|\vec{E}| \simeq 1.2\,\mathrm{kV/cm}$ and $|\vec{B}| = 1.43\,\mathrm{T}$. It is filled with a gas mixture of argon, CO_2 and ethane. The drift velocity is $|\vec{\omega}| \simeq 50\,\mu\mathrm{m/ns}$.

The CTD is equipped with 4,609 thin ($30\,\mu$) sense wires and 19,584 thick field-shaping wires. The wires are arranged in 72 radial drift layers, organised in 9 superlayers as can be seen in Figure 3.5 which shows a diagram of a CTD octant. The odd superlayers are *axial* layers with the sense wires arranged parallel to the beam axis. The even superlayers are called *stereo* layers, here the sense wires are inclined at angles of 5° with respect to the beam axis. Combined information of the axial and stereo layers permits determination the Z -position of the hits with a resolution of $\sigma_z = 1.4\,\mathrm{mm}$.

The three inner axial layers are additionally equipped with a z-by-timing system [Ba97]. It is implemented on all the wires of superlayer 1 and on half the wires of the superlayers 3 and 5. This system allows a fast determination of the Z coordinate of a track with a resolution of $\sigma_{\mathrm{zbt}} \simeq 3\,\mathrm{cm}$. It is used in the first and second level trigger (see below).

The resolution of the CTD is $230\,\mu\mathrm{m}$ in r-ϕ, leading to a track momentum resolution of $(0.005 \pm 0.0016)\,p_T$ for long tracks. Details of the track recognition are given in Section 5.2 in the chapter on particle definitions. The angle θ may be used to derive the *pseudorapidity* η, which is more commonly used and dined as:

$$\eta = -\ln\left(\tan\frac{\theta}{2}\right). \tag{3.1}$$

The Main Calorimeter

The main calorimeter [An91, Ber93, cal3] almost hermetically (with the exceptions of two $20 \pm 20\,\mathrm{cm}^2$ holes for the beam pipe) encloses the inner detector components. See [Kr92] for a detailed description and the results of test measurements. It is built as a sandwich calorimeter with alternating depleted uranium plates (3.3 mm thick $\simeq 1\,X_\circ$ radiation length) as the absorber material and plastic scintillator SCSN38 plates (2.6 mm thick) as the active material. Careful choice of materials and thickness of the plates results in complete compensation, one of the strongest features of the calorimeter, i.e. electromagnetic and hadronic showers induced by particles of the same incident energy yield equal response. The energy resolutions measured under test beam conditions were $\sigma(E)/E = 18\%/\sqrt{E} \oplus 1\%$ for electromagnetic showers and $\sigma(E)/E = 35\%/\sqrt{E} \oplus 2\%$ for hadronic showers.

The calorimeter is divided into three parts, referred to as FCAL, BCAL and RCAL for the forward, barrel and rear regions respectively. The three parts have overlapping polar regions as listed in Table 3.2. These overlapping regions are also called “crack regions”. Each part is divided into 3 (2 for RCAL) *sections*, the inner one is called *electromagnetic section* (EMC section) the outer one/two are called *hadronic sections* (HAC resp. HACI and HACII sections). Each calorimeter part is further divided into a number of *modules*. The RCAL and FCAL modules are 20 cm wide, and are further divided into readout cells

	FCAL	BCAL	RCAL
θ range	2.2° – 39.9°	36.7° – 129.1°	128.1° – 176.5°
Z coord. of EMC section	-152 cm		214 cm
$X_\circ$ of electromagnetic section	24	24	24
hadronic interaction length λ	7.14	4.92	3.99
size of EMC cells	$5 \oplus 20\,\mathrm{cm}^2$	11.25° in ϕ	$10 \oplus 20\,\mathrm{cm}^2$
transverse separation	3 sections	3 sections	2 sections
projectivity	no	only in EMC section	no

Table 3.2: *Technical details of the three parts of the main calorimeter*

Figure 3.6: *Diagram of a FCAL calorimeter module.*

measuring $20 \times 20\,\mathrm{cm}^2$ in the HAC sections, $10{\times}20\,\mathrm{cm}^2$ in the EMC section of the RCAL, and $5{\times}20\,\mathrm{cm}^2$ in the EMC section of the FCAL.

The three BCAL sections form cylindrical rings around the beam axis. The BCAL is subdivided into 32 modules of a wedge-shaped design, each module extends over an azimuthal angle of $11.25°$ in ϕ. Further devisions perpendicular to the beam axis form the BCAL readout cells.

Figure 3.6 shows a diagram of a FCAL module. It also illustrates the readout mechanism: light in the scintillator tiles of each readout cell is read out on both sides via a coupling to wavelength shifters guiding the signal to photomultipliers. Differences in the signal heights from the two photomultipliers allow reconstruction of the position of the incident particle relative to the centre of the tower.

The calorimeter provides accurate timing information with a time resolution better than

1 ns for energy deposits greater than 4.5 GeV. This has proven to be a powerful tool to reject beam-gas-related background efficiently at the trigger level.

The performance of the readout channels is monitored daily. For the calibration of their photomultipliers the natural radioactivity of U^{238} is used. It provides a very stable reference signal with <0.2% stability.

The Luminosity Monitor

The luminosity is monitored and measured using bremsstrahlung photons from the Bethe-Heitler process $ep \rightarrow e\gamma p$. The cross section of this process is known from QED to an accuracy of 0.5%. Thus measuring the photon rate allows a very precise determination of the ep luminosity at the ZEUS interaction point.

Photons with $\theta_\gamma < 0.5\,\mathrm{mrad}$ are measured in a small lead-scintillator calorimeter placed at $Z = -107\,\mathrm{m}$ [An92, Pi93]. The photons exit the beampipe through a copper-beryllium window at $Z = -92\,\mathrm{m}$. Under test beam conditions the energy resolution of the calorimeter was found to be $18\%/\sqrt{E}$. A carbon-lead filter placed in front of the calorimeter as a shield against synchrotron radiation reduces the energy resolution to $23\%/\sqrt{E}$. Two layers of 1 cm wide crossing scintillator strips are installed at a depth of $7\,X_\circ$ to provide a means for position reconstruction. The achieved resolution is 0.2 cm in both X and Y.

The Online Trigger System

The total interaction rate observed at HERA is dominated by interactions of the proton beam with the residual beam gas. These interactions take place at a rate of 10 – 100 kHz and thus are a severe source of background to deep inelastic scattering , which takes place at a rate of only a few Hz. *Photoproduction*, i.e. neutral current ep scattering in the limit of very low values of momentum transfer ($Q^2 \ll 1\,\mathrm{GeV}^2$), also has a much higher cross section than DIS and presents another source of background. It is an interesting field of study in itself and thus photoproduction events are also written to tape. However, they need to be *prescaled*, i.e. only a fraction of them is recorded. Other sources of background to the DIS events are interactions of the electron beam with beam gas, beam halo interactions and cosmic ray events.

It is thus the task of the trigger system to identify the process type (DIS, photoproduction or other) and to suppress background-induced events efficiently without losing interesting physics events. It is a challenging task given a bunch crossing time of 96 ns and roughly 250,000 readout channels to cope with. The eventual rate with which events are written out on tape must not be higher than a few Hz. Deadtime caused by the trigger or by the readout process must be avoided.

As even the fastest trigger needs more time than 96 ns to give a reliable decision, the information from the readout channels needs to be stored for up to 58 bunch crossings, allowing for in total $5.6\,\mu$s trigger decision time. For the calorimeter special pipeline chips were designed [He91] which meet this requirement and which are used also in other detector components.

The ZEUS online trigger system consists of three levels, referred to as FLT, *first level trigger*, SLT, *second level trigger* and TLT, *third level trigger*. Figure 3.7 shows the structure

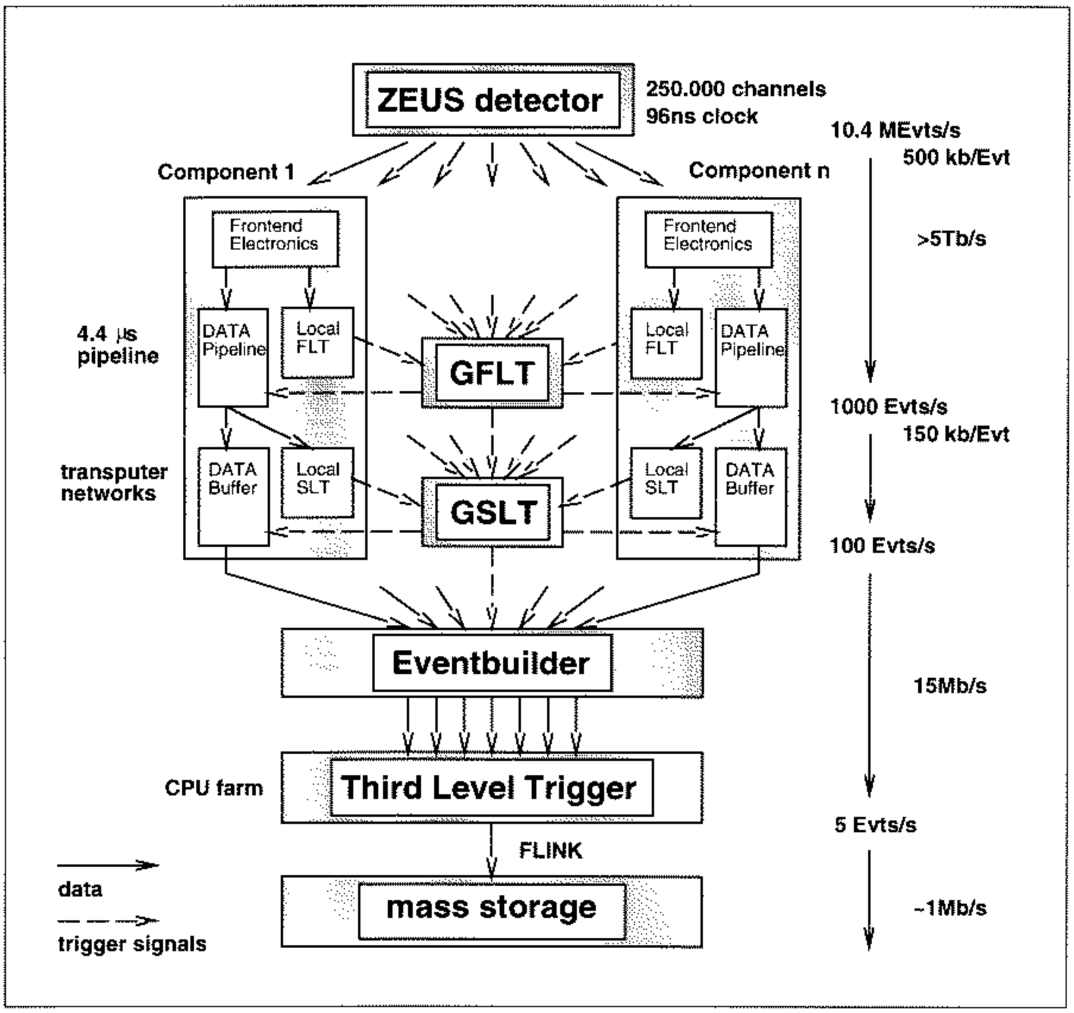

Figure 3.7: *The ZEUS three level online trigger system*

of the different levels schematically.

The FLT is a hardware trigger, with each component having its own FLT and storing information in seperate pipelines. The individual component decisions are reported to the *GFLT* (general FLT) $2\,\mu s$ after the bunch crossing. A GFLT decision is made based on the component information. The output rate must be kept below 1 kHz.

The SLT consists of a programmable transputer network. This permits the use of more sophisticated algorithms for identifying and rejecting background. The output rate has to be degrades to below 100 Hz.

After a positive decision of the GSLT, the data is sent to the *event builder*. Component information is combined into a single data set, then made accessible for the TLT, and is transferred into ADAMO [Fi94] format. Following a positive TLT decision the data is written to tape remotely via a fibre link (FLINK) connection and is then available for offline reconstruction.

Offline Event Reconstruction and Detector Simulation Packages

The program package ZEPHYR [Ts91] is the ZEUS offline event reconstruction program. It can be fed with either real data – the TLT output – or Monte Carlo generated events.

Monte Carlo events are generated using the AMADEUS environment, which provides an interface to the Monte Carlo generators ARIADNE [Lo] and HERWIG [Ma91, Ma96], which are used in this analysis. The AMADEUS output is passed to the program package MOZART [ZEUS93a], a full simulation of the ZEUS detector using the CERN GEANT package [Br89]. The trigger simulation program ZGANA [ZEUSa] is run before the generated events are passed to the reconstruction program.

A Common Ntuple for DIS Analyses

Data access and analysis processing can be further facilitated by creating a data structure called *ntuple*. Ntuples can be accessed very quickly in comparison to ADAMO banks, the output format of ZEPHYR. While creating the ntuples, an event preselection can be applied to reduce the ntuple size and to frther speed up the later ntuple-based analysis.

Common group ntuples [ZEUSb] have been created for the data sets 1995 – 1997 as well as for several sets of neutral current Monte Carlo generated events. Only DIS events with $Q^2 > 4\,\mathrm{GeV}^2$ are selected. All relevant information such as calorimeter cell information, reconstructed tracks and electron information is included. Thus these ntuples are the ideal data structure for the analysis of the hadronic-final state of DIS.

A detailed description of the applied data selection is given in the following chapter.

Chapter 4

Preparing the Data Sample

This chapter provides detailed information on the process of selecting the event sample for the analysis from the 1996 and 1997 ZEUS data sets. The methods for reconstructing the kinematic variables are presented in Section 4.2. A list is given of the applied kinematic cuts. These limit the theoretically-accessible kinematic region provided by the HERA machine to a region where reconstruction tools work reliably.

The key signature of neutral current DIS is the presence of the scattered electron in the final state. Thus the main requirement of DIS filter in the ZEUS three-level online trigger system as introduced on page 29 is a significant amount of energy observed in the electromagnetic sections of the calorimeter. Section 4.3 lists the requirements which an electromagnetic cluster in the calorimeter has to fulfil in order to be designated as the scattered electron candidate.

Events from various types of background processes contaminate the data sample, for example cosmic muon events or beam interactions with the residual gas in the beam pipe. In Section 4.4 a set of cleaning cuts is introduced, which have been applied in order to minimize the number of background events in the sample.

The accessible kinematic plane was then divided into 14 *analysis bins*. They are defined in Section 4.5. Events passing all cuts are assigned to them according to their reconstructed values of x_{DA} and Q^2_{DA}. The efficiencies and purities of the bins are very good, typically they are higher than 70%.

At the end of this chapter the obtained resolutions of Q^2_{DA}, x_{DA}, E' and γ_{boost} in the analysis bins are shown. An additional cut – named *infrared cut* – has to be applied (Section 4.5). This cut suppresses events with soft particle migration into the current region.

4.1 Available Data and Monte Carlo Samples

The analysis is performed with the 1996 and 1997 data sets taken with the ZEUS detector. The amount of useful data written to tape corresponds to a luminosity of $10.7\,\mathrm{pb}^{-1}$ for the year 1996 and of $27.7\,\mathrm{pb}^{-1}$ for 1997 respectively. This adds up to a total of $35.4\,\mathrm{pb}^{-1}$ of luminosity.

Two different Monte Carlo samples were available. ARIADNE [Lo] was chosen to be the default Monte Carlo model. Almost $220\,\mathrm{pb}^{-1}$ worth of luminosity was generated in three samples of 200 k events each and with a threshold of $Q^2 > 40\,\mathrm{GeV}^2$, $Q^2 > 100\,\mathrm{GeV}^2$ and $Q^2 > 400\,\mathrm{GeV}^2$ respectively. ARIADNE Version 4.08 was used for the simulation, it was interfaced to HERACLES [Kw92] with DJANGO6, version 2.4 [Ch94]. The CTEQ-4D set of structure functions [CTEQ85] was used.

A HERWIG [Ma91, Ma97, Ma96] sample was used for cross checks and for determining the systematic error arising from the model dependence of the analysis. The available sample was smaller than the ARIADNE sample, it consists of 150 k events above a threshold of $Q^2 > 100\,\mathrm{GeV}^2$, which corresponds to a luminosity of $21\,\mathrm{pb}^{-1}$. For the HERWIG sample the GRV-94, H0 set of structure functions [Gl95] was used.

4.2 Kinematic Reconstruction and Kinematic Cuts

Several methods have been proposed for reconstructing the kinematic variables x_{bj}, Q^2 and y from the final state observed in the detector [Bent92]. In this analysis three different methods have been used, which are presented here. Only two of the three kinematic variables are independent, thus only the equations for Q^2 and y are given below.

A. Electron Method

As the name suggests, this method uses only information from the scattered electron. Q^2_{ele} and y_{ele} are derived from the scattering angle θ' and the energy of the scattered electron E' :

$$Q^2_{\mathrm{ele}} = 2E_e E'(1+\cos\theta') \tag{4.1}$$

$$y_{\mathrm{ele}} = 1 - \frac{E'}{2E_e}(1-\cos\theta') \tag{4.2}$$

B. Jacquet-Blondel Method

This method was proposed in [Ja79]. Q^2 and y are derived only from hadronic information in the sense that the sums in the following equations are over all calorimeter cells with an energy deposit not associated with the scattered electron.

$$\delta_{\mathrm{h}} = \sum_h (E_{\mathrm{h}} - p_{\mathrm{z,h}}) \tag{4.3}$$

$$P_{\mathrm{T,h}} = \sqrt{\left(\sum_h p_{x,h}\right)^2 + \left(\sum_h p_{y,h}\right)^2} \tag{4.4}$$

$$y_{\mathrm{JB}} = \frac{\delta_h}{2E_e} \quad \text{with } E_e \text{initial electron energy} \tag{4.5}$$

$$Q^2_{\mathrm{JB}} = \frac{P^2_{\mathrm{T,h}}}{1-y_{\mathrm{JB}}} \tag{4.6}$$

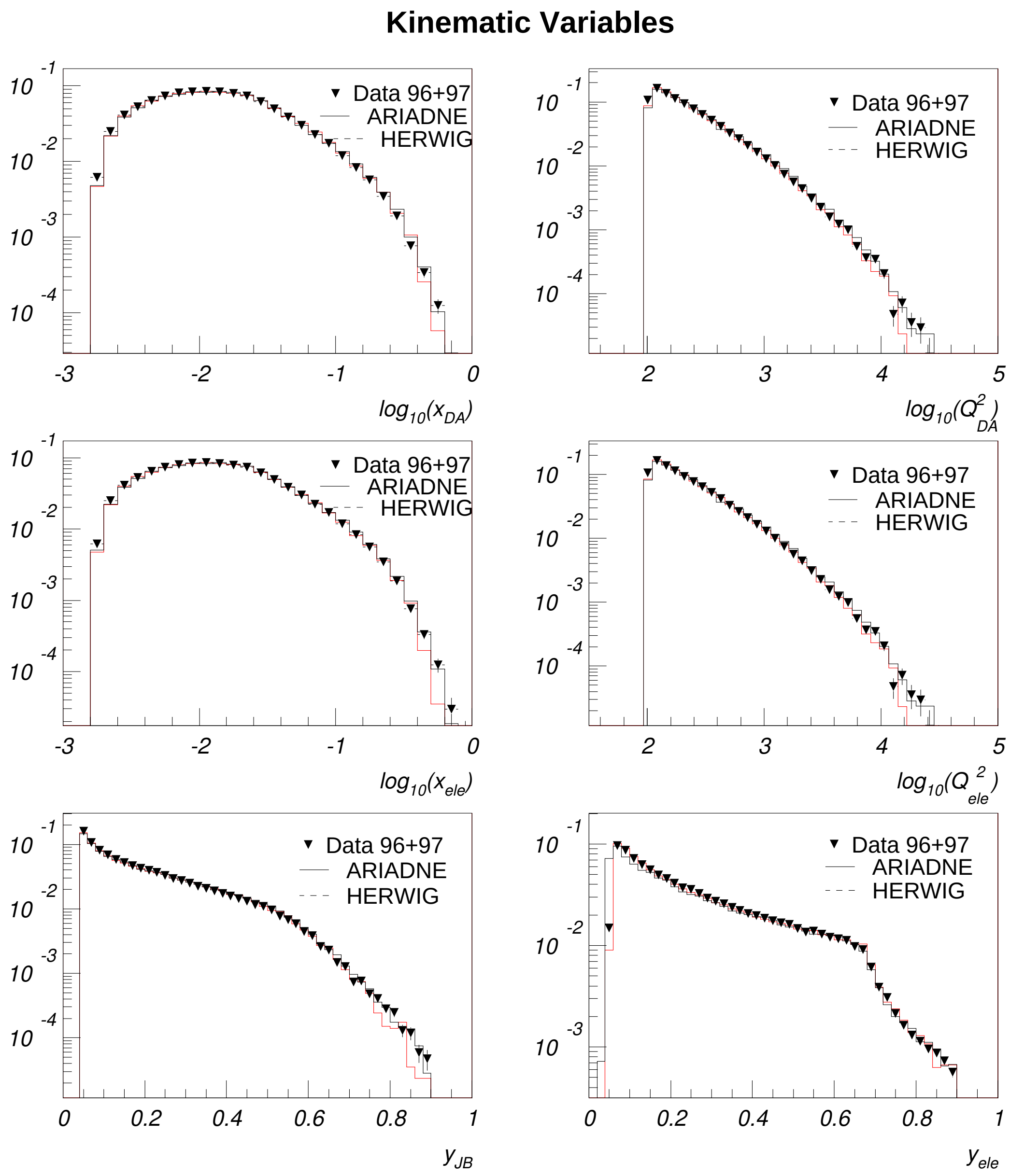

Figure 4.1: *Reconstructed kinematic variables. The data sample (triangles) is compared to the ARIADNE and HERWIG Monte Carlo samples (solid and dashed line respectively). The overall agreement is very good, however, the HERWIG sample slightly underestimated the data in the high y - high x_{bj} region.*

C. Double Angle Method

This method determines the kinematic variables from the scattering angles θ' of the electron and γ_h of the current jet. The scattering angles can be measured accurately and are in particular independent of the calorimeter energy scale.

$$\cos\gamma_h = \frac{P_{T,h}^2 - \delta_h^2}{P_{T,h}^2 + \delta_h^2} \tag{4.7}$$

$$Q_{\mathrm{DA}}^2 = 4E_e^2 \frac{\sin\gamma_h\,(1+\cos\theta')}{\sin\gamma_h + \sin\theta' - \sin(\theta'+\gamma_h)} \tag{4.8}$$

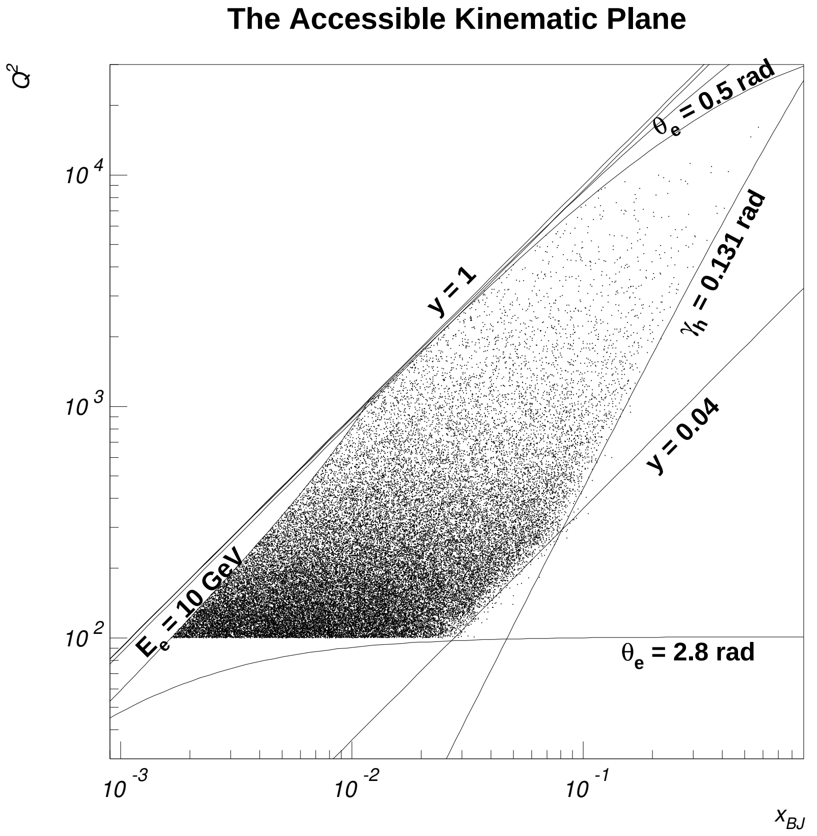

Figure 4.2: *The accessible kinematic plane as it is restricted by the kinematic cuts. A point is plotted for each event passing the kinematic cuts, where the values of* x_{bj} *and* Q^2 *have been derived with the double angle reconstruction method. (Only the 1996 data set is shown in this histogram.)*

$$y_{\mathrm{DA}} = \frac{\sin\theta'\,(1-\cos\gamma_h)}{\sin\gamma_h + \sin\theta' - \sin(\theta'+\gamma_h)} \tag{4.9}$$

Figure 4.1 shows the kinematic variables x_{DA}, Q^2_{DA}, x_{ele}, Q^2_{ele}, y_{ele} and y_{JB} for the data sample compared to the detector level of the Monte Carlo samples. An overal good agreement is observed. The HERWIG sample shows slight disagreement to the data in the high y - high x_{bj} region. A set of *kinematic cuts* is applied as described in the following. The resulting accessible kinematic region for the analysis is shown in Figure 4.2.

1. **$Q^2_{\mathrm{DA}} > 100\,\mathrm{GeV}$**

   As will be discussed in more detail in the following Section 4.3, a track is required to match the electron cluster. The geometrical acceptance of the CTD allows electron angles to be measured only in the angular range $\theta' \in [0.3,\ 2.8]\,\mathrm{rad}$. Thus the kinematic region of the analysis is limited at the lower end to values of $Q^2 > 100\,\mathrm{GeV}$, as may be derived from Equation 4.1.

2. **$\gamma_h > 0.131\,\mathrm{rad}$**

   For very low values of γ_h the current jet overlaps with the proton remnant or particles of the current jet escape into the forward beam pipe. Consequently measurement errors of the double angle variables increase, especially in higher x_{DA} regions. This will also lead to a mismeasurement of multiplicity and energy in the current region of the Breit frame. The choice of $\gamma_h > 0.131\,\mathrm{rad}$ (15°) was motivated by the acceptance region of the CTD.

3. **$y_{\mathrm{JB}} > 0.04$**

   The resolution of the hadronic scattering angle γ_h increases with increased hadronic energy in the calorimeter. Kinematic reconstruction for events with very little hadronic energy is sensitive to the effects of uranium noise and noise in the electronics. According to Equation 4.5, y_{JB} is a measure of the amount of hadronic energy in the calorimeter. Thus cutting on very low values of y_{JB} ensures the double angle variables are reconstructed with satisfactory precision.

4. **$y_{\mathrm{ele}} < 0.9$**

   Photoproduction events with a faked electron have the tendency to give values of very high reconstructed y_{ele}. A cut of $y_{\mathrm{ele}} < 0.95$ is therefore applied at the trigger level. This cut is tightened further to $y_{\mathrm{ele}} < 0.9$ in the offline analysis.

5. **$y_{\mathrm{JB}} < 0.9$**

   For the same reason, a cut of < 0.9 is applied to y_{JB}.

4.3 Electron Finding

The electron-finding algorithm used in this analysis is based on a neural network[1] [Ab95]. The network was trained with Monte Carlo events and test beam data. Details can be found in [Si97]. In a first step all calorimeter cells with an energy deposition above the noise threshold (see below) are clustered into *tower islands.* A probability is assigned to each island according to the cluster topology, thus providing a measure of the likelihood that the island was produced by an electromagnetically-showering particle. The probability values range from 0 to 1, with higher values associated to electronmagnetically induced showers.

1. **Energy $> 10\,\mathrm{GeV}$**

   The neural network electron finder has been shown to be almost 100% efficient for electron energies above 10 GeV [Ab95]. For lower electron energies, the efficiency drops to 50%. Furthermore this drop is not exactly reproduced in the Monte Carlo. Therefore a minimum energy of 10 GeV is required.

---

[1] more precisely: a feed-forward neural network with an error back-propagation (FFBP) training algorithm

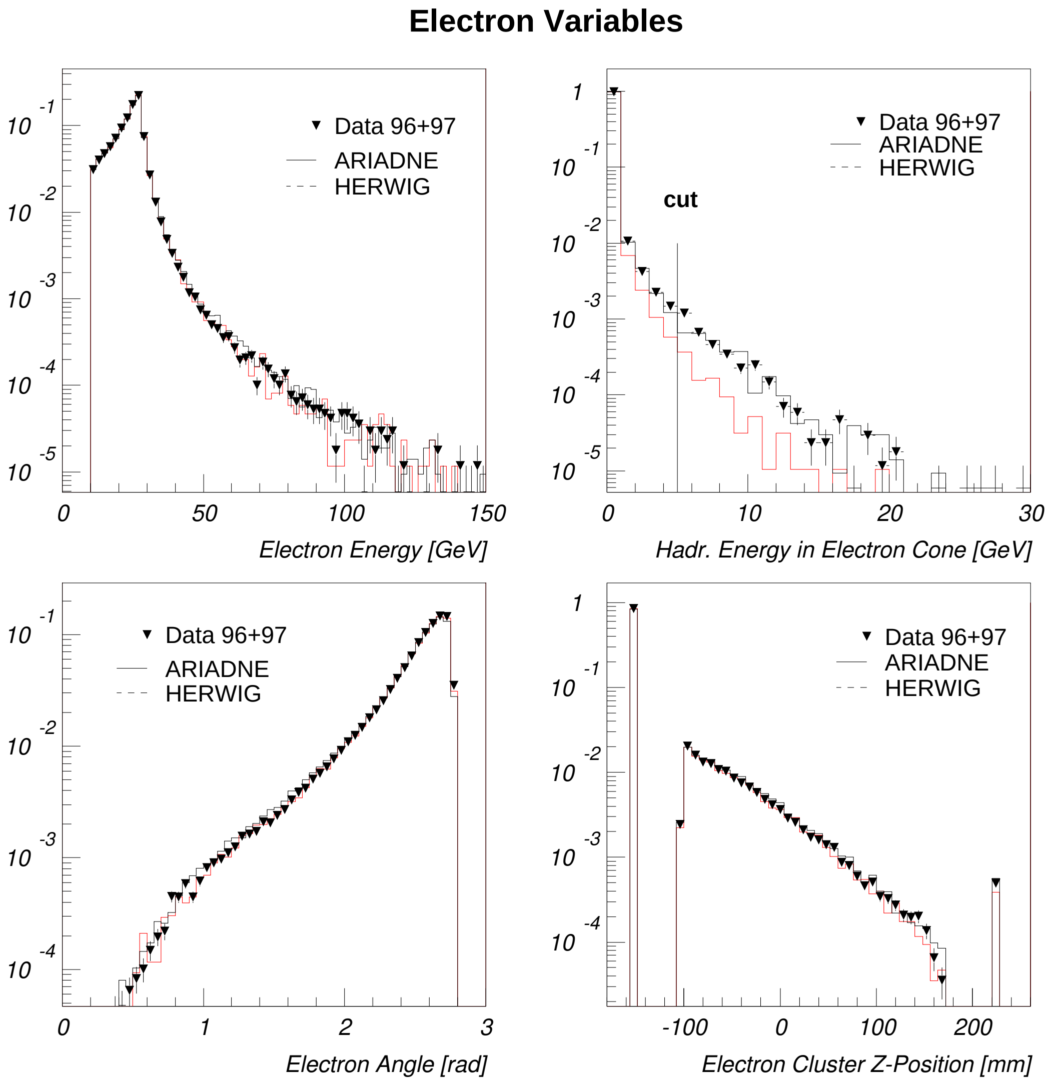

Figure 4.3: *Electron observables. The data sample (triangles) is compared to the two Monte Carlo samples (solid lines for ARIADNE and dashed lines for HERWIG). The number of events with an electron scattered into the forward part of the BCAL ($Z_{\mathrm{ele}} > 50\,\mathrm{mm}$) is underestimated in the HERWIG sample, and also the number of events with a significant amount of energy in the η-ϕ cone around the electron center position.*

2. Probability > 0.9

For electron candidates only islands with an assigned probability value of more than 0.9 are accepted. If more than one island passes this cut, the candidate with the highest probablity is chosen to be the electron candidate.

3. Cone Isolation

Electrons within jets may be misidentified as the scattered electron. These fake electrons are in close proximity to energy deposits from other particles belonging to the same jet. They are suppressed by requiring the scattered electron to be isolated. Electron candidates are rejected if, within a cone of radius 0.8 in the η-ϕ plane, the energy deposition not identified with the scattered electron cluster exceeds 5 GeV.

4. **Matching Track with $p_{trk} > 8\,\text{GeV}$**

The number of falsely-identified electrons is further reduced by requiring a track in the CTD pointing to the electron cluster. The extrapolation of the track must coincide within 10 cm with the centre of the electron cluster. The geometrical acceptance of the CTD limits the measurable scattering angle to $\theta' \in [0.3, 2.8]$ rad.

A minimal momentum of $p > 8$ GeV is required for the electron track. The numerical value is deliberately chosen to be smaller than the required minimal energy of 10 GeV in order to allow for fluctuations in the energy measurement.

A calorimeter island fulfilling all the above requirements is identified with the scattered electron. The electron observables E', θ', the Z-position of the scattered electron and the amount of hadronic energy inside the electron cone are shown in Figure 4.3. An overall good agreemen between the data and the two Monte Carlo samples is observed. However, the HERWIG sample underestimates the number of electrons scattered into the forward region of the BCAL. Also the amount of hadronic energy inside the electron cone is found to be underestimated in the HERWIG sample.

The four-vector of the scattered electron is reconstructed using the angles θ' and φ' as measured in the CTD. The energy of the electron cluster is replaced by a double-angle corrected energy: the Q^2 value obtained with the double angle method and the electron scattering angle determine the electron energy according to Equation 4.1 where Q^2_{DA} replaces Q^2_{ele} . The double angle reconstruction method neglects the effects of initial state radiation on the kinematic variables and the reconstructed Q^2_{DA} values are slightly biased towards higher values (see Section 4.5 and the resolution histograms therein). Consequently also the double angle corrected electron energy is biased towards higher values of E'. This bias is tolerated since this method succeeds in eliminating uncertainties in the energy measurement arising from the calorimeter energy scale and calorimeter inhomogenities.

4.4 Cleaning Cuts and Applied Corrections

This section lists the applied *cleaning cuts*. Event selection cuts applied at trigger level are looser than cuts in the final offline analysis, a practice which leaves room for later offline correction of the data and minimises the danger of losing interesting physics events. Consequently, similar cuts are applied at each selection stage becoming tighter at more advanced stages. In this context offline analysis is regarded as a fourth selection level. In the following the applied cuts are presented in their final and tightest form, not distinguishing between the different trigger levels.

1. Require Valid *ep* Crossing Bunch

Several electron and proton bunches are accelerated in the HERA machine without a colliding proton or electron bunch. These *pilot bunches* are used for calibration of the luminosity system (as described on page 29) and for background studies. They are used for determining the amount of beam-gas background which is subtracted in cross section measurements. Events associated with one of the pilot bunches are likely to be either electron or proton beam gas events and are rejected in the DIS analysis.

2. Calorimeter Timing

The timing information of the calorimeter is an important tool for background rejection. An arrival time t_{iCAL} of particles is calculated for each calorimeter section iCAL $\in$ [FCAL, BCAL, RCAL] separately. Timing offsets are tuned such that particles from an *ep* collision at the nominal interaction point arrive at the calorimeter iCAL at the time $t_{iCAL} = 0\,\mathrm{ns}$. The times t_{iCAL} are computed as an energy-weighted mean of all photomultipliers with a signal above 200 MeV. If the summed energy in a calorimeter section exceeds 4.5 GeV, the following cuts are applied:

$$|t_{RCAL}| < 6\,\mathrm{n}s$$
$$|t_{FCAL}| < 8\,\mathrm{n}s$$
$$|t_{global}| < 8\,\mathrm{n}s$$
$$|t_{FCAL} - t_{RCAL}| < 8\,\mathrm{n}s$$

3. Longitudinal Momentum Containment

The quantity δ in the Equation 4.10 below gives a measure of how well the final state of an event is contained in the detector. Energy and momentum conservation requires the sum over energy and momenta of particles in the final state to be the same as for particles in the initial state. Since the momenta p_i of the incident electron and the incident proton consist almost entirely of a longitudinal component $p_{z,i}$, δ is derived from the energies and longitudinal momenta of the final-state particles as follows:

$$\delta \equiv \sum_f (E - p_z)_f = \sum_i (E - p_z)_i = \sum_i (E - \vec{p})_i = 2E_e \tag{4.10}$$

In practice δ is evaluated as a sum over the energy deposits in all calorimeter cells. At the trigger level, the energy measured in the photon calorimeter of the luminosity system is added to this quantity.

A histogram of δ is shown in Figure 4.4. The peak at twice the incident electron beam energy for events without energy loss inthe electron beam direction is smeared due to detector effects. A cut of $\delta \in [38, 60]$ GeV was applied in order to suppress hard initial-state radiation or photoproduction events. For these processes either the Bremsstrahlung photon or the scattered electron exits through the rear beam pipe

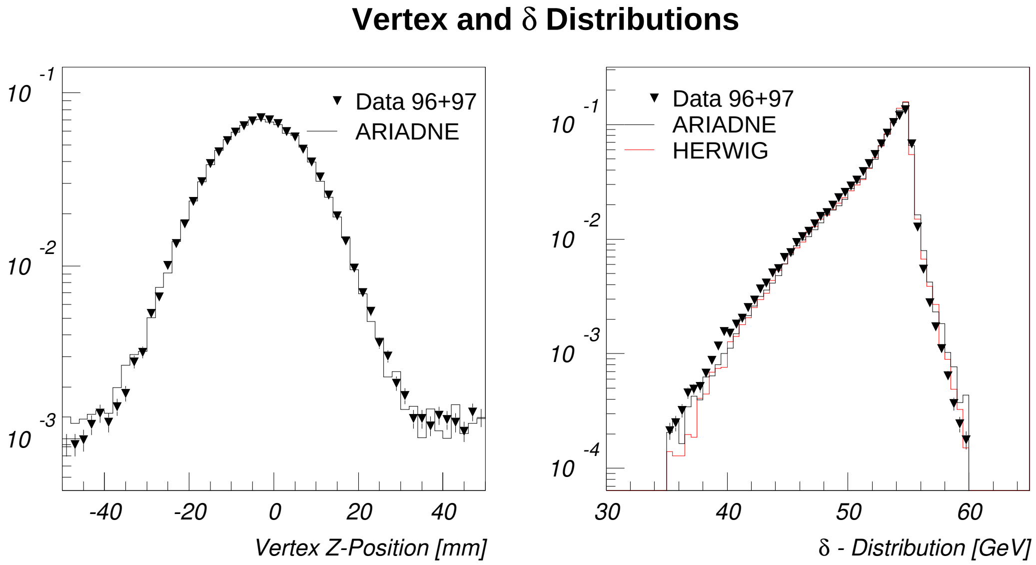

Figure 4.4: *Comparisons of data with Monte Carlo.* **Left:** *vertex distribution.* **Right:** *δ (or "$E - p_z$") distribution. The shape of the δ distribution is well reproduced by the monte Carlos, however the MC histograms are slightly offset to the data histogram. This may indicate remaining energy scale uncertainties (see point 10).*

resulting in considerably lower values of δ. Particle losses through the forward beam pipe are neglected: with a polar angle of almost 0° in the ZEUS coordinate system these particles do not contribute to δ.

4. Vertex $\in [-50, 50]$ cm

The reconstructed vertex is required to be close to the nominal interaction point. This ensures tracks to be reconstructed with high efficiency. The vertex distribution for the analysis data sample is shown in Figure 4.4

5. Cosmic Muon Rejection

Muons from cosmic showers can be identified by their characteristic signature. The detector is penetrated from top to bottom with detector components triggering sequentially along the muon path. An asymmetry is observed in the calorimeter timing derived for the top half and the bottom half seperately.

6. Beam Halo Muon Rejection

Muons from the beam halo penetrate the detector parallel to the beam axis and leave a pattern analogous to the cosmic muon signature: i.e. the calorimeter timing shows an asymmetry between forward and backward timing.

7. Elastic Compton Rejection

The characteristic signature of elastic Compton events is the exclusive presence of two electromagnetic clusters in the final state, one from the electron and one from the Compton-photon respectively. Consequently two electron candidates are found by the electron finder. Events are excluded if the energy deposits not associated with the two electromagnetic clusters is less than 2 GeV.

8. Data Quality Flagged Good

The aim of Data Quality Monitoring (DQM) is to provide databases for offline analysis with infomation concerning the data quality of a particular run. Runs – or part of runs – are rejected for instance if the CTD was partially off or suffered many trips, the magnets were not powered, or too many dead channels were detected in the calorimeter readout.

9. Calorimeter Noise Suppression

Calorimeter noise has two main sources: noise induced by uranium decays and noise in the photomultipliers. Offline noise suppression routines are available for both kinds of background.

On average energy deposition of 1 GeV per event is found in the calorimeter due to uranium decays. These deposits are randomly distributed over the calorimeter. Isolated energy deposition of $E < 100(150)$ MeV in EMC(HAC) cells are most likely to have been caused by uranium decays and are thus suppressed in the analysis.

Comparatively high signals can be induced in the photomultipliers by "sparks". These are sudden discharges of the static charge between a photomultiplier and its shielding. They can be detected by a large imbalance between the signal of the two photomultipliers of a cell. Cells with a relative imbalance > 0.8 for isolated cells with $E < 0.7$ GeV are suppressed.

A hit frequency is determined for each of the calorimeter cells. Some cells fire much more frequently than the average hit rate. These cells are referred to as *hot cells* and are suppressed in the analysis.

10. Energy Correction

Comparisons between data and Monte Carlo have shown a discrepancy in the calorimeter energy scale. In order to correct for this deviation, the energy measured in the calorimeter is scaled for data by + 5% in the RCAL and by + 2.5% in the BCAL. Since recently, more sophisticated values are recommeded which could not be implemented in this analysis anymore. The use of the older energy reconstruction here may explain the slight shift observed in the comparison between data and Monte Carlo δ distributions (Figure 4.4). As will be shown in Section 6.3, a variation of energy scale showed a negligible effect on the measurement result.

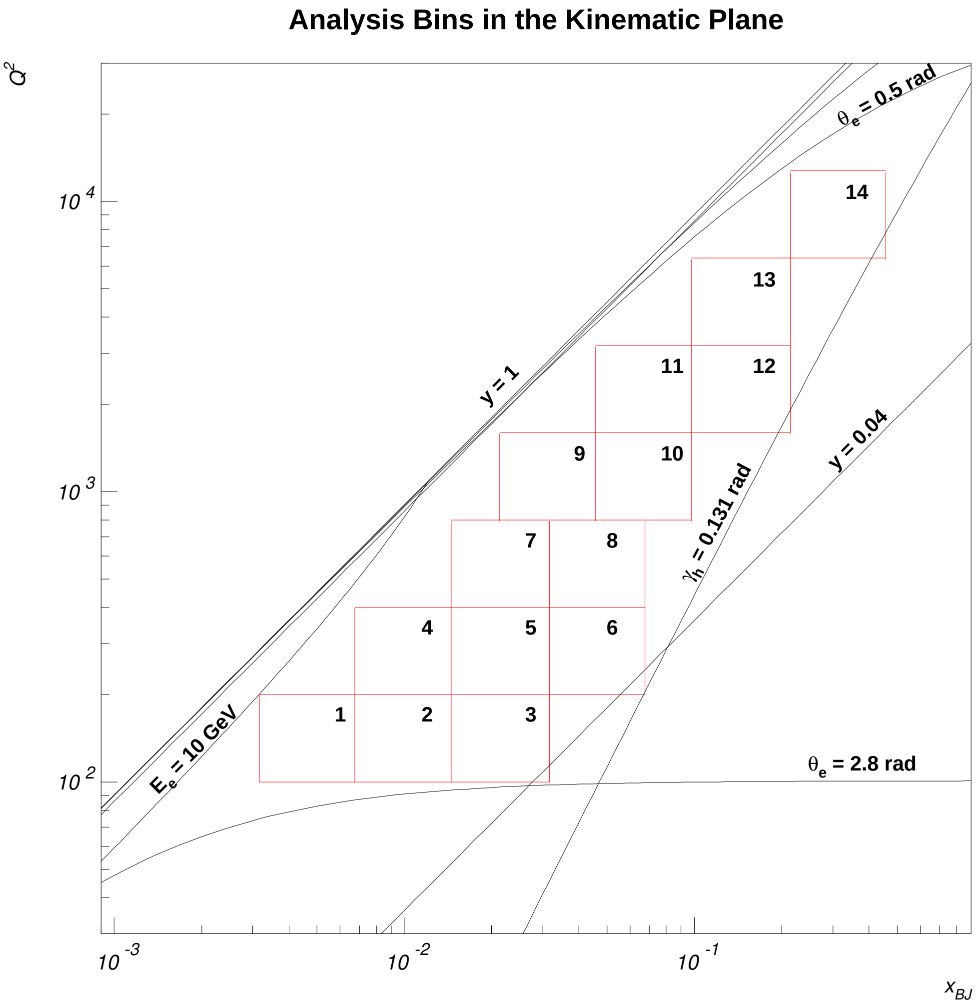

Figure 4.5: *Position of the 14 analysis bins inside the accessible (x_{bj}, Q^2) kinematic plane, which is limited by the kinematic cuts as shown.*

4.5 Analysis Binning and Resolution of Kinematic Variabels

A set of 14 analysis bins with different x_{bj} and Q^2 boundaries was defined in a way that they fit into the accessible kinematic plane. The analysis bins are shown in Figure 4.5 and their definitions are listed in Table 4.1.

Events are assigned to the analysis bins according to the reconstructed values of x_{DA} and Q^2_{DA} obtained with the double angle reconstruction method. At hadron level events are assigned according to the true generated values of x_{bj} and Q^2. The *resolutions* δ_{Q^2} and δ_x are a measure of how well a variable can be reconstructed. δ_{Q^2} and δ_x are determined from a Monte Carlo study using only the ARIADNE sample. The resolutions are defined as follows for a given bin i:

$$\delta_{Q^2} = \frac{Q^2_{\mathrm{da}} - Q^2_{\mathrm{true}}}{Q^2_{\mathrm{da}}} \qquad \text{resp.} \qquad \delta_x = \frac{x_{\mathrm{da}} - x_{\mathrm{true}}}{x_{\mathrm{da}}} \tag{4.11}$$

Bin number	x range	Q^2 range	efficiency [%]	purity [%]
1	0.00316 – 0.00676	100 – 200	71.6	64.2
2	0.00676 – 0.0145	100 – 200	72.3	67.6
3	0.0145 – 0.03162	100 – 200	69.6	60.9
4	0.00676 – 0.0145	200 – 400	70.	70.5
5	0.0145 – 0.03162	200 – 400	71.	71.5
6	0.03162 – 0.0676	200 – 400	63.8	64.9
7	0.0145 – 0.03162	400 – 800	78.6	76.6
8	0.03162 – 0.0676	400 – 800	74.4	72.6
9	0.0213 – 0.0457	800 – 1600	72.9	76.5
10	0.0457 – 0.0977	800 – 1600	75.1	76.2
11	0.0457 – 0.0977	1600 – 3200	75.3	78.2
12	0.0977 – 0.2137	1600 – 3200	69.7	76.1
13	0.0977 – 0.2137	3200 – 6400	78.2	79.3
14	0.2137 – 0.456	6400 – 12800	71.3	76.6

Table 4.1: *The Analysis Bins.*

δ_{Q^2} and δ_x are shown in the Figures 4.6 and 4.7 for each analysis bin individually. A Gaussian was fitted to each of the histograms, the mean and σ values of the fits are summarised in an additional histogram.[2]

The Q^2_{DA} resolution is very good and increases in bins with higher Q^2_{DA} values. For a small fraction of events a systematic pull is observed towards higher Q^2_{DA} values. (These are the events which end up in the right hand side of the δ_{Q^2} resolution histograms.) This pull is explained with initial state radiation where the photon carries away a fraction of the electron energy. This leads to a reduced Q^2 of the event, a shift which is neglected by the double angle reconstruction method.

The x_{DA} resolution is poorer than the Q^2_{DA} resolution, but still acceptable with a σ of $\leq 20\%$ and an improvement towards higher Q^2 bins. For a small fraction of events the reconstructed x_{DA} value systematically underestimates the true x_{bj} value. The fraction of wrongly reconstructed events increases in bins at larger x_{bj} for a fixed Q^2 range. For these higher x_{bj} values the current jet as arising from the struck parton is scattered into the forward region where it may overlap with the proton remnant. Consequently measurement errors may increase.

---

[2] A gaussian function obviously does not fit the histograms correctly. For example, for a small fraction of events the reconstructed Q^2 value is systematically biased to higher values. This systematic pull has a strong effect on the resulting mean and RMS of the distribution. So fitting a gaussian can still prove useful for *most* of the events.

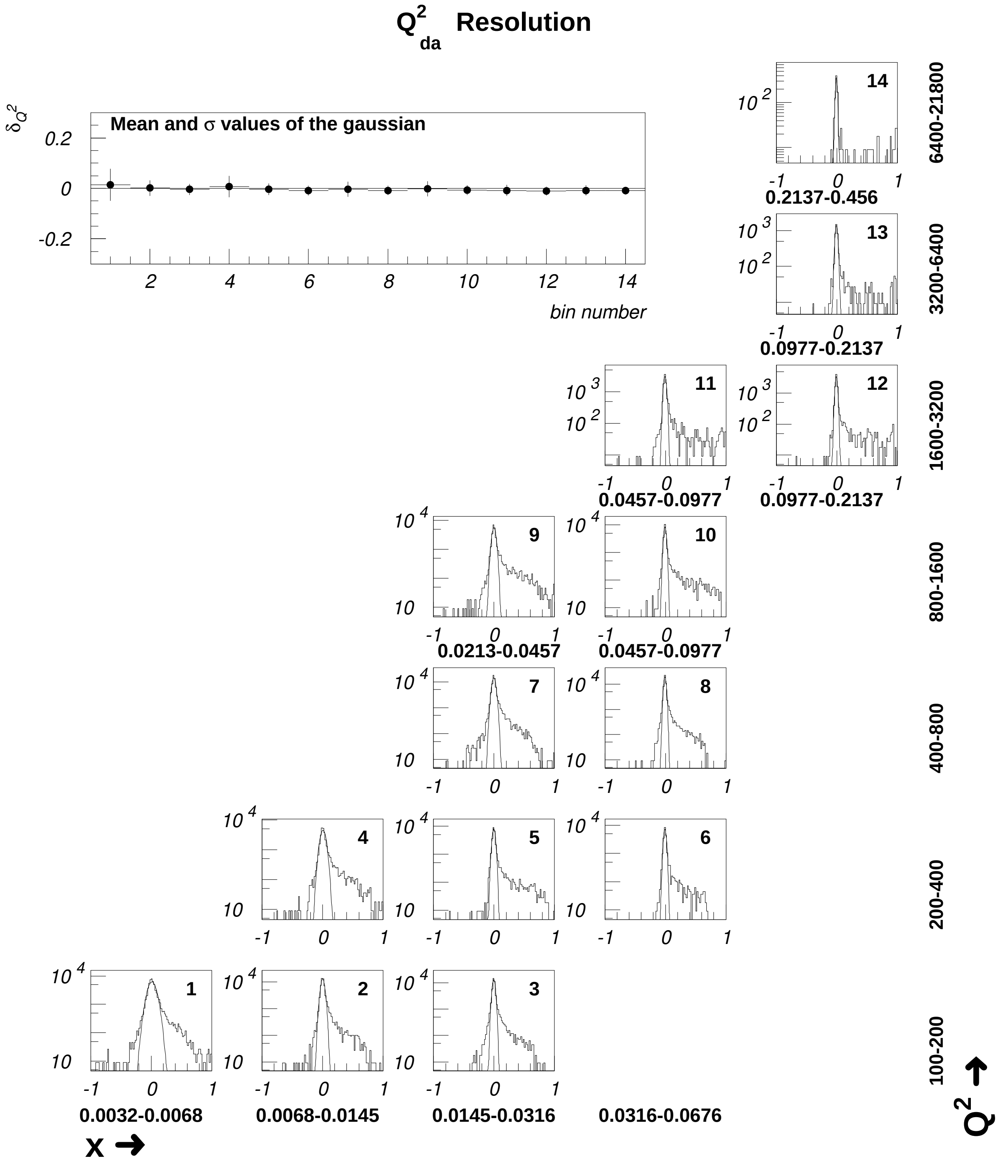

Figure 4.6: *Resolution of* Q^2_{DA} *for each analysis bin. The resolutions are very good with further improvements in bins at higher* Q^2_{DA} *values. A gaussian was fitted to each of the histograms. The resulting mean and* σ *values of the fits are shown in the large histogram. A small fraction of events is systematically pulled towards higher* Q^2_{DA} *values. This effect is explained by initial state radiation which is simulated in the Monte Carlo but neglected in the double angle reconstruction method.*

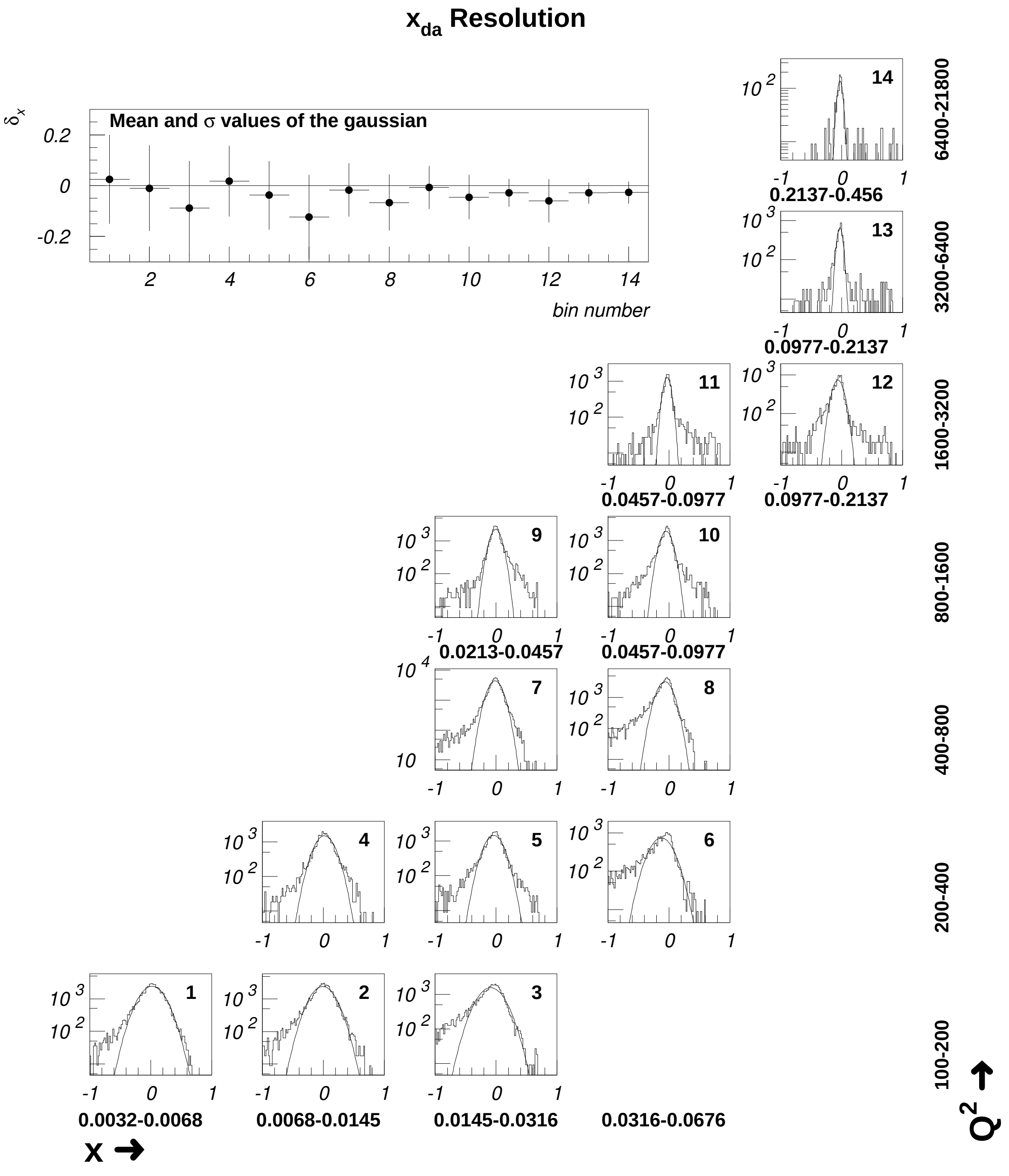

Figure 4.7: *Resolution of x_{DA} for each analysis bin. A gaussian was fitted to each of the histograms. The resulting mean and σ values of the fits are shown in the large histogram. The observed resolutions are generally poorer than the Q^2_{DA} resolutions, but increase for bins at higher Q^2_{DA} values. The fraction of events where the x_{DA} underestimates the true x_{bj} value is increasing in bins at larger x_{bj} at a given Q^2 range. This effect is explained by overlap of the current jet with the proton remnant.*

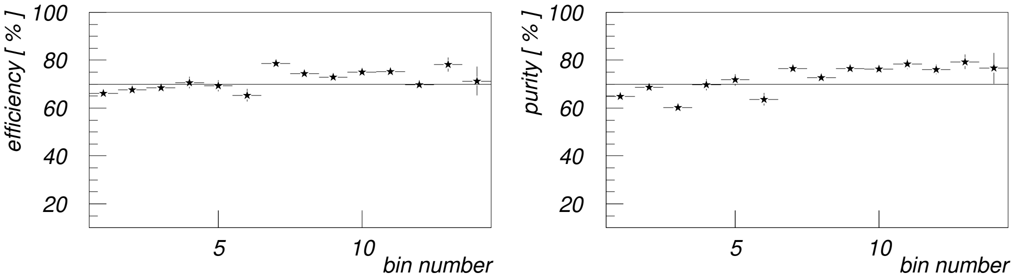

Figure 4.8: *Efficiencies (left hand side) and purities (right hand side) for each* $(x_{\rm bj}, Q^2)$ *bin. The line is indicating 70%.*

The quality of a choice of bins is reflected in the resulting *efficiencies* and *purities* of the bins. They are obtained from the a Monte Carlo study with the ARIADNE sample and are defined as followes:

$$\text{efficiency in } i = \frac{\text{number of events generated } \oplus \text{ reconstructed in } i}{\text{number of events reconstructed in } i}$$

$$\text{purity of } i = \frac{\text{number of events generated } \oplus \text{ reconstructed in } i}{\text{number of events generated in } i}$$

Figure 4.8 shows the efficiencies and purities for the used set of bins. They are both very high with values above 70% in most of the bins.

Electron and Boost Resolution

Figure 4.9 shows the resolution δ_E of the electron energy for each analysis bin. The overall resolution is excellent. However, for a small fraction of events the resolution is biased to higher values. (These are the events which end up in the right hand side of the δ_E histograms.) This bias is connected to the bias already observed in the δ_{Q^2} histograms: the reconstructed value of Q^2_{DA} is used for correcting the electron energy, if Q^2_{DA} is overestimated, also $E_e^{'}$ is overestimated.

The value of γ_{boost} is determined from the scattered electron and the reconstructed x_{DA} value. Measurement errors of these observables will propagate into the measurement error of γ_{boost}. Since the resolution of $E^{'}$ (Figure 4.9) is better than the resolution of x_{DA} (Figure 4.7), it is expected that the measurement error of x_{DA} gives the larger contribution to the measurement error of γ_{boost}.

Figure 4.10 shows the resolution $\delta_{\gamma_{\mathrm{boost}}}$ of the boost vector. The resolution is poorer in bins at larger x_{bj} for a given Q^2 range, as has already been observed in the histograms showing the x_{DA} resolutions. This decrease in resolution leads to poorer effciency and purity in the differential event shape distributions for bins at higher x_{bj}, as will be shown later.

Infrared Cut Against Soft Particle Migration

For some events the current region of the Breit frame is depopulated and all particles are found in the target region. However, soft particles may migrate from the target into the current region and thus smear out the event topology. An *infrared cut* is applied in order to suppress these events in the calculations. Figure 4.11 shows the energy E_{CR} found in the current region divided by the reconstructed Q^2 of an event. The distributions peak at around 0.4 in all analysis bins. Events with very low values of E_{CR}/Q are likely to be events with no particles in the current region. As can be seen from the histograms, a cut of $E_{CR}/Q > 0.1$ is reasonable. This cut is equivalent to requiring 10% of the hadronic final state energy to be found in the current region.

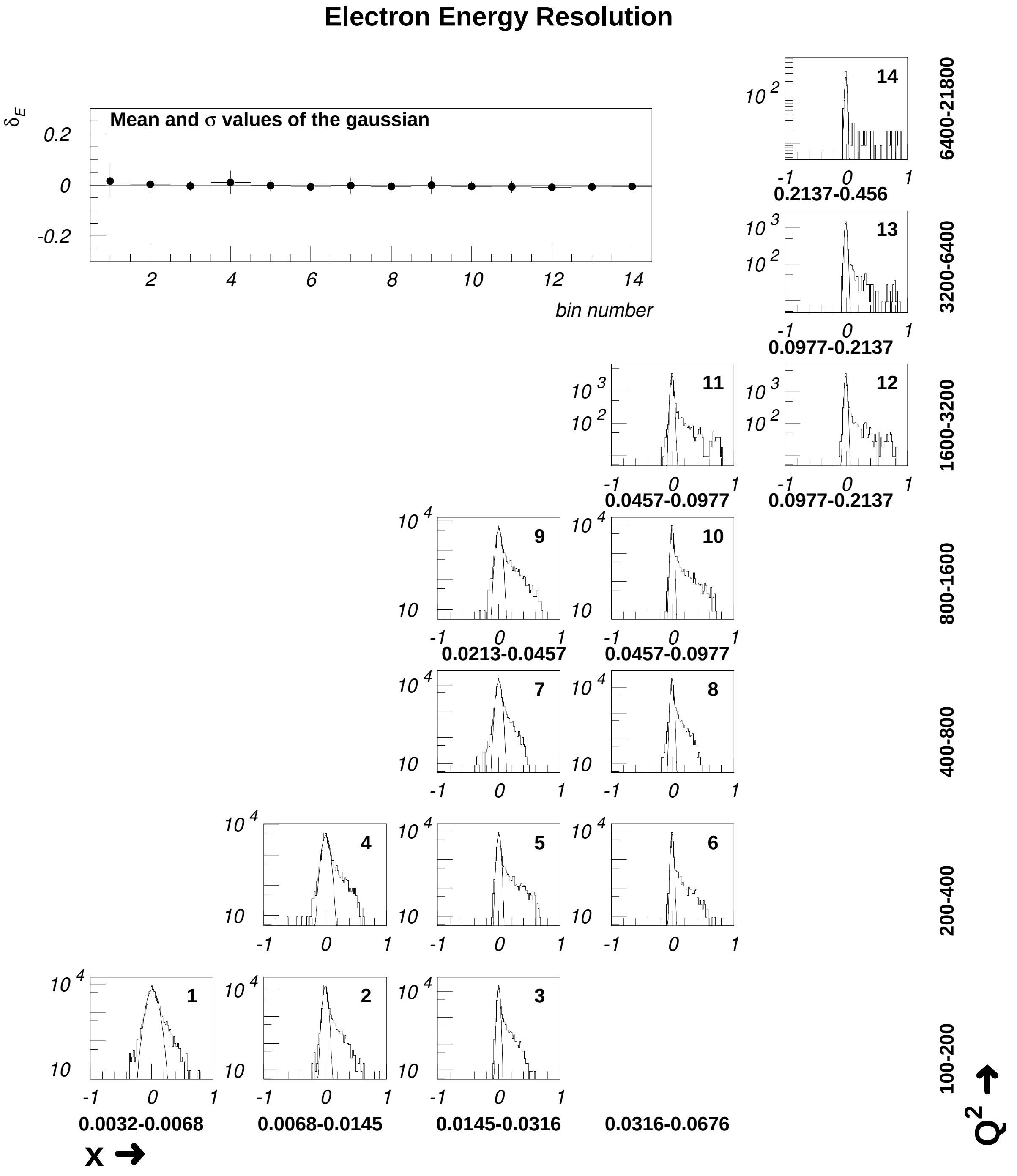

Figure 4.9: *Electron energy resolution. The reconstructed value of* Q^2_{DA} *is used for correcting the measured electron energy. This method minimizes the influence of calorimeter inhomogeneties. However it leads to a systematic overestimation of the electron energy for events with initial state radiation, as observed in the histograms of the* Q^2_{DA} *resolution.*

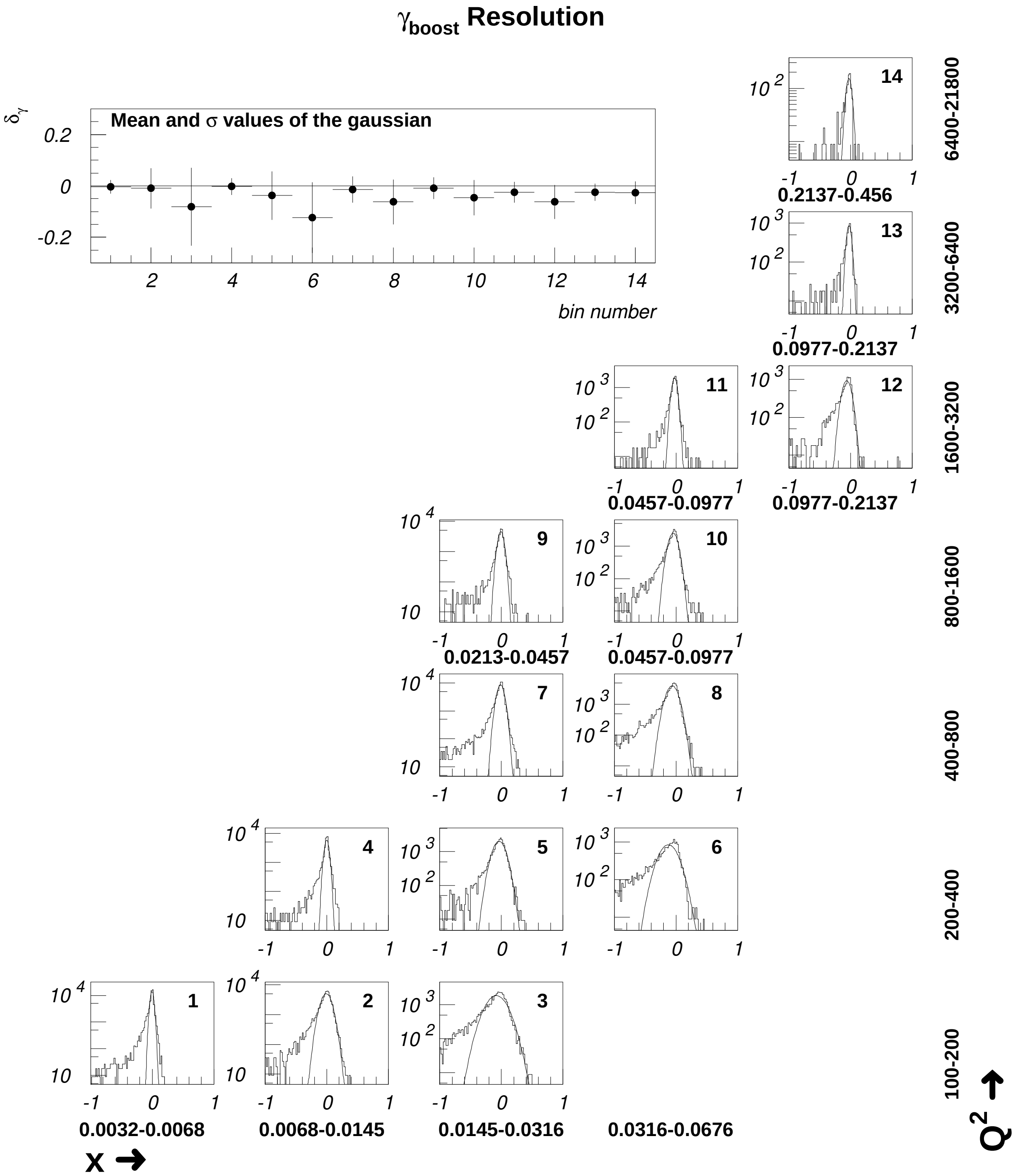

Figure 4.10: *Boost resolution. The resolution $\delta_{\gamma_{\rm boost}}$ is determined by the resolution of E' and $x_{\rm DA}$, where $x_{\rm DA}$ is expected to give the larger contribution. In fact the histograms show a pattern similar to the one observed in Figure 4.7.*

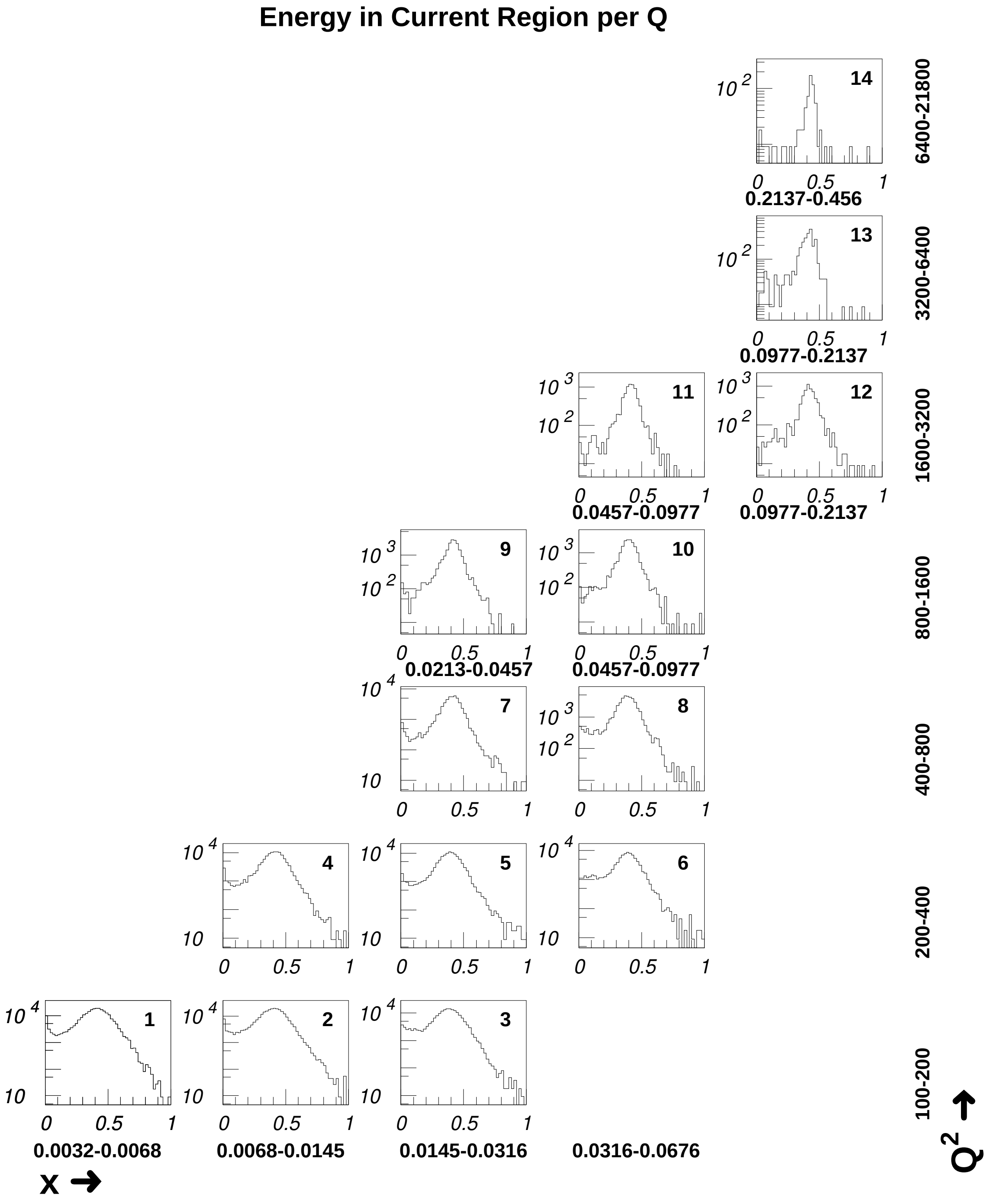

Figure 4.11: *Energy in the current region of the Breit frame E_{CR} divided by Q. For event with very low values of E_{CR}/Q the energy in the current region is produced by a soft parton migrating in from the target region and the current Region was originally depopulated. A cut of $E_{CR}/Q > 0.1$ is applied.*

Chapter 5

Tracking, Clustering and Matching

The event shape variables under study are defined as sums of particle four momenta found in the Current Region of the Breit frame (Equations 2.10 to 2.13). Thus the analysis results depend crucially on how well the particle four-momenta are reconstructed. Errors in the momentum reconstruction not only propagate into errors of the event shape variables, but also lead to migrations of particles from the Current Region into the Target Region and vice versa.

In the first section a definition is given of what is refered to as *hadron level* in the event generation. A classification according to lifetime is made. Particles at the hadron level are used to calculate the "true" event shape variables. Consequently they are used for resolution studies and for the correction of detector effects.

Tracks in the CTD are used for identifying charged particles. In Section 5.2 a description is given of the track reconstruction. The achieved resolution is very good. However the acceptance region of the CTD is limited to $|\eta| < 2$ and only charged particles are detected.

The calorimeter is sensitive to both neutral and charged particles. Energetic calorimeter cells are combined to cell cluster using an algorithm as described in Section 5.3. Information from energetic clusters is then combined with the reconstructed tracks. Section 5.4 gives details of the applied matching algorithm. The final objects of this merging procedure are associated with particles in the hadronic final state.

5.1 The Hadron Level of Monte Carlo Simulations

The term *hadron level* in general refers to particles at the end of an event generation, i.e. the end-products of the simulated fragmentation, hadronisation and resonance decay processes. These particles are handed over to the detector simulation where detector effects are simulated and further particle decays (i.e. of relatively short-lived kaons or pions) are possible. The end-product of the detector simulation, i.e. the simulated detector signals, is referred to as the *detector level* of a Monte Carlo.

Various definitions of what is regarded as a *stable particle* are possible. For this analysis a classification of particles was made according to their lifetime: particles with a lifetime longer than $3 \cdot 10^{-10}$ s are taken as stable. Consequently the short-lived vector mesons ρ, ω etc. and the neutral pions π^0 are defined as unstable. If one of these "unstable" particles

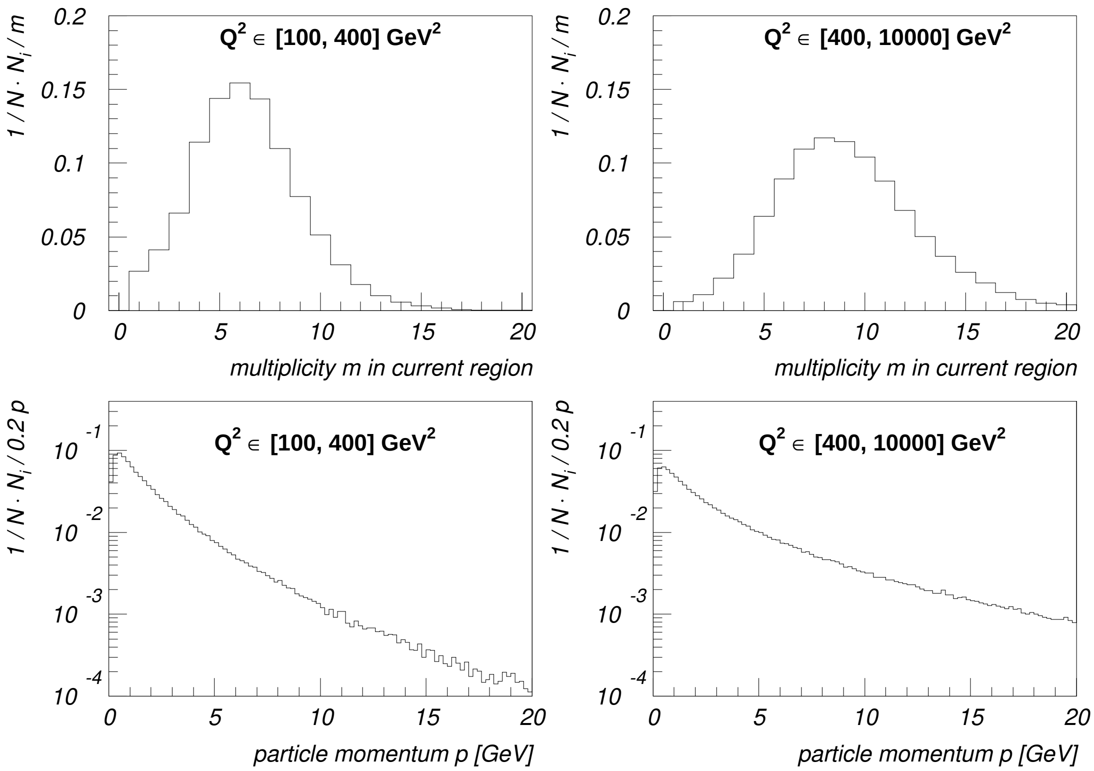

Figure 5.1: *Multiplicity and momentum spectrum of hadron level particles in the Current region of the Breit frame. The kinematic region was divided into a medium-Q^2 region ($Q^2 \in$ [100, 400] GeV) and a high-Q^2 ($Q^2 \in$ [400, 10,000] GeV) region.*

is handed over from the generator to the detector simulation then its daughter particles – if stable – rather than the particle itself are taken for the computation of the event shape variables. If a daughter particle is also unstable then a search is performed through the subsequent generations of the particle cascade until a stable particle is found.

Charged pions and kaons may decay during the detector simulation i.e. into a muon μ and a neutrino ν_μ. Strictly speaking, the μ and the ν_μ are the final particles, but pions and kaons are stable particles according to the lifetime classification. Thus kaons and pions are taken for the computations of the event shape variables. This is further justified by the fact that both kaons and pions generally live long enough to produce tracks in the CTD before decaying.

In the following the term *hadron level* will refer to the set of these stable particles. The hadron level consists of approximately 45% photons, 40% charged pions, 8% neutral and charged kaons, 5% protons and neutrons (both particles and anti-particles), 1% Λ and $\overline{\Lambda}$ baryons and 1% electrons, positrons, muons and neutrinos. During the analysis, the particles of the hadron level are boosted to the Breit frame. The resulting multiplicity and the momentum spectrum of the particles found in the Current Region are shown in Figure 5.1. Separate histograms are shown for a medium-Q^2 region ($Q^2 \in [100, 400]$) and a high-Q^2 region ($Q^2 \in [400, 10,000]$) region.

5.2 Track Reconstruction

Tracks in the CTD are used for identifying charged particles. Several different track recognition programs are available. Here the VCTRAK package is used. This package offers several reconstruction modes, from which the CTD-only mode and the multi-vertex mode are chosen. In the CTD-only mode the forward tracking chambers are not used, track seeds are taken only from hits in the CTD. In the multi-vertex mode more than one vertex is permitted. Decay vertices, for example from K^0 or Λ particles, may be found with this option.

The track recognition starts in the outer superlayers (see page 26) where the hit densities are lower, and proceeds inwards from there. In the first step hits in the axial superlayers are combined to circles in the xy-plane. During the second step hits in the z-by-timing system and in the stereo layers are superimposed on the circles. It is stressed that in order to reconstruct the Z-coordinates of the trajectories information is needed from both the stereo and the axial superlayers. From the trajectories a helix is determined which gives the track parameters momentum, initial angle and charge.

As soon as tracks are reconstructed they are used for fitting a vertex. The reconstruction of several vertices is possible. The fit of the track parameters is repeated with the vertex as an additional trajectory point.

The track resolution is particularly good for long tracks which are well contained within the acceptance region of the CTD. The momentum resolution is a function of the transverse momentum p_T of a track and is influenced by three different effects: the p_T-dependent measurement error, which is the resolution of the drift chamber (A), a constant term for multiple scattering in the CTD (B) and a $1/p_T$-dependent term for multiple scattering before the CTD (C):

$$\frac{\sigma(p_T)}{p_T} = A \cdot p_T \oplus B \oplus \frac{C}{p_T} \tag{5.1}$$

with $A = 0.0058\,\mathrm{GeV}^{-1}$, $B = 0.0065$ and $C = 0.0014\,\mathrm{GeV}$.

In order to be used in the analysis the tracks must fulfill the following quality requirements:

1. The track must be associated with the primary vertex.
2. The track must reach at least superlayer 3.
3. The track must lie within good acceptance of the CTD: $|\eta| < 2$.
4. The track must have sufficiently large p_T : $p_T > 0.2\,\mathrm{GeV}$.

Figure 5.2 shows the track multiplicity and momentum spectrum of selected tracks which are boosted into the Current Region of the Breit frame. They are compared to charged particle multiplicities at the hadron level. Separate histograms are shown for a medium-Q^2 region ($Q^2 \in [100, 400]$) and a high-Q^2 region($Q^2 \in [400, 10,000]$).

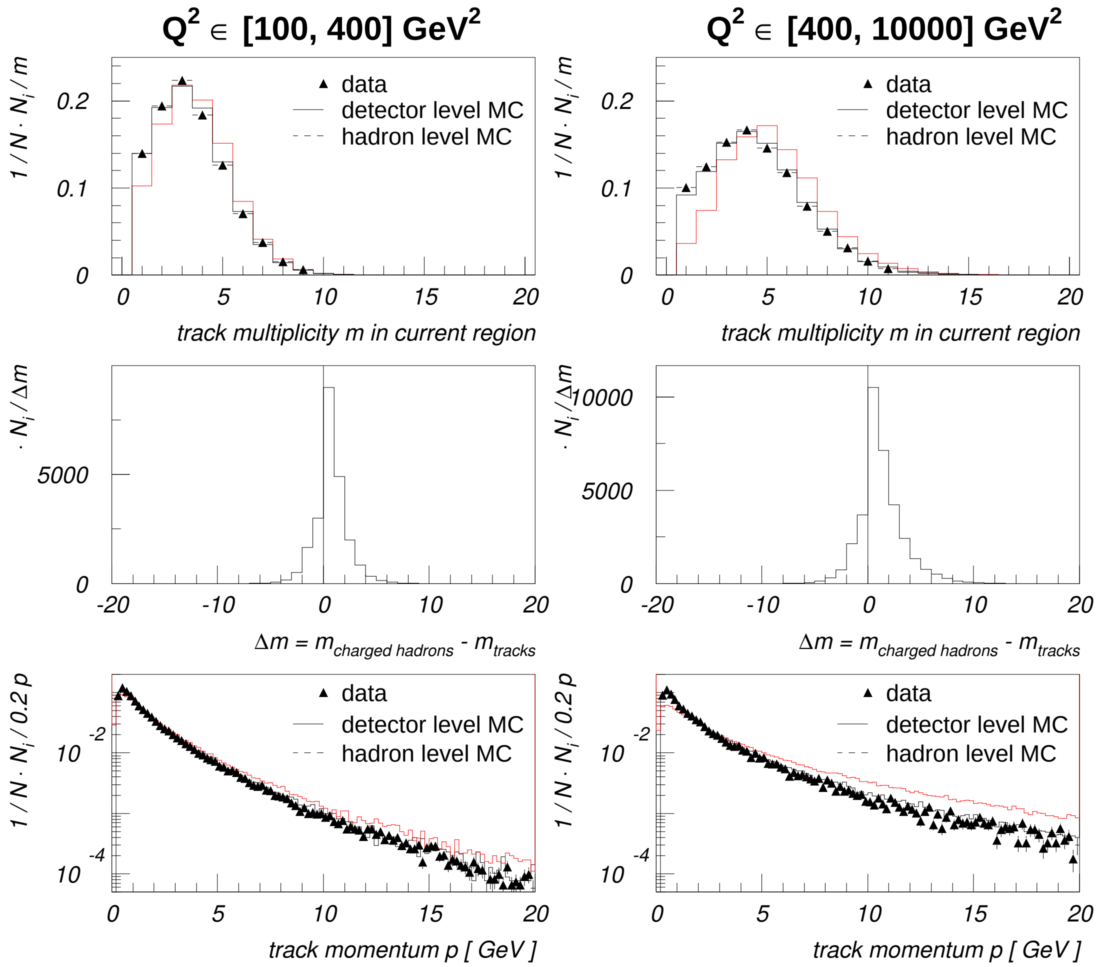

Figure 5.2: *Multiplicities and momentum spectra of tracks in the Current Region compared to charged particles at the hadron level. The kinematic region is split into a medium-Q^2 (left) and a high-Q^2 (right) region. Also shown is the difference in multiplicity Δm between charged particles and tracks. On average fewer tracks than charged particles are found. This difference is explained by the limited acceptance of the CTD.*

5.3 Calorimeter Clustering

The ZEUS calorimeter almost hermetically encloses the interaction region with only two small holes for the beam pipe. Incident particles induce a particle cascade or *shower* and thus deposit their energy. The measured calorimeter signal is proportional to the energy of the particle. The only exceptions are neutrinos ν, which do not deposit any energy at all, and high energetic muons, which deposit only minimum ionisation and do not start a particle shower.

The particle shower may extend over several calorimeter cells. If two (or more) particles hit the calorimeter close to each other their particle showers may overlap. Thus the challenge for a cluster algorithm is to connect cells with energy deposits in such a way that the four-momenta derived from the cluster objects approximate the four-momenta of the incident particles. Combining clusters from two or more particles into one cluster as well

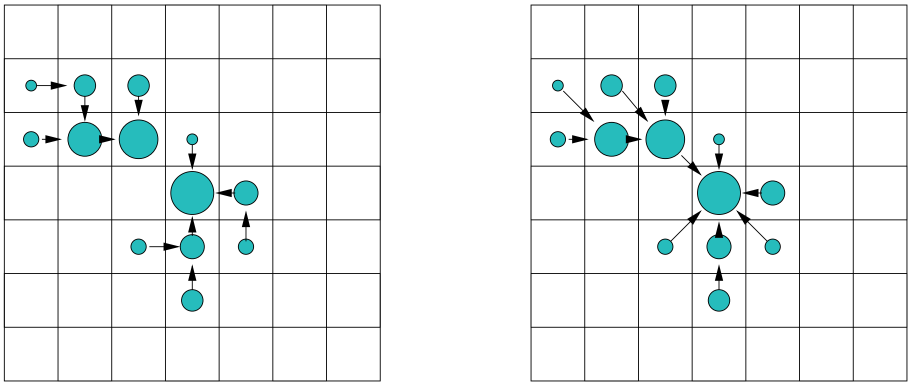

Figure 5.3: *The two different Cellisland Modes. For a given ensemble of energetic cells the nearest neighbour mode (left hand side) reconstructs 2 distinct Cellislands whereas the corner connect mode (right hand side) reconstructs only one Cellisland. A switch between the modes obviously may change the multiplicity of an event.*

as splitting up a cluster originating from only one particle must be minimised.

The cluster algorithm used in the analysis consists of two distinct steps. During the first step cells in local neighbourhoods are merged into *Cellislands*, separately for each calorimeter section. In the second step the Cellislands are combined in a projective way into *Cone Islands*. In the following the terms *islands* or *cones* will be used as alternative expressions for Cone Islands. Cellislands will be denoted only as Cellislands, whereas the term *cluster* will be used as a general expression.

Cellislands

The Cellislands algorithm searches for local neighbourhoods of cells with energy deposition separately within each of the 8 calorimeter sections (REMC, BHAC1, FHAC2 etc.). The algorithm starts with the most energetic cell as a local maximum. If any of the neighbouring cells shows an energy deposition, it is connected to the local maximum in a unique way. In other words each cell is pointing to and connected with the highest energetic cell among its neighbouring cells, unless it is a local maximum itself.

Two different types of merging the neighboring cells are possible. In the *nearest neighbour* mode a connection is made only to the four directly-neighbouring cells, i.e. excluding diagonal neighbours. In the *corner connect* mode a connection is allowed also to the four diagonally-neighbouring cells. Association is possible to eight cells in total.

The two different algorithm modes are illustrated in Figure 5.3. Shown is an ensemble of cells with their energy depositions. The nearest neighbour mode results in two distinct Cellislands, whereas the corner connect mode reconstructs only one Cellisland. A switch between the modes obviously leads to a change of multiplicity. The nearest neighbour mode is chosen as default mode. The switch to the corner connect mode is used as a systematic check (see page 93).

Position Reconstruction for Cellislands

Once all the cells i belonging to one cluster have been determined, the cluster position is reconstructed. First the geometrical centre position $x_{0,i}$ (in ZEUS coordinates) of each cell i is corrected according to the measured imbalance in the two photomultipliers of the cell:

$$x_i = x_{0,i} + \delta x \qquad \text{with} \qquad \delta x = \frac{\lambda}{2} \ln \left(\frac{E_R}{E_L} \right) \tag{5.2}$$

E_R and E_L refer to the energy mesured in the right and left photomultiplier of the cell. The value of $\lambda = 54\,\mathrm{cm}$ was obtained from fits to test beam data ([Kr92]). It is used within ± 8 cm from the centre of a cell. In the outer regions $\delta x = \pm\ 10\,\mathrm{cm}$ is used.

The centre of gravity (*cog*) of the cluster is calculated with the corrected cell positions:

$$\vec{R}_{\mathrm{cog}} = \frac{\sum_i w_i \vec{r}_i}{\sum_i w_i} \tag{5.3}$$

The weights w_i incorporate a logarithmic energy weighting of the cells:

$$w_i(EMC) = \max \left[0\,, \left\{ W_e + \ln \left(\frac{E_i}{E_{tot}} \right) \right\} \right] \tag{5.4}$$

$$w_i(HAC) = \max \left[0, \left\{ W_h + \ln \left(\frac{E_i}{E_{tot}} \right) \right\} \right] \tag{5.5}$$

where E_i refers to the energy in cell i, E_{tot} to the total energy of the cluster. W_e and W_h are tuned cutoff parameters. The values of $W_e = 4$, $W_h = 2$ are derived from single-pion Monte Carlo ([GB]) and test beam data. The difference of the numerical values is due to the different sizes of the EMC and HAC cells. W_e and W_h function as a threshold on the fraction of total shower energy E_{tot} a cell must contain at least in order to be included in the position weighting. The chosen value $W_e = 4$ ($W_h = 2$) corresponds to a minimal fractional energy of 1.8%(13.5%) for EMC(HAC) cells.

For very large values of W_i all cells are included into the weighting, which is basically a simple geometrical weight of the energetic cells. The result is a poorer angular resolution. On the other hand for $W_i \to 0$ only the cells with the highest energy deposit contribute to the weighting. This in turn imposes a bias on the resulting impact position. However the general advantage of logarithmic weighting is a lower sensitivity to shower fluctuations and to the correct simulation of transverse shower shapes in the Monte Carlo [Aw77].

From Cellislands to Cone Islands

Cellislands which are behind each other in different calorimeter sections can be merged into three-dimensional Cone Islands. The merging procedure starts with Cellislands in the outer HAC sections. The angular separation with respect to Cellislands in the inner sections is computed. A probability as a function of this angular separation is assigned to a specific Cellisland combination. If the probability is larger than a user-supplied cut a link is made between the two Cellislands. Links are possible between a Cellisland in a

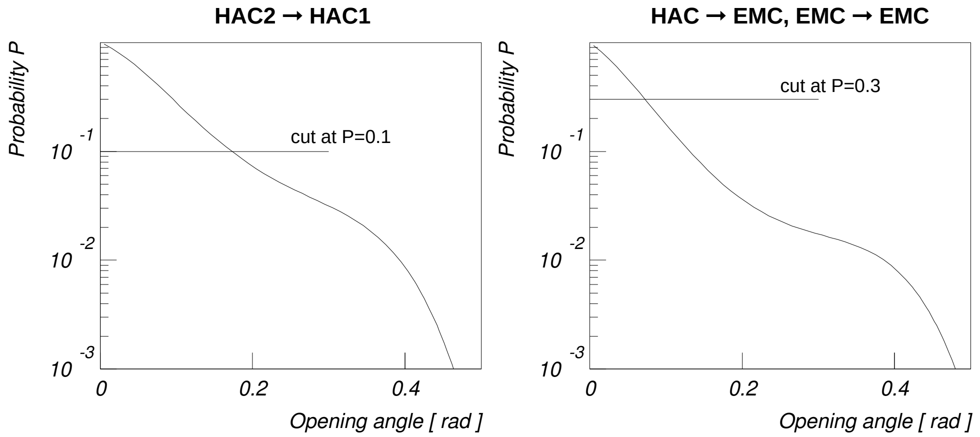

Figure 5.4: *Probability functions for combining Cellislands into Cone Islands. Two different functions of the form* $\exp(a_1x^3 + a_2x^2 + a_3x + a_4)$ *with different parameters* a_i *are used for combining HAC2 with HAC1 Cellislands (left hand side) and for combining HAC with EMC and EMC with EMC Cellislands (right hand side).*

HAC2 section and an EMC section directly without a connecting Cellisland in a HAC1 section. Links are also possible over crack regions, i.e. a Cellisland in the BCAL can be linked to a Cellisland in the RCAL or FCAL, if the assigned probability exceeds the cut value. However, no special probability functions are used for these crack regions. Figure 5.4 shows the probability functions and the chosen cut values of 0.1 for HAC2 $\rightarrow$ HAC1 merges and of 0.3 for HAC $\rightarrow$ EMC and EMC $\rightarrow$ EMC merges.

A position for the resulting Cone Islands is computed in an analogous way to that described above for the Cellislands. The method of combining Cellislands according to their angular separation overcomes the non-projectivity of the ZEUS calorimeter. Figure 5.5 shows the Cone Island multiplicity and momentum spectrum in the Current Region of the Breit frame, compared with hadron-level multiplicities.

Radius of Cone Islands

For each cell i belonging to a Cone Island a distance d_i is calculated from the centre position of the cell i perpendicular to a straight line going through the vertex and the Cone Island centre position. The maximum value of all d_i is taken to be the *radius* of the Cone Island.

5.4 Combining Cluster and Track Information

The angular resolution of the CTD is much better than the angular resolution of the calorimeter, especially for charged particles which are bent in the magnetic field. Furthermore for low-energy particles the momentum measurement of the CTD has a better

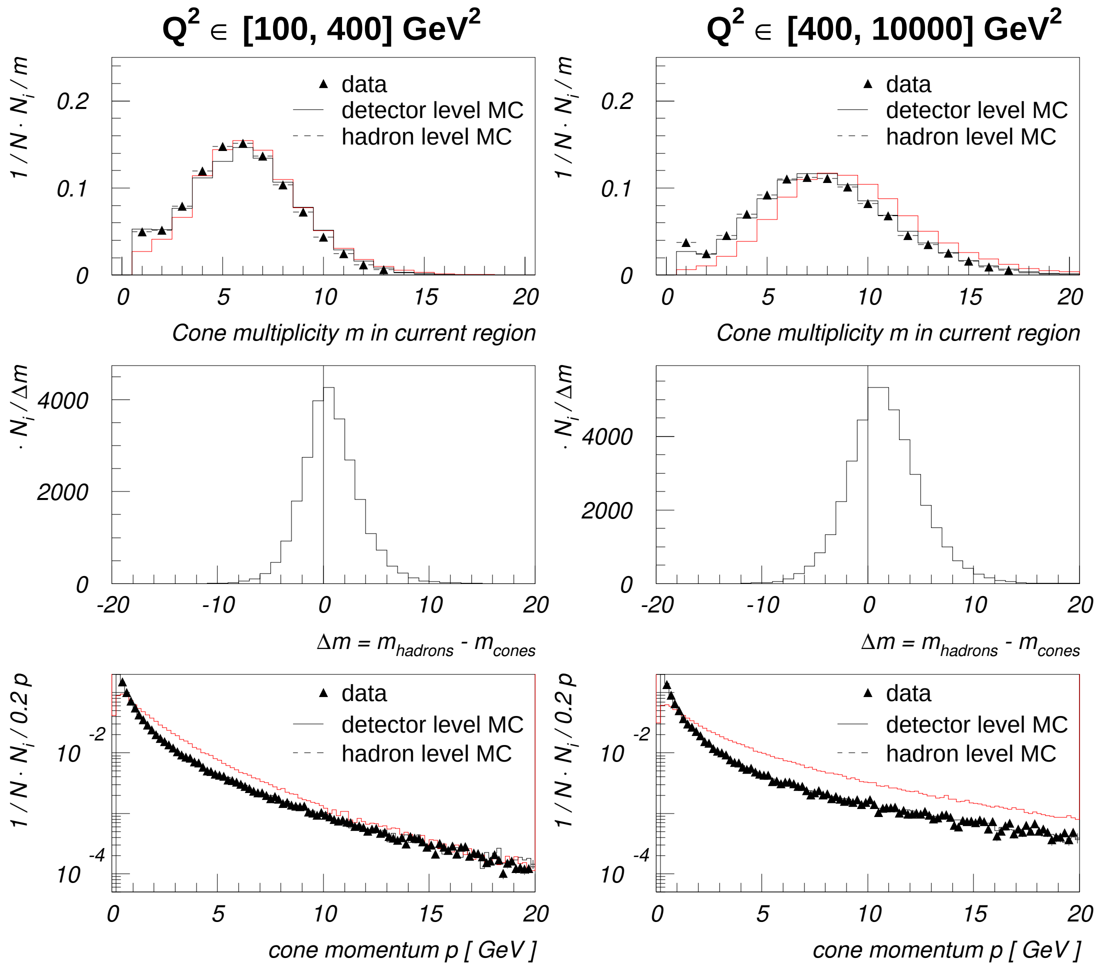

Figure 5.5: *Multiplicities and momentum spectra of Cone Islands in the Current Region compared to particles at hadron level separately for medium and high* Q^2*. Also shown is the difference in multiplicity* Δm *between Cone Islands and hadron level.*

resolution than the energy measurement of the calorimeter. In order to make use of the CTD information, and thus to maximize the obtainable resolution and in order to minimize systematic biases, calorimeter and track information are combined for reconstructing particle four-momenta. The applied matching algorithm is described in this section. The presented algorithm is based on a matching scheme developed by G. Briskin [GB], the final objects of which are referred to as *ZUFOs.*[1]

Tracks passing the quality cuts listed on page 55 are extrapolated to the calorimeter surface. A distance is calculated between the track impact position and the central positions of the calorimeter clusters. An association is made between a track-cluster pair if they lie sufficiently close to each other. However, an unambigious match between exactly one

---

[1] The algorithm used is basically the same as the ZUFO algorithm with two minor changes: G. Briskin's algorithm takes calorimeter clusters as starting points and substitutes the island information with track information only if both distance and $\frac{E}{p}$ requirement are fulfilled. Here the CTD information was used more widely, i.e. it is also used if only the distance requirement is fulfilled.
The second difference is the mass assignment: G. Briskin uses a p dependent calculation, whereas here simply a pion mass is assigned to tracks and combined objects.

track and one island – so-called *1-to-1 pairs* – is possible only for about 60% of the tracks.

The discussion will treat the 1-to-1 pairs first. For highly-energetic particles the energy measurement of the calorimeter is better than the momentum measurement of the CTD. Thus the calorimeter energy should be used in these cases. For low-energy particles the situation is reversed and the CTD information should be used. However care has to be taken since a cluster originating from a neutral particle may overlap with the cluster belonging to the charged particle. Blindly substituting the calorimeter information with the CTD information may neglect the energy of the neutral particle.

The approach suggested by G. Briskin, and also applied here, uses an E (from the calorimeter) and p (from the CTD) dependent cut with flexible tolerances. This approach is extended to more complicated track-island configurations.

Almost 30% of the tracks cannot be associated with any island at all. These tracks have very low energy and thus fail to induce a detectable signal in the calorimeter. They are added to the list of reconstructed particles in the final state.

1. Extrapolation of Tracks and Distance to Islands

Each track in the CTD is extrapolated, or *swum*, to the surface of the calorimeter giving an incident position of the track at the calorimeter. For each pair of track i and island j the distance of the impact position of i from the centre of j is calculated. This distance is referred to as *distance of closest approach*, or *DCA*. A track-island pair (i, j) becomes a matching candidate if

$$\left.\begin{array}{l}\mathrm{DCA}\,(i,j) < 20\,\mathrm{cm} \\ \mathrm{.or.} \\ \mathrm{DCA}\,(i,j) < r_j\end{array}\right\} \quad \mathrm{with}\, r_j : \;\; \mathrm{radius\, of\, island}\, j$$

The matching information is stored in association matrices. A histogram of the number of islands a particular track is pointing to is shown in Figure 5.6. A significant fraction of tracks, about 12%, match two or more islands. Also shown is the number of tracks pointing to the same island. About 15% of the islands hit by any track, are hit by more than 1 track. Thus a more intricate matching logic than a simple 1 track to 1 island logic is required.

2. 1-to-1 pairs

The term *1-to-1* pair refers to track-island pairs (i, j) where the track i is pointing only to 1 island, namely island j, and j in turn is hit only by i. For each 1-to-1 pair the ratio E/p is calculated with E taken from the island and p taken from the track. The resulting distribution is shown in Figure 5.7. A peak is observed at a value of 0.8 as expected from single pion Monte Carlo [GB]. For an ideal detector the ratio should take a value of 1. However particle energy is lost in the inactive material between the CTD and the calorimeter as well as in the inactive material between different calorimeter modules.

In Figure 5.7 a tail to larger values of E/p is observed. Two explanations for this tail are possible: (a) cluster overlap: A charged particle is bent in the magnetic field and can enter at a similar calorimeter position as a neutral particle. The cluster energy

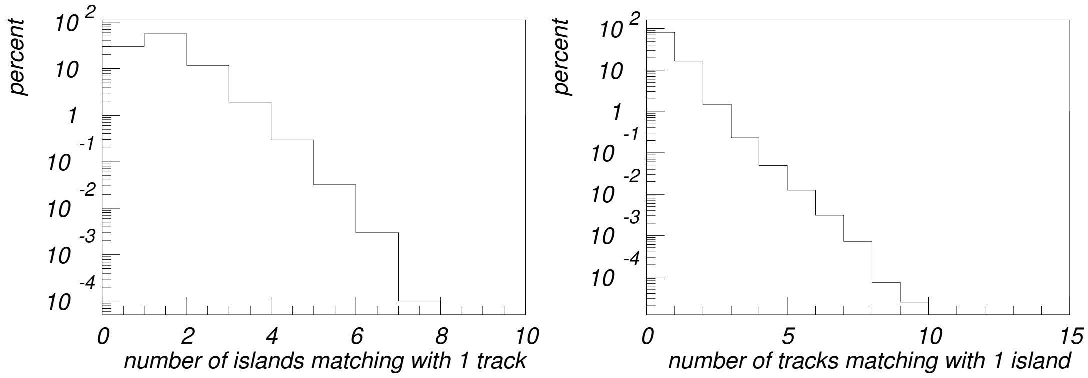

Figure 5.6: *Track-Island Associations. Left hand side: Shown is the number of islands one particular track is pointing to. About 12% of the tracks can be combined with more than one island and about 30% of the tracks cannot be matched with any island at all.*
Right hand side: About 15% of the islands are hit by more than one track and three-quarters of the islands cannot be matched with any track at all. This high number (expected is 50%) is due to the limited angular acceptance of the CTD compared to the calorimeter.

then equals the sum of the energies of the two (or more) incident particles. (b) high measurement uncertainties especially of calorimeter energy for low energetic particles.

3. Substituting Island with Track Information

In substituting island with track information care has to be taken in order to avoid neglecting energy from neutral particles which may overlap with clusters originating from charged particles. One should also take into account the measurement errors of the track and the island. The resolution of energy E and momentum p are functions of E and p. (See their definitions on page 27 for CAL and Equation 5.2 for CTD respectively.) As can be seen in Figure 5.7, the track-momentum resolution is much better for low-energy particles whereas at around an energy of 10–15 GeV the situation reverses.

An energy-, momentum- and resolution-dependent criterion is applied for deciding whether to take track or island information. If for a given 1-to-1 pair E/p is below a cut value given by

$$\frac{E}{p} < \kappa + n \cdot \Delta\left(\frac{E}{p}\right) \qquad \kappa = 0.9, \quad n = 2 \tag{5.6}$$

$$\Delta\left(\frac{E}{p}\right) = \frac{E}{p} \cdot \sqrt{\frac{\Delta E}{E} + \frac{\Delta p}{p}}$$

then the island information is substituted with the track information. Rather generous values of of $\kappa = 0.9$ and a 2 σ deviation are chosen in order to allow for some

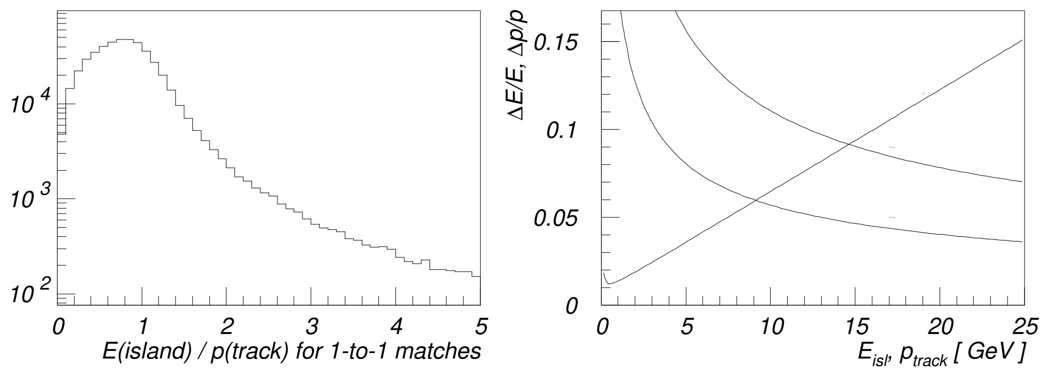

Figure 5.7: *The histogram on the left hand side shows the ratio of* E_{island} *over* p_{track} *for 1-to-1 matches. The right hand side shows track momentum resolution (linear, according to Equation 5.2) and the calorimeter energy resolution for hadronic (upper curve) and electromagnetic (lower curve) clusters according to the quoted values on page 27.*

extra tolerance. If E/p is larger than the cut value $\kappa + n \cdot \Delta(E/p)$ then only the angular information is taken from the CTD – which is generally better than the angular measurement of the calorimeter.

4. Other Track-Island Configurations

A similar substitution procedure is applied in the more complicated cases where a) two or three tracks match one island, and the island in turn is hit only by these tracks (*cluster overlap*), b) one track points to two islands and these two islands are hit only by this track (*split island case*) or c) each of two tracks is pointing to two islands and these islands in turn are hit both by these tracks (*2-to-2 pairs*). The substitution criterion from Equation 5.6 is applied to the total energies and total momenta of the tracks and islands involved.

Figure 5.8 shows the relative frequencies of the various track-island combinations. For 21% of the islands hit by any number of tracks the configuration is too complicated to make an unambigious decision. For these objects the information is taken from the calorimeter island alone.

5. Mass Assignment

The great majority of tracks in the CTD are due to charged pions. Therefore one pion mass (139 MeV) is assigned to all tracks and all islands which are hit by a track, even if the island information is not substituted by track information. This mass assignment leads to an improved four-momentum resolution with respect to the four-momenta of hadron-level particles. No mass is assigned to islands which have not been hit. In the vast majority of cases they are due to massless photons.

6. Unmatched Tracks

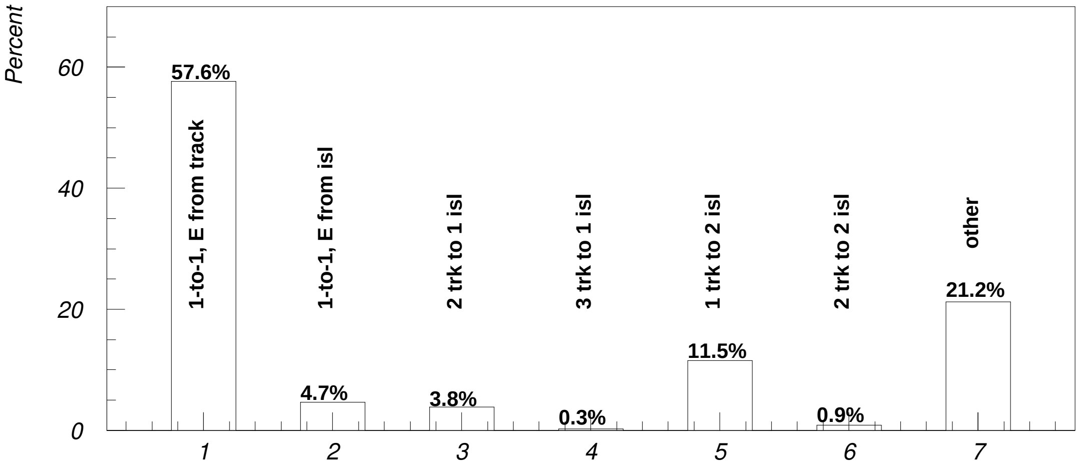

Figure 5.8: *Track-Island Configurations for all islands hit by any number of tracks (*$= 100\,\%$*). 1-to-1 matches occur with the highest frequency. For 57.6% the* E/p *is smaller than the discrimination value and the energy of the object is determined from the track momentum. For 4.7% the energy is taken from the island. 12% of the islands can be identified as "split islands", where one track is pointing to two islands. For 21% of the islands no simple classification is possible.*

About 30% of the tracks cannot be matched with any island. These *loose tracks* usually are of very low momentum and they appear with higher probability in the crack regions. It can be concluded that these tracks are caused by low momentum particles which do not have enough energy to give rise to a detectable signal in the calorimeter. These tracks are thus also treated as particles in the calculation of the event shape variables.

General Performance

It is not possible to write a particle reconstruction algorithm which reconstructs objects which correspond precisely in multiplicity and four-momenta to the underlying hadrons. The granularity of the ZEUS detector is relatively coarse; showers induced by different particles may overlap partially, especially in the forward region where particle densities are higher. Energy depositions in calorimeter cells may be produced simultaneously by different particles. Shower fluctuations also have an effect. The energy deposition due to a single particle may be distributed over non-adjacent calorimeter cells which would then not be merged by a clustering algorithm such as the one described above.

On average such effects are somewhat reduced. Thus the overall energy flow and particle flow is more indicative of the capability of the reconstruction algorithm, i.e. whether the overall energy flow and particle density are correctly reconstructed or whether there are inhomogeneities – regions of the detector in which reconstruction is better or worse than in others.

The term *energy flow* in the following refers to the differential distribution of fractional energy E_i/E_{tot} per θ bin i: $\frac{\mathrm{d}E_i/E_{tot}}{\mathrm{d}\theta_i}$. This distribution may be normalised to N, the total number of events. This is shown in Figure 5.9 for Cone Islands and for Combined Objects. The energy flow is shown for data and for hadron-level Monte Carlo. Since the histograms are hard to distinguish, the ratios between them are also shown explicitly. A broadly good agreement between data and detector-level Monte Carlo is seen. When comparing detector-level and hadron-level Monte Carlo however, large discrepancies are seen in the overlap regions of the calorimeter, the "crack regions" between the RCAL and the BCAL ($\theta \approx 128\,^\circ$) and between the BCAL and the FCAL ($\theta \approx 38\,^\circ$). In these regions up to 20% less energy is measured, due to the inactive material between the separate calorimeter parts.

Combined Objects show a lower discrepancy in the crack regions. This is explained by the fact that they make greater use of the CTD information. The CTD performance is very good in the angular regions corresponding to the calorimeter cracks. Tracks in these regions are very long, passing through (and hence measured by) most CTD superlayers.

A similar situation is observed in the particle flow, defined analagously as the fraction of particles in each θ bin. The normalisation is now to the total number of particles N rather than the total number of events. As in the case of the energy flow, inhomogeneities are observed in the overlap regions. Reconstruction is generally better with Combined Objects than with Cone Islands. However a bump is visible just before (i.e. on the vertex side of) the forward crack region. The excess of reconstructed particles may be explained by splitting of clusters over the cracks. Another explanation is backscattering – particles passing through the forward tracking chambers which are scattered backwards towards the BCAL.

Resolutions of Event Shape Variables

In Figures 5.11 to 5.14 are shown the resolutions of the event shape variables calculated from the Combined Objects (with a boost vector determined from the scattered electron). They are shown for each analysis bin separately. The mean and rms values of the resolution histograms are shown in an inset.

The event shape resolution is a convolution of the resolutions of the Combined Objects and the boost resolution. Figures 5.15 to 5.18 show the resolutions observed if the event shape variables are calculated from the Combined Objects after they have been boosted to the Breit frame with a *true* boost. This shows the influence of the cluster algorithm on the final event shape resolutions. Figures 5.19 to 5.22 show the resolutions observed if the event shape variables are calculated from the hadron level particles which have been boosted with the boost vector calculated from the scattered electron.

It is seen that the cluster and matching algorithms have a larger impact on the event shape resolutions than the boost reconstruction. C_p and J_m show larger deviations than T_z and J_b. As will be shown in the systematic study (Chapter 6) C_p and J_m are sensitive to changes of multiplicity in the current region. This also accounts for the broader resolutions.

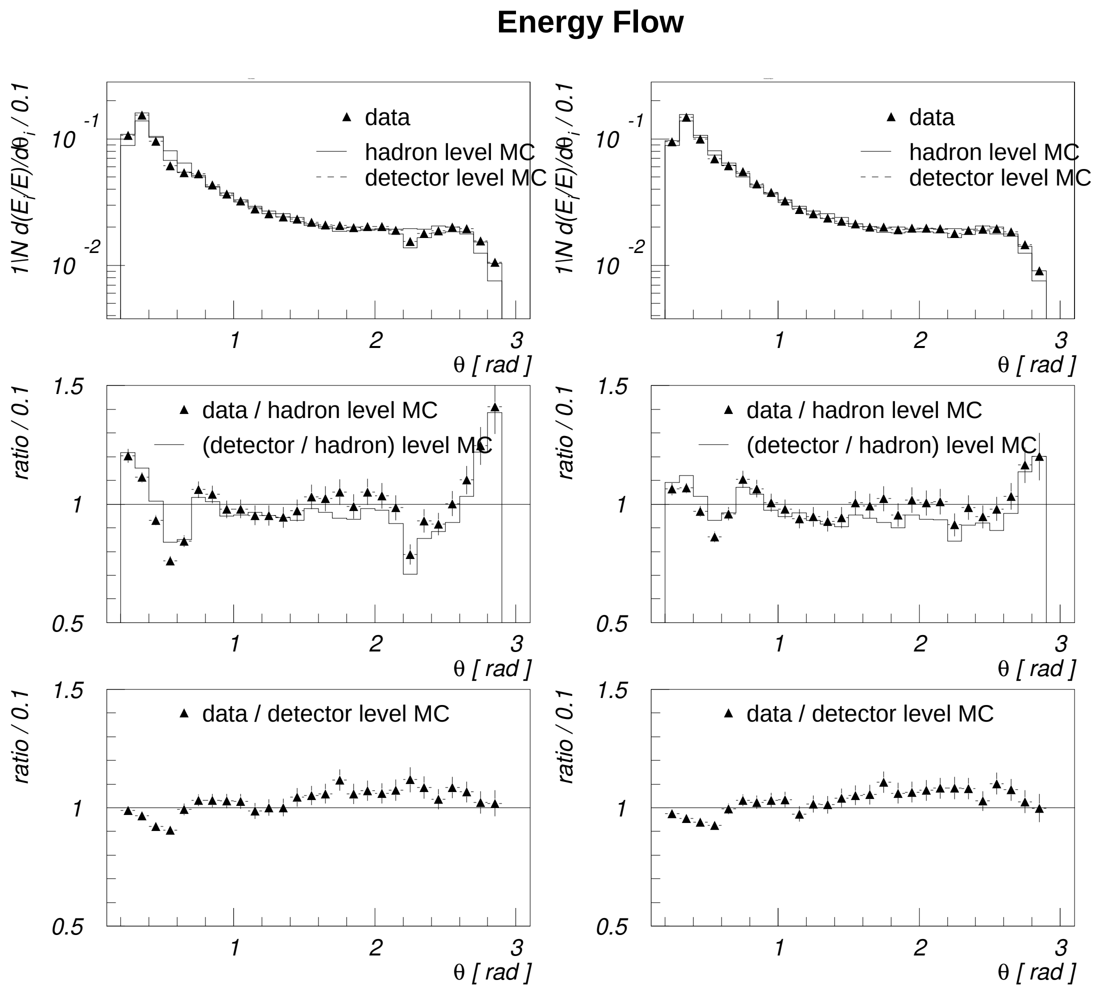

Figure 5.9: *Energy flow, defined as fractional energy* E_i/E_{tot} *per* θ *bin:* $\frac{\mathrm{d}E_i/E_{tot}}{\mathrm{d}\theta}$. **left:** *Cone Islands.* **right:** *Combined Objects. a) and d) show the energy flow for data and for detector level and hadron level Monte Carlo. Since the three distributions are difficult to distinguih, the ratios between them are explicitely shown in the histograms below. b) and e) show the ratio of data and detector level compared to hadron level each, in c) and f) data is compared to detecto level Monte Carlo.*

Energy flow from Cone Islands shows a lack of reconstructed energy around the crack regios between the RCAL/BCAL and FCAL/BCAL respectively. Combined objects make wider use of CTD information – which is very reliable in these angular regions – and thus shows significantly smaller energy deficit.

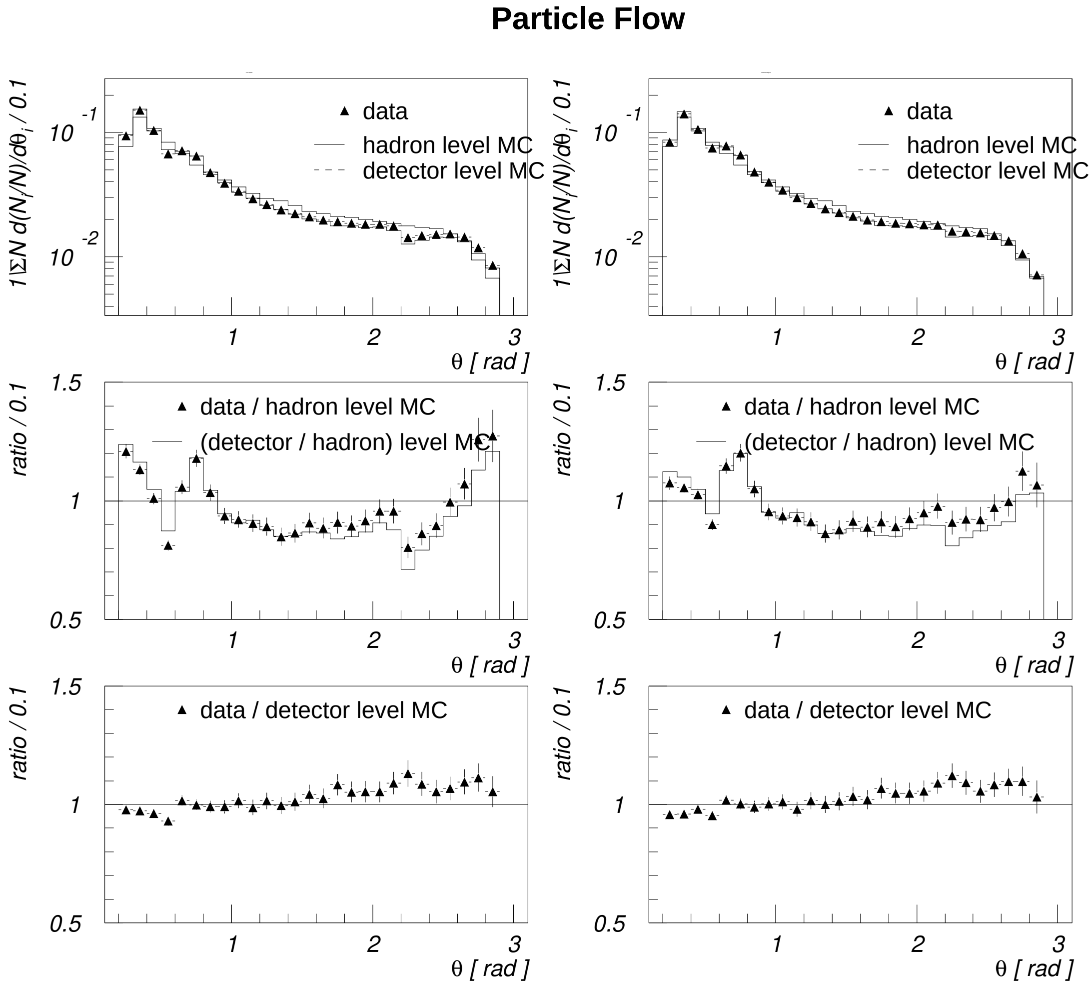

Figure 5.10: *Particle flow versus polar angle θ. Results from Cone Islands are compared with results from Combined Objects.*

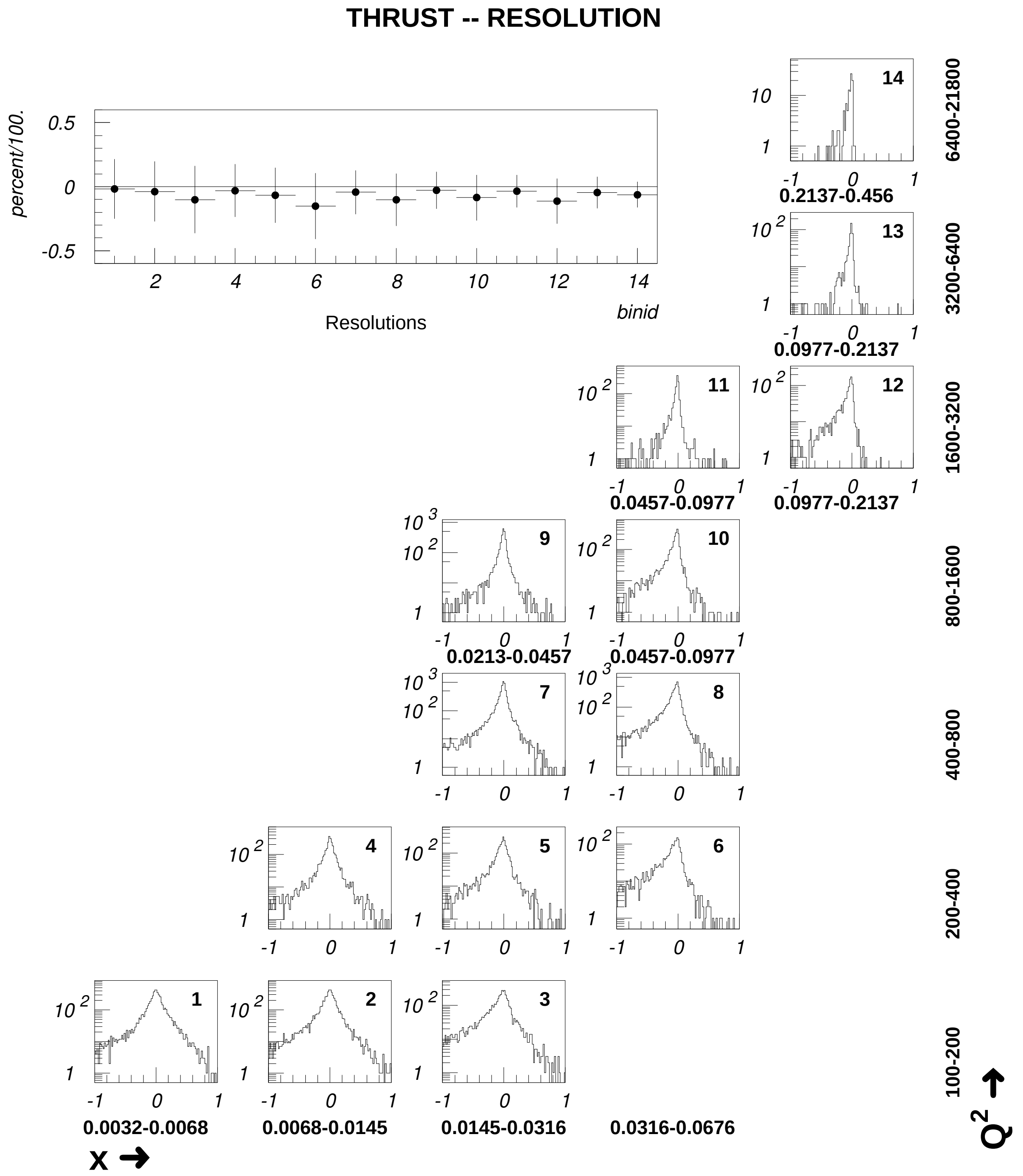

Figure 5.11: *Resolution of T_z. The inset shows mean and rms values of the histograms.*

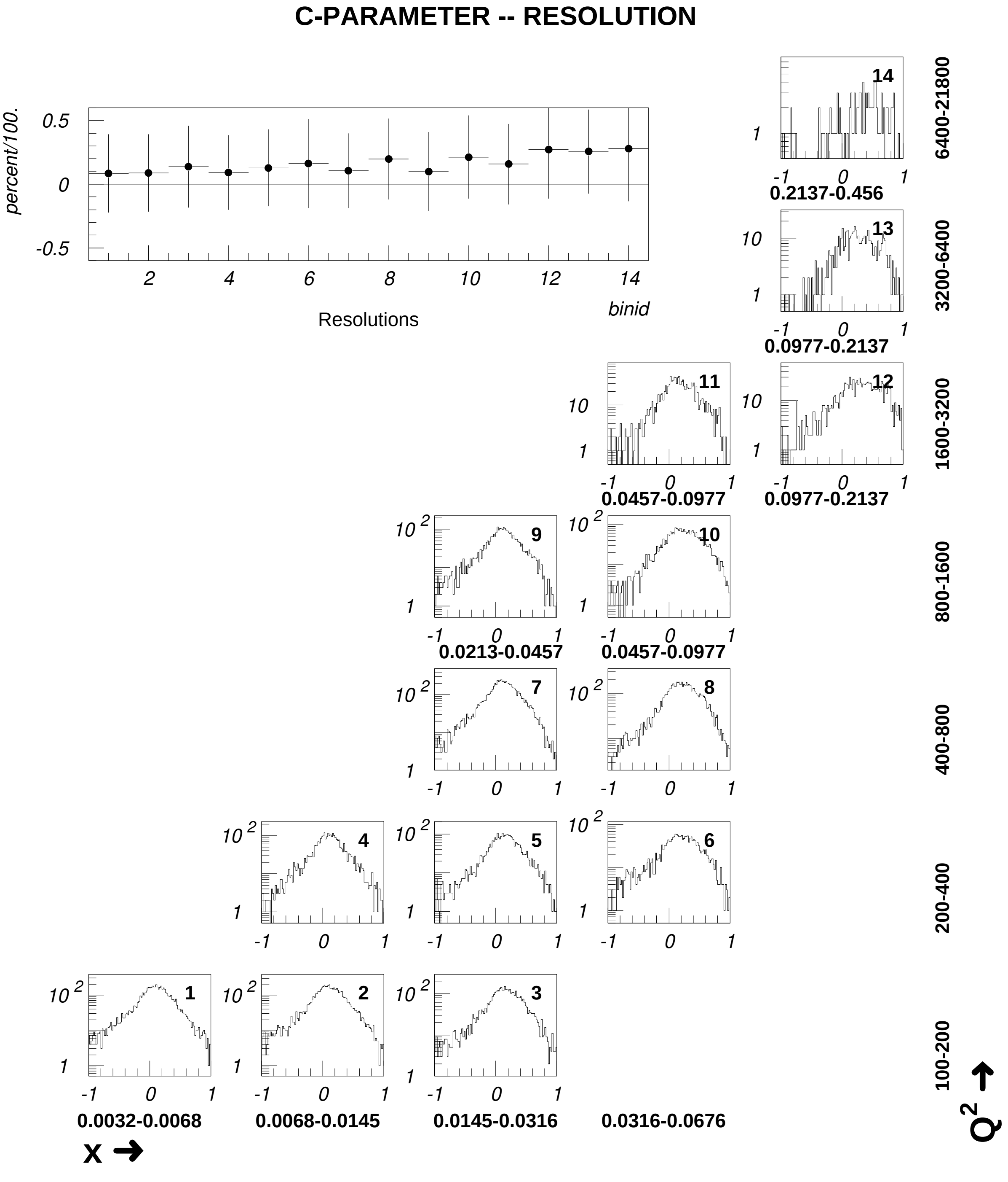

Figure 5.12: *Resolution of C_p. The inset shows mean and rms values of the histograms.*

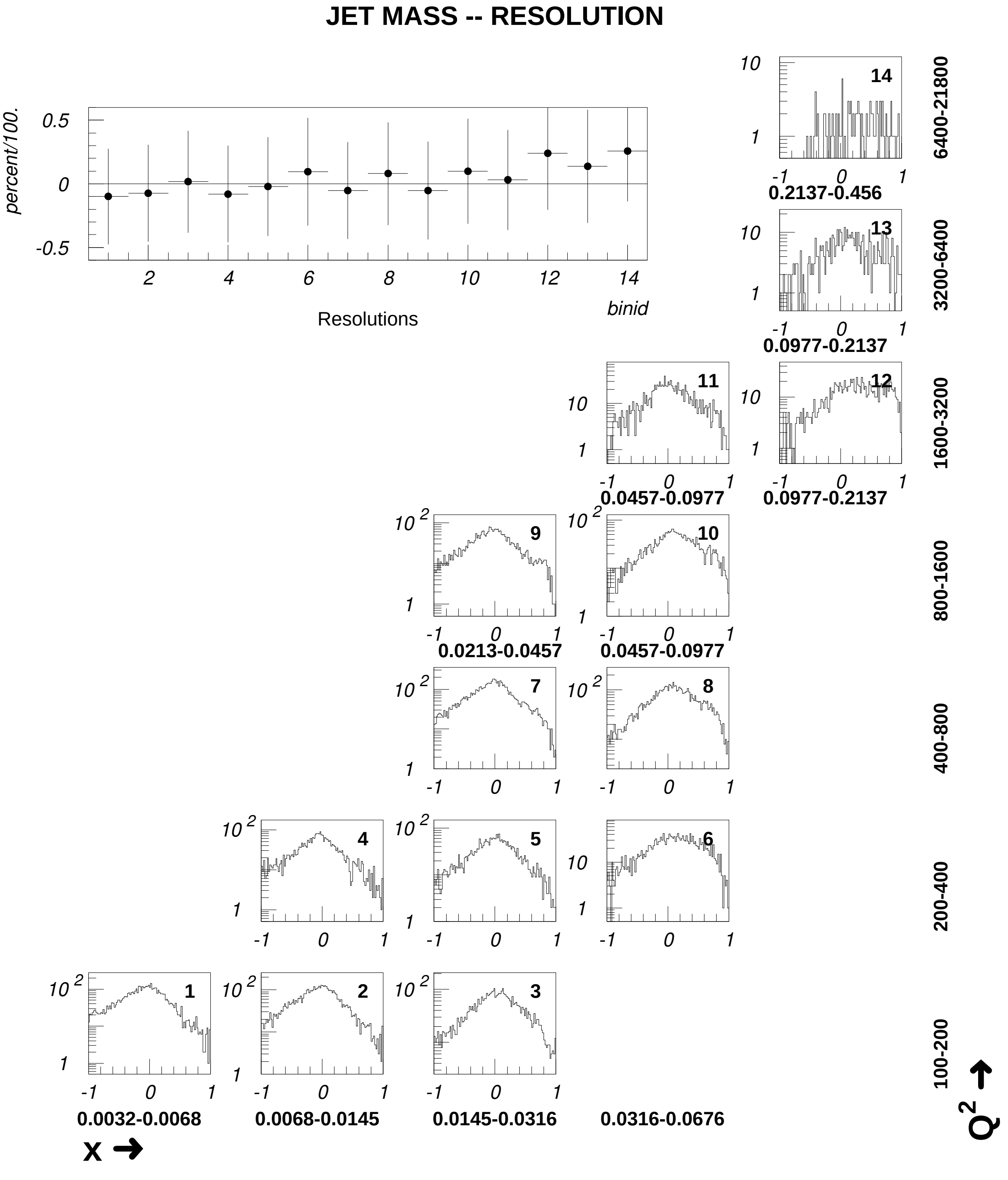

Figure 5.13: *Resolution of J_m. The inset shows mean and rms values of the histograms.*

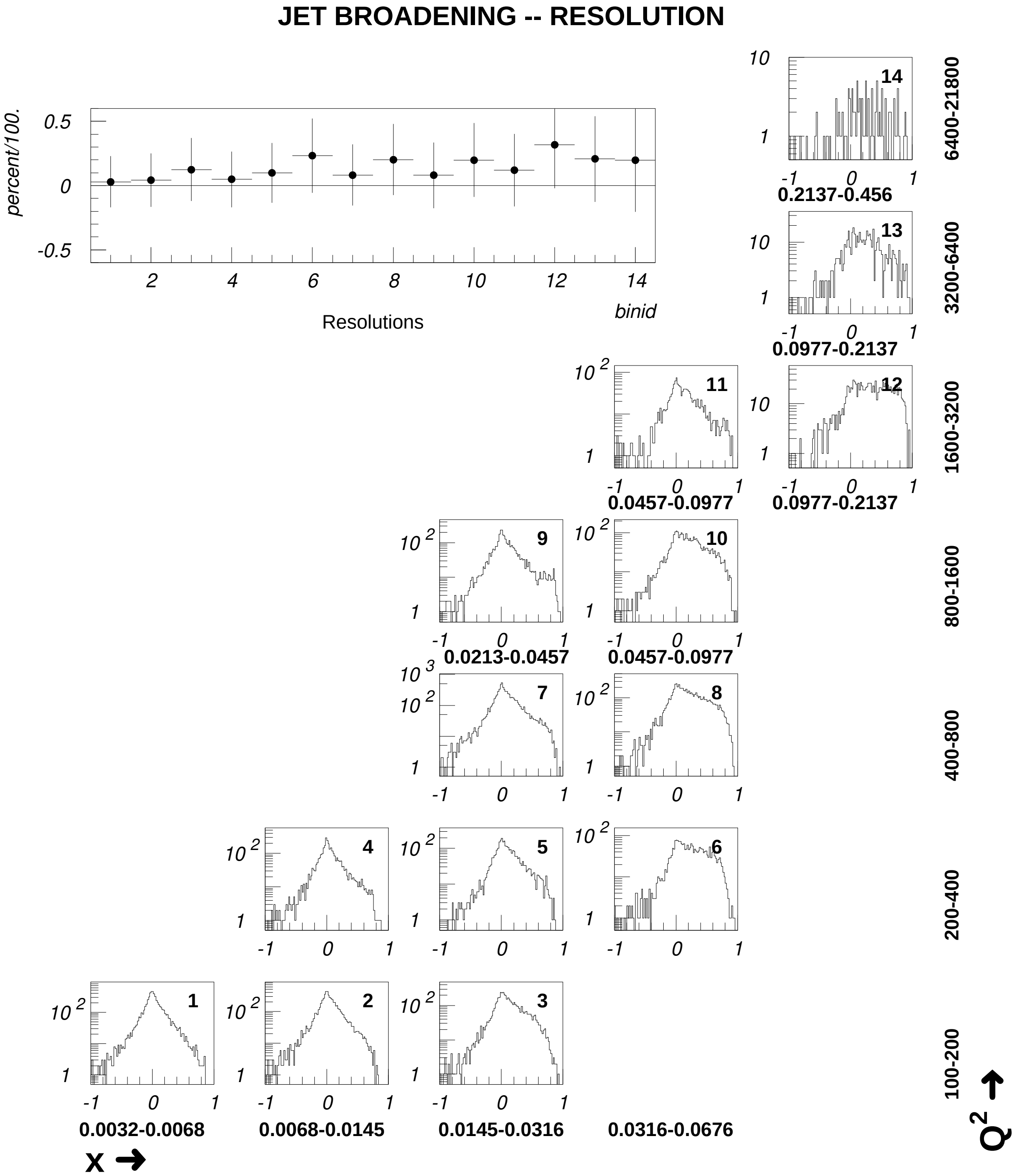

Figure 5.14: *Resolution of J_b. The inset shows mean and rms values of the histograms.*

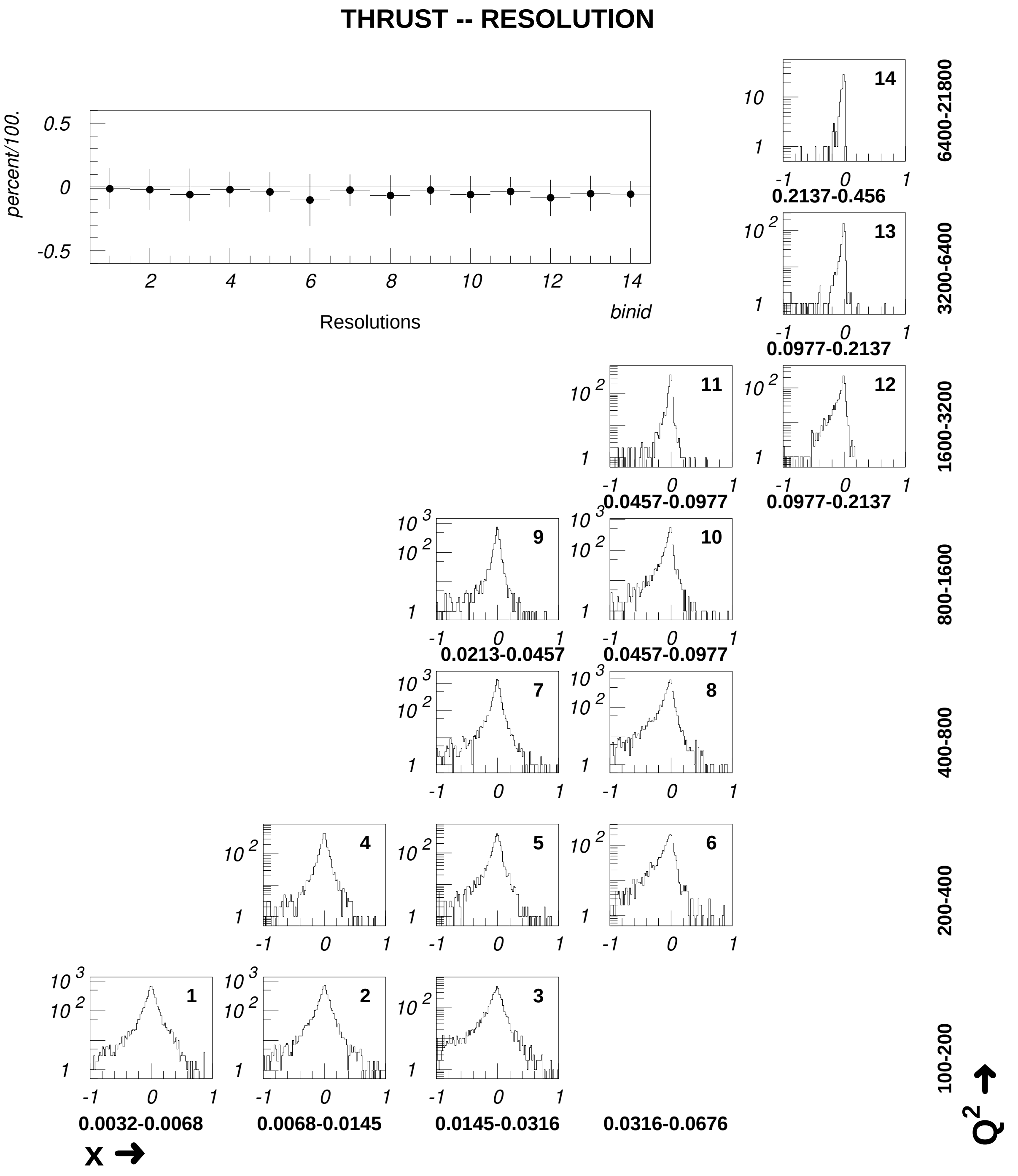

Figure 5.15: *Resolution of T_z, using Combined objects boosted with the* true *boost vector.*

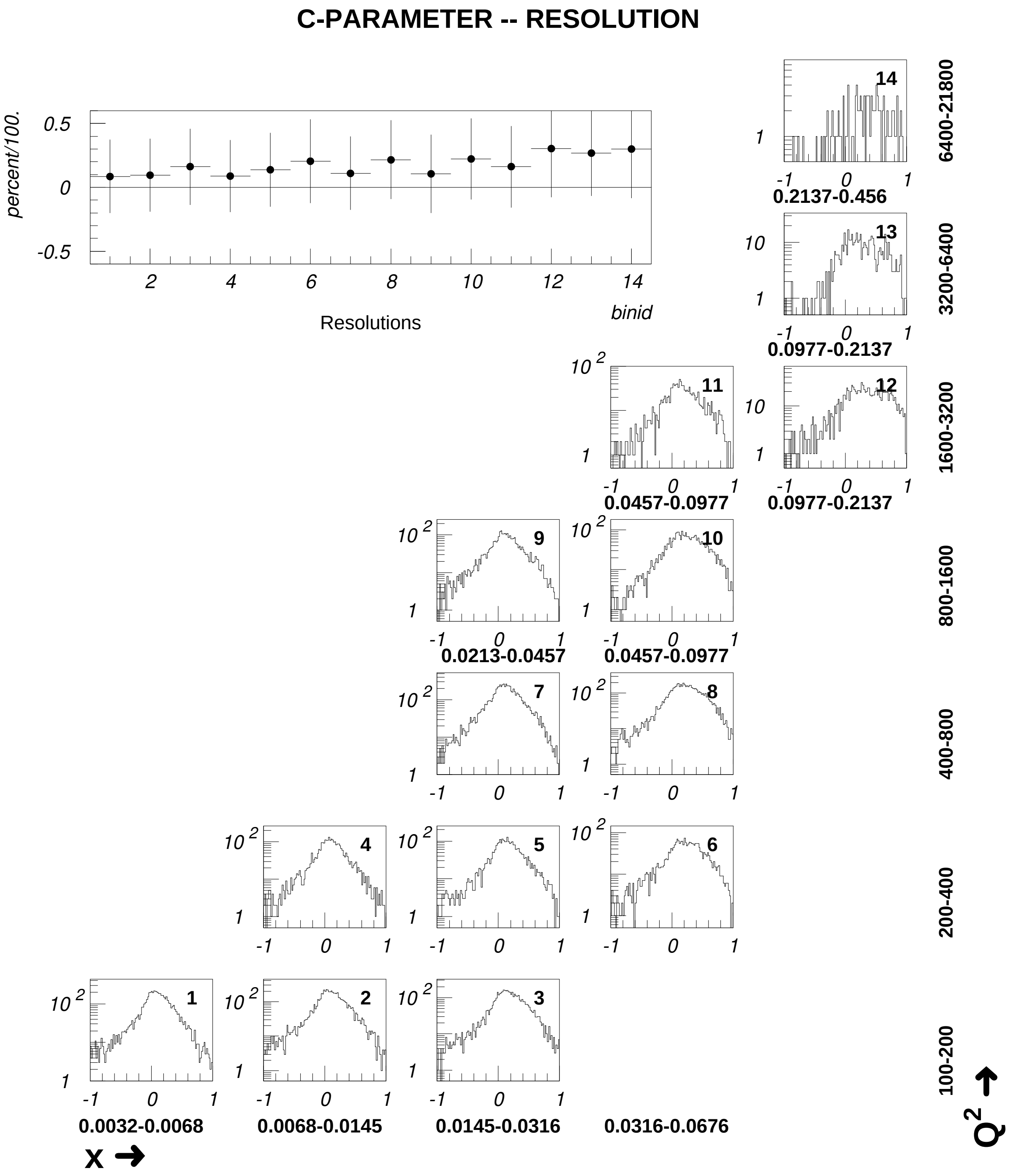

Figure 5.16: *Resolution of* C_p*, using Combined objects boosted with the* true *boost vector.*

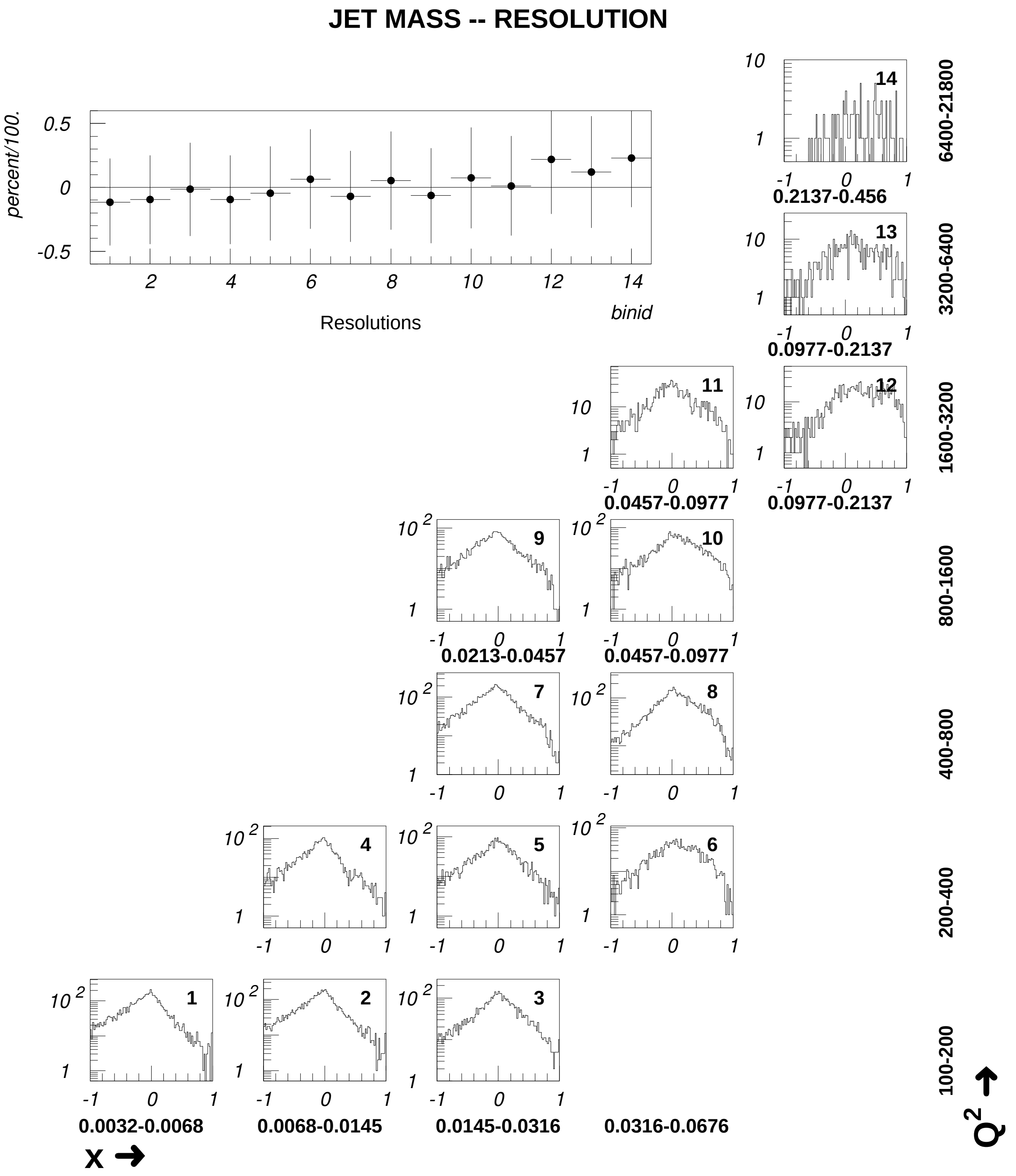

Figure 5.17: *Resolution of J_m, using Combined objects boosted with the* true *boost vector.*

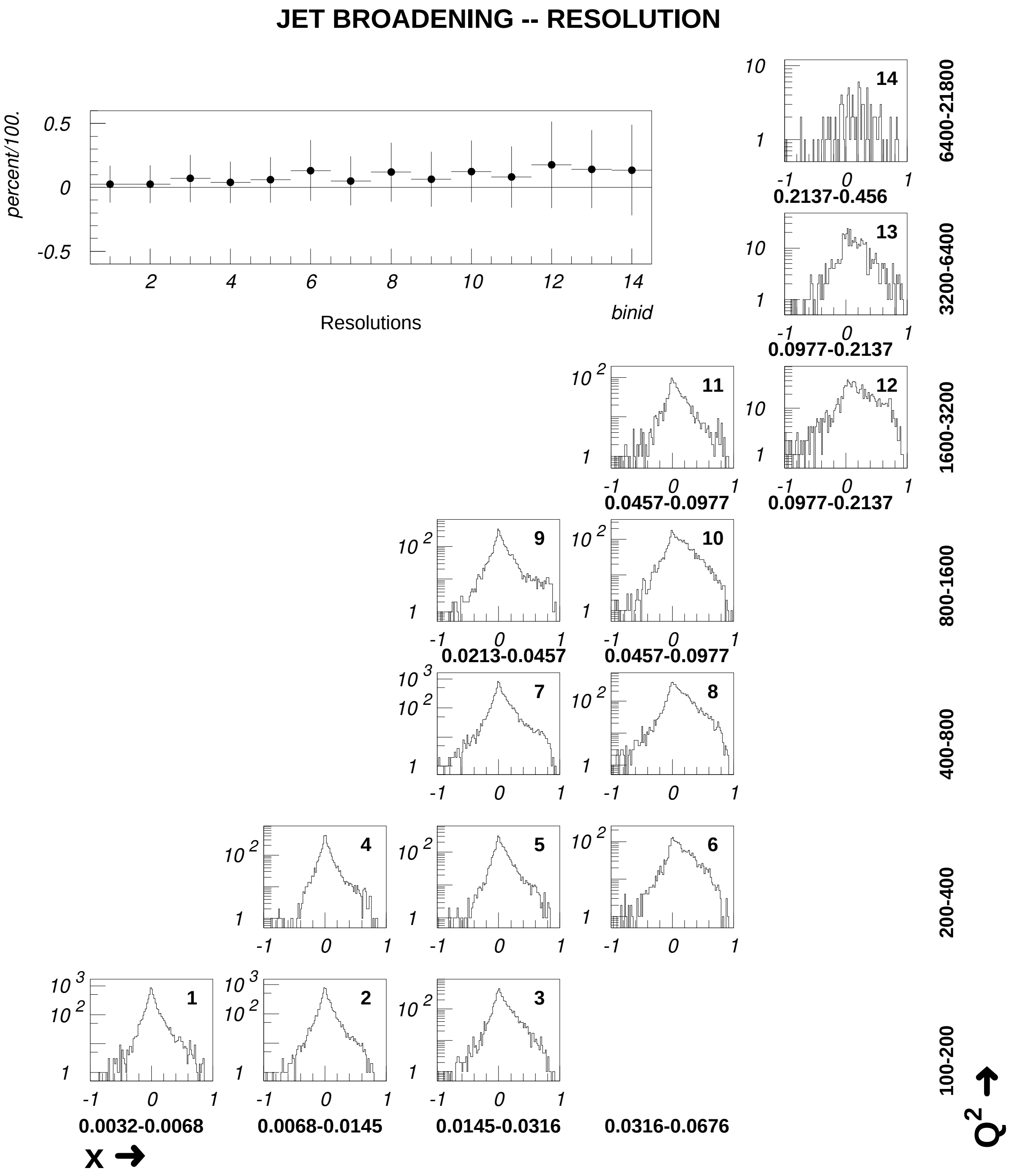

Figure 5.18: *Resolution of* J_b*, using Combined objects boosted with the* true *boost vector.*

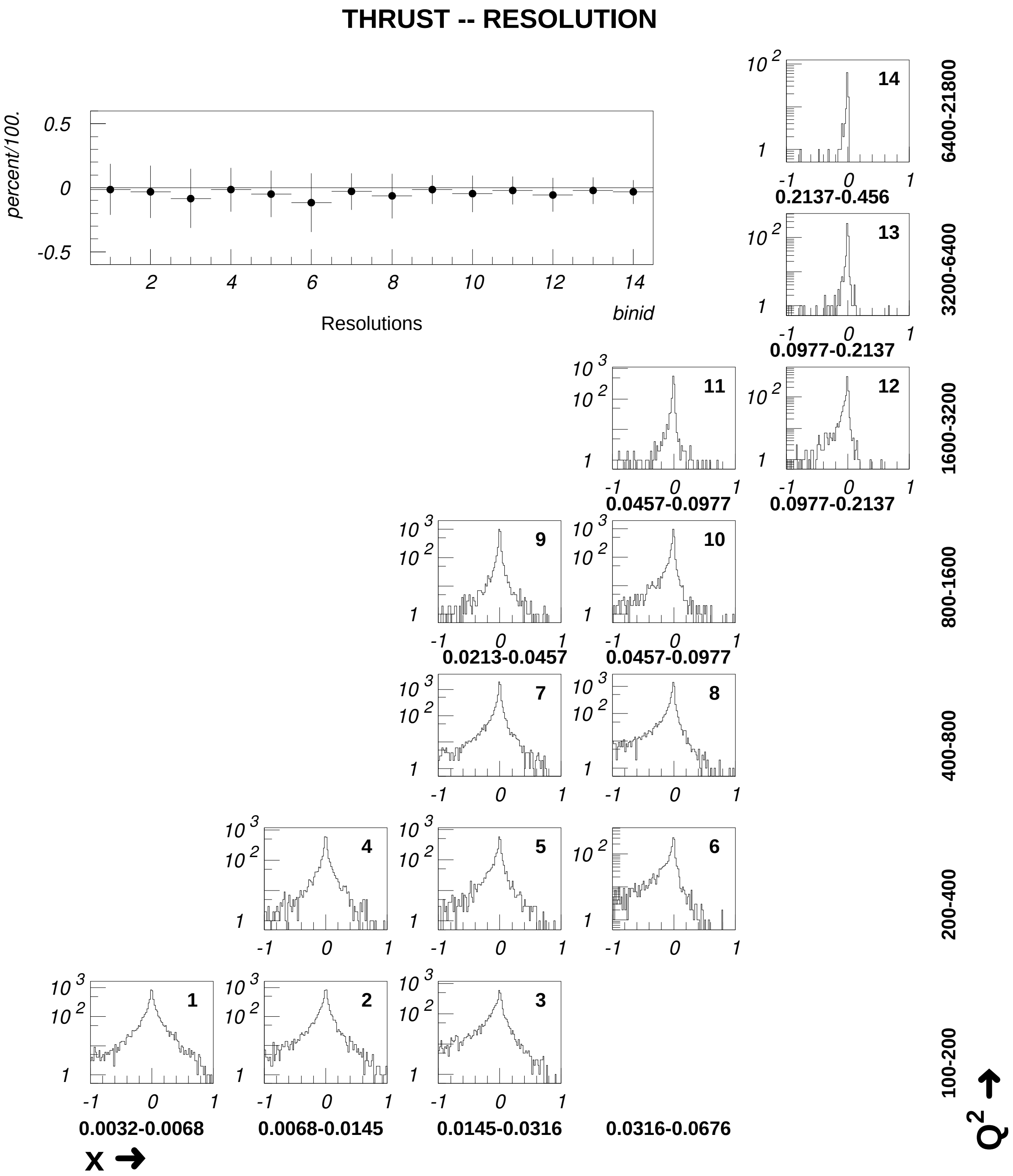

Figure 5.19: *Resolution of T_z, using hadron level particles boosted with the reconstructed boost vector.*

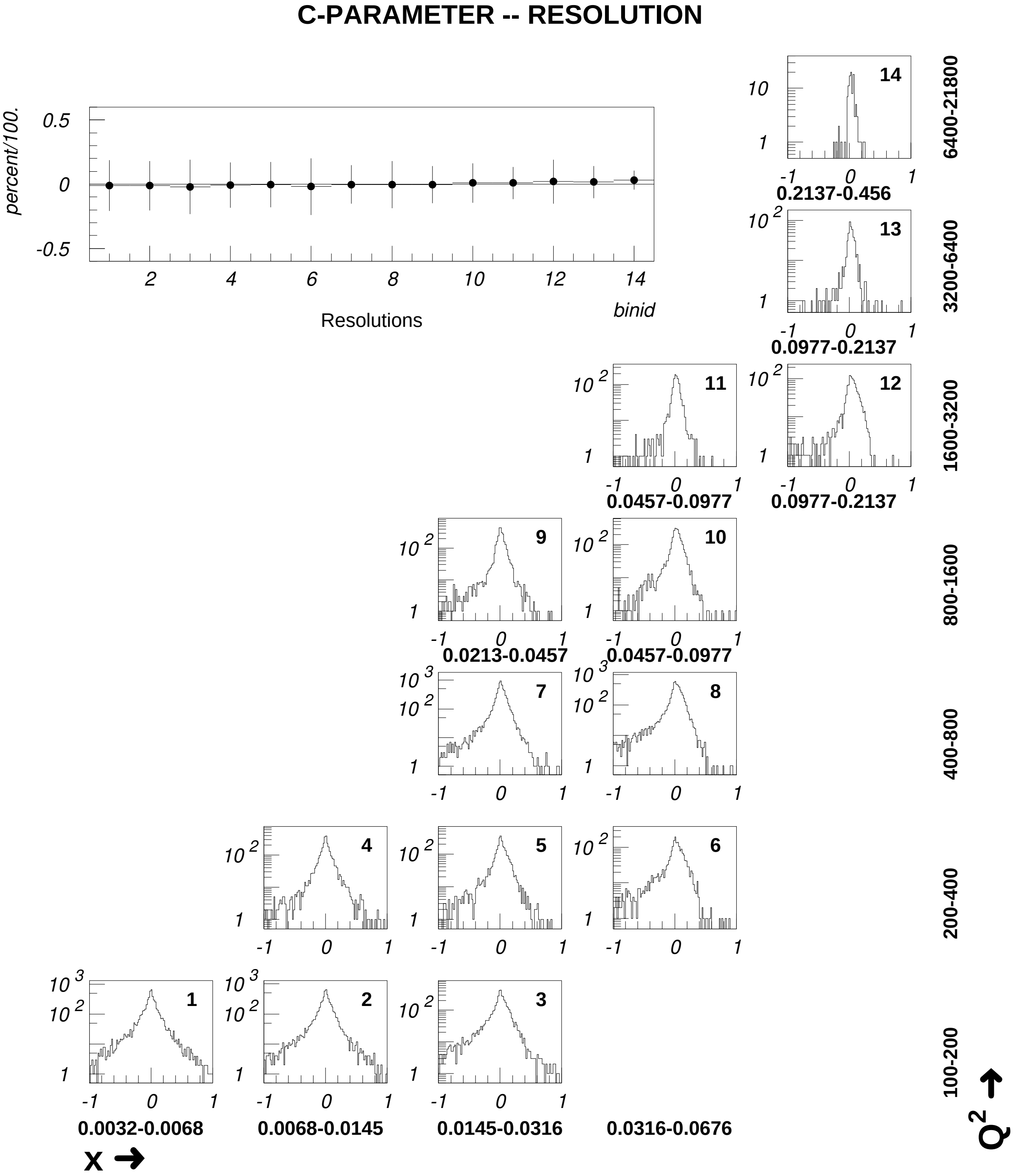

Figure 5.20: *Resolution of C_p, using hadron level particles boosted with the reconstructed boost vector.*

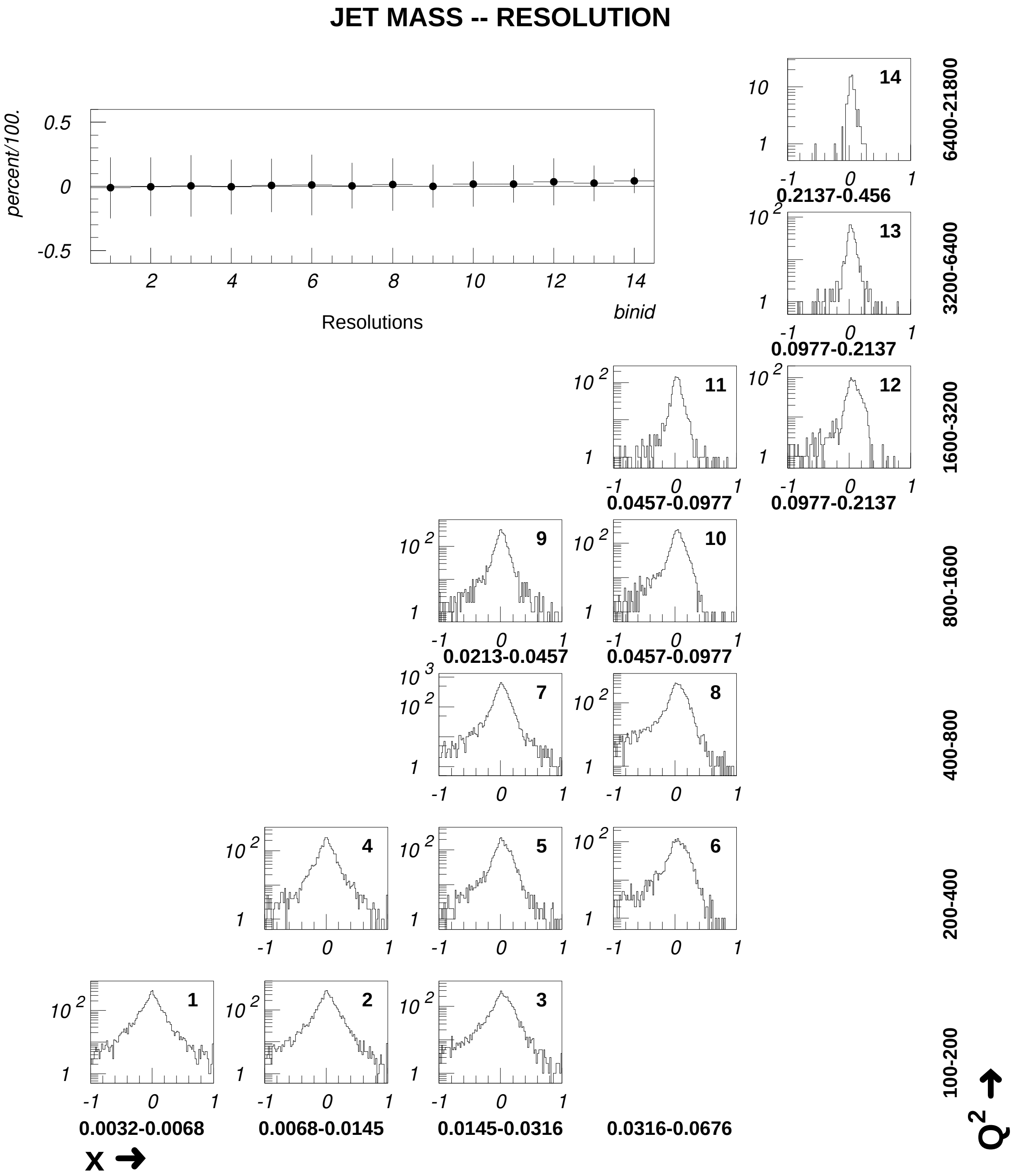

Figure 5.21: *Resolution of J_m, using hadron level particles boosted with the reconstructed boost vector.*

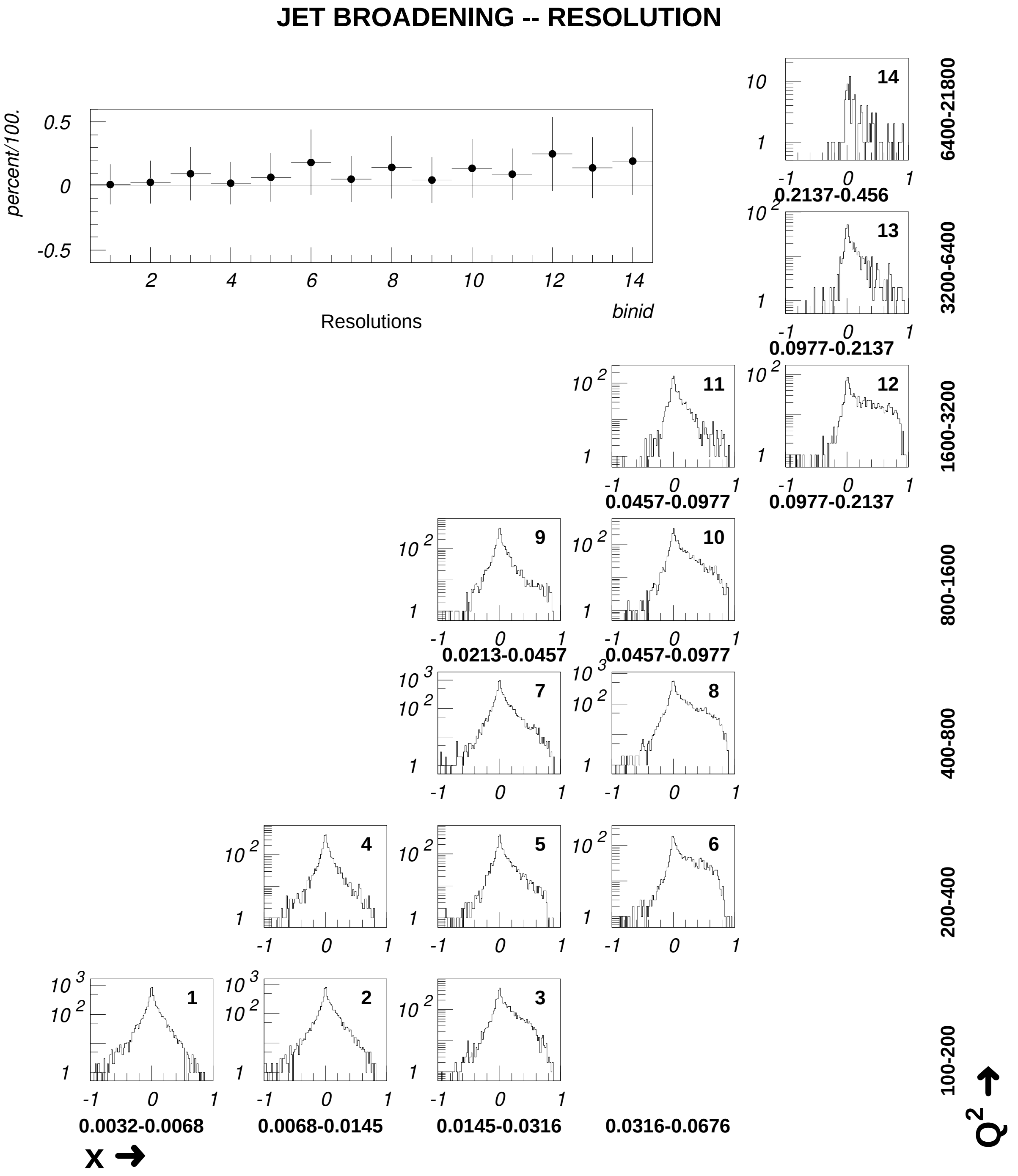

Figure 5.22: *Resolution of J_b, using hadron level particles boosted with the reconstructed boost vector.*

Chapter 6

Measurement Results

This chapter presents the measurement results. First the uncorrected differential distributions are shown (Section 6.1) and compared to the results of the two Monte Carlo samples (see Section 4.1). The chapter then focuses on the analysis of the mean values (Section 6.2), whereas the differential distributions are further discussed in the Appendix. Section 6.3 contains the results of a study of systematic effects on the measured mean values.

It is recalled that the analysis of event shape variables is performed in the Breit frame of reference (Section 2.3). The boost vector γ_{boost} from the laboratory frame to the Breit frame is computed using the four-vector of the scattered electron (Section 4.3). Once γ_{boost} is determined, the four-momenta of all particles in the hadronic final state (i.e. the combined track-calorimeter objects described in Section 5.4) are boosted to the Breit frame. The variables thrust T_z, C-parameter C_p, Jet mass J_m and Jet broadening J_b are computed from the particles found in the current hemisphere, according to their definition Equations 2.10 to 2.13. The infrared cut introduced in Section 4.5 restricts the analysis to a region in phase space where always a significant amount of energy is found in the current hemisphere.

The analysis is strongly model-dependent. Thus a fundamental question is how well a Monte Carlo model describes the observed data. The shape of the differential distributions is reproduced fairly well by both models, although neither of the models describes the data perfectly. The poorest agreement is observed for the J_b distributions. The mean values in the lower Q^2 bins are well reproduced by ARIADNE, but large discrepancies are observed in the higher Q^2 bins. HERWIG gives a better description in the higher Q^2 bins but in the lower Q^2 bins the mean values are systematically off.

Consequently model-dependence is found to be the largest contribution to the systematic error for all four event shape variables. Furthermore C-parameter and Jet mass are found to be susceptible to any changes in the cluster and matching algorithms which affect the particle multiplicity.

6.1 Uncorrected Differential Distributions

In each analysis bin a binning in T_z, C_p, J_m and J_b was choosen with typically 6 – 8 bins ranging from zero to the respective maximum value (1 for T_z and C_p, 0.5 for J_b and 0.25 for J_m). The number of bins is a compromise between a desired high number of bins and equally desired high efficiencies and purities for each of them. The exact numerical ranges of the event shape bins are listed in the Tables C.1 to Table C.14 in the Appendix. Also efficiencies and purities of the bins are presented there.

The measured, uncorrected differential distributions of the four event shape variables are shown in Figures 6.1, 6.2, 6.3 and 6.4. The distributions have a rather broad shape in the bins at lower values of Q^2, and they become more peaked in the higher Q^2 bins. T_z peaks at its maximum value 1, C_p and J_m peak at lower values $\rightarrow 0$. The strongest change in the shape of the distributions is observed for J_b: in bins at higher Q^2 the peak of the distributions is observed at rather low values ($J_b \approx 0.1$), whereas in bins at lower Q^2 values only very few events have small J_b values. According to the explanations in Section 2.4, the interpretation is that particles in the events become more collimated and centred around the photon axis for larger values of momentum transfer.

The Figures 6.1 to 6.4 also show the results for the ARIADNE and HERWIG samples. In general both models succeed in describing the shape of the distributions, however, deviations are observed at the edges of the distributions, i.e. for very low or very high values of the event shape variables.

In both models the tendency is observed to systematically overestimate the number of events with very high values of T_z. As was discussed in Section 2.4, high values are characteristic to events with a collimated particle distribution centred around the photon axis in the current region of the Breit frame. This kind of events is further characterised by Jet broadening values of ≈ 0. Consistently, an overestimation of events with low values of J_b is found in both Monte Carlo models. These observations may indicate a general underestimation of the contribution from boson-gluon fusion in the higher order processes simulated in the Monte Carlo models.

It is also discussed in Section 2.4 that the variables C_p and J_m are measures of the broadness of particle distributions (or *jets* if one prefers) in an event. Both variables take on larger values for more isotropic particle distributions. As can be seen in Figure 6.2 and Figure 6.3, the number of events with high values of C_p and J_m is systematically underestimated by HERWIG. ARIADNE shows a similar underestimation in the higher Q^2 bins. It is concluded that the particle distributions in HERWIG generally and in ARIADNE in the higher Q^2 bins are more collimated than in the data. This conclusion gets further evidence by the observation that the number of events with low C_p and J_m values is generally higher in both Monte Carlos compared to the data measurement.

It may be concluded that the Monte Carlo models give an acceptable, but not completely satisfactory description of the differential distributions in the data. Further fine tuning of the models is neccessary, although this is a task which goes beyond the scope of this thesis.

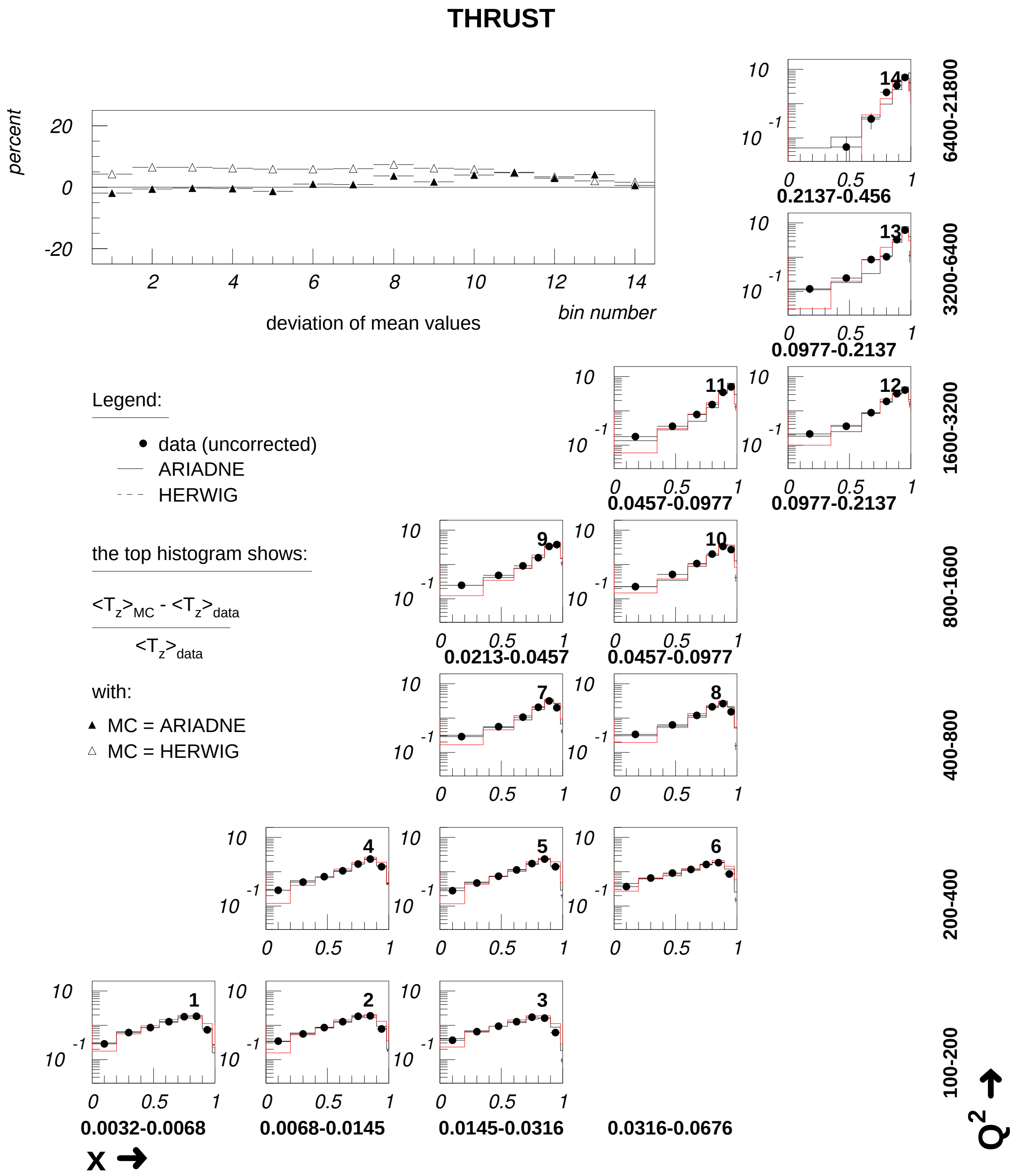

Figure 6.1: *Uncorrected differential distributions of thrust T_z. The data (circles) is compared to the ARIADNE (solid lines) and HERWIG (dashed lines) Monte Carlo samples. The inset shows the comparison of the mean values, where the errors shown are the relative errors of the data mean values.*
The shape of the distributions is well reproduced by the Monte Carlos, larger deviations are observed only in the bins for very low and very high T_z. The mean values are described better by the ARIADNE sample, larger deviations are observed only in the higher Q^2 bins. The HERWIG sample generally underestimates the amount of events with very low T_z, consequently the mean values are systematically higher than the data mean values.

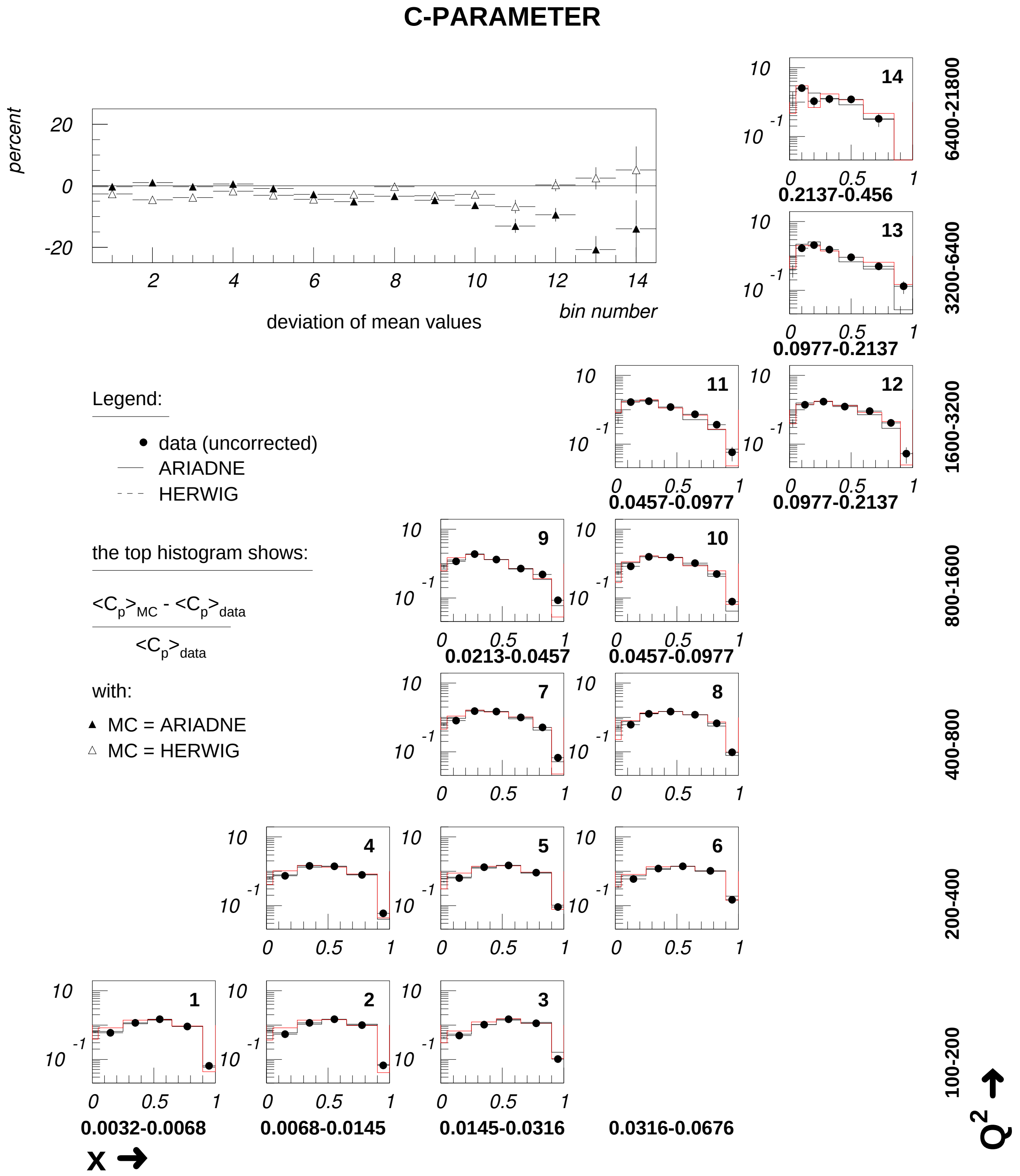

Figure 6.2: *Uncorrected differential distributions of C-parameter C_p. The data (circles) is compared to the ARIADNE (solid lines) and HERWIG (dashed lines) Monte Carlo samples. The inset shows the comparison of the mean values, where the errors shown are the relative errors of the data mean values.*

The shape of the distributions are generally reproduced by both Monte Carlo models, HERWIG systematically overestimates the number of events with very low C_p, ARIADNE on the other hand underestimates the number of events with large C_p. This discrepancy is particularly large in the bins at higher Q^2, and consequently the ARIADNE mean values in bins with id > 10 differ by more than 10% from the data. In the bins at lower Q^2 the HERWIG mean values show the same order of 5% discrepancy observed already for the T_z mean values.

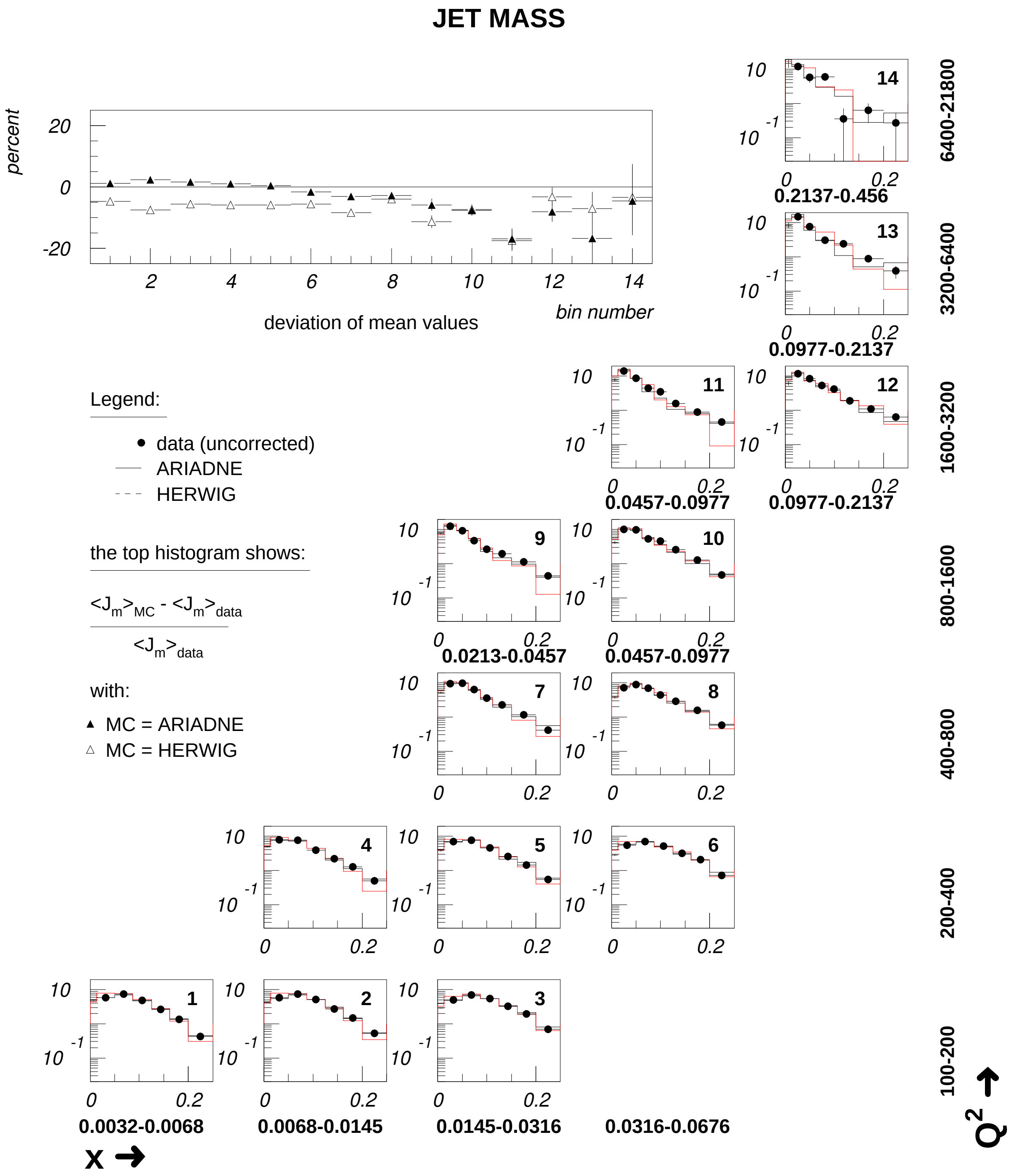

Figure 6.3: *Uncorrected differential distributions of Jet mass J_m. The data (circles) is compared to the ARIADNE (solid lines) and HERWIG (dashed lines) Monte Carlo samples. The inset shows the comparison of the mean values, where the errors shown are the relative errors of the data mean values.*
The HERWIG sample systematically underestimates the number of events with high J_m, this is also seen for the ARAIDNE sample in the higher Q^2 bins. Additionally, the HERWIG sample shows an overestimation of events with low J_m values in the lower Q^2 bins. The mean values of the low Q^2 bins are well reproduced by ARIADNE and are systematically too low when computed from the HERWIG sample. However, in the higher Q^2 bins ARIADNE does not describe the mean values correctly.

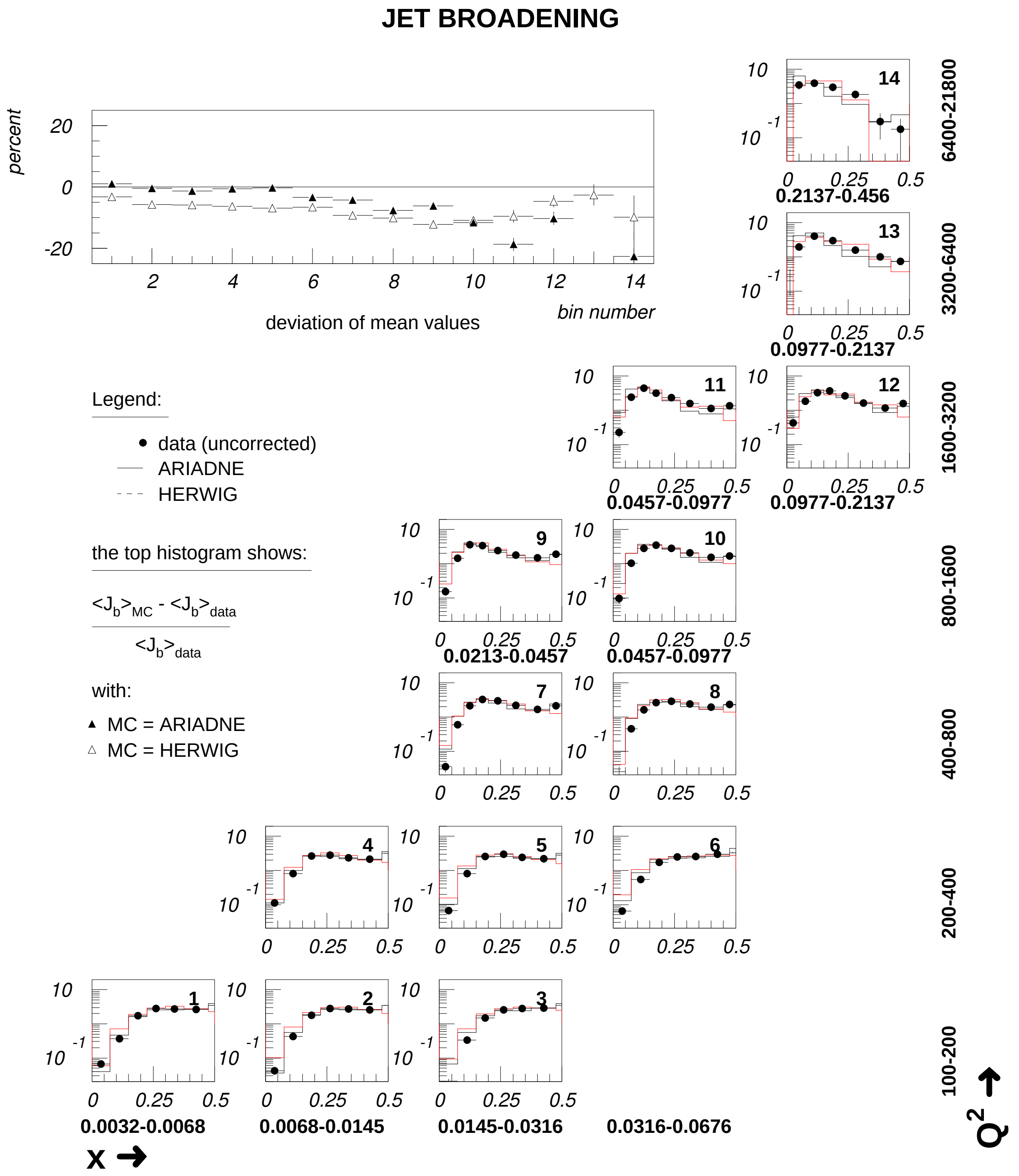

Figure 6.4: *Uncorrected differential distributions of Jet broadening J_b. The data (circles) is compared to the ARIADNE (solid lines) and HERWIG (dashed lines) Monte Carlo samples. The inset shows the comparison of the mean values, where the errors shown are the relative errors of the data mean values.*

Both ARIADNE and HERWIG describe rather poorly the J_b differential distributions as measured in the data. Both overestimate the number of events wth low values of J_b. Additionally, HERWIG fails to describe the number of events with a large value of J_b, which is generally well described by ARIADNE. The mean values are consequently systematically too low in the HERWIG sample, and much too low in the high Q^2 bins in the ARIADNE sample.

6.2 Mean Values of Event Shape Distributions

Figures 6.1, 6.2, 6.3 and 6.4 each contain an inset where the relative deviation

$$\delta_F = (\langle F \rangle_{\mathrm{MC,detlevel}} - \langle F \rangle_{\mathrm{data}}) / \langle F \rangle_{\mathrm{data}} \tag{6.1}$$

is shown between the mean value $\langle F \rangle_{\mathrm{data}}$ obtained in data and the mean value $\langle F \rangle_{\mathrm{MC,detectorlevel}}$ obtained at detector level Monte Carlo. F is used here as a general symbol for one of the four event shape variables T_z, C_p, J_m and J_b. The error bars shown are the relative errors of the *data* mean values. In lower Q^2_{DA} bins ARIADNE describes the mean values very well, however, large deviations of up to 15% are observed in the higher Q^2 bins. HERWIG shows a poorer description of the mean values in the lower Q^2 bins, typically off by 5%. However, the mean values in the higher Q^2 bins are better reproduced by the HERWIG sample. Thus the agreement of data and Monte Carlo is not fully satisfactory. As was pointed out above, further tuning of the models is necessary.

The Monte Carlo samples are used for *unfolding* the data, i.e. for correcting the data for detector resolution and acceptance effects. This procedure is basically a correction of data to Monte Carlo hadron level.

The correction factors c_F for the mean value $\langle F \rangle_{\mathrm{data}}$ of event shape distributions are determined from the mean values at detector and hadron level Monte Carlo, $\langle F \rangle_{\mathrm{MC,detectorlevel}}$ and $\langle F \rangle_{\mathrm{MC,hadronlevel}}$ respectively. The correction factors in turn are used for deriving the corrected mean value $\langle F \rangle_{\mathrm{corrected}}$:

$$\begin{aligned} c_F &= \langle F \rangle_{\mathrm{MC,hadronlevel}} / \langle F \rangle_{\mathrm{MC,detectorlevel}} \\ \langle F \rangle_{\mathrm{corrected}} &= c_F \cdot \langle F \rangle_{\mathrm{data}} \qquad \mathrm{with} \langle F \rangle \in \{ \langle T_z \rangle, \langle C_p \rangle, \langle J_b \rangle, \langle J_m \rangle \} \end{aligned}$$

The corrected mean values for T_z, C_p, J_m and J_b are shown in Figure 6.5. The error bars correspond to the total error which is the quadratic sum of the statistical and systematic errors. The systematic errors were determined from a study of systematic effects, which is discussed in the following section. The uncorrected and corrected mean values, the correction factors and the total statistical and systematic errors in each of the analysis bins are listed in the Tables 6.1, 6.2, 6.3 and 6.4.

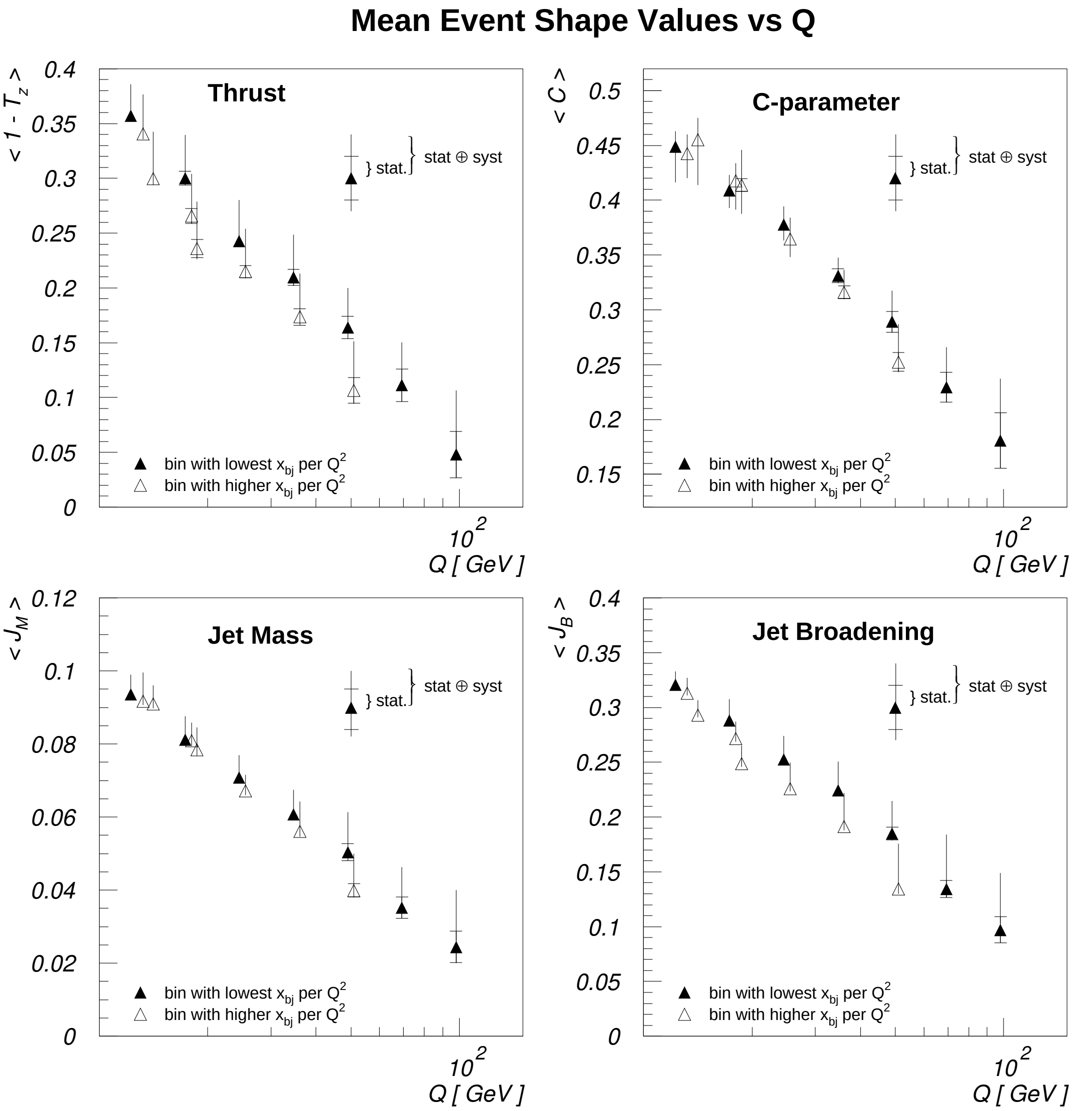

Figure 6.5: *Mean values of the event shape variables thrust, C-parameter, Jet mass and Jet broadening. Note that* $\tau_z = 1 - T_z$ *is plotted rather than* T_z*. For most of the* Q^2 *values more than one bin in* x_{bj} *was defined. These* x_{bj} *bins are plotted slightly offset horizontally for better visibility. Filled triangles refer to mean values obtained in the lowest* x_{bj} *bin for each* Q^2 *value. Thus they refer to a set of bins with similar* y*. Both statistical and systematical errors are shown. The mean values are plotted logarithmically versus* Q *and not versus* Q^2 *in order to better show their* $1/Q$ *functional dependence.*

Bin	uncorr. mean	error	correction factor	error	corrected mean	error (stat.)	pos. system.	neg system.
1	0.617	0.002	1.043	0.007	0.643	0.004	0.002	−0.029
2	0.620	0.002	1.063	0.007	0.659	0.005	0.002	−0.035
3	0.596	0.003	1.176	0.008	0.700	0.005	0.003	−0.042
4	0.663	0.003	1.056	0.009	0.700	0.006	0.001	−0.039
5	0.664	0.003	1.106	0.010	0.734	0.007	0.002	−0.038
6	0.609	0.004	1.255	0.013	0.764	0.008	0.004	−0.042
7	0.713	0.004	1.062	0.005	0.757	0.005	0.002	−0.037
8	0.684	0.005	1.148	0.006	0.785	0.006	0.003	−0.039
9	0.747	0.006	1.058	0.007	0.790	0.007	0.002	−0.038
10	0.739	0.007	1.118	0.007	0.827	0.008	0.001	−0.039
11	0.789	0.009	1.059	0.009	0.836	0.010	0.002	−0.034
12	0.776	0.010	1.151	0.010	0.894	0.012	0.003	−0.043
13	0.824	0.013	1.079	0.011	0.889	0.015	0.002	−0.036
14	0.884	0.015	1.077	0.018	0.952	0.021	0.002	−0.055

Table 6.1: *Results for thrust.*

Bin	uncorr. mean	error	correction factor	error	corrected mean	error (stat.)	pos. system.	neg system.
1	0.476	0.003	0.943	0.008	0.449	0.004	0.014	−0.032
2	0.487	0.003	0.908	0.007	0.442	0.004	0.017	−0.022
3	0.518	0.003	0.878	0.008	0.455	0.004	0.020	−0.041
4	0.450	0.004	0.908	0.011	0.409	0.005	0.013	−0.015
5	0.479	0.004	0.872	0.010	0.418	0.005	0.016	−0.025
6	0.502	0.005	0.824	0.011	0.414	0.006	0.032	−0.025
7	0.423	0.007	0.894	0.008	0.378	0.004	0.016	−0.014
8	0.464	0.007	0.786	0.007	0.364	0.004	0.019	−0.016
9	0.377	0.012	0.879	0.013	0.331	0.006	0.015	−0.003
10	0.425	0.011	0.743	0.011	0.316	0.006	0.020	−0.002
11	0.361	0.020	0.801	0.021	0.289	0.010	0.027	−0.003
12	0.382	0.020	0.661	0.018	0.252	0.009	0.033	−0.003
13	0.343	0.036	0.670	0.031	0.230	0.014	0.034	−0.001
14	0.307	0.081	0.588	0.067	0.181	0.025	0.051	−0.002

Table 6.2: *Results for C-parameter.*

Bin	uncorr. mean	error	correction factor	error	corrected mean	error (stat.)	pos. system.	neg system.
1	0.081	0.004	1.155	0.012	0.094	0.001	0.005	0.000
2	0.083	0.004	1.106	0.011	0.092	0.001	0.008	0.000
3	0.092	0.004	0.993	0.011	0.091	0.001	0.005	−0.001
4	0.075	0.006	1.083	0.017	0.081	0.001	0.006	−0.001
5	0.080	0.006	1.011	0.016	0.081	0.001	0.005	−0.001
6	0.090	0.006	0.869	0.015	0.078	0.001	0.006	−0.001
7	0.068	0.009	1.039	0.013	0.071	0.001	0.006	0.000
8	0.078	0.010	0.864	0.011	0.067	0.001	0.004	−0.001
9	0.061	0.017	1.001	0.020	0.061	0.002	0.006	0.000
10	0.070	0.016	0.800	0.016	0.056	0.001	0.008	0.000
11	0.058	0.028	0.865	0.031	0.050	0.002	0.011	−0.001
12	0.065	0.029	0.616	0.022	0.040	0.002	0.010	−0.001
13	0.054	0.050	0.656	0.043	0.035	0.003	0.011	0.000
14	0.045	0.107	0.538	0.077	0.024	0.004	0.015	−0.001

Table 6.3: *Results for jet mass.*

Bin	uncorr. mean	error	correction factor	error	corrected mean	error (stat.)	pos. system.	neg system.
1	0.334	0.002	0.960	0.005	0.321	0.002	0.012	−0.001
2	0.331	0.002	0.946	0.006	0.313	0.002	0.014	−0.001
3	0.342	0.002	0.858	0.006	0.293	0.002	0.014	−0.001
4	0.308	0.003	0.936	0.009	0.288	0.003	0.019	−0.001
5	0.307	0.003	0.884	0.009	0.271	0.003	0.015	−0.001
6	0.335	0.003	0.744	0.009	0.249	0.003	0.016	−0.001
7	0.279	0.006	0.906	0.007	0.252	0.002	0.022	−0.001
8	0.294	0.006	0.770	0.007	0.226	0.002	0.023	−0.001
9	0.254	0.010	0.884	0.013	0.224	0.004	0.026	−0.001
10	0.259	0.010	0.739	0.011	0.192	0.003	0.030	−0.001
11	0.226	0.018	0.820	0.022	0.185	0.006	0.029	−0.001
12	0.233	0.019	0.577	0.015	0.134	0.004	0.041	−0.001
13	0.201	0.034	0.668	0.032	0.134	0.008	0.049	−0.001
14	0.165	0.065	0.588	0.061	0.097	0.012	0.051	−0.002

Table 6.4: *Results for jet broadening.*

6.3 Study of Systematic Effects

This section gives a list of systematic checks which have been perfomed in order to estimate the systematic errors of the analysis. The ARIADNE Monte Carlo sample is used as default Monte Carlo model and the HERWIG sample is used for an additional systematic check. For each of the listed checks i the ARIADNE sample was reanalysed and correction factors $c_{\text{sys}\,i}$ were computed. These correction factors were used for correcting the – unchanged – data mean values. The result is a set of new corrected mean values $\langle F\rangle_{\text{sys}\,i}$ for each systematic check. The deviations of these new mean values relative to the default mean values $\langle F\rangle_{\text{default}}$ are computed according to:

$$(\Delta\langle F\rangle)_{\text{sys}\,i} = \frac{\langle F\rangle_{\text{sys}\,i} - \langle F\rangle_{\text{default}}}{\langle F\rangle_{\text{default}}}$$

The checks performed can be divided into three distinct categories. First the selection cuts and the energy scale of the calorimeter is varied. To the second category belong all checks where parameters in the cluster and matching algorithms are changed. The third category consists of only one check, namely the model-dependance check where the HERWIG sample is used for data unfolding.

The performed checks are listed in detail below. The observed deviations according to Equation 6.3 are shown in the Figures 6.6, 6.7, 6.8 and 6.9.

Changes of Selection Cuts and Energy Correction

1. **Tighter $E - p_z$ cut**

   The cut on the $E - p_z$ variable which ensures longitudinal energy containment is tightened from $E - p_z \in [35, 60]$ GeV to $E - p_z \in [40, 60]$ GeV. This check leaves the results virtually unchanged. A shift in the order of 1% is observed only in bin 13.

2. **Stronger Electron Isolation**

   Isolation of the scattered electron is required in the analysis. The hadronic energy within a cone around the electron of radius 0.8 in the $\eta - \phi$ plane is required to be less than 5 GeV. For this check the radius of the cone is raised to 0.9. The effect on the mean values is below 1% in all bins.

3. **Raise Cut on Minimum y_{JB}**

   For this check the minimum y_{JB} reconstructed is required to be 0.05 instead of 0.04. This change has an effect of more than 1% only in the bins 3 and 6. As was shown in Figure 4.5, these bins extend slightly over the cut border of $y_{\text{JB}} = 0.04$, which explaines the variation.

4. **Energy Scale Up**

   The measured hadronic energy was scaled up by 5% in order to simulate the effect of an incorrectly-scaled calorimeter energy. The effect with less than 1% in all bins is clearly negligible.

5. Energy Scale Down

The measured energy was scaled down by 5%. The effect is less than 1% in all bins.

6. Calorimeter Energy Correction Switched Off

In the analysis a global energy correction of 5% for RCAL and 2.5% for BCAL was applied – only to the data – prior to reconstructing the kinematic variables. In order to simulate the effect of this global correction, the energy in the Monte Carlo was scaled for this check by -2.5% for BCAL and by -5% for RCAL prior to reconstructing the kinematic variables. Consequently this systematic check biases the selection of events and the assignment of events into the analysis bins. (This is in contrast to the two checks above, where the energy was scaled only after the assignment of events into the bins.) As expected, a larger systematic effect is observed compared to the checks above, but all shifts still lie within 1% for all bins. It can be concluded that energy scale uncertainties present no problem in this analysis.

7. Lower the Infrared Cut

The infrared cut was lowered by 2% for this check requiring a minimum energy in the current region of 0.08 Q instead of 0.1 Q. The effect of this change is less than 1% in all bins.

8. Raise the Infrared Cut

The infrared cut was raised by 2% for this check requiring a minimal energy in the current region of 0.12 Q instead of 0.1 Q. The effect of this change is less than 1% in all bins.

Changes in the Matching Algorithm

9. Lower Cutoff in Cluster Position Reconstruction

The set of cutoff parameters for the logarithmic position reconstruction of calorimeter islands as introduced on page 58 was changed from 4 (electromagnetic islands) and 2 (hadronic islands) to 3 and 1 for electromagnetic and hadronic islands respectively. This corresponds to a raise of energy threshold a calorimeter cell must exceed before included in the logarithmic weighting. No significant change is observed.

10. Raise Cutoff in Cluster Position Reconstruction

The cutoff parameters were changed to 5 and 3 for electromagnetic and hadronic clusters respectively. This corresponds to lowering the energy threshold a cell must exceed in order to be included in the logarithmic weighting. The variations remain within 1%, except in the highest Q^2_{DA} bin (bin 14) where a change of 2% is observed.

11. Switch to Corner Connect Mode for Cellislands

The two available options in the Cellisland cluster algorithm were explained on page 57. The nearest neighbour mode was chosen to be the default mode and is changed to the corner connect mode in this check. Since the corner connect mode combines on average more cells into one Cellisland, the multiplicity is lowered with this check. A change of multiplicity has only a small effect on T_z and J_b, however for C_p and J_m changes of up to 6% are observed.

12. Different Probability Cuts for Cone Islands

The probability cuts for combining Cellislands to Cone Islands are altered from 0.1 and 0.3 to 0.05 and 0.2 respectively. This also affects the mupltiplicity in the Breit frame, the multiplicity is lowered on average since Cellislands are more easily combined. Again, for T_z and J_b only a small change is observed, whereas C_p and J_m suffer from changes of more than 6%.

13. Tighter $\frac{E}{p}$ Cut

The cut value κ on a maximum $\frac{E}{p}$ (see Equation 5.6) for substituting island with track information is lowered from 0.9 to 0.8. The effect of this change is negligible.

14. Smaller Δ $\frac{E}{p}$ Tolerance

The value n in Equation 5.6 denotes the number of standard deviation which are allowed for $\frac{E}{p}$ to be larger than the cut value κ. For this check n was lowered from 2 to 1. This alternation has no effect on the mean values.

15. Omit Unmatched Tracks

For this check unmatched tracks were not used as “particles” for deriving the event shape variables. Omitting these *loose tracks* decreases the multiplicity in the current region. Thus the mean values of the C-parameter, as an observable sensitive to multiplicity, are strongly affected by this change. Shifts of the order of 1% to 4% are observed for C_p and up to 7% for J_m. For T_z and J_b the observed changes are of the order of 1%.

16. Less CTD Information Used

The default algorithm makes use of the angular measurement of the CTD for 1-to-1 track-cluster matches, where the energy of the cluster is larger than the momentum of the track ($\frac{E}{p}$ criterion). The algorithm used for this check uses only island information for these objects. This change affects the mean values less than 1% in all bins.

17. Backsplash Correction

Some of the low-energy islands in the forward BCAL can be identified as having been induced by backscattered particles. Removing these islands before the track-calorimeter matching is performed and before the event shape variables are computed obviously lowers the multiplicity. The mean values for T_z and J_b change by up to 2% for some of the bins. As expected the mean values of C_p and J_m are affected most strongly. Changes of more than 10% in some of the bins are observed.

Model Dependance

18. Using HERWIG for Unfolding

For this check the HERWIG Monte Carlo sample was used for deriving the correction factors. The insets of the Figures 6.1 to 6.4 show large deviations between the two models ARIADNE and HERWIG, where neither of the two describes the data mean values in a fully satisfactory way. Consequently it is not surprising that the change of Monte Carlo model calls for the largest systematic error. T_z is with an overall deviation of 5% comparatively moderatly changed, the other event shape variables suffer from changes of up to 20% in the higher Q^2 bins.

The deviations of the various systematic checks are used for deriving the total systematic error of the mean values. For each bin and for each event shape variable separately all positive deviations are combined in quadrature in order to give the positive systematic error. Respectively, all negative deviations are combined in quadrature to give the negative systematic error. This method results in asymmetric systematic errors, as is shown in Figure 6.5 and as is also listed in the Tables 6.1 to 6.4.

It may be concluded from the systematic study that checks which vary selection cuts or the energy scale of the calorimeter have a negligible effect on the measurement result. The reasons for the slightly larger deviations observed in a few bins are well understood.

Changes in the cluster and matching algorithms have only small effects on thrust and on jet broadening. However, C-parameter and jet mass are sensitive to the multiplicity in the current region and, as was shown, every check which changes the multiplicity calls for larger deviations of the mean values.

The largest systematic deviation for all four event shape variables is observed in the check for model dependence. Furthermore it results in a highly asymmetric error. It is common practice to choose one Monte Carlo model as the default model and treat the other(s) as systematic checks. This method is rather questionable if, as observed in this analysis, none of the considered models describes the data very closely and the truth appears to lie somewhere in between. Alternatively, the final result could be derived from the mean values of the results obtained with different Monte Carlo models, in which case the model dependence error would become symmetric.

However, this is not done in this analysis. The conventional method is applied.

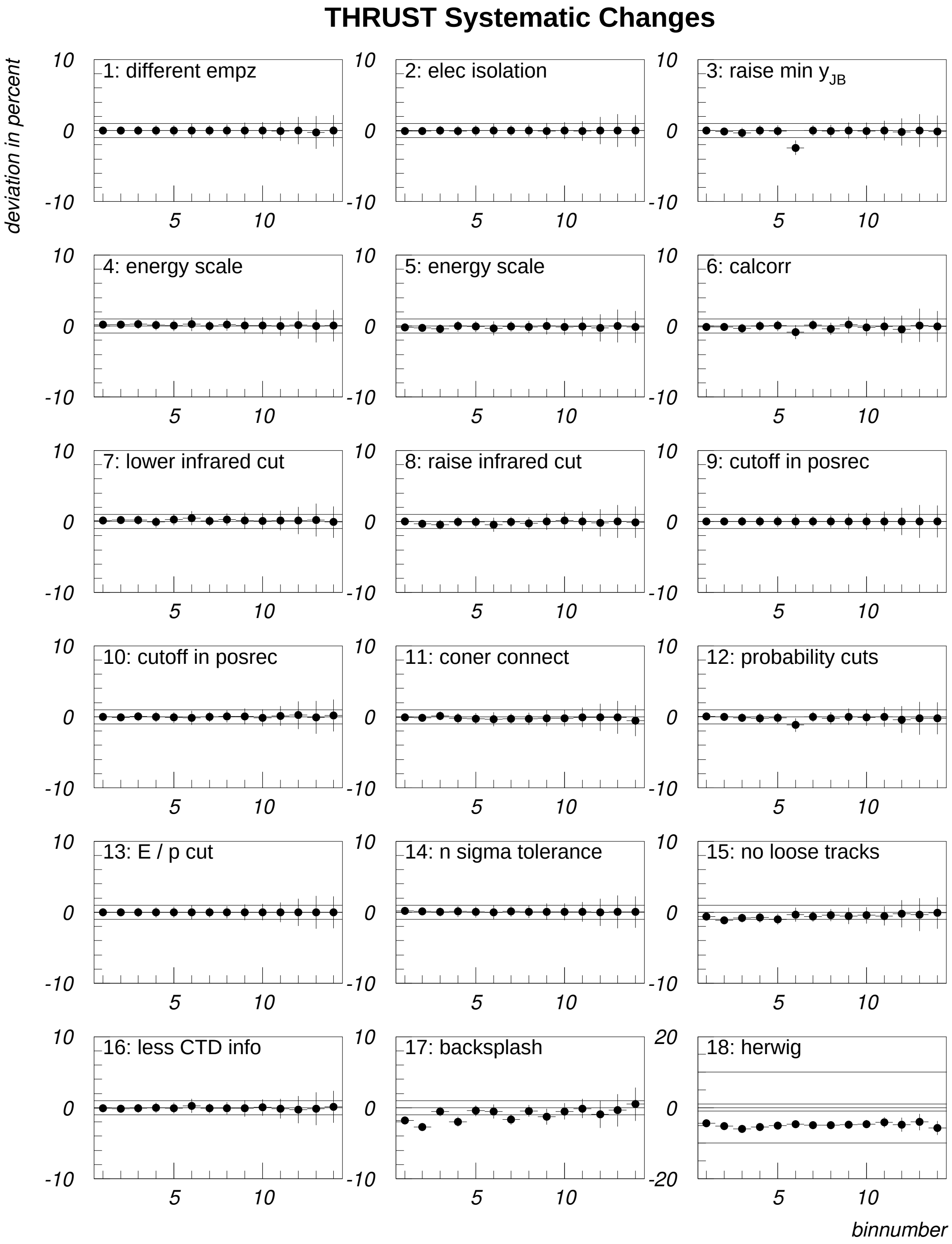

Figure 6.6: *Changes of the mean thrust values for each of the systematic checks performed. Each histogram shows the shift of the mean values in the 14 analysis bins for the corresponding systematic check. The horizontal lines indicate a ±1 % shift except for the HERWIG systematic, where the lines indicate a ±1% and a ±10% shift.*

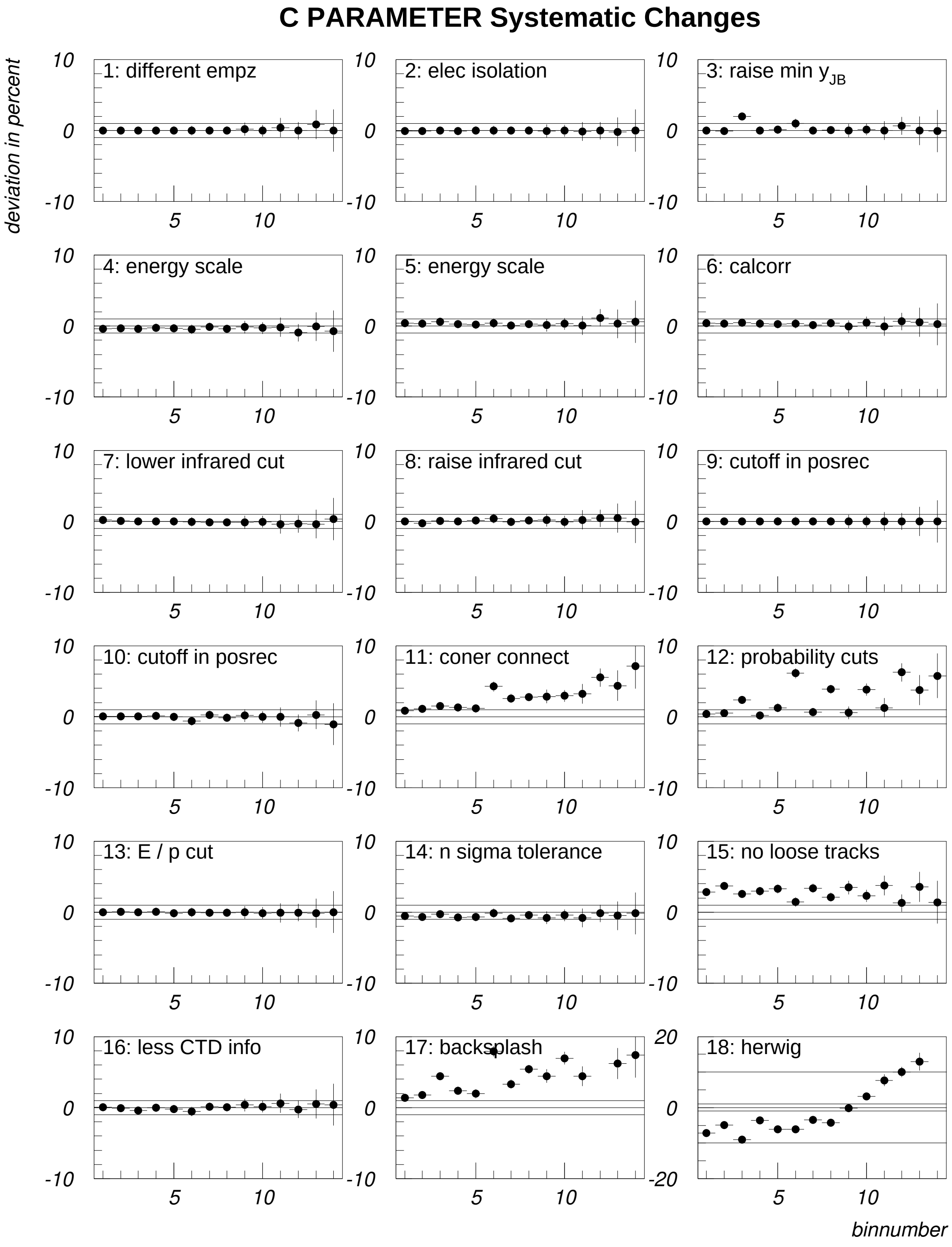

Figure 6.7: *Changes of the mean c-parameter values for each of the systematic checks performed. Each histogram shows the shift of the mean values in the 14 analysis bins for the corresponding systematic check. The horizontal lines indicate a ±1 % shift except for the HERWIG systematic, where the lines indicate a ±1% and a ±10% shift.*

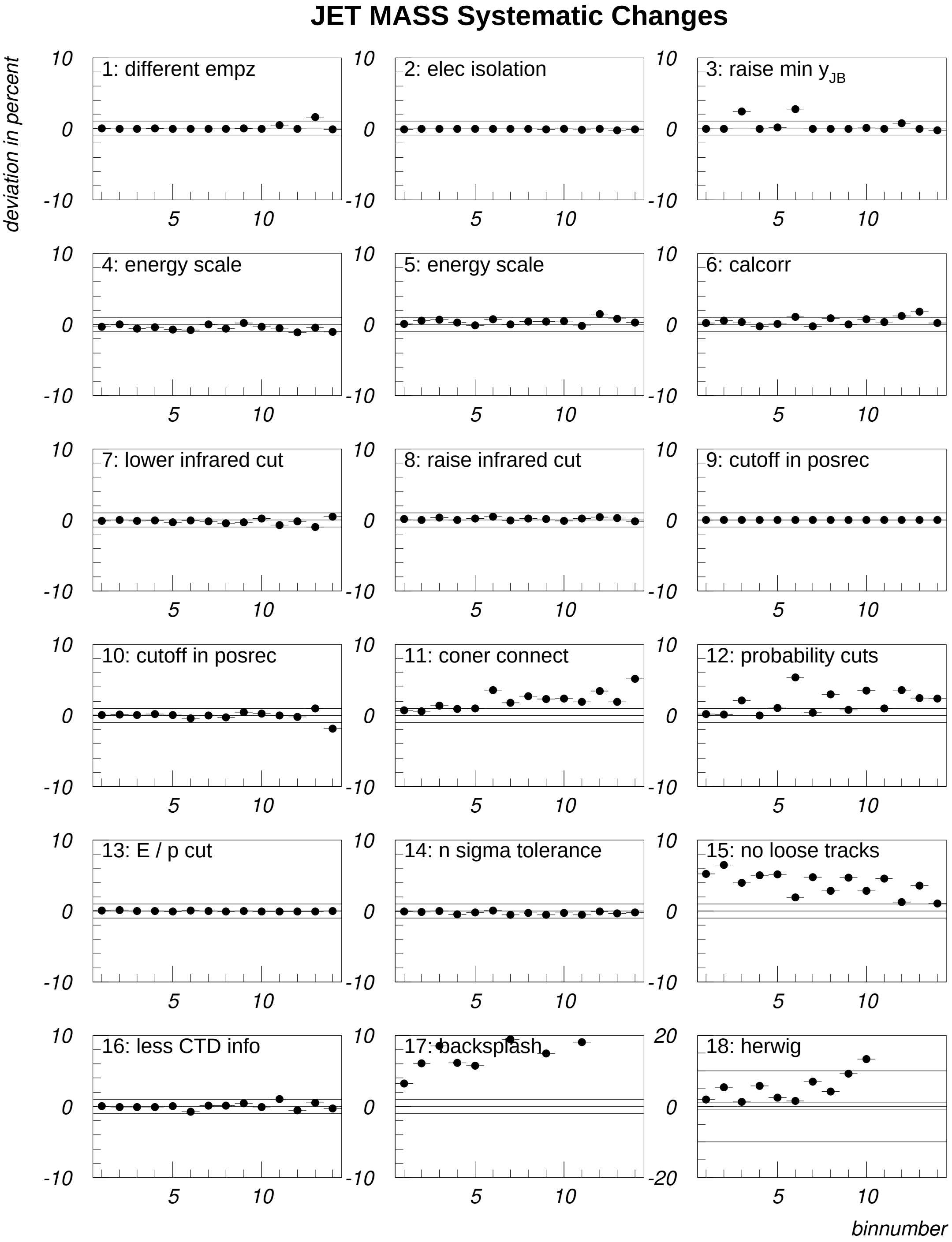

Figure 6.8: *Changes of the mean jet mass values for each of the systematic checks performed. Each histogram shows the shift of the mean values in the 14 analysis bins for the corresponding systematic check. The horizontal lines indicate a ±1 % shift except for the HERWIG systematic, where the lines indicate a ±1% and a ±10% shift.*

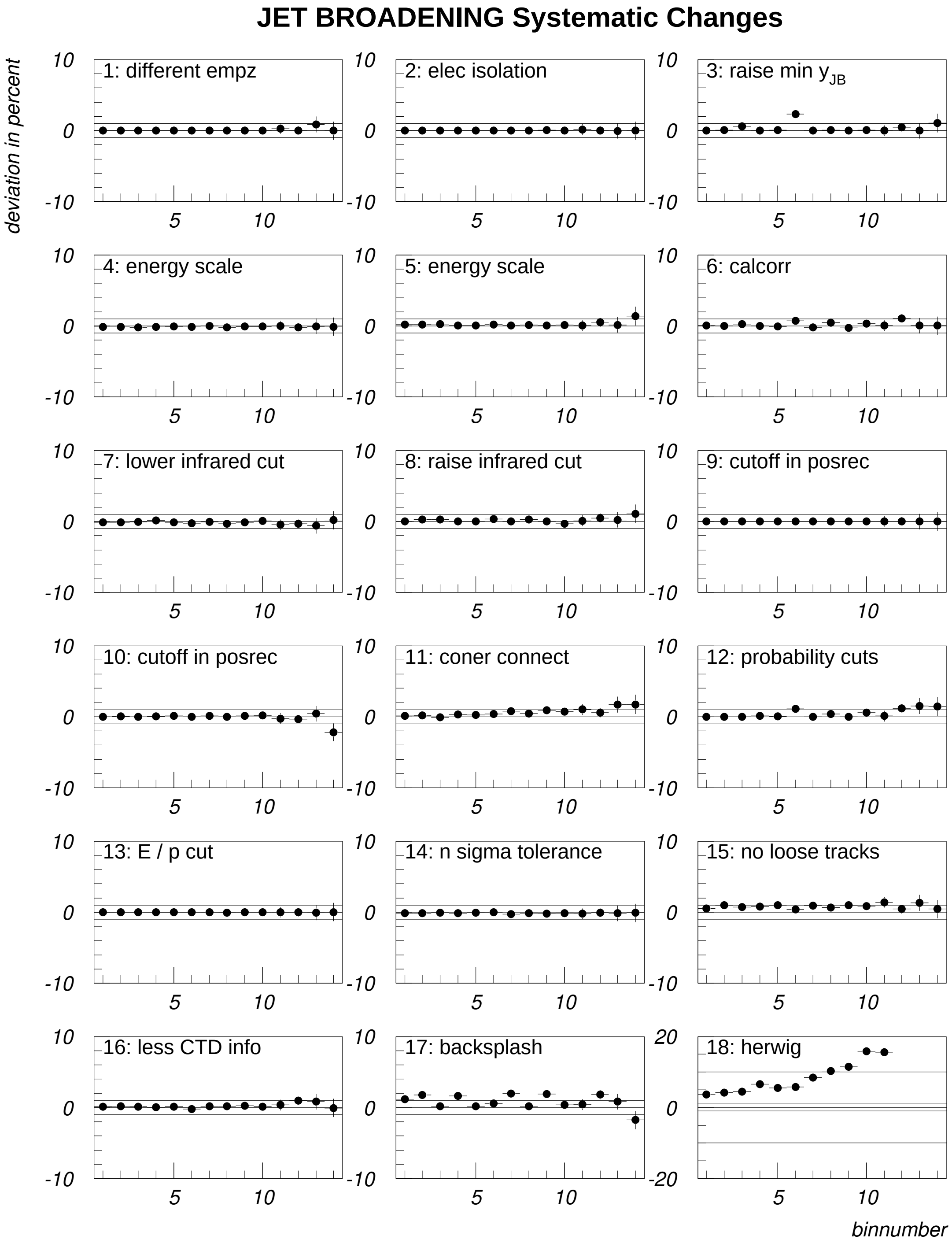

Figure 6.9: *Changes of the mean Jet broadening values for each of the systematic checks performed. Each histogram shows the shift of the mean values in the 14 analysis bins for the corresponding systematic check. The horizontal lines indicate a ±1 % shift except for the HERWIG systematic, where the lines indicate a ±1% and a ±10%.*

Chapter 7

QCD Analysis

This chapter presents the results of a QCD analysis based on the measurement results shown in the previous chapter. Within the framework of the dispersive approach presented in Chapter 2, fits are performed to the data points and their calculations at next-to-leading order accuracy. The goal is to extract both α_s – the running coupling as it is computed in perturbative QCD – and $\overline{\alpha_0}$ – the parameter accounting for the non-perturbative contribution to the event shape values.

The program DISENT [Ca96a, Ca97a] is used for the NLO calculations. Detailed results are presented in Section 7.1. As will be shown, changing the renormalisation scale in these calculations is the major source of systematic uncertainties both of the calculations and of the final result.

The fitting method leading to the extraction of α_s and $\overline{\alpha_0}$ is explained in Section 7.2. Actually the two fit parameters are $\overline{\alpha_0}$ and $\Lambda^{[4]}_{\mathrm{QCD}}$, but the results for $\Lambda^{[4]}$ are easily transformed into results for $\alpha_s(Z^0)$. χ^2 fits are performed for each of the event shape variables separately. The four results are then combined to the final values.

It is recalled that the method of "power coorection" fits is regarded as reliable only if the results for $\overline{\alpha_0}$ show a certain level of universality, since this is one of the major assumptions in the dispersive method. The obtained values for $\overline{\alpha_0}$ agree within errors, yet the values are spread by about 12%. However, with the available level of accuracy the universality assumption can thus be concluded to hold.

The results for α_s and $\overline{\alpha_0}$ are compared to results from e^+e^- experiments which were obtained using the same approach. The value for $\overline{\alpha_0}$ agrees within errors with values from e^+e^- experiments, however a trend towards lower values is observed. The combined value for $\alpha_s(Z^0)$ is in agreement with the world average value of $\alpha_s(Z^0)$.

7.1 Next-to-leading Order Calculation

The next-to-leading order (NLO) program DISENT [Ca96a, Ca97a] was used for calculating the perturbative prediction of the event shape distributions and their mean values. For each of the analysis bins (see Table 4.1 for the respective x_{bj} and Q^2 boundaries) several event-generation runs were made with 3 million events each. For the central or default run the renormalisation scale μ_{R} and the factorisation scale μ_{F} were both set to

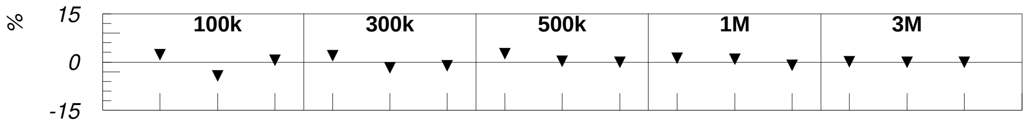

Thrust, deviation vs. seed value

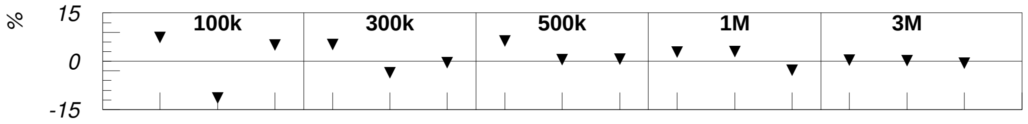

C-parameter, deviation vs. seed value

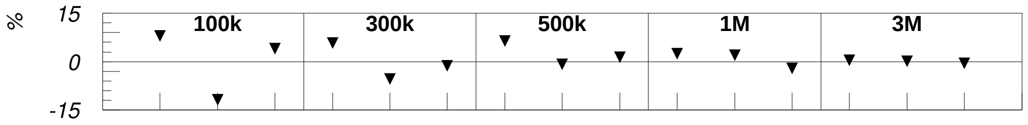

Jet Mass, deviation vs. seed value

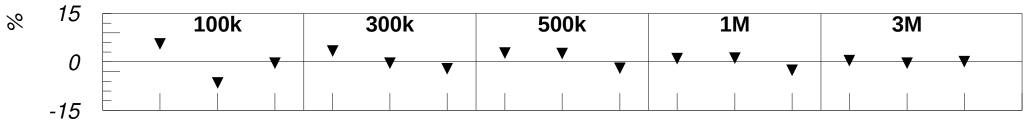

Jet Broadening, deviation vs. seed value

Figure 7.1: *From top to bottom: the dependence of the NLO calculations for T_z, C_p, J_m and J_b on the seed value and the sample size. Shown are the relative deviations of the mean event shape values as obtained in one test bin and for three different seed values. They are compared to the results of a run with 10 M of generated events. The remaining spread of the 3 M event sample is less than 1% compared to the 10 M result.*

Q^2, as has become conventional. The CTEQ-4M set of structure functions [CTEQ85] was used, evaluated in the $\overline{MS}$ scheme.

Influence of the Seed Value

If the number of generated events is too small, the obtained result will depend on the seed value for the random generator. In order to investigate this dependence samples of 100 k, 300 k, 500 k, 1 M and 3 M events were generated for one test bin and three different seed values. The resulting event shape means F_i are compared with the mean values $F_{10\mathrm{M}}$ obtained from a run with 10 M events. The relative deviations $(F_{10\mathrm{M}} - F_i)/F_{10\mathrm{M}}$ are shown in Figure 7.1. The spread of the mean values is large for the smaller event samples – up to 15% – and decreases down to $\leq 1\%$ for the 3 M event samples. The remaining seed-value uncertainty in the 3 M sample can be neglected, especially when compared to the size of systematic uncertainties arising from other sources (see below). Since the computing time was a limiting factor, it was chosen to use samples of 3 M events as a good compromise between obtaining sufficiently low statistical errors and generating the events within a reasonable amount of time.

	NLO calculation (DISENT results)					parametrisation	
Bin	$\tau_z(\Lambda_1)$	$\tau_z(\Lambda_2)$	$\tau_z(\Lambda_3)$	$\tau_z(\Lambda_4)$	$\tau_z(\Lambda_5)$	$\tau_z(0)$	$d(\tau_z)/d\Lambda$
1	0.2766	0.2880	0.2979	0.3086	0.3207	0.2261	0.2372
2	0.2586	0.2689	0.2786	0.2884	0.2992	0.2120	0.2185
3	0.2349	0.2442	0.2536	0.2626	0.2721	0.1923	0.2001
4	0.2318	0.2398	0.2474	0.2550	0.2632	0.1958	0.1691
5	0.2110	0.2183	0.2257	0.2327	0.2401	0.1777	0.1563
6	0.1836	0.1902	0.1972	0.2037	0.2104	0.1528	0.1444
7	0.1902	0.1960	0.2019	0.2075	0.2133	0.1637	0.1244
8	0.1660	0.1714	0.1771	0.1823	0.1877	0.1411	0.1167
9	0.1614	0.1660	0.1707	0.1751	0.1796	0.1405	0.0981
10	0.1387	0.1431	0.1475	0.1517	0.1560	0.1190	0.0928
11	0.1261	0.1298	0.1335	0.1369	0.1405	0.1096	0.0774
12	0.1007	0.1040	0.1072	0.1104	0.1137	0.0858	0.0700
13	0.0925	0.0953	0.0981	0.1007	0.1035	0.0798	0.0595
14	0.0609	0.0629	0.0647	0.0665	0.0685	0.0523	0.0406

Table 7.1: *Results of the DISENT runs for $\tau_z = 1 - T_z$ (left hand side) and parametrisation of the mean τ_z in terms of $\Lambda^{[4]}$. The results are shown in Figure 7.2*

Dependence on the $\Lambda^{[4]}$ Value

The numerical values of the event shape variable means obtained in the DISENT runs obviously depend on the $\Lambda^{[4]}$ value – or α_s if one prefers – and the structure functions, too, depend on $\Lambda^{[4]}$. Since this $\Lambda^{[4]}$ dependence is rather complicated, is is common practice to evaluate the structure function sets at several fixed values of $\Lambda^{[4]}$. The CTEQ-4M set of structure functions is available at the five different points $\Lambda_1^{[4]} = 0.213\,\text{GeV}$, $\Lambda_2^{[4]} = 0.253\,\text{GeV}$, $\Lambda_3^{[4]} = 0.296\,\text{GeV}$, $\Lambda_4^{[4]} = 0.344\,\text{GeV}$ and $\Lambda_5^{[4]} = 0.399\,\text{GeV}$.

With each of the five distinct $\Lambda^{[4]}$ values and the respective set of structure functions 3 M events were generated in each analysis bin. The results for the event shape means are listed in the Tables 7.1 to Table 7.4 and are visualized in Figure 7.2. A straight line fit is used to derive a parametrization of the mean values in terms of $\Lambda^{[4]}$. The respective parametrizations are also given in the Tables 7.1 to 7.4. These parametrisations will be used in the power correction fits described in the following section instead of the 5 discrete values. Thus greater freedom is given to the fit extracting $\overline{\alpha_0}$ and $\Lambda^{[4]}$, and an improved convergence and χ^2 is observed.

Systematic Uncertainties

Three possible sources for systematic deviations of the DISENT results were investigated: the influence of the chosen set of structure functions, a change of renormalisation scale and a change of factorisation scale. For each of these variations the DISENT calculation was repeated with 3M events for the 5 different $\Lambda^{[4]}$ values in the 14 analysis bins and the $\Lambda^{[4]}$ parametrizations of the event shape means are redetermined.

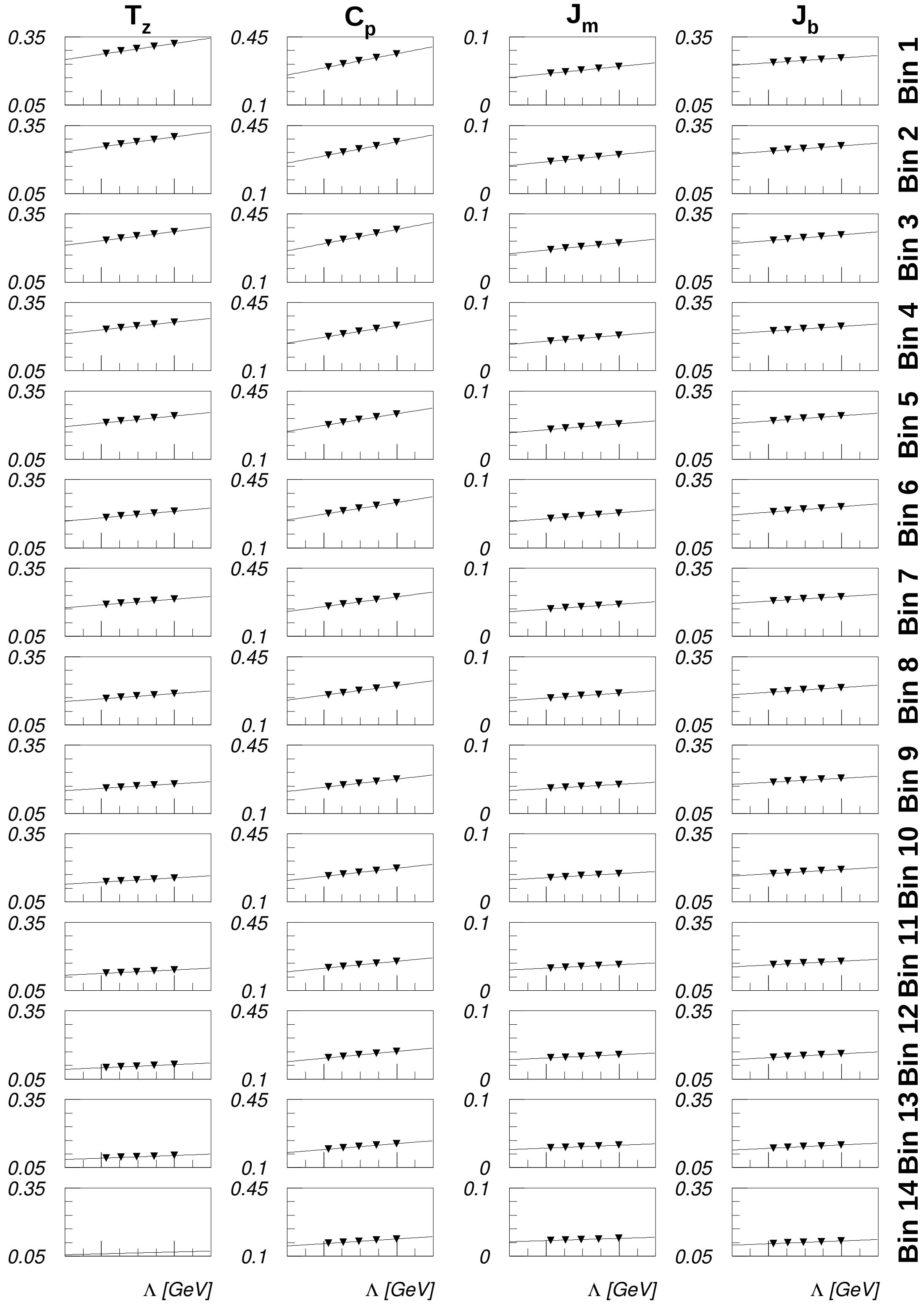

Figure 7.2: *DISENT results for the mean values of the event shape variables in each analysis bin as a function of* $\Lambda^{[4]}$*. In each analysis bin a straight line is fitted which yields the parametrisation of the event shape mean values in terms of* $\Lambda^{[4]}$*. The results of both the DISENT and the linear fits are summarised in the Tables 7.1, 7.2, 7.3 and 7.4.*

	NLO calculation (DISENT results)					parametrisation	
Bin	$C_p(\Lambda_1)$	$C_p(\Lambda_2)$	$C_p(\Lambda_3)$	$C_p(\Lambda_4)$	$C_p(\Lambda_5)$	$C_p(0)$	$dC_p/d\Lambda$
1	0.2954	0.3117	0.3271	0.3440	0.3631	0.2179	0.3639
2	0.2979	0.3141	0.3297	0.3467	0.3654	0.2207	0.3628
3	0.3022	0.3184	0.3345	0.3516	0.3702	0.2243	0.3656
4	0.2756	0.2892	0.3023	0.3163	0.3317	0.2113	0.3018
5	0.2772	0.2907	0.3040	0.3180	0.3330	0.2133	0.3001
6	0.2767	0.2900	0.3034	0.3173	0.3322	0.2130	0.2986
7	0.2556	0.2670	0.2782	0.2898	0.3022	0.2023	0.2505
8	0.2551	0.2663	0.2776	0.2892	0.3015	0.2019	0.2498
9	0.2367	0.2464	0.2559	0.2657	0.2761	0.1915	0.2120
10	0.2339	0.2434	0.2529	0.2626	0.2729	0.1892	0.2098
11	0.2166	0.2248	0.2329	0.2412	0.2499	0.1785	0.1791
12	0.2092	0.2172	0.2252	0.2332	0.2418	0.1719	0.1751
13	0.1947	0.2017	0.2085	0.2155	0.2228	0.1625	0.1512
14	0.1660	0.1716	0.1771	0.1826	0.1884	0.1402	0.1207

Table 7.2: *Results of the DISENT runs for c-parameter (left hand side) and parametrisation of the mean C_p in terms of $\Lambda^{[4]}$. The results are shown in Figure 7.2*

1. Influence of the Structure Functions

In order to investigate the dependence of the final result on the chosen set of structure functions the DISENT runs were repeated using the MRSA′ set of structure functions [Mar95]. They are available at slightly different $\Lambda^{[4]}$ values, namely: $\Lambda_1^{[4]} = 0.150\,\mathrm{GeV}$, $\Lambda_2^{[4]} = 0.201\,\mathrm{GeV}$, $\Lambda_3^{[4]} = 0.266\,\mathrm{GeV}$, $\Lambda_4^{[4]} = 0.344\,\mathrm{GeV}$ and $\Lambda_5^{[4]} = 0.435\,\mathrm{GeV}$.

2. Influence of the Renormalisation Scale

The renormalisation scale was lowered to $\mu_\mathrm{R} = 0.5\,Q$ and raised to $\mu_\mathrm{R} = 2\,Q$ and new event samples were generated. A change of renormalisation scale leads to the largest systematic deviation and also to the largest contribution to the systematic error of the final result (see below).

3. Influence of the Factorisation Scale

Similar to the case of the renormalisation scale, the factorisation scale was changed to $\mu_\mathrm{F} = 0.5\,Q$ and $\mu_\mathrm{F} = 2\,Q$. Although a small variation is observed, the effect is much smaller than the change caused by the change of renormalisation scale.

	NLO calculation (DISENT results)					parametrisation	
Bin	$J_m(\Lambda_1)$	$J_m(\Lambda_2)$	$J_m(\Lambda_3)$	$J_m(\Lambda_4)$	$J_m(\Lambda_5)$	$J_m(0)$	$dJ_m/d\Lambda$
1	0.0466	0.0490	0.0512	0.0537	0.0566	0.0351	0.0539
2	0.0472	0.0497	0.0520	0.0544	0.0572	0.0358	0.0537
3	0.0477	0.0501	0.0525	0.0550	0.0577	0.0363	0.0537
4	0.0437	0.0457	0.0477	0.0497	0.0520	0.0342	0.0445
5	0.0438	0.0458	0.0477	0.0498	0.0519	0.0344	0.0439
6	0.0432	0.0452	0.0471	0.0492	0.0513	0.0340	0.0434
7	0.0403	0.0419	0.0436	0.0453	0.0470	0.0325	0.0364
8	0.0397	0.0414	0.0430	0.0447	0.0464	0.0320	0.0361
9	0.0370	0.0384	0.0398	0.0412	0.0426	0.0304	0.0306
10	0.0360	0.0373	0.0387	0.0401	0.0416	0.0296	0.0301
11	0.0332	0.0343	0.0355	0.0367	0.0379	0.0277	0.0255
12	0.0311	0.0323	0.0334	0.0345	0.0357	0.0259	0.0247
13	0.0289	0.0299	0.0308	0.0318	0.0328	0.0243	0.0213
14	0.0231	0.0238	0.0246	0.0253	0.0261	0.0196	0.0162

Table 7.3: *Results of the DISENT runs for jet mass (left hand side) and parametrisation of the mean* J_m *in terms of* $\Lambda^{[4]}$. *The results are shown in Figure 7.2*

	NLO calculation (DISENT results)					parametrisation	
Bin	$J_b(\Lambda_1)$	$J_b(\Lambda_2)$	$J_b(\Lambda_3)$	$J_b(\Lambda_4)$	$J_b(\Lambda_5)$	$J_b(0)$	$dJ_b/d\Lambda$
1	0.2373	0.2430	0.2471	0.2519	0.2573	0.2143	0.1078
2	0.2378	0.2438	0.2489	0.2542	0.2599	0.2125	0.1186
3	0.2340	0.2403	0.2464	0.2523	0.2583	0.2063	0.1302
4	0.2248	0.2301	0.2348	0.2395	0.2446	0.2022	0.1063
5	0.2200	0.2255	0.2308	0.2360	0.2412	0.1957	0.1141
6	0.2082	0.2139	0.2197	0.2252	0.2309	0.1822	0.1219
7	0.2063	0.2110	0.2157	0.2202	0.2248	0.1850	0.0996
8	0.1946	0.1996	0.2046	0.2094	0.2143	0.1721	0.1059
9	0.1879	0.1922	0.1965	0.2005	0.2046	0.1689	0.0896
10	0.1750	0.1795	0.1840	0.1883	0.1927	0.1548	0.0950
11	0.1634	0.1674	0.1713	0.1751	0.1789	0.1457	0.0831
12	0.1451	0.1492	0.1531	0.1570	0.1610	0.1269	0.0857
13	0.1359	0.1395	0.1430	0.1464	0.1499	0.1199	0.0751
14	0.1054	0.1084	0.1112	0.1141	0.1170	0.0922	0.0622

Table 7.4: *Results of the DISENT runs for Jet broadening (left hand side) and parametrisation of the mean* J_b *in terms of* $\Lambda^{[4]}$. *The results are shown in Figure 7.2*

7.2 Fits to the Mean Values

The NLO results from the previous section are used to make so-called "power correction" fits to the measurement results (Chapter 2.7). The goal is to simultaneously extract α_s and the power correction parameter $\overline{\alpha_0}$. In practice the two fit parameters used were $\Lambda^{[4]}$ and $\overline{\alpha_0}$.

Fitting Method

The expected mean value $\mathcal{F}$ of an event shape variable is given by the sum of a perturbatively-calculated term $\mathcal{F}_{\text{pert}}$ and a power correction term $\mathcal{F}_{\text{pow}}$:

$$\mathcal{F} = \mathcal{F}_{\text{pert}} + \mathcal{F}_{\text{pow}}$$

The perturbative term $\mathcal{F}_{\text{pert}}$ is the result of a NLO calculation carried out in the $\overline{MS}$ scheme, obtained here from DISENT. As discussed in the previous section $\mathcal{F}_{\text{pert}}$ may be parametrised as linearly dependent on the QCD parameter $\Lambda^{[4]}$. The parametrizations vary for the individual analysis bins. The power correction term $\mathcal{F}_{\text{pow}}$ on the other hand is a function of the two free parameters α_s and $\overline{\alpha_0}$ and is written in the following way:

$$\mathcal{F}_{\text{pow}} = a_F \cdot \mathcal{M} \cdot \frac{C_F}{2\pi^2}\frac{\mu_I}{Q} \cdot \left[\overline{\alpha_0}(\mu_I) - \alpha_s(Q) - \alpha_s^2(Q)2b\left(\frac{k}{2b} + 1 + \ln\left(\frac{Q}{\mu_I}\right)\right)\right] \tag{7.1}$$

where C_F is the colour factor $\frac{4}{3}$, b is the first coefficient of the β-function (see Equation 2.17), and k is an additional factor originating in the change of scheme, see Equation 2.24. $\mathcal{M}$, the Milan factor, entered the equation after the calculations were extended to 2-loop accuracy. Its value is 1.79 with a 20% uncertainty due to the as yet unevaluated higher order corrections. a_F is an observable-dependent coefficient. For the event shape variables under study it takes the following values:

$$a_F = \begin{cases} 4 & \text{for} \quad \text{Thrust} \\ 6\pi & \text{for} \quad \text{C}-\text{parameter} \\ 2 & \text{for} \quad \text{Jet mass} \\ 2 & \text{for} \quad \text{Jet broadening} \end{cases}$$

Since α_s may be written in terms of $\Lambda^{[4]}$ (Equation 2.23), $\mathcal{F}_{\text{pow}}$ may consequently be written as a function of the two free fit parameters $\Lambda^{[4]}$ and $\overline{\alpha_0}$. During the fitting procedure the functions $\mathcal{F}_{\text{pert}}(Q, \Lambda^{[4]})$ and $\mathcal{F}_{\text{pow}}(\overline{\alpha_0}, Q, \Lambda^{[4]})$ are evaluated at the Q-values Q_i of the analysis bins. The resulting function values $F_{i,\text{pert}}(Q_i)$ and $F_{i,\text{pow}}(Q_i)$ enter a χ^2 function:

$$\chi^2(\overline{\alpha_0}, \Lambda^{[4]}) = \sum_{i=1}^{8} \frac{\left(F_{i,\text{data}} - F_{i,\text{pow}}(\overline{\alpha_0}, \Lambda^{[4]}) - F_{i,\text{pert}}(\Lambda^{[4]})\right)}{\sigma_i^2} \tag{7.2}$$

which is minimised to obtain $\overline{\alpha_0}$ and $\Lambda^{[4]}$ for each event shape variable F. The variance σ_i in Equation 7.2 is the quadratic sum of the statistical error of the data analysis and the 1% seed uncertainty of the DISENT result.

Special Treatment of the Jet Broadening

It has been observed in e^+e^- analyses that a fit with a parametrisation of $\mathcal{F}_{\rm pow}$ according to Equation 7.1 leads to unsatisfactory results for the e^+e^- jet broadening measures B_T and B_W. The obtained values for α_s were found to be too low. The results stimulated a revised calculation of the predicted power corrections to the jet broadening measures [Do98b].

A similar behaviour was observed here: for a simple fit with $a_F = 2$ for the Jet broadening as listed above very low values for α_s were obtained.

A revised calculation for the Jet broadening in DIS has not yet become available. The first step would be a resummed perturbative calculation of the jet broadening, which has not been done so far. However, the correspondence between one e^+e^- hemisphere and the current region of the Breit frame can be used to give some estimations. It is anticipated [Do98b] that a_F changes by an extra factor ΔB which is given by:

$$\Delta B = \left(\frac{\pi}{2\sqrt{2\,C_F\,\alpha_{\rm CMW}\,(\bar{Q})}} + \frac{3}{4} - \frac{\pi b}{3C_F} + \eta_0 + \mathcal{O}(1) \right) \tag{7.3}$$

with:

$$\begin{aligned} \alpha_{\rm CMW} &= \alpha_{\overline{\rm MS}} \cdot \left(1 + \frac{k}{2\pi} \cdot \frac{\alpha_{\overline{\rm MS}}}{2\pi} \right) \\ \bar{Q} &= Q\,{\rm e}^{-3/4} \\ \eta_0 &= -0.6137056 \end{aligned}$$

and b, k as defined in Equation 2.26. In the fits presented below the term $a_F \cdot \Delta B$ was used for the jet broadening, leading to encouraging results.

Hadron Level with Zero Mass Assumption

The power correction fits were first performed to the numerical results as presented in the previous chapter. An uncomfortably large spread in the values for $\overline{\alpha_0}$ is observed, as can be seen in Appendix B.

In the theoretical calculations of the power corrections the hadron mass was neglected, which offers an explanation of this effect. The fits were then repeated to data which was corrected to hadron level using a zero mass assumption: after the hadrons were boosted to the Breit frame their energies were recalculated with the assumption that they are massless.

The results for T_z and J_b are unchanged. C-parameter and J_m however have an explicit particle energy dependence in their definitions. In the lower Q^2 bins the mean values of C_p increase by up to 10% and those for J_m decrease by up to 10% (see Appendix A). The fits to the results obtained with the zero mass assumption show more satisfactory results and are shown below.

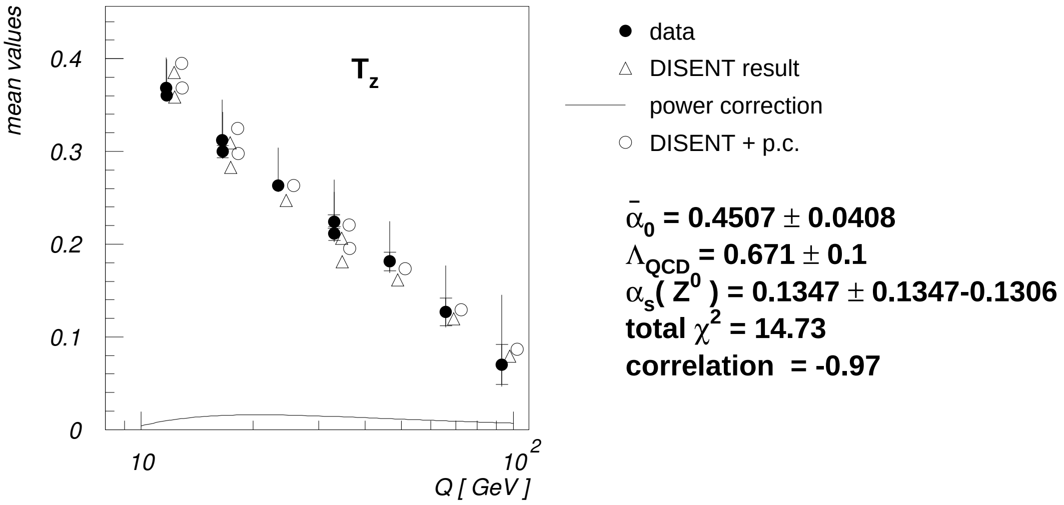

Figure 7.3: *Fit result for thrust.*

Results

The fits were performed for each event shape variable separately. The results for the central analysis are summarised in Table 7.5. Figures 7.3 to 7.6 show the data points, the DISENT points at the fitted $\Lambda^{[4]}$ value and the power correction term as resulting from the fit. The fit values are explicitely listed as well. For better visibility, Figure 7.7 shows the fitted power correction term and $F_{i,\mathrm{data-NLO}}$, i.e. the difference between the data and the NLO results.

The general description of the $F_{i,\mathrm{data-NLO}}$ by the power correction term is very good. However, there is a tendency to overshoot the $F_{i,\mathrm{data-NLO}}$ at larger Q values. The significantly smaller errors at lower Q values mean that they tend to determine the final values of the fit parameters.

A problem for the fits is seen in the different x_{bj} -dependence observed for bins at the same Q^2 in data and in the DISENT result. This difference is particularly large for the thrust, as can be seen in Figure 7.7. This raises the question whether x_{bj} -dependent power corrections are necessary.

Variable	$\overline{\alpha_0}$	$\Delta\overline{\alpha_0}$	$\Lambda^{[4]}$	$\Delta\Lambda$	$\alpha_s(Z^0)$	$\Delta\alpha_s$	χ^2	*cor*
T_z	0.4507	0.0408	0.6711	0.1005	0.1347	0.0041	14.7306	0.9719
C_p	0.4173	0.0024	0.3597	0.0255	0.1202	0.0015	16.7222	0.5671
J_m	0.4316	0.0037	0.2422	0.0400	0.1126	0.0032	23.1521	0.0542
J_b	0.4382	0.0065	0.3118	0.0364	0.1173	0.0024	1.5300	0.8721

Table 7.5: Values of $\overline{\alpha_0}$ and $\Lambda^{[4]}$ determined using χ^2 fits to four event shape variables. The quoted errors are the uncertainties arising from the fit. Only the statistical errors of the data analysis were put into the fitting procedure, thus the fit errors are identified with the *statistical* errors of the fitted parameters.

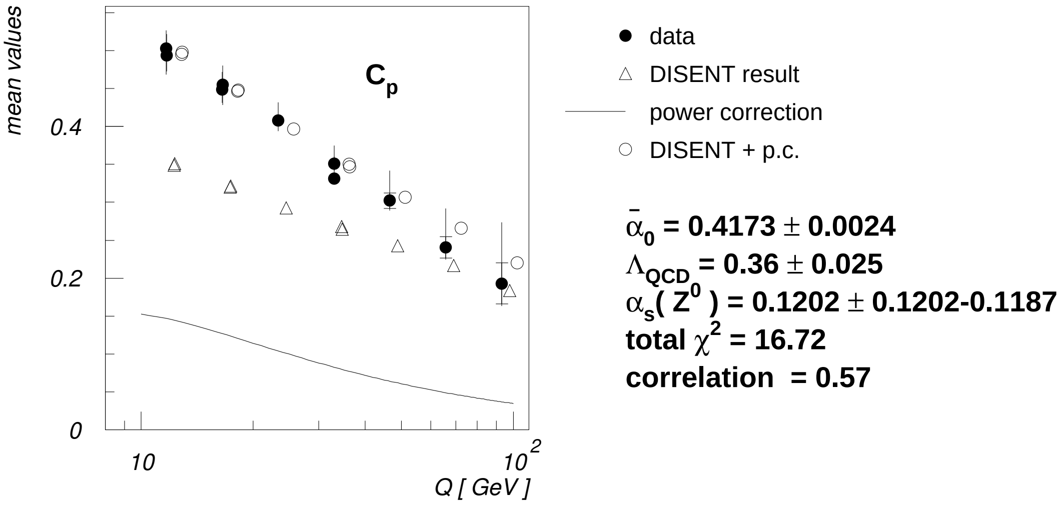

Figure 7.4: *Fit result for C-parameter.*

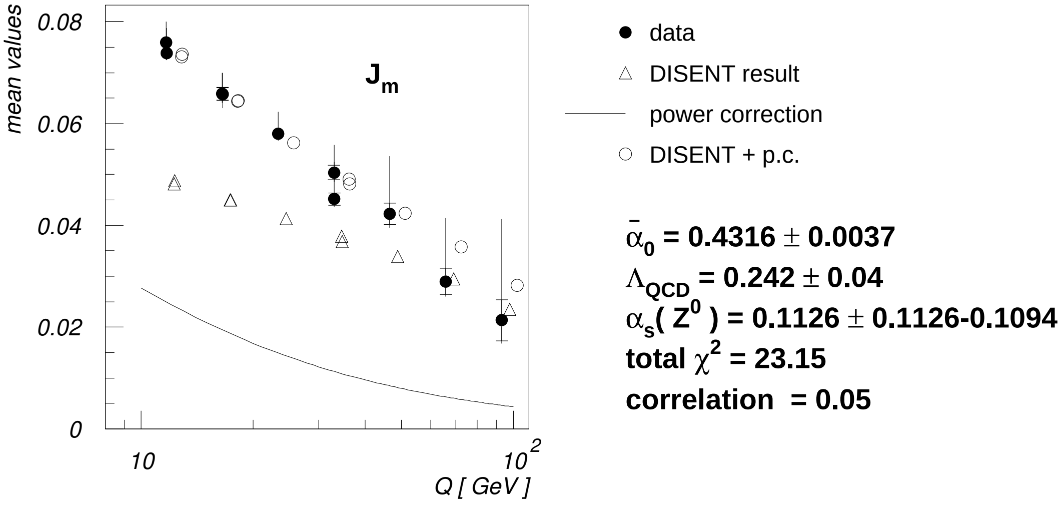

Figure 7.5: *Fit result for Jet mass.*

Systematic Error Evaluation

The systematic errors of the fitted parameters $\overline{\alpha_0}$ and $\Lambda^{[4]}$ (and hence of α_s) are composed of three parts: the experimental systematic error and two theoretical errors for the NLO and power correction calculations. The errors were obtained by repeating the χ^2 fit for each of the systematic checks described in Section 6.3 (for experimental systematic checks) and in Section 7.1 (for the NLO calculations). The fits were not repeated for experimental checks which had only a negligible influence on the mean values. The power correction error was obtained from a single systematic check, namely varying the value of the Milan factor by ±20%.

The variations with respect to the central analysis are identified with systematic errors of

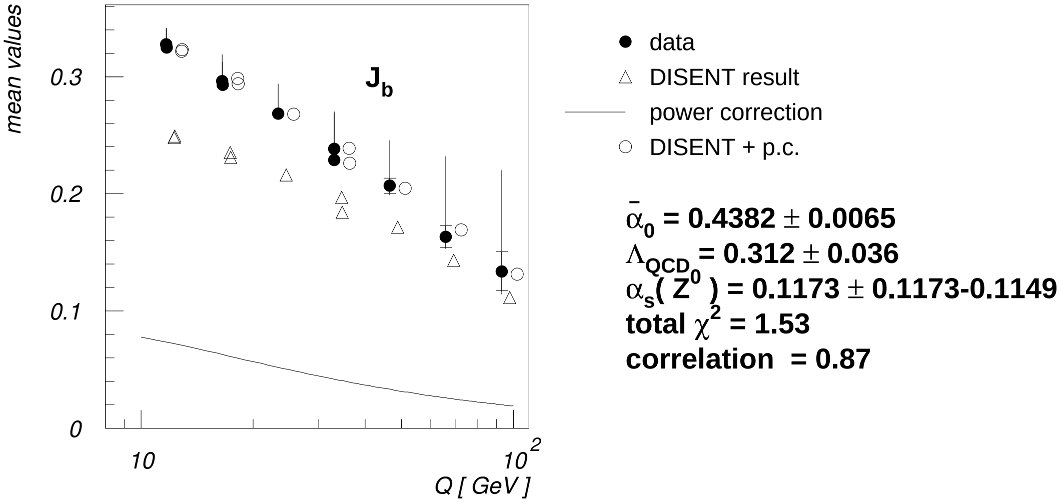

Figure 7.6: *Fit result for Jet broadening.*

the fit parameters $\overline{\alpha_0}$ and $\Lambda^{[4]}$. Each systematic error was treated asymmetrically. They were combined in quadrature to obtain positive and negative experimental, perturbative, power correction and total errors. The results for the individual checks and the combined errors are summarised in Table 7.8 for $\overline{\alpha_0}$ and in Table 7.9 for α_s . Again the results for the actual fit parameter $\Lambda^{[4]}$ are not shown, rather they were translated to $\alpha_s(Z^0)$ first.

The change in renormalisation scale accounts for the largest contribution to the total systematic error.

Combination of individual results

In order to obtain final combined results for α_s and $\overline{\alpha_0}$, the separate results obtained from measurements of each of the event shape variables were combined using a weighted mean. The weights used were the reciprocals of the squares of the individual total errors.

A combined result was also calculated for each of the systematic checks. The differences between these systematically-varied combined results and the results of the central analysis were added in quadrature in order to calculate final systematic errors for the combined measurements of α_s and $\overline{\alpha_0}$. This method takes into account the correlations of the systematic errors between the four event shape variables.

The final, combined result for $\overline{\alpha_0}$ is the following:

$$\boxed{\overline{\alpha_0}(\mu_I = 2\,GeV) = 0.4265 \pm 0.0012\ (\text{stat.})\ ^{+0.0182}_{-0.0026}\ (\text{exp.})\ ^{+0.0869}_{-0.0756}\ (\text{theo.})}$$

The final, combined result for $\alpha_s(Z^0)$ is the following:

$$\boxed{\alpha_s(Z^0) = 0.1201 \pm 0.0006\ (\text{stat.})\ ^{+0.0117}_{-0.0008}\ (\text{exp.})\ ^{+0.0082}_{-0.0108}\ (\text{theo.})}$$

The final, combined systematic results and systematic errors for α_s and $\overline{\alpha_0}$ are summarised in Table 7.10 and are visaulised in Figure 7.9.

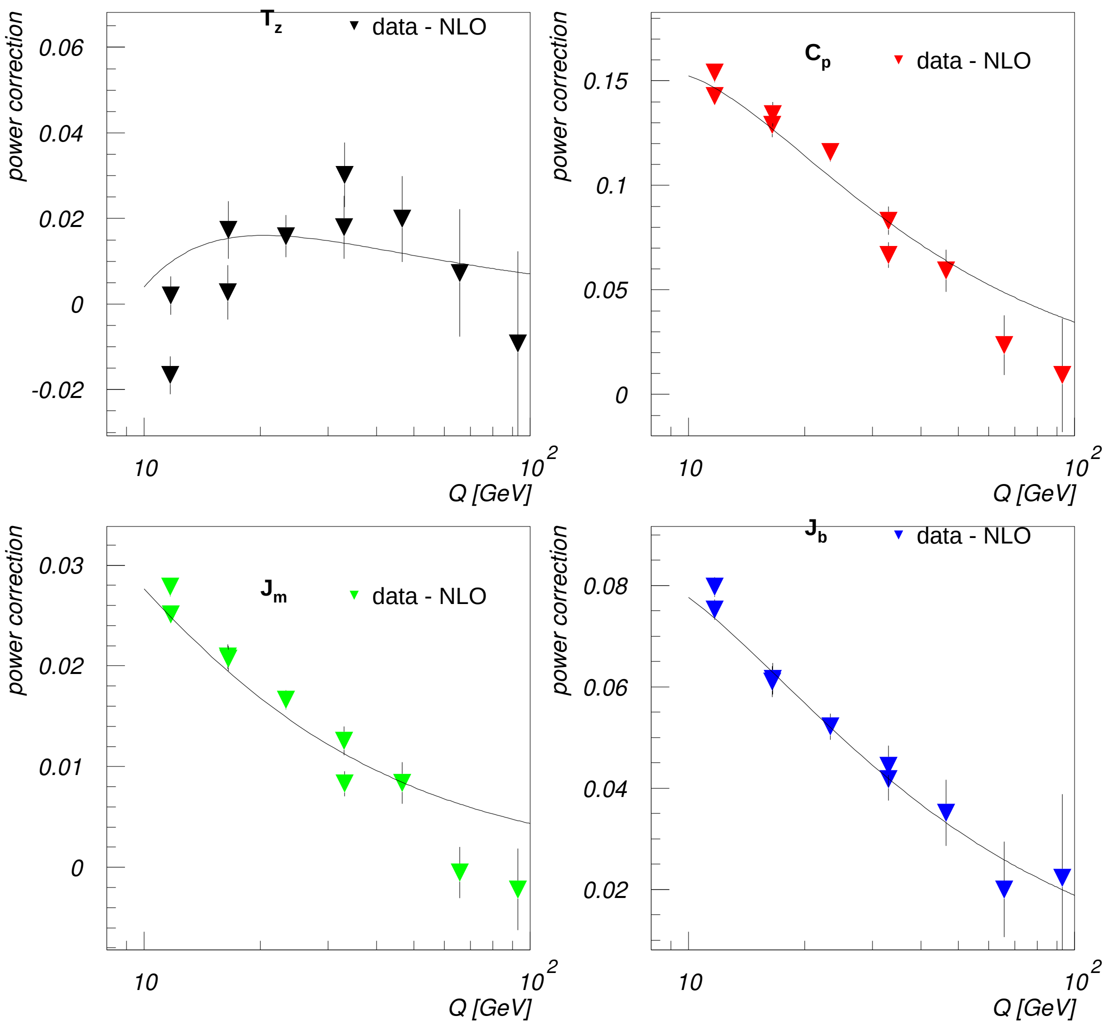

Figure 7.7: *Power Corrections from the* χ^2 *fits. Shown are the* $F_{i,\mathrm{data-NLO}}$ *points, i.e. the data points with the NLO results subtracted, compared with the fit result for the power correction term. The errors shown are the statistical errors of the data analysis. The agreement is very good within the errors, although the fits are pinned at the lower* Q *values.*

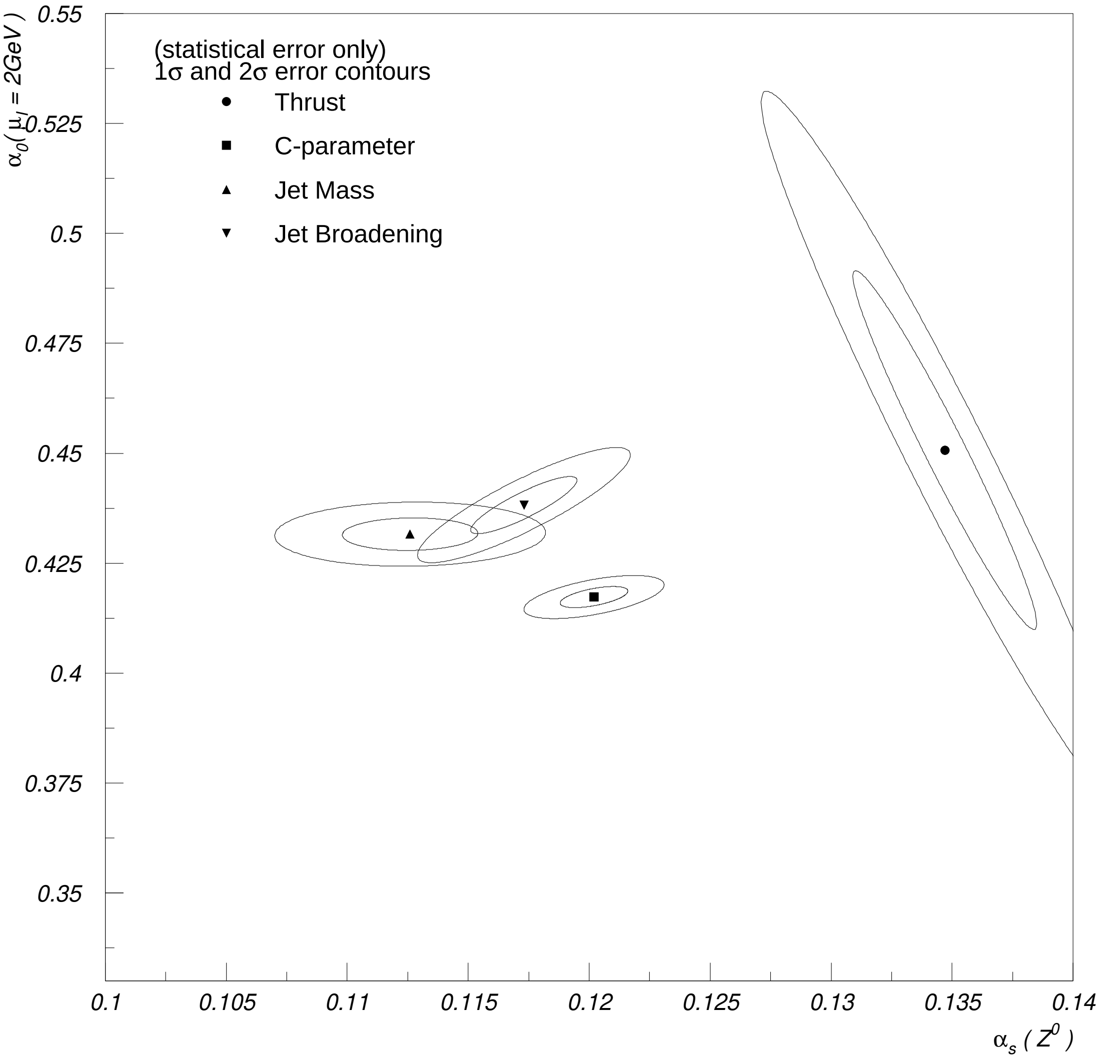

Figure 7.8: *Contours of the fit results. Shown are the 1 and 2 σ contours for statistical errors only*

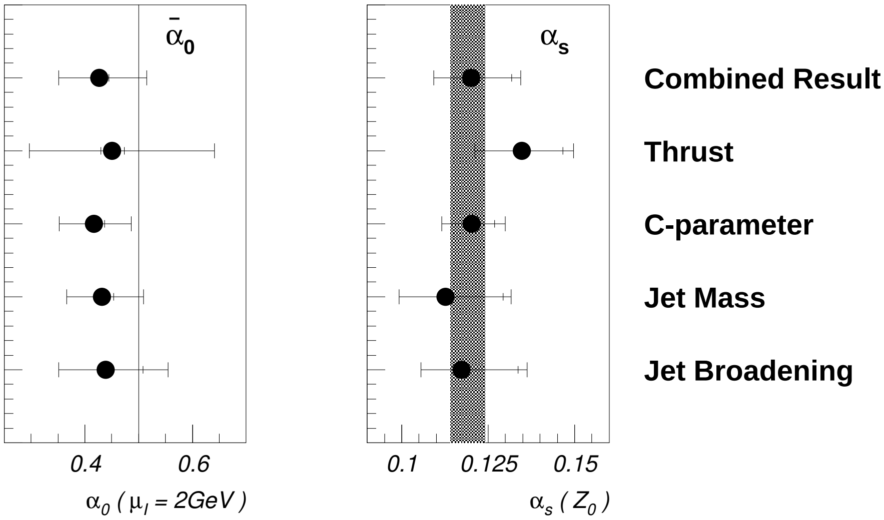

Figure 7.9: *Combined results with experimental systematic (smaller error bars) and total errors.*

Results of other experiments

The results of other experiments are listed in Tables 7.6 and 7.7. Results are shown from JADE[JADE99], DELPHI [DELPHI98a], ALEPH [ALEPH98], L3 [L3] and H1 [H199].

The results are averaged for each experiment, the mean and rms values are listed in Table 7.7. The results were also averaged for each variable, combining for instance the different jet broadening measures in e^+e^- and in DIS into a *general broadening* average.

The results of the different experiments agree well within errors. The universality assumption for $\overline{\alpha_0}$ is found to hold within the (admittedly large) error. This supports the phenomenological method of power corrections. The extracted as well as the averaged values for $\alpha_s(Z^0)$ are in good agreement with the world average value, in which they are *not* included since there is still a large theoretical uncertainty associated with this method. However the results are encouraging for further theoretical work.

Experiment / Variable	$\alpha_s(\mu_I = 2\,GeV)$	$\alpha_s(Z^0)$
DELPHI		
$\langle\tau\rangle$	$0.494 \pm 0.008\,(stat) \pm 0.003\,(scale)$	$0.1176 \pm 0.0016\,(stat) \pm 0.0055\,(scale)$
$\langle M_h^2/E_{vis}^2\rangle$	$0.558 \pm 0.022\,(stat) \pm 0.012\,(scale)$	$0.1172 \pm 0.0013\,(stat) \pm 0.0035\,(scale)$
ALEPH		
$\langle\tau\rangle$	$0.449 \pm 0.003\,(stat) \pm 0.071\,(pert)$	$0.1193 \pm 0.0004\,(stat) \pm 0.0059\,(pert)$
$\langle C\rangle$	$0.462 \pm 0.003\,(stat) \pm 0.046\,(pert)$	$0.113 \pm 0.0003\,(stat) \pm 0.0032\,(pert)$
L3		
$\langle\tau\rangle$	0.567 ± 0.054	0.1097 ± 0.0047
$\langle\rho\rangle$	0.469 ± 0.041	0.1032 ± 0.0039
$\langle B_T\rangle$	0.480 ± 0.034	0.1148 ± 0.0028
$\langle B_W\rangle$	0.450 ± 0.069	0.1131 ± 0.0035
$\langle C\rangle$	0.482 ± 0.031	0.112 ± 0.0033
JADE		
$\langle\tau\rangle$	$0.509 \pm 0.012 \pm^{+0.059}_{-0.042}$	$0.1198 \pm 0.0013 \pm^{+0.0068}_{-0.0055}$
$\langle M_h^2/E_{vis}^2\rangle$	$0.614 \pm 0.018 \pm^{+0.087}_{-0.067}$	$0.1141 \pm 0.0010 \pm^{+0.0043}_{-0.0030}$
$\langle B_T\rangle$	$0.442 \pm 0.015 \pm^{+0.052}_{-0.037}$	$0.1183 \pm 0.0020 \pm^{+0.0054}_{-0.0044}$
$\langle B_W\rangle$	$0.392 \pm 0.028 \pm^{+0.117}_{-0.055}$	$0.1176 \pm 0.0020 \pm^{+0.0029}_{-0.0022}$
$\langle C\rangle$	$0.451 \pm 0.010 \pm^{+0.051}_{-0.036}$	$0.1176 \pm 0.0013 \pm^{+0.0058}_{-0.0049}$
H1		
$\langle T_z\rangle$	$0.48 \pm 0.028 \pm^{+0.048}_{-0.062}$	$0.1174 \pm 0.003 \pm^{+0.0097}_{-0.0081}$
$\langle J_b\rangle$	$0.491 \pm 0.005 \pm^{+0.032}_{-0.036}$	$0.1106 \pm 0.0012 \pm^{+0.0060}_{-0.007}$
$\langle T_c\rangle$	$0.475 \pm 0.003 \pm^{+0.044}_{-0.048}$	$0.1284 \pm 0.0014 \pm^{+0.01}_{-0.0092}$
$\langle J_m\rangle$	$0.561 \pm 0.004 \pm^{+0.051}_{-0.058}$	$0.1347 \pm 0.0015 \pm^{+0.0111}_{-0.0100}$
$\langle C_p\rangle$	$0.425 \pm 0.002 \pm^{+0.033}_{-0.039}$	$0.1273 \pm 0.0009 \pm^{+0.0104}_{-0.0093}$

Table 7.6: Results of other experiments.

Variable/ Experiment	$\langle\overline{\boldsymbol{\alpha}_0}\rangle$	RMS($\overline{\alpha_0}$)	$\langle\boldsymbol{\alpha_s(Z^0)}\rangle$	RMS (α_s)
Thrust	0.4916	0.0439	0.1198	0.0082
C-parameter	0.4475	0.0266	0.1180	0.0062
Jet mass	0.5127	0.0729	0.1115	0.0052
Broadening	0.4489	0.0350	0.1153	0.0030
L3	0.4896	0.0451	0.1106	0.0045
JADE	0.4816	0.0849	0.1175	0.0021
ALEPH	0.4555	0.0092	0.1162	0.0045
DELPHI	0.5620	0.0453	0.1174	0.0003
H1	0.4918	0.0412	0.1237	0.0096
this analysis	0.4345	0.0139	0.1212	0.0095
Total	0.4778	0.0537	0.1178	0.0075

Table 7.7: Values of $\overline{\alpha_0}$ and α_s per averaged over variable and experiment.

	1 — T_z	C_p	J_m	J_b
$\overline{\alpha_0}$	0.4507	0.4173	0.4316	0.4382
Exp. stat.	0.0408 -0.0408	0.0024 -0.0024	0.0037 -0.0037	0.0065 -0.0065
pQCD	**+ 0.1886** **− 0.1508**	**+ 0.0607** **− 0.0609**	**+ 0.0640** **− 0.0573**	**+ 0.0845** **− 0.0818**
Pow. corr.	**+ 0.0057** **− 0.0190**	**+ 0.0257** **− 0.0216**	**+ 0.0371** **− 0.0282**	**+ 0.0393** **− 0.0302**
Exp. syst.	**+ 0.0228** **− 0.0213**	**+ 0.0191** **− 0.0099**	**+ 0.0223** **− 0.0129**	**+ 0.0704** **− 0.0020**
Total	**+ 0.1901** **− 0.1534**	**+ 0.0686** **− 0.0654**	**+ 0.0773** **− 0.0651**	**+ 0.1168** **− 0.0872**
Energyscale	-0.0089	-0.0009	-0.0027	-0.0005
Energyscale	0.0125	0.0009	0.0031	0.0006
Infrared Cut	-0.0046	-0.0002	0.0001	-0.0007
Infrared Cut	0.0182	0.0001	0.0001	-0.0008
Corner Connect Mode	-0.0187	0.0089	0.0054	0.0062
Prob Cuts	-0.0015	0.0057	0.0053	0.0018
EovP	0.0013	-0.0001	-0.0001	-0.0003
Δ	0.0033	-0.0024	-0.0022	-0.0016
no loose tracks	0.0038	0.0158	0.0207	0.0082
less CTD	0.0004	0.0002	0.0000	0.0016
Herwig	0.0015	-0.0096	-0.0125	0.0696
$\mu_{\mathrm{R}} = 2\,\mathrm{Q}$	0.1853	0.0601	0.0632	0.0844
$\mu_{\mathrm{R}} = 0.5\,\mathrm{Q}$	-0.1490	-0.0604	-0.0564	-0.0815
$\mu_{\mathrm{R}} = 2\,\mathrm{Q}$	-0.0228	-0.0076	-0.0100	-0.0067
$\mu_{\mathrm{R}} = 0.5\,\mathrm{Q}$	0.0062	0.0077	0.0086	0.0022
MRSA$'$ pdf	0.0343	0.0023	0.0046	0.0011
$\mu_I = 2.5\,\mathrm{GeV}$	-0.0114	-0.0336	-0.0409	-0.0423
$\mu_I = 1.5\,\mathrm{GeV}$	0.0018	0.0462	0.0601	0.0621
$\mathcal{M} + 20\%$	0.0057	-0.0216	-0.0282	-0.0302
$\mathcal{M} - 20\%$	-0.0190	0.0257	0.0371	0.0393

Table 7.8: $\overline{\alpha_0}$ *and systematic errors*

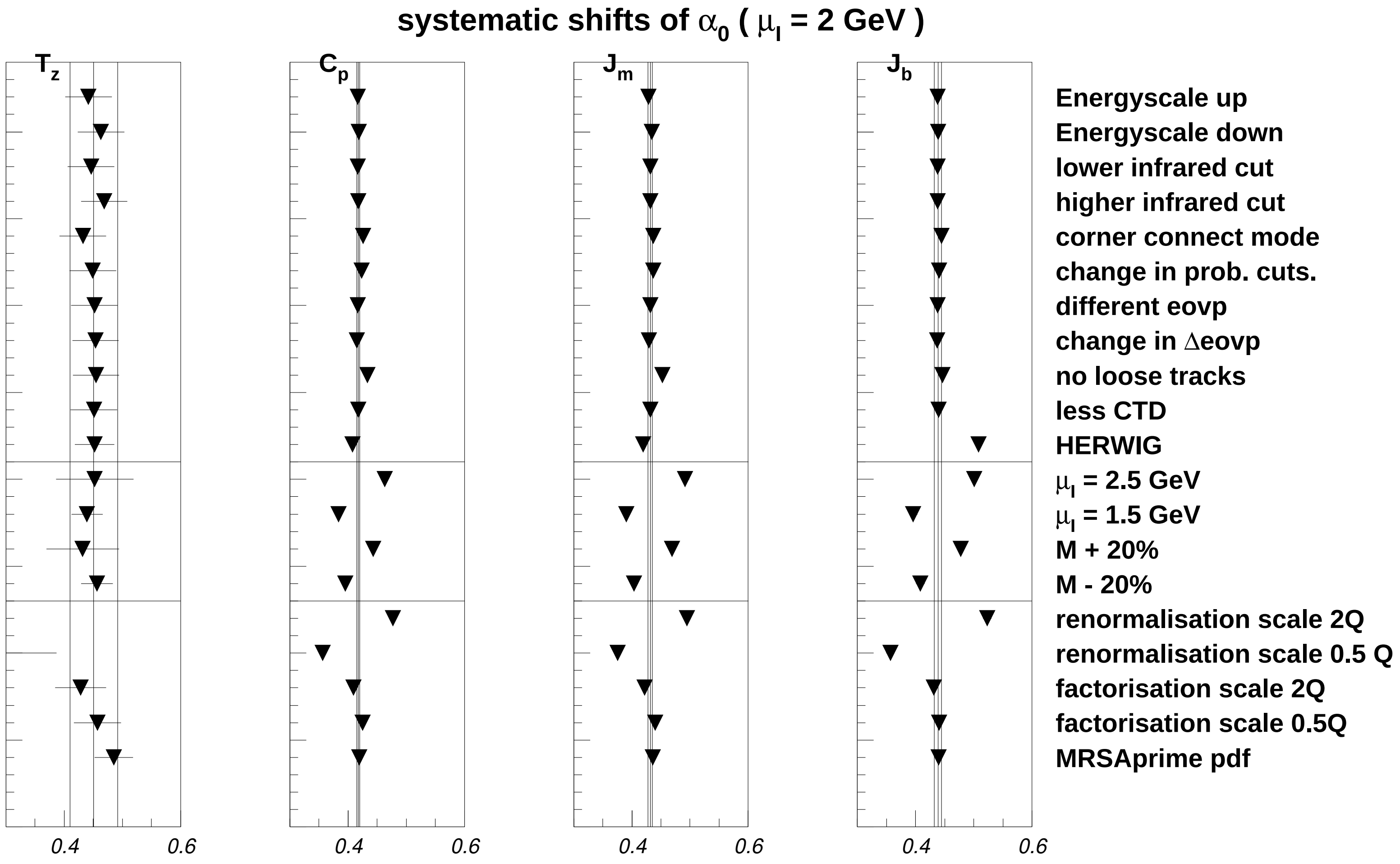

Figure 7.10: *Systematic changes of the fitted values of* $\overline{\alpha_0}$.

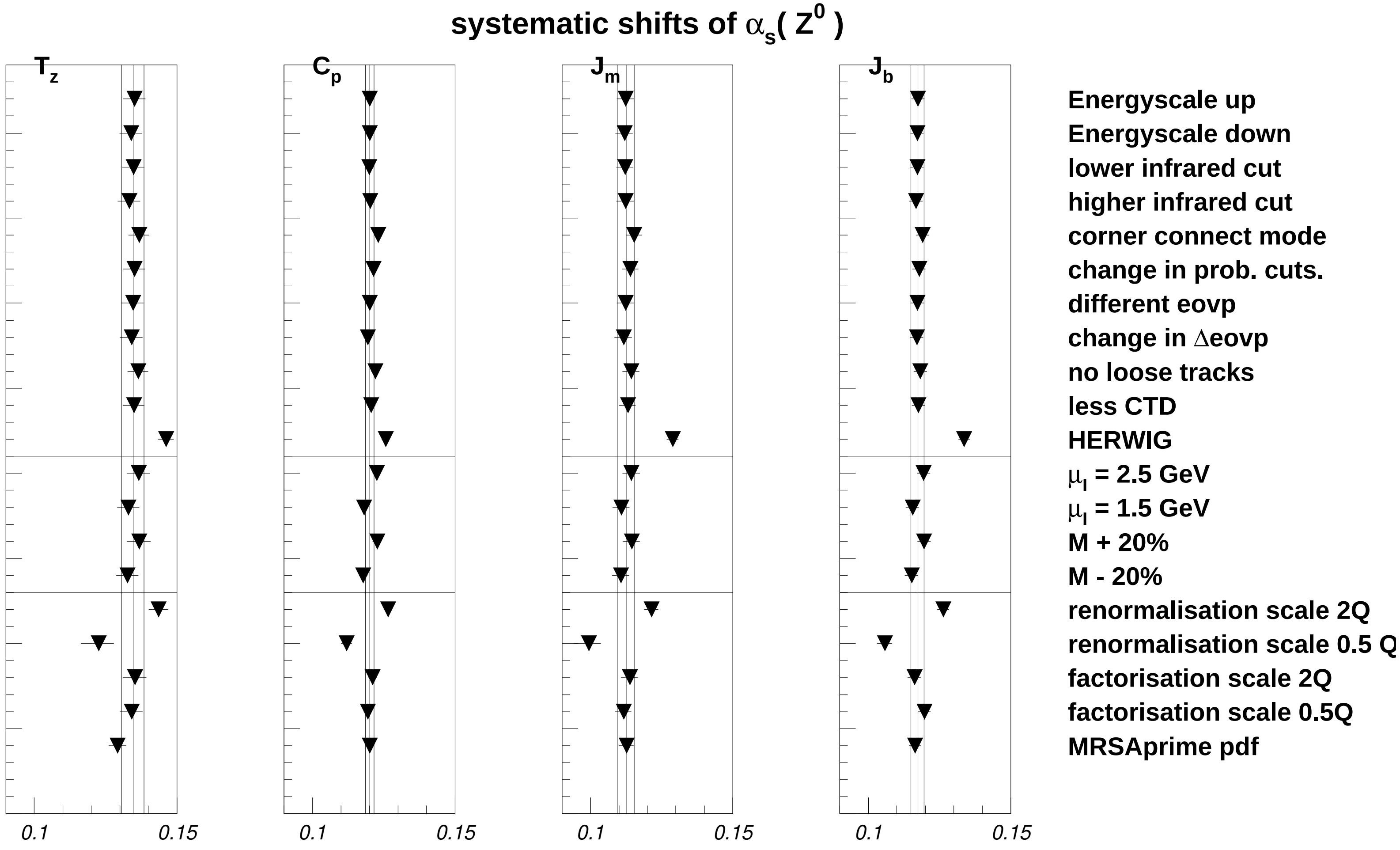

Figure 7.11: *Systematic changes of the fitted values of* α_s .

	1 — T_z	C_p	J_m	J_b
$\alpha_s(\mathrm{M}_{\mathrm{Z}^0})$	0.1347	0.1202	0.1126	0.1173
Exp. stat.	0.0038	0.0014	0.0028	0.0022
	-0.0041	-0.0015	-0.0031	-0.0024
pQCD	**+ 0.0089**	**+ 0.0066**	**+ 0.0090**	**+ 0.0093**
	− 0.0133	**− 0.0082**	**− 0.0131**	**− 0.0116**
Pow. corr.	**+ 0.0021**	**+ 0.0025**	**+ 0.0020**	**+ 0.0023**
	− 0.0020	**− 0.0023**	**− 0.0019**	**− 0.0021**
Exp. syst.	**+ 0.0119**	**+ 0.0067**	**+ 0.0167**	**+ 0.0164**
	− 0.0016	**− 0.0008**	**− 0.0012**	**− 0.0006**
Total	**+ 0.0150**	**+ 0.0097**	**+ 0.0191**	**+ 0.0190**
	− 0.0135	**− 0.0086**	**− 0.0133**	**− 0.0118**
Energyscale	0.0005	0.0000	-0.0002	0.0001
Energyscale	-0.0007	-0.0001	-0.0006	-0.0001
Infrared Cut	0.0002	-0.0002	-0.0003	-0.0001
Infrared Cut	-0.0013	0.0002	-0.0002	-0.0005
Corner Connect Mode	0.0021	0.0029	0.0028	0.0018
Prob Cuts	0.0004	0.0012	0.0015	0.0006
EovP	-0.0001	-0.0001	-0.0001	-0.0001
Δ	-0.0005	-0.0007	-0.0009	-0.0003
no loose tracks	0.0017	0.0019	0.0018	0.0010
less CTD	0.0003	0.0005	0.0006	0.0003
Herwig	0.0115	0.0056	0.0163	0.0163
$\mu_{\mathrm{R}} = 2\,\mathrm{Q}$	0.0089	0.0065	0.0089	0.0090
$\mu_{\mathrm{R}} = 0.5\,\mathrm{Q}$	-0.0121	-0.0082	-0.0130	-0.0115
$\mu_{\mathrm{F}} = 2\,\mathrm{Q}$	0.0007	0.0009	0.0013	-0.0011
$\mu_{\mathrm{F}} = 0.5\,\mathrm{Q}$	-0.0005	-0.0007	-0.0009	0.0024
MRSA$'$ pdf	-0.0054	-0.0001	0.0001	-0.0009
$\mu_I = 2.5\,\mathrm{GeV}$	-0.0017	-0.0020	-0.0016	-0.0018
$\mu_I = 1.5\,\mathrm{GeV}$	0.0020	0.0024	0.0019	0.0021
$\mathcal{M} + 20\%$	-0.0020	-0.0023	-0.0019	-0.0021
$\mathcal{M} - 20\%$	0.0021	0.0025	0.0020	0.0023

Table 7.9: *α_s and systematic errors*

	$\overline{\alpha_0}$	α_s
combined result	0.4265	0.1201
statistical	± **0.0012**	± **0.0006**
pQCD	+ **0.0695** − **0.0660**	+ **0.0080** − **0.0106**
Pow. corr.	+ **0.0522** − **0.0368**	+ **0.0022** − **0.0018**
Exp. syst.	+ **0.0182** − **0.0026**	+ **0.0117** − **0.0008**
Total	+ **0.0888** − **0.0756**	+ **0.0143** − **0.0108**
Energyscale	-0.0016	0.0001
Energyscale	0.0019	-0.0003
Infrared Cut	-0.0003	-0.0002
Infrared Cut	0.0005	-0.0003
Corner Connect Mode	0.0065	0.0025
Prob Cuts	0.0047	0.0010
EovP	-0.0001	-0.0001
Δ	-0.0020	-0.0006
no loose tracks	0.0157	0.0016
less CTD	0.0004	0.0004
Herwig	0.0039	0.0113
$\mu_{\mathrm{R}} = 2\,\mathrm{Q}$	0.0690	0.0079
$\mu_{\mathrm{R}} = 0.5\,\mathrm{Q}$	-0.0654	-0.0106
$\mu_{\mathrm{F}} = 2\,\mathrm{Q}$	-0.0086	0.0004
$\mu_{\mathrm{F}} = 0.5\,\mathrm{Q}$	0.0070	0.0001
MRSA$'$ pdf	0.0037	-0.0010
$\mu_I = 2.5\,\mathrm{GeV}$	-0.0368	-0.0018
$\mu_I = 1.5\,\mathrm{GeV}$	0.0522	0.0022
$\mathcal{M} + 20\%$	-0.0245	-0.0021
$\mathcal{M} - 20\%$	0.0305	0.0023

Table 7.10: *Combined results for* α_s *and* $\overline{\alpha_0}$

Chapter 8

Summary and Conclusions

In this thesis the results of measurements of event shape variables in deep inelastic scattering have been presented. The mean values and differential distributions of Thrust, Jet Broadening, Jet Mass and the C-parameter were obtained with the 1996 and 1997 data sets of the ZEUS experiment at the electron-proton collider HERA in Hamburg. The measurement was performed in a kinematic region extending from $Q^2 = 100\,\mathrm{GeV}^2$ to $Q^2 = 12,800\,\mathrm{GeV}^2$.

The event shape variables have been used for a QCD analysis in terms of "power corrections", which incorporate the existence of a universal coupling at low scales as a phenomenological concept. Perturbative calculations at next-to-leading order accuracy were made with the DISENT program, and the sum of the NLO result and a power correction term was fitted to the data points. The fit results were used to address the question of whether the method of power corrections actually holds.

The numerical predictions from the dispersive approach presented in Chapter 2 are based on the assumption that a universal and meaningful coupling exists down to very low values of momentum transfer, in contrast to the pertubative description of α_s which diverges at the Λ_{QCD}-pole. Although the functional dependence of this coupling is unknown, it is sufficient for the predictions to extract the value of its first moment, $\overline{\alpha_0}$, from fits to the data.

α_s and $\overline{\alpha_0}$ were extracted from separate fits to the different event shape variables under study. The fits were performed to data corrected to hadron level with the zero mass assumption yield values of $\overline{\alpha_0}$ which agree within ±4%, a spread which is smaller than the total errors of the individual results. The four values are combined into the following result:

$$\boxed{\overline{\alpha_0}(\mu_I = 2\,GeV) = 0.4265 \pm 0.0012\ (\mathrm{stat.})\ ^{+0.0182}_{-0.0026}\ (\mathrm{exp.})\ ^{+0.0869}_{-0.0756}\ (\mathrm{theo.})}$$

This result is in good agreement with results from various $\mathrm{e}^+\mathrm{e}^-$ experiments. It can thus be concluded that the assumption of universality of the $\overline{\alpha_0}$ parameter holds and the method of extracting α_s from power corrections is applicable. α_s was extracted from separate fits to the four different event shape values and the combined result is the following:

$$\boxed{\alpha_s(Z^0) = 0.1201 \pm 0.0006\ (\mathrm{stat.})\ ^{+0.0117}_{-0.0008}\ (\mathrm{exp.})\ ^{+0.0082}_{-0.0108}\ (\mathrm{theo.})}$$

Some questions remain. The $x_{\rm bj}$ dependence of the NLO calculations is not the same as the $x_{\rm bj}$ dependence observed in the measurement results. However, the power correction is expected to be an $x_{\rm bj}$ -independent function. What should be done about this? Secondly, what about mass treatment? So far mass effects have been neglected in the theoretical calculations, and consequently the measurement data was obtained with a “zero-mass assumption”. However, it was shown that fits to analysis results which do not neglect the particle masses lead to significantly different results. Answers are to be awaited from the theoreticians.

The fits to the Jet Broadening need to be treated with care since the full calculation to 2-loop accuracy is not yet available. However, an estimation extrapolated from the 2-loop calculation for $\rm e^+e^-$ was applied in the fits presented here. The results are encouraging, and precise calculations are awaited.

Bibliography

[Ab95] H. Abramowicz, A. Caldwell, R. Sinkus, *Neural Network Based Electron Identification in the ZEUS Calorimeter*, DESY 95-054
R. Sinkus, Nucl. Instrum. Methods A 361, 290(1995).

[Ak95] R. Akhoury, V.I. Zakharov, *On the Universality of the Leading, 1/Q Power Corrections in QCD.*, hep-ph/9504248, Phys. Lett **B**357:646-652,1995

[Ak96] R. Akhoury, V.I. Zakharov, *Leading Power Corrections in QCD: from Renormalons to Phenomenology.*, hep-ph/9507253, Nucl. Phys. **B**465:295-314,1996.

[ALEPH98] ALEPH Collaboration, *Measurement of* α_s *with* e^+e^- *annihilation data from 91 to 183 GeV*, ALEPH 98-049 CONF 98-023, Paper submitted to ICHEP'98, Ref. 940

[An83] B. Andersson, G. Gustafson, G. Ingelman B. Söderberg, in Phys. Rep. 97(1983)33

[An86] B. Andersson, G. Gustafson, B. Söderberg, in Zeit. Phys. C20(1983)317; Nucl.Phys. B264(1986)29.

[An91] A. Andresen et al., Nucl. Instr. and Meth. A 309 (1991) 101

[An92] J. Andruskow at al., DESY 92-066 (1992).

[Ar74] X. Artru and G. Mennessier, in Nucl. Phys. B70(1974)93.

[Aw77] T. C. Awes et al, Nucl. Instr. and Meth. A311(1977)130.

[Az85] Y.I. Azimov, Y.L. Dokshitzer, V.A. Khoze, S.I. Troyan in Phys. Lett. B 165*1985)147; Zeit. Phys. C27(1985)65

[Ba97] D.S. Bailey et al., *The Design and Performance of the ZEUS Central Tracking Detector Z by timing System*, Nuncl. Instr. Meth. A396 (1997) 320-349.

[Bene96] M. Beneke *Power Corrections, Renormalons and Resummation.*, hep-ph/9609215, Presented at 28th International Conference on High-energy Physics (ICHEP 96), ICHEP 96:787-792.

[Bene97] M. Beneke *Renormalon Phenomenology: Questions and Directions.*, Talk given at 5th International Workshop on Deep Inelastic Scattering and QCD (DIS 97), hep-ph/9706457.

[Bene99] M. Beneke *RENORMALONS.* hep-ph/9807443, Phys.Rept.317:1-142,1999.

[Bent92] S. Bentvelsen, J. Engelen and P. Koijman, *Reconstruction of (x_{bj} ,Q^2) and extraction of structure functions in neutral current scattering at HERA*, Proc. Workshop pn physics at HERA, vol. 1(1992)23.

[Ber93] B. Bernstein et al., Nucl. Instr. and Meth. A 336 (1993) 23

[Bet98] S. Bethke, *E_T Physics at LEP and World Summary of α_s.*, hep-ex/9812026, Presented at 4th International Symposium on Radiative Corrections (RADCOR 98).

[Br89] R. Brun et al, GEANT3, CERN DD/EE/81-1 (1989).

[Bo81] M.G. Bowler, Zeit. Phys. C11(1981)169.

[Ca92] S. Catani, G. Turnock and B.R. Webber, *Jet Broadening Measures in e^+e^- Annihilation.*, Phys. Lett **B**295:269-276,1992.

[Ca96a] S. Catani, M.H. Seymour, *The Dipole Formalism for the Calculation of QCD Jet Cross-sections at Next-to-leading Order.*, hep-ph/9602277, Phys. Lett **B**378:287-301,1996.

[Ca96b] S. Catani, M.H. Seymour, *QCD Jet Calculations in DIS Based on the Subtraction Method and Dipole Formalism.*, hep-ph/9609237, published in DIS 1996:454-458.

[Ca97a] S. Catani, M.H. Seymour, *A General Algorithm for Calculating Jet Cross-sections in NLO QCD.*, hep-ph/9605323, Nucl. Phys. **B**485:291-419,1997, Erratum-ibid.B510:503-504,1997.

[Ca97b] S. Catani, M.H. Seymour, *Jet Cross-sections at Next-to-leading Order.*, hep-ph/9612236, Invited talk at Cracow International Symposium on Radiative Corrections (CRAD 96), Acta Phys. Polon. **B**28:863-881,1997.

[Ca97c] S. Catani, B.R. Webber, *Infrared Safe but Infinite: Soft Gluon Divergences Inside the Physical Region.*, hep-ph/9710333, JHEP 9710:005,1997.

[Ca98] S. Catani, B.R. Webber, *Resummed C Parameter Distribution in e^+e^- Annihilation.*, hep-ph/9801350, Phys. Lett **B**427:377-384,1998.

[Ch94] K. Charchula, G.A. Schuler, H. Spiesberger, *Combined QED and QCD radiative effects in deep inelastic Lepton-proton Scattering. The Monte Carlo Generator DJANGO6.*, Comput. Phys. Commun. 81(1994)381-402.

[Co85] J.C. Collins, D.E. Soper, G. Sterman in Nucl. Phys. B 162 (1985) 104

[CTEQ85] CTEQ Collaboration: MSUHEP-60426, CTEQ-604; also: CTEQ Collaboration: J. Botts et al.,Phys. Lett. 304B(1993)159.

[cal3] M. Derrick et al., Nucl. Instr. and Meth. A 309 (1991) 77

[Da96] M. Dasgupta, B.R. Webber, *Power Corrections and Renormalons in Deep Inelastic Structure Functions.*, hep-ph/9604388, Phys. Lett **B**382:273-281,1996.

[Da97a] M. Dasgupta and B.R. Webber, *Power Corrections to Event Shapes in Deep Inelastic Scattering*, hep-ph/9704297, Eur. Phys. J. **C**1:539-546,1998.

[Da97b] M. Dasgupta, B.R. Webber, *Power Corrections and Renormalons in e^+e^- Fragmentation Functions.*, hep-ph/9608394, Nucl. Phys. **B**484:247-264,1997.

[Da98] M. Dasgupta and B.R. Webber, *Two-loop enhancement factor for $1/Q$ corrections to event shapes in deep inelastic scattering*, hep-ph/9809247, JHEP 9810:001,1998.

[DELPHI98a] DELPHI Collaboration (D. Wicke, J. Drees, U. Flagmeyer and K. Hamacher), *α_s from DELPHI Measurements at LEP2*, DELPHI 98-81 CONF 149, Paper submitted to ICHEP'98 Conference, ICHEP'98#137

[DELPHI98b] By DELPHI Collaboration (S. Hahn), *The Strong Coupling: Measurements and Running.*, hep-ex/9812021, Presented at International Conference on Hadron Structure (HS 98).

[Do95] Yu.L. Dokshitzer, B.R. Webber, *Calculation of Power Corrections to Hadronic Event Shapes.*, hep-ph/9504219, Phys. Lett **B**352:451-455,1995.

[Do96] Y.L. Dokshitzer, G. Marchesini and B.R. Webber, *Dispersive Approach to Power-Behaved Contributions in QCD Hard Processes*, hep-ph/9512336, Nucl. Phys. **B**469:93-142,1996.

[Do97] , Yu.L. Dokshitzer and B.R. Webber, *Power Corrections to Event Shape Distributions.*, hep-ph/9704298, Phys. Lett **B**404:321-327,1997.

[Do98a] Y.L. Dokshitzer, A. Lucenti, G. Marchesini and G.P. Salam, *Universality of $1/Q$ corrections to jet-shape observables rescued*, hep-ph/9707532, Nucl. Phys. **B**511:396-418,1998.

[Do98b] Yu.L. Dokshitzer, G. Marchesini, G.P. Salam, *Revisiting Nonperturbative Effects in the Jet Broadenings.* hep-ph/9812487.

[Do98c] Yu.L. Dokshitzer, A. Lucenti, G. Marchesini, G.P. Salam, *On the Universality of the Milan Factor for 1/Q Power Corrections to Jet Shapes.*, hep-ph/9802381, JHEP 9805:003,1998.

[Do98d] *Perturbative QCD Theory (Includes our Knowledge of α_s).*, hep-ph/9812252, Talk given at 29th International Conference on High-Energy Physics (ICHEP 98).

[Do99] Yu.L. Dokshitzer, G. Marchesini and B.R. Webber, *Nonperturbative Effects in the Energy-Energy Correlation.*, hep-ph/9905339, JHEP 9907:012,1999.

[El80] R.K. Ellis, D.A. Ross, A.E. Terrano, *Calculation of Event Shape Parameters in e^+e^- Annihilation.*, Phys.Rev.Lett.45:1226-1229,1980.

[El81] R.K. Ellis, D.A. Ross, A.E. Terrano, *The Perturbative Calculation of Jet Structure in e^+e^- Annihilation.*, Nucl. Phys. **B**178:421,1981.

[El96] R.K. Ellis, W.J. Stirling, B.R. Webber, QCD and Collider Physics, Cambridge University Press, 1996.

[Fe72] R.P. Feynman, *Photon-Hadron Interactions*, Benjamin N.Y., 1972

[Fi94] S.M.Fisher and P.Palazzi, *ADAMO Entity-Relationship Programming System, Version 3.3, Reference Manual*, CERN PTG, Programming Techniques Group, ECP Division, February 21, 1994.

[Fo94] B. Foster et al., Nucl. Instr. and Meth. A338 (1994) 254.

[GB] see the thesis of Gennadi Briskin

[Gl95] M. Glück, E. Reya and A. Vogt, in Z. Phys. C67(1995)433.

[Gu88] G. Gustafson, Phys. Lett. B175(1986)453; G. Gustafson and U. Pettersson, in Nucl. Phys. B306(1988)(764).

[H199] H1, *Event Shapes and Power Corrections in ep DIS*, hep-ex/9906002, To be published in the proceedings of 7th International Workshop on Deep Inelastic Scattering and QCD (DIS 99), Zeuthen, Germany, 19-23 Apr 1999.

[H197] H1, *Measurement of Event Shape Variables in Deep Inelastic ep Scattering.*, hep-ex/9706002, Phys. Lett **B**406:256-270,1997.

[Ha84] F. Halzen and A.D. Martin. Quarks and Leptons: An Introductory Course in Modern Particle Physics. John Wiley and Sons, New York 1984.

[He91] L. Hervas, *The pipelined Readout for the ZEUS-Calorimeter*, DESY F35D-91-01, 1991.

[HERAB] HERA-B Collaboration, Technical Design Report, DESY-PRC 95/01 (1995).

[HERMES] HERMES Collaboration, Technical Design Report (1993)

[JADE97] By JADE Collaboration (P.A. Movilla Fernandez et al.), *A Study of Event Shapes and Determinations of α_s Using Data of e^+e^- Annihilations at $\sqrt{s}$ = 22 GeV to 44 GeV.*, hep-ex/9708034, Eur. Phys. J. **C**1:461-478,1998.

[JADE98] Pedro A. Movilla Fernandez, *Event Shapes from JADE Data and Studies of Power Corrections.*, hep-ex/9808005, Nucl.Phys.Proc.Suppl.74:384-387,1999.

[JADE99]) O. Biebel, P.A. Movilla Fernandez, S. Bethke and the JADE-Collaboration, *C-Parameter and Jet Broadening at PETRA Energies*, hep-ex/9903009

[Ja79] F. Jaquet and A. Blondel, in: *Proc. of the study of an ep facility for Europe*, DESY 79-48(1979, edited by U. Amaldi, p.391.

[In97] G. Ingelman, A. Edin, J. Rathsman, *A Monte Carlo Generator for deep inelastic Lepton-nucleon Scattering.*, hep-ph/9605286, Comput. Phys. Commun. 101(1997)108-134.

[Kr92] J. Kr"uger, *The Uranium Scintillator Calorimeter for the ZEUS-detector at the Electron Proton Collider HERA*, Hamburg 1992.

[Ko94] Gregory P. Korchemsky, George Sterman, *Nonperturbative Corrections in Resummed Cross-sections.*, hep-ph/9411211, Nucl. Phys. **B**437:415-432,1995.

[Ko95] Gregory P. Korchemsky, George Sterman, *Universality of Infrared Renormalons in Hadronic Cross-sections.*, hep-ph/9505391, Published in Moriond 1995: Hadronic:0383-392, Contributed to 30th Rencontres de Moriond: QCD and High Energy Hadronic Interactions.

[Kw92] A. Kwiatkowsky, H. Spiesberger, H.J. Mohring, *An Event Generator for ep interactions at HERA energies including radiative processes: Version 1.0.*, Comput. Phys. Commun. 69(1992)155-172.

[L3] L3 Collaboration, *QCD Studies and Determination of α_s using Hadronic Event Structures from 30 GeV to 189 GeV*, L3 Note 2414, Paper submitted to IECHEP'99

[Li98] S. Liuti, *A Systematic Study of Power Corrections from World Deep Inelastic Scattering Measurements*, hep-ph/9809248, Talk given at QCD98, published in the proceedings.

[Lo] Leif Lönnblad, *ARIADNE Version 4: A program for simulation of QCD cascades implementing the color dipole model.*

[Man95] Aneesh V. Manohar, Mark B. Wise, *Power-suppressed Corrections to Hadronic Event Shapes.*, hep-ph/9406392, Phys. Lett **B**344:407-412,1995.

[Mar95] A.D. Martin, R.G. Roberts, W.J. Stirling in Phys. Lett. B354(1995)155

[Ma91] G. Marchesini, B.R. Webber, G. Abbiendi, I.G. Knowles, M.H. Seymour, L. Stanco, *A Monte Carlo Generator for simulating hadron emission reactions with interfering gluons. Version 5.1 – April 1991*, Comput. Phys. Commun. 67(1992)465-508.

[Ma96] G. Marchesini, B.R. Webber, G. Abbiendi, I.G. Knowles, M.H. Seymour, L. Stanco, *HERWIG manual Version 5.9*, hep-ph/9607393

[Ma97] G. Marchesini, B.R. Webber, G. Abbiendi, I.G. Knowles, M.H. Seymour, L. Stanco, *HERWIG Version 5.8d*, at: http://hepwww.rl.ac.uk/theory/seymour/herwig/HERWIG58d.FOR

[Mu92] A.H. Mueller, The QCD Perturbation Series, QCD – 20 Years Later, Aachen, June 9-13, 1992. World Scientific, Singapore, 1993.

[Na95] P. Nason and M.H. Seymour, *Infrared Renormalons and Power Suppressed Effects in e^+e^- Jet Events*, hep-ph/9506317, Nucl. Phys. **B**454:291-312,1995.

[Pi93] K. Piotrzkowski, DESY F35D-93-06 (1993).

[Pl96] H. Plothow-Besch. PDFLIB: Nucleon, Pion, Photon Parton Density Functions and α_s Calculations – User's Manual – Version 7.06. CERN, 1996. CERN-PPE-1996.11.14.

[Sa98] G.P. Salam, *The Milan Factor for Jet Shape Observables.*, hep-ph/9805323, In *Brussels 1998, Deep inelastic scattering and QCD* 518-522.

[Se98] Michael H. Seymour, *Jet Shapes in Hadron Collisions: Higher Orders, Resummation and Hadronization.*, hep-ph/9707338, Nucl. Phys. **B**513:269-300,1998.

[Se97] Michael H. Seymour, *Jet Phenomenology.*, hep-ph/9707349, Contributed to 11th Les Rencontres de Physique de la Vallee d'Aoste, *La Thuile 1997, Results and perspectives in particle physics* 475-491.

[Si97] R. Sinkus, T. Voss, Nucl. Instr. and Methods A 391(1997)360.

[SJ86] T. Sjöstrand, Computer Phys. Commun. 39(1986)347; M. Bengtsson and T. Sjöstrand, Computer Phys. Commun. 43(1987)367.

[SLAC] SLAC-MIT collaboration, G. Miller et. al., Phys. Rev. D5(1972)528.

[SLD] SLD Collaboration (K. Abe et al.), *Measurement of $\alpha_s(M_Z^2)$ from Hadronic Event Observables at the Z^0 Resonance.*, hep-ex/9501003, Phys.Rev.D51:962-984,1995.

[St79] K.H. Streng, T.F. Walsh, P.M. Zerwas, *Quark and Gluon Jets in the Breit Frame of Lepton-Nucleon Scattering.*, Z.Phys.C2:237,1979.

[Th98] John C. Thompson, *Measurements of α_s from Hadronic Event Shapes in e^+e^- Annihilation.*, hep-ex/9812004, Talk given at 29th International Conference on High-Energy Physics (ICHEP 98).

[Ts91] E.Tscheslog, *ZEUS Reconstruction Program Organisation and Control*, ZEUS Note 91-37. See also references herein.

[We94] B.R. Webber *Estimation of Power Corrections to Hadronic Event Shapes.*, hep-ph/9408222, Phys. Lett **B**339:148-150,1994.

[We95] B.R. Webber, *HHadronic Final States.*, hep-ph/9510283, Paris DIS 1995:0115-126.

[We96] B.R. Webber, *Deep Inelastic Scattering: Theory and Phenomenology.*, hep-ph/9607441, Talk given at International Workshop on Deep Inelastic Scattering and Related Phenomena (DIS 96), Rome, Italy, 15-19 Apr 1996, DIS 1996:77-96.

[We99] B.R. Webber *Renormalon Phenomena in Jets and Hard Processes.*, hep-ph/9712236, Nucl.Phys.Proc.Suppl.71:66-75,1999.

[Wi98] Daniel Wicke, *Determination of α_s from Event Shapes and Power Corrections.*, hep-ph/9708467, Nucl.Phys.Proc.Suppl.64:27-31,1998.

[Za92] V.I. Zakharov, *QCD Perturbative Expansions in Large Orders.*, Nucl. Phys. **B**385:452-480,1992.

[ZEUS93a] ZEUS Collaboration, *The ZEUS Detector*, Status report 1993.

[ZEUSa] ZGANA, ZEUS trigger simulation library, Els de Wolf (editor) et al..

[ZEUSb] ZEUS-note on the DISTUPLEs, in preparation.

[ZEUS97] ZEUS-Collaboration, J.Breitweg et al., *Measurement of the Proton Structure Function* F_2 *and* $\sigma_{tot}^{\gamma^* p}$ *at Low* Q^2 *and Very Low* x *at HERA*, Physics Letters B 407 (1997) 432-448.

Appendix A

Zero Mass Assumption

"Zero mass assumption" means that at the hadron level the event shape variables are calculated from the momentum of the hadrons only. The mass is "stripped off" after the determination of x_{bj} and Q^2 and after the boost to the Breit frame. Correcting to a hadron level with massless hadrons is advised by theoreticians, since the calculations of power corrections are performed neglecting the hadron masses as well.

Bin	uncorr. mean	error	correction factor	error	corrected mean	error (stat.)	pos. system.	neg system.
1	0.617	0.002	1.023	0.007	0.631	0.004	0.002	−0.028
2	0.620	0.002	1.031	0.007	0.639	0.005	0.002	−0.034
3	0.596	0.003	1.096	0.008	0.653	0.005	0.003	−0.040
4	0.663	0.003	1.038	0.009	0.688	0.006	0.001	−0.038
5	0.664	0.003	1.055	0.010	0.700	0.007	0.001	−0.036
6	0.609	0.004	1.143	0.012	0.696	0.008	0.005	−0.038
7	0.714	0.004	1.033	0.005	0.737	0.005	0.002	−0.036
8	0.684	0.005	1.074	0.006	0.734	0.006	0.002	−0.036
9	0.747	0.006	1.038	0.007	0.776	0.007	0.002	−0.038
10	0.739	0.007	1.067	0.007	0.789	0.008	0.001	−0.037
11	0.790	0.009	1.037	0.009	0.819	0.010	0.002	−0.033
12	0.776	0.010	1.087	0.010	0.844	0.012	0.002	−0.041
13	0.824	0.013	1.060	0.012	0.873	0.015	0.002	−0.035
14	0.884	0.015	1.052	0.019	0.930	0.022	0.002	−0.053

Table A.1: Results for Thrust, Zero mass assumption

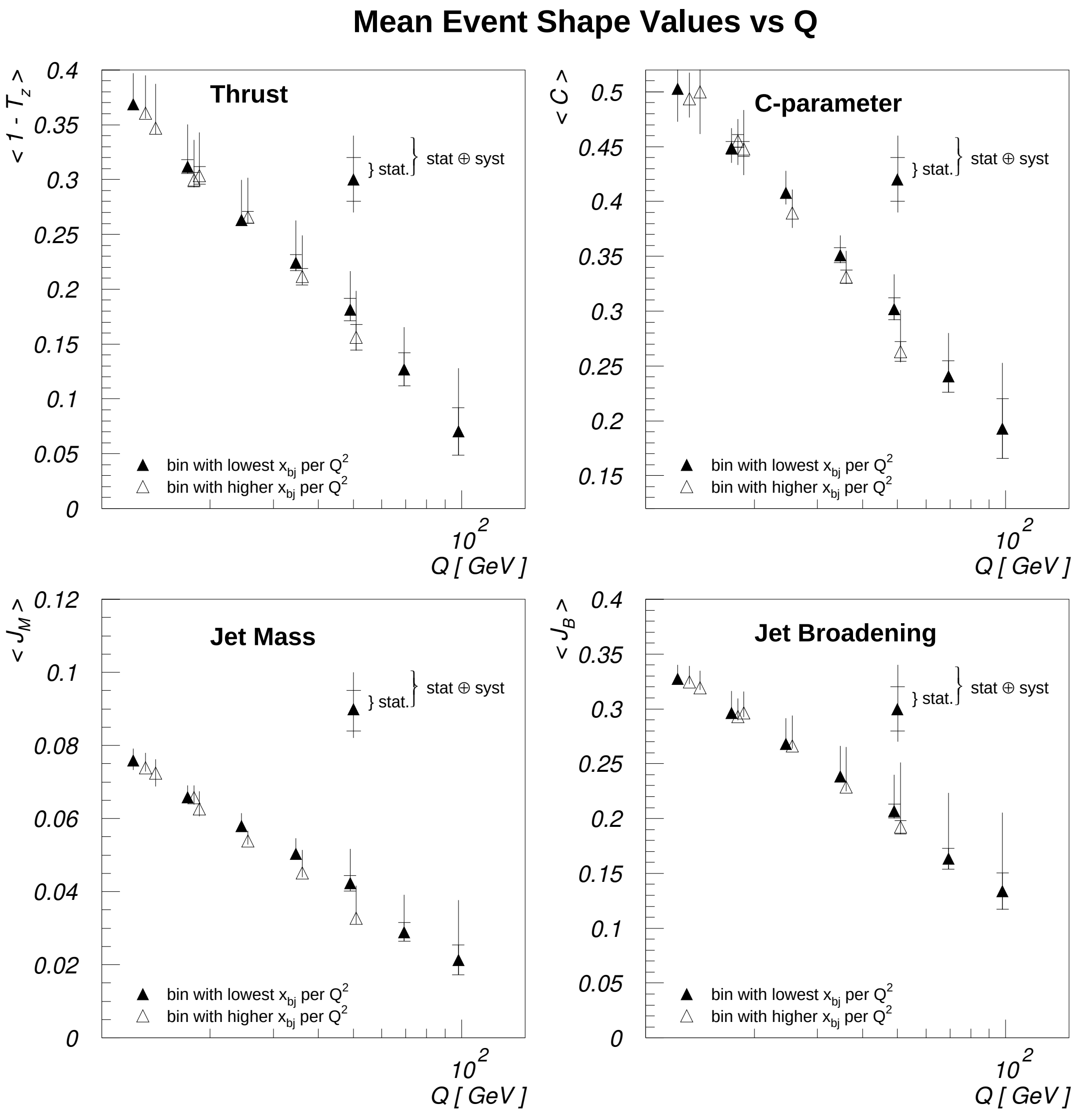

Figure A.1: *Mean values of the event shape variables thrust , c-parameter and Jet Broadening. Here shown for* zero mass *assumption,* i.e. *the data was corrected to a hadron level where the hadron masses are neglected. Compare with Figure 6.5.*

Bin	uncorr. mean	error	correction factor	error	corrected mean	error (stat.)	pos. system.	neg system.
1	0.490	0.003	1.025	0.009	0.503	0.004	0.020	−0.030
2	0.502	0.003	0.985	0.008	0.494	0.004	0.023	−0.017
3	0.531	0.003	0.942	0.008	0.500	0.005	0.023	−0.038
4	0.460	0.004	0.976	0.012	0.449	0.006	0.017	−0.012
5	0.489	0.004	0.932	0.012	0.455	0.006	0.019	−0.021
6	0.506	0.005	0.884	0.013	0.448	0.007	0.035	−0.023
7	0.429	0.007	0.952	0.008	0.408	0.005	0.019	−0.010
8	0.468	0.007	0.831	0.008	0.389	0.005	0.021	−0.012
9	0.381	0.012	0.921	0.014	0.351	0.007	0.017	−0.003
10	0.429	0.011	0.773	0.012	0.331	0.006	0.023	−0.002
11	0.363	0.020	0.831	0.022	0.302	0.010	0.030	−0.003
12	0.383	0.020	0.688	0.019	0.263	0.009	0.037	−0.004
13	0.344	0.036	0.699	0.033	0.240	0.014	0.037	−0.002
14	0.307	0.081	0.627	0.073	0.193	0.027	0.053	−0.002

Table A.2: Results for C Parameter, zero mass assumption

Bin	uncorr. mean	error	correction factor	error	corrected mean	error (stat.)	pos. system.	neg system.
1	0.077	0.004	0.992	0.012	0.076	0.001	0.003	−0.003
2	0.079	0.004	0.937	0.011	0.074	0.001	0.004	0.000
3	0.088	0.004	0.821	0.010	0.072	0.001	0.004	−0.004
4	0.072	0.006	0.921	0.016	0.066	0.001	0.003	−0.001
5	0.077	0.006	0.853	0.015	0.066	0.001	0.003	−0.001
6	0.089	0.006	0.704	0.014	0.063	0.001	0.005	−0.001
7	0.066	0.010	0.884	0.012	0.058	0.001	0.003	0.000
8	0.076	0.010	0.708	0.010	0.054	0.001	0.003	−0.001
9	0.059	0.018	0.852	0.019	0.050	0.001	0.004	0.000
10	0.069	0.016	0.655	0.015	0.045	0.001	0.006	0.000
11	0.057	0.029	0.739	0.029	0.042	0.002	0.009	−0.001
12	0.064	0.029	0.508	0.020	0.033	0.002	0.009	0.000
13	0.053	0.050	0.546	0.039	0.029	0.003	0.010	0.000
14	0.045	0.107	0.471	0.074	0.021	0.004	0.016	0.000

Table A.3: Results for Jet Mass, zero mass assumption

Bin	uncorr. mean	error	correction factor	error	corrected mean	error (stat.)	pos. system.	neg system.
1	0.334	0.002	0.981	0.005	0.328	0.002	0.012	−0.001
2	0.331	0.002	0.982	0.006	0.325	0.002	0.014	−0.001
3	0.341	0.002	0.936	0.006	0.319	0.002	0.015	−0.001
4	0.308	0.003	0.962	0.009	0.296	0.003	0.020	−0.001
5	0.307	0.003	0.954	0.010	0.293	0.003	0.016	0.000
6	0.335	0.003	0.886	0.010	0.296	0.004	0.019	−0.001
7	0.279	0.006	0.963	0.008	0.268	0.003	0.023	−0.001
8	0.294	0.006	0.907	0.008	0.266	0.003	0.027	−0.001
9	0.254	0.010	0.940	0.013	0.239	0.004	0.028	−0.001
10	0.259	0.010	0.883	0.013	0.229	0.004	0.036	−0.001
11	0.225	0.018	0.918	0.024	0.207	0.007	0.032	−0.002
12	0.233	0.019	0.823	0.021	0.192	0.006	0.059	−0.001
13	0.201	0.034	0.812	0.038	0.163	0.009	0.059	−0.001
14	0.165	0.065	0.811	0.085	0.134	0.017	0.070	−0.003

Table A.4: Results for Jet Broadening, zero mass assumption

Appendix B

Fits to Results with Massive Hadron Level

The fits were first performed to the results where the data was corrected to massive hadron level. They show a very large spread in $\overline{\alpha_0}$, as can be seen in Figure B.3.

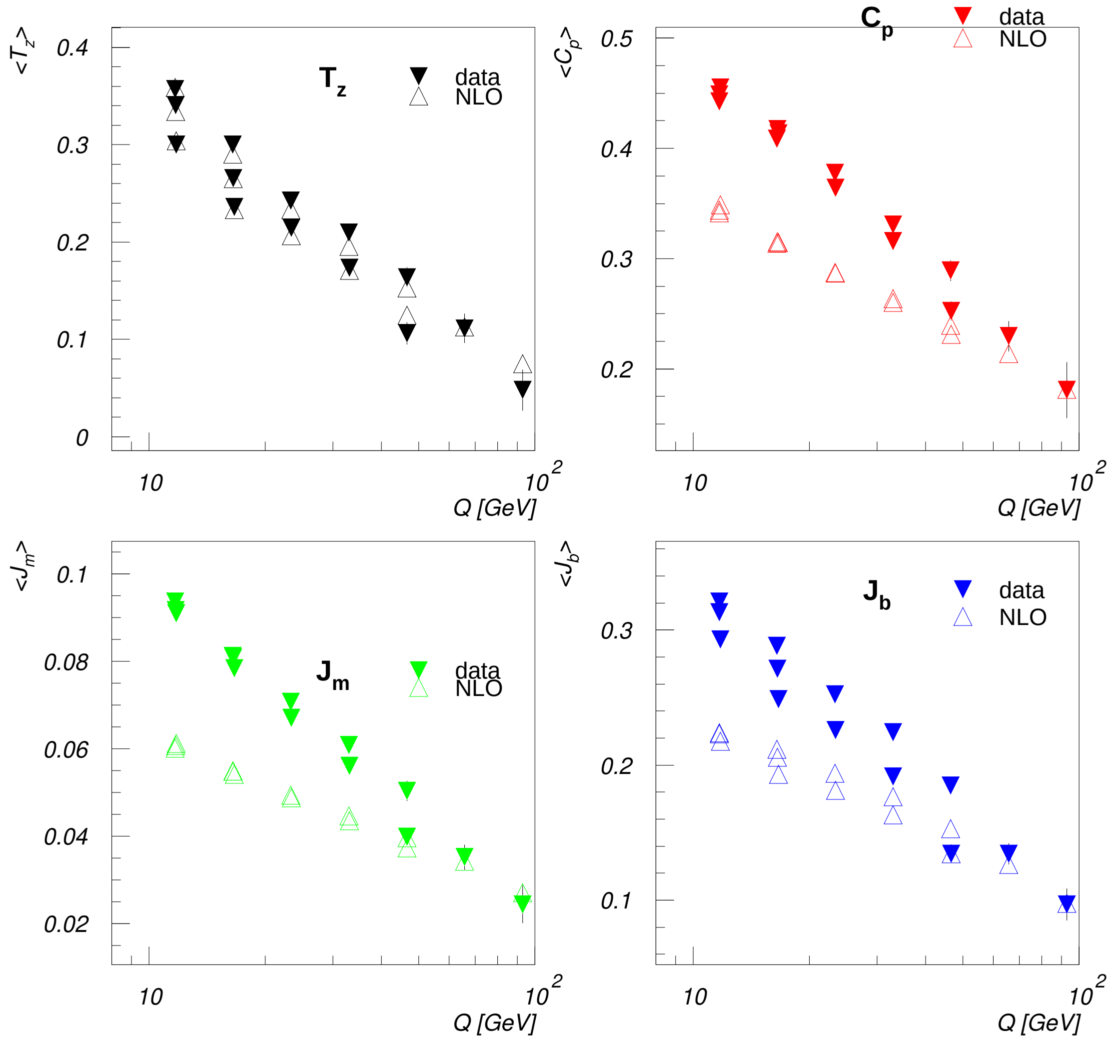

Figure B.1: *Measurement results (filled triangles) compared to NLO calculation (open triangles). The NLO result is shown for the* $\Lambda^{[4]}$ *value as obtained in the* χ^2 *fits (see Table 7.5). The* $1/Q$ *deviations between data and NLO results are clearly visible.*

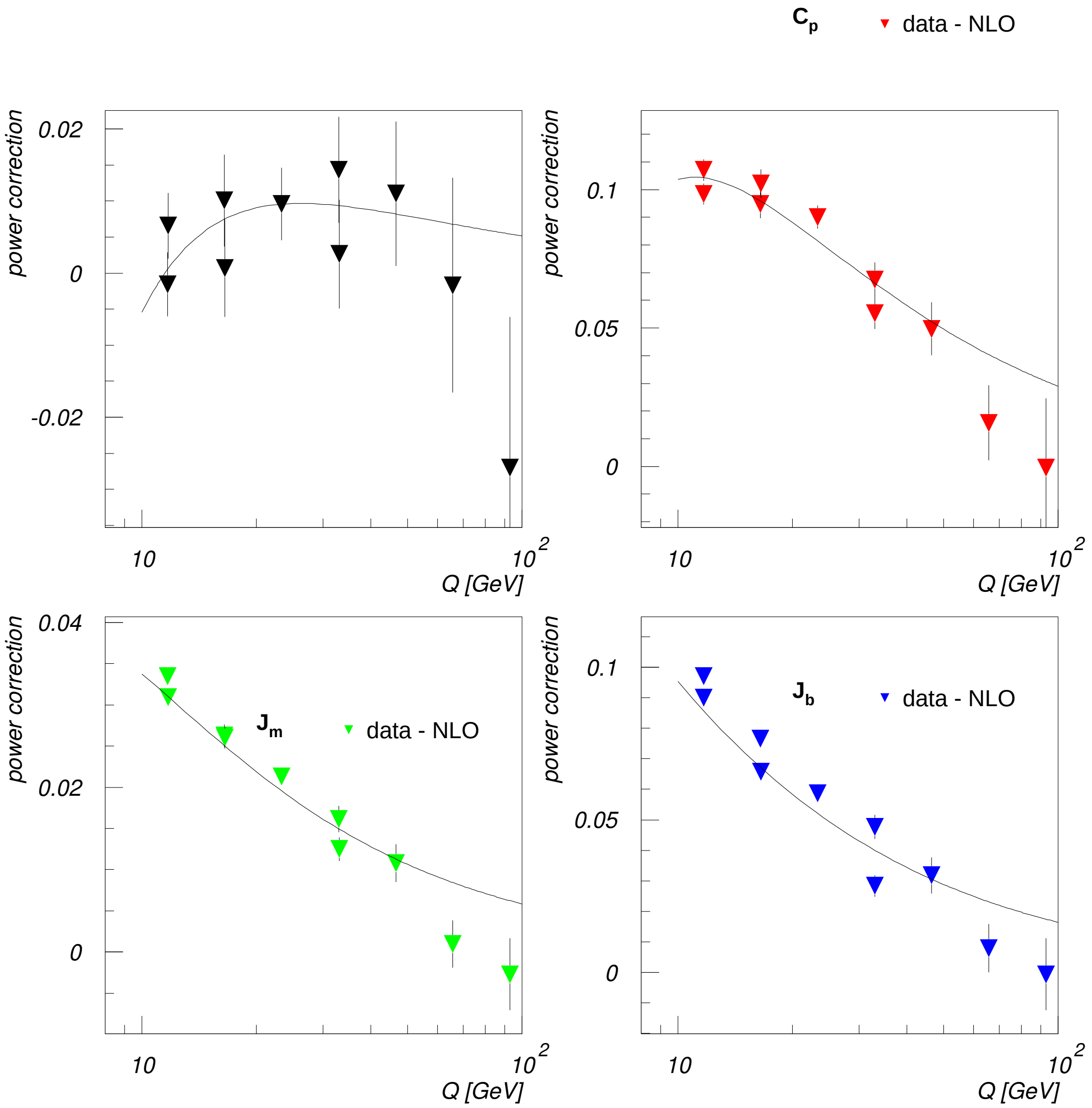

Figure B.2: *Power Corrections from the* χ^2 *fits. Shown are the* $F_{i,\mathrm{data-NLO}}$ *points, i.e. the data points with the NLO results subtracted, compared with the fit result for the power correction term. The errors shown are the statistical errors of the data analysis as they are used in the fit. The 1% error of the NLO results due to the seed uncertainty is neglected. The agreement is very good within the errors, although the fits are pinned at the lower* Q *values.*

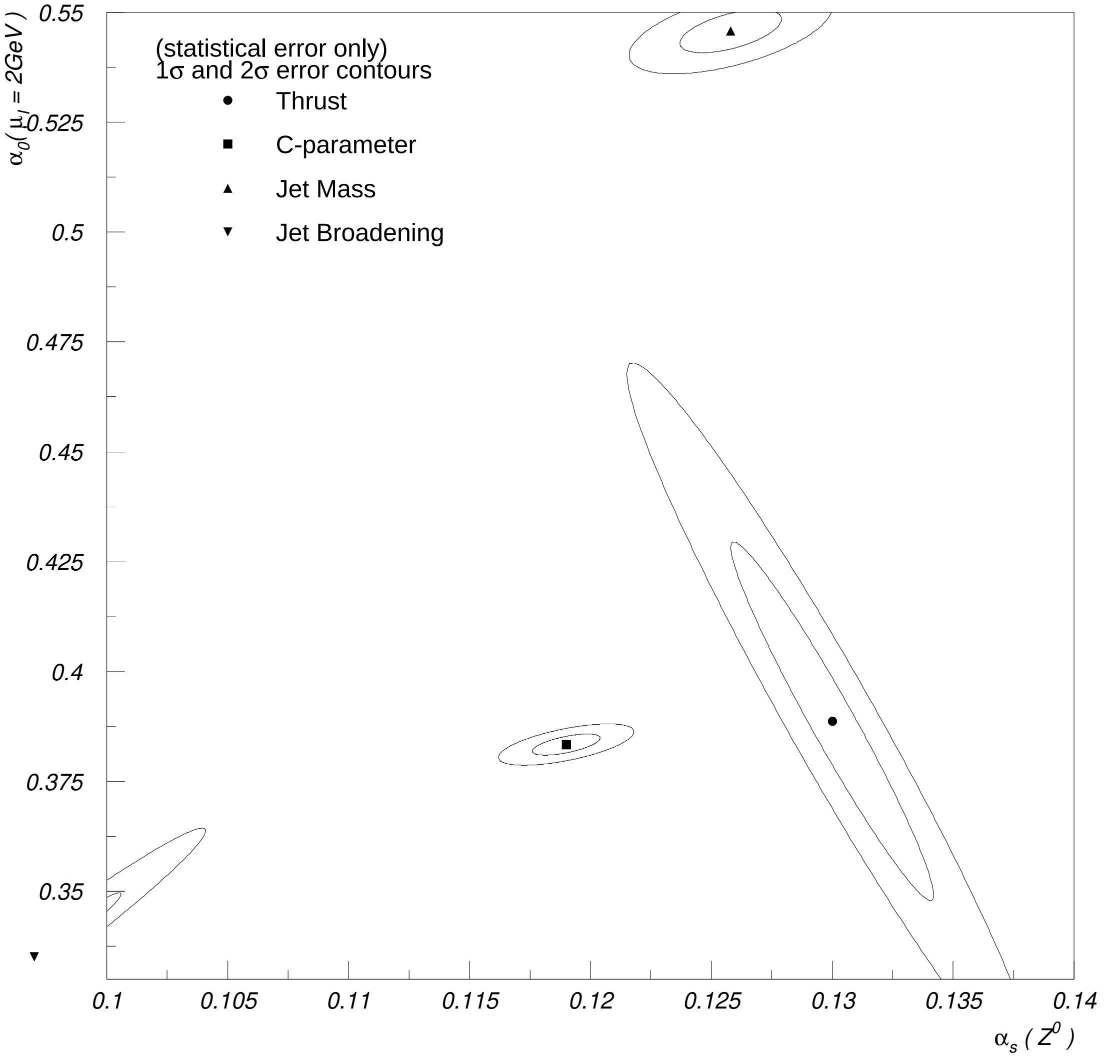

Figure B.3: *Contours of the fit results. Shown are the 1 σ contour for statistical errors as well as the 1 σ contour for statistical plus experimental systematic. Experimental systematic errors are highly asymmetric. Here is shown the contour for an avarage value of the positive and negative systematic error.*

Appendix C

Differential Distributions

This section shows more detailed histograms of the differential distributions. The numerical results as well as histograms showing the efficiencies, purities and the correction factors of the differential distributions are shown.

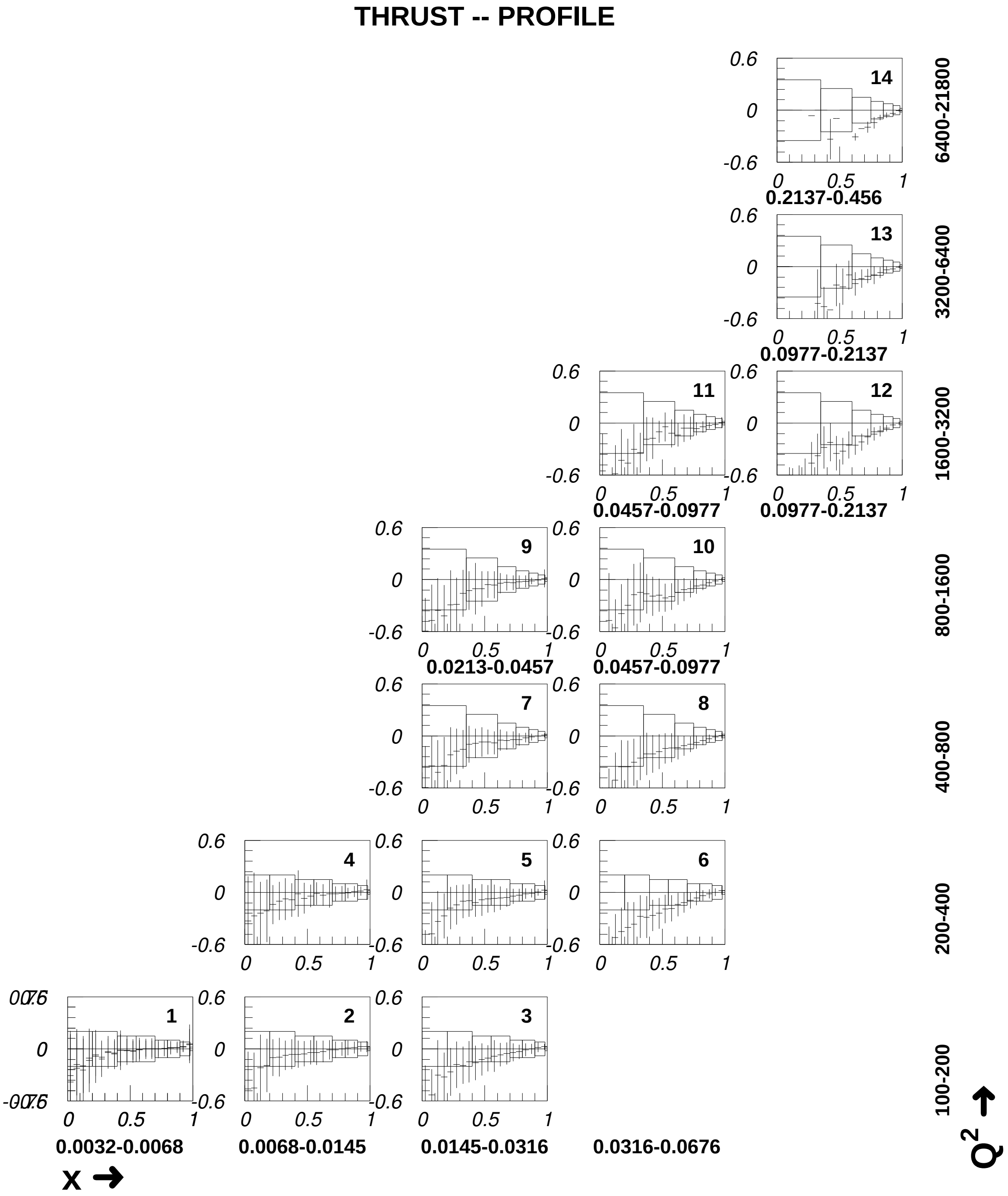

Figure C.1: *Profile histogram of* T_z

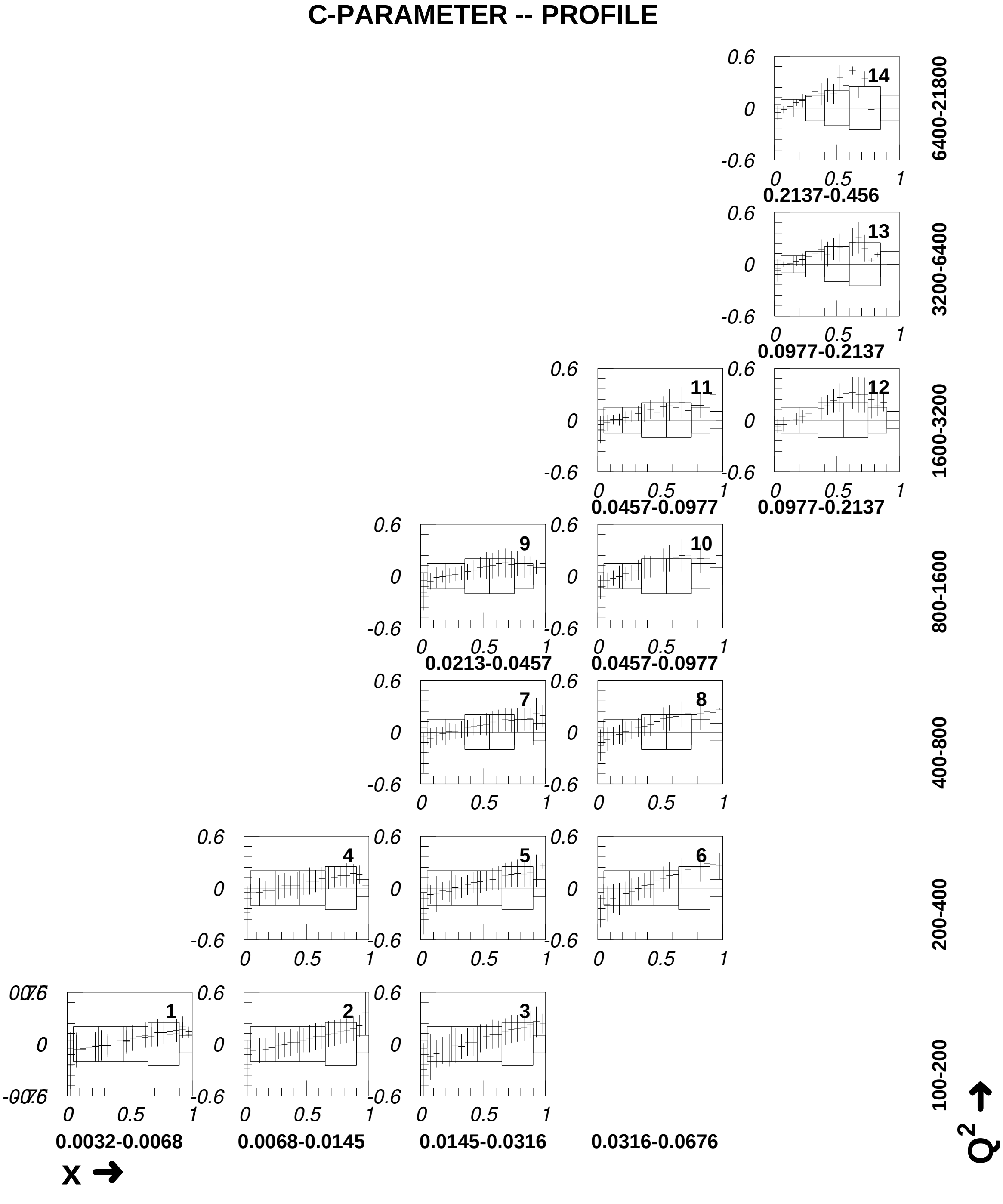

Figure C.2: *Profile histogram of* C_p

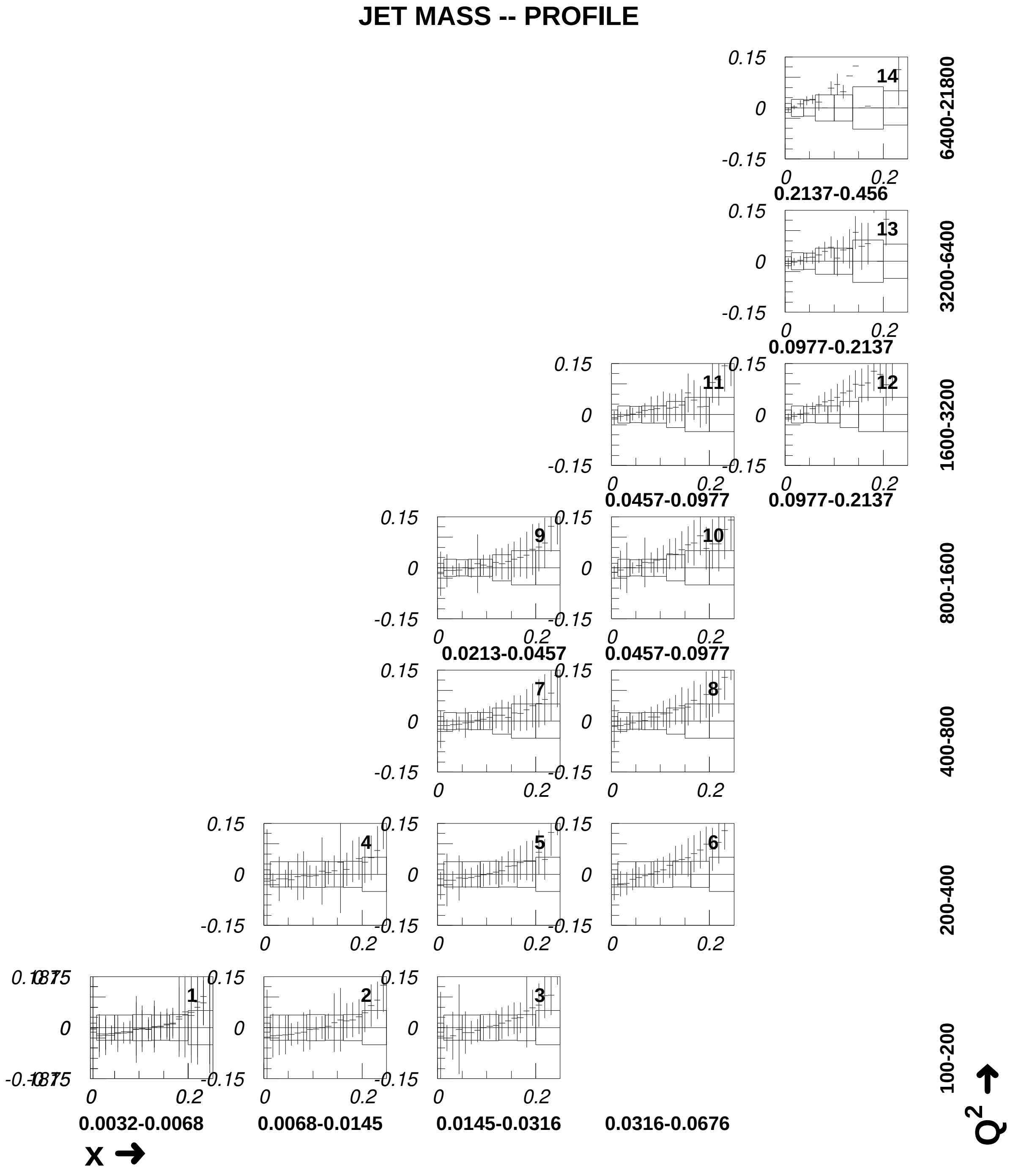

Figure C.3: *Profile histogram of* J_m

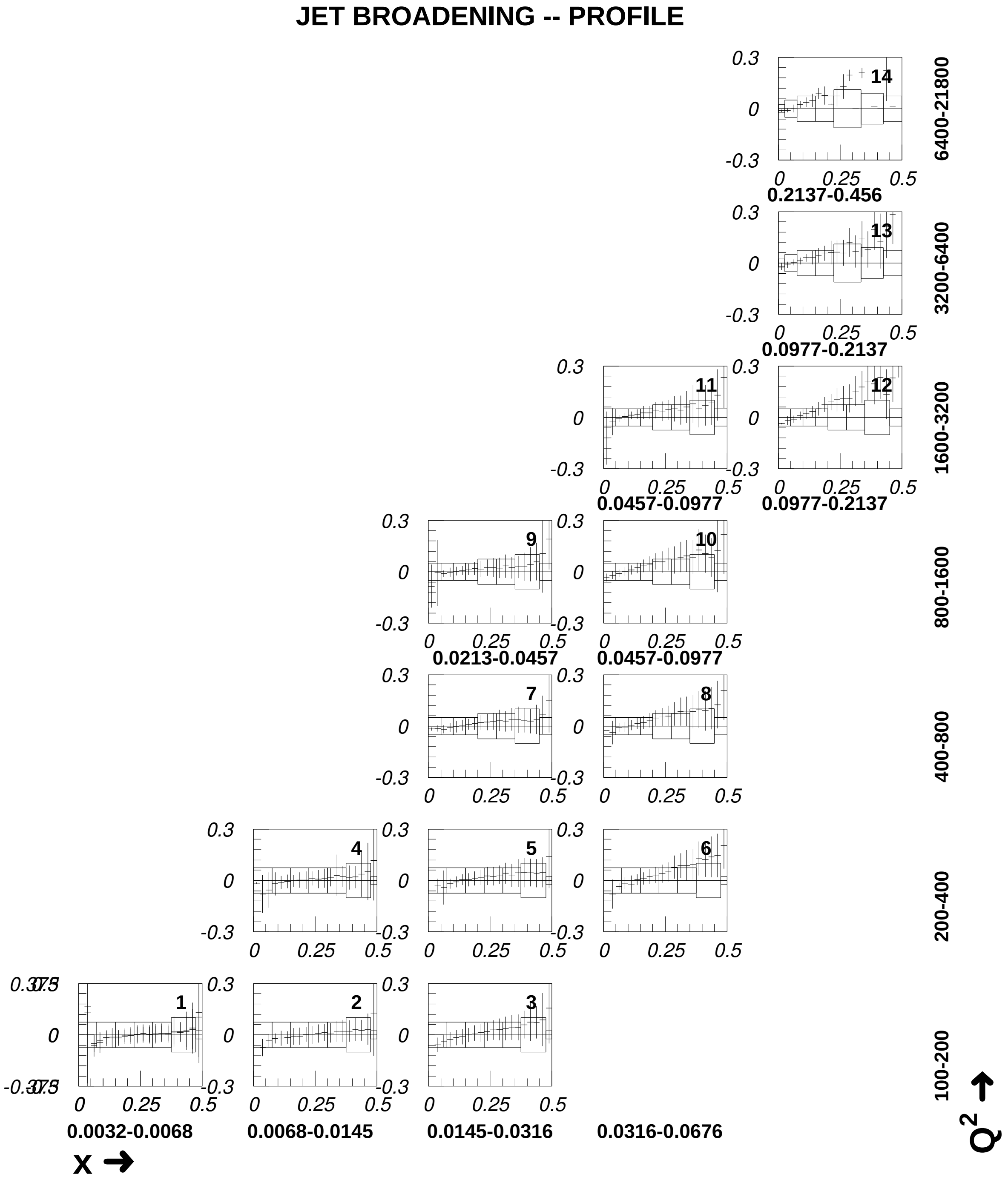

Figure C.4: *Profile histogram of* J_b

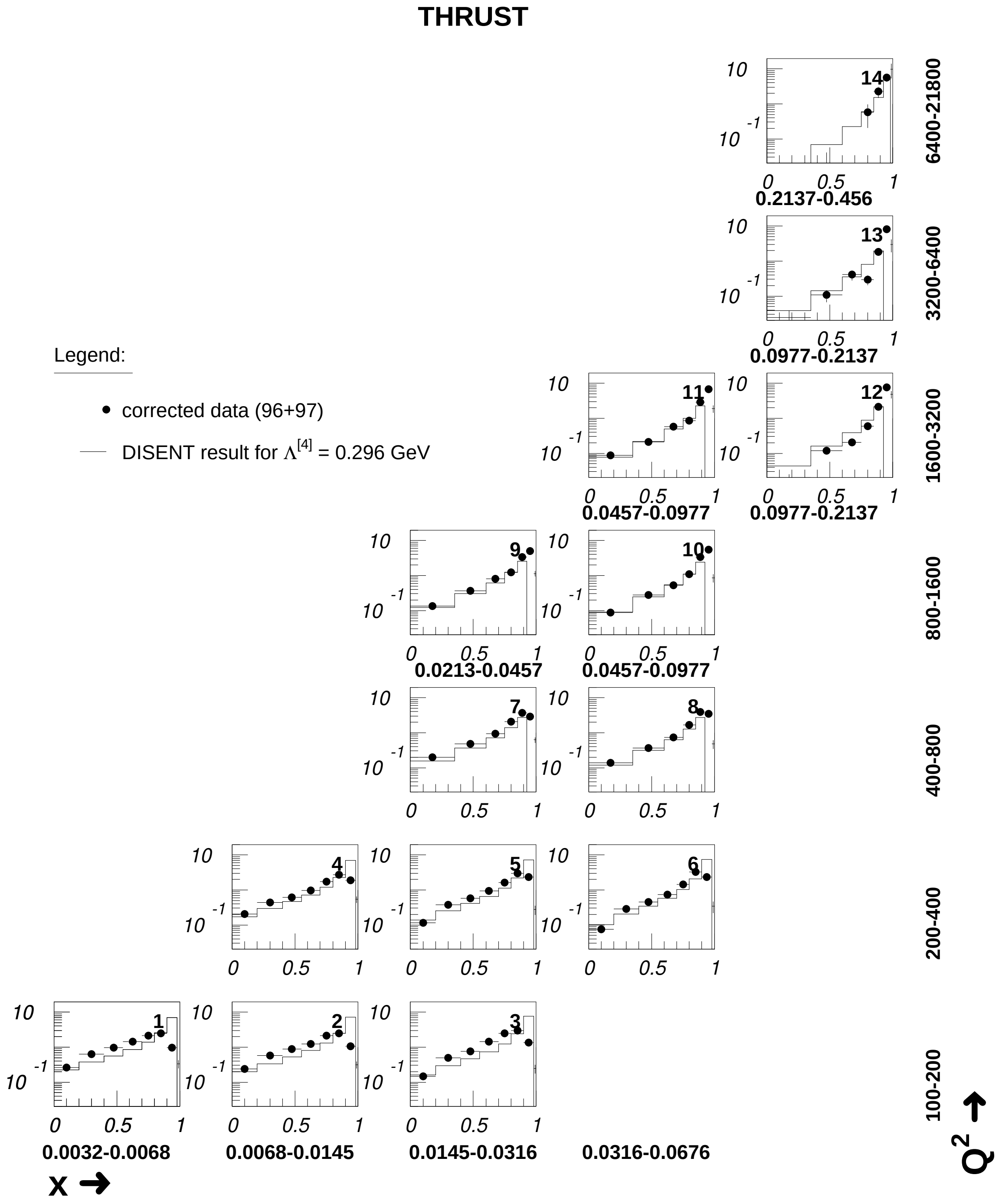

Figure C.5: *differential distribution thrust . Data corrected to hadron level compared with results of NLO generation with DISENT.*

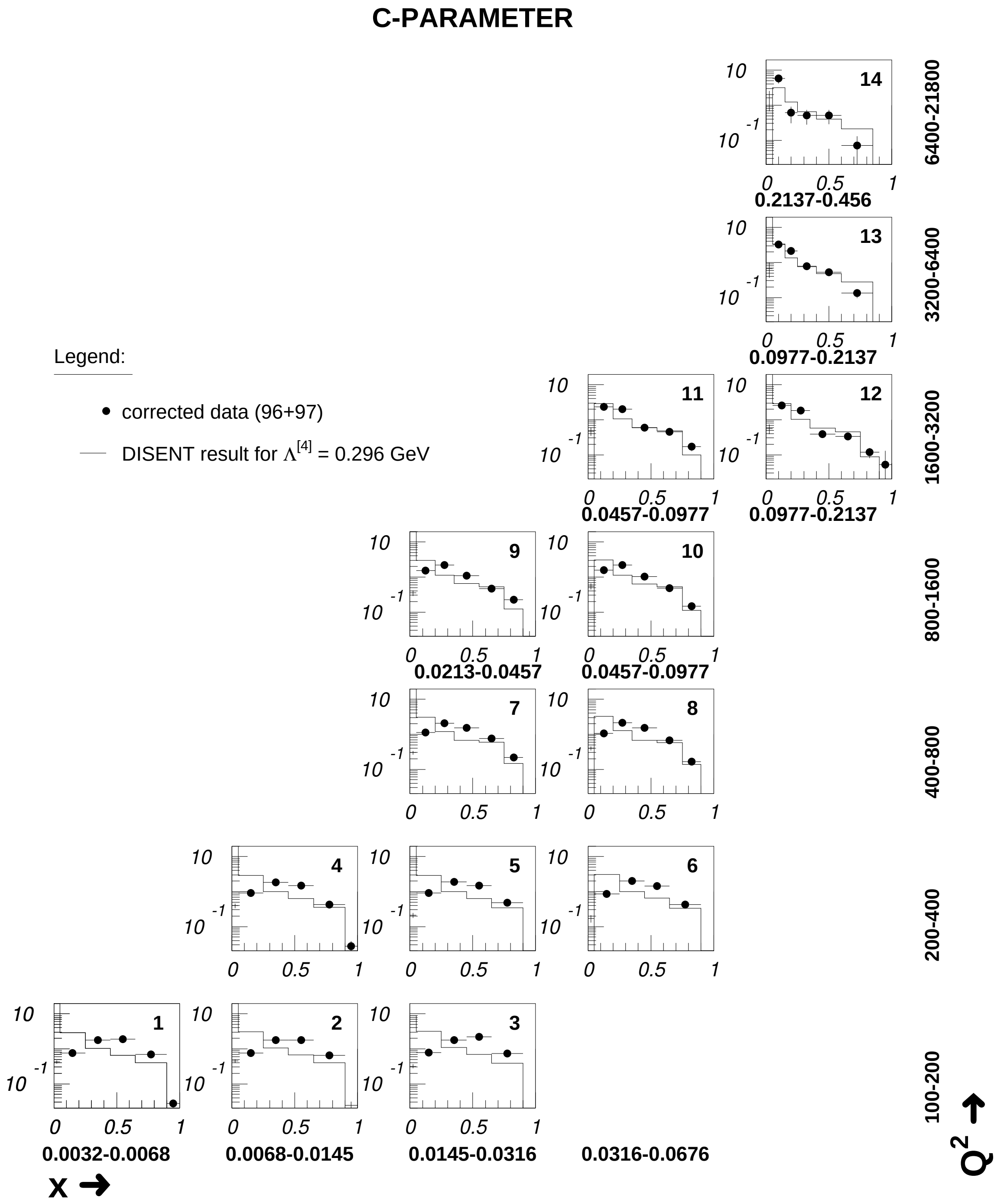

Figure C.6: *differential distribution C-parameter. Data corrected to hadron level compared with results of NLO generation with DISENT.*

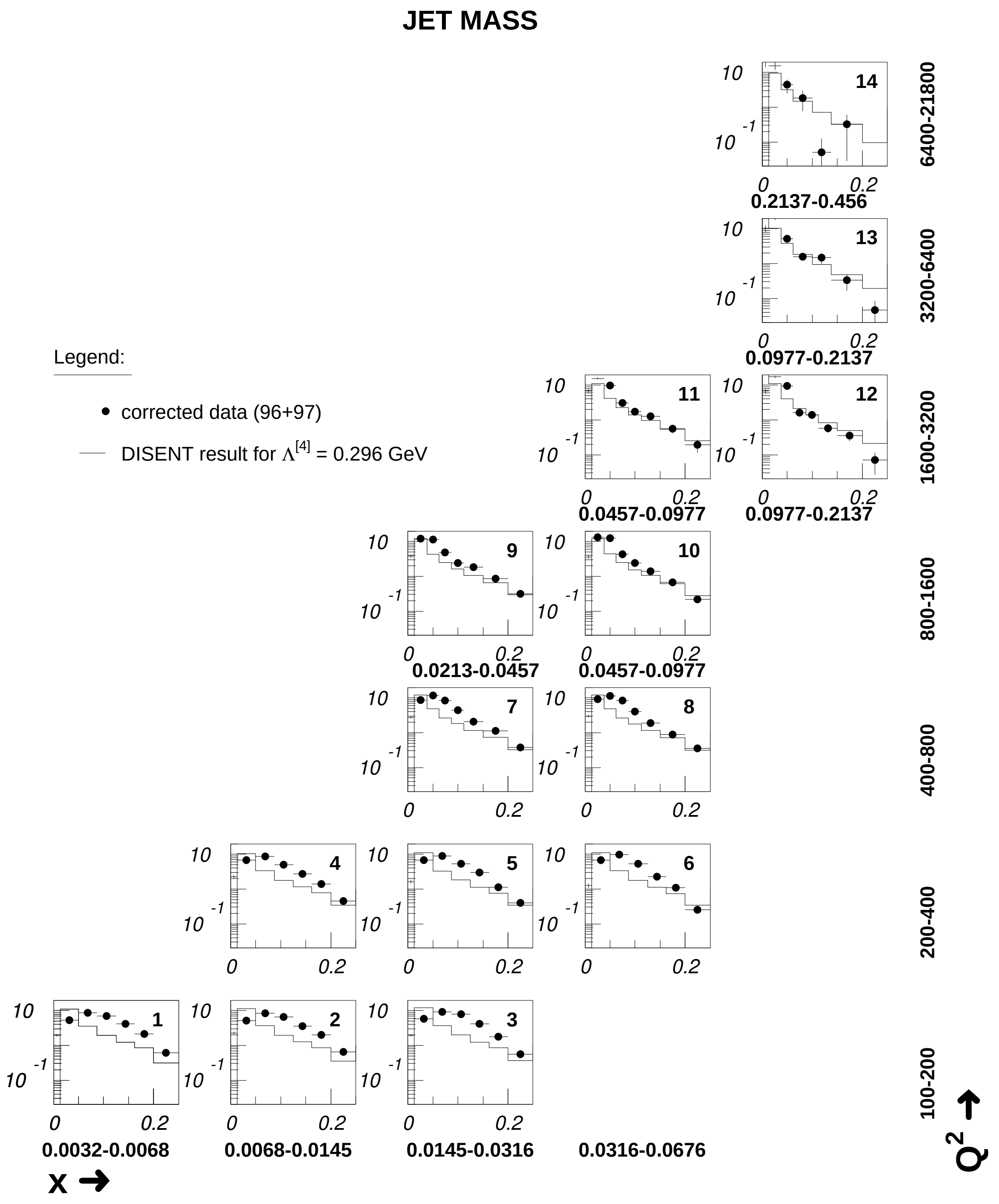

Figure C.7: *differential distribution Jet Mass. Data corrected to hadron level compared with results of NLO generation with DISENT.*

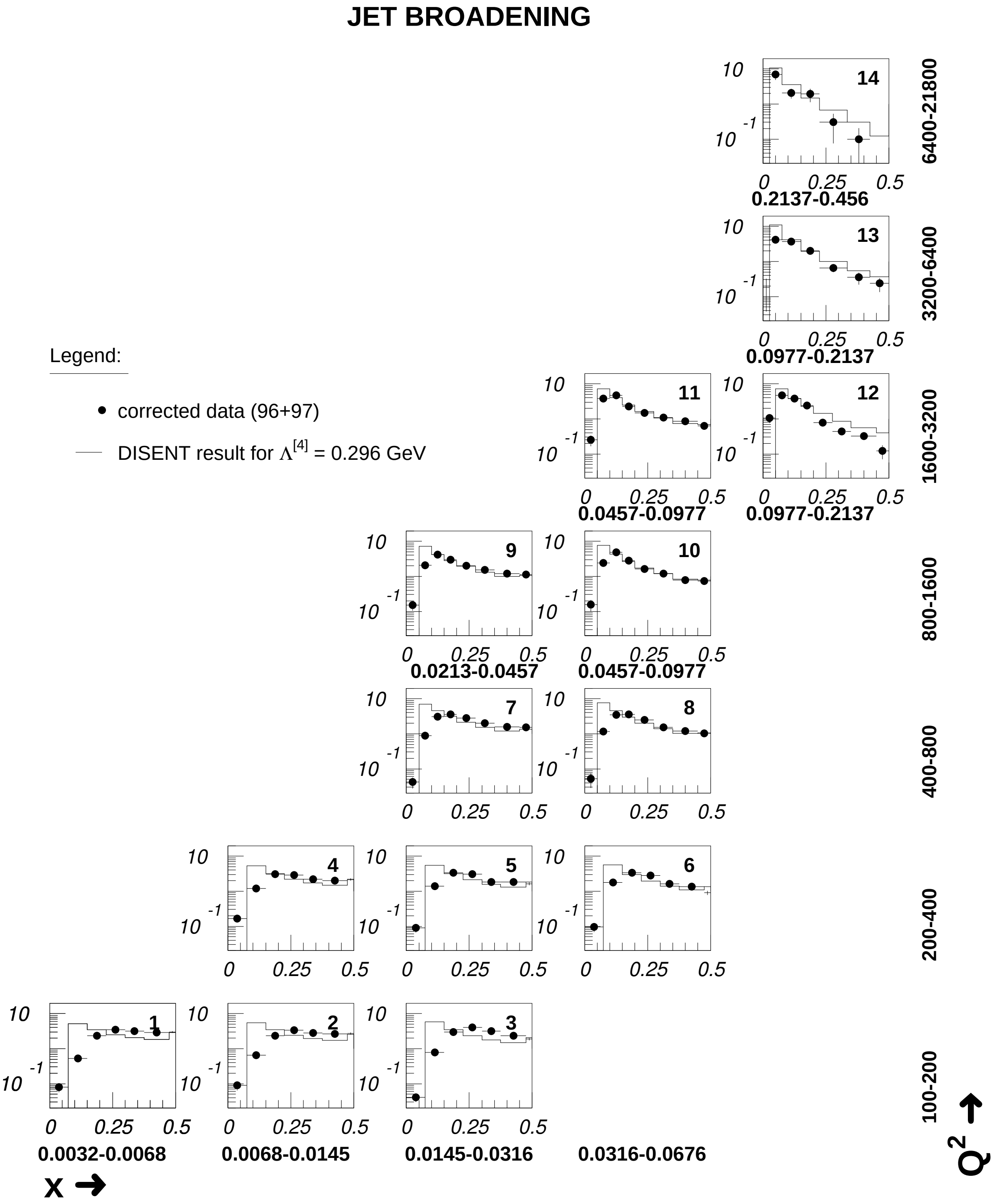

Figure C.8: *differential distribution Jet Broadening. Data corrected to hadron level compared with results of NLO generation with DISENT.*

bin	range	data	eff.	pur.	cor.fac.	corr. data
T_z 1	0.000 – 0.200	0.286±0.007	0.220	0.248	0.909±0.059	0.260±0.018
T_z 2	0.200 – 0.400	0.611±0.010	0.398	0.418	1.047±0.040	0.640±0.027
T_z 3	0.400 – 0.550	0.870±0.014	0.374	0.346	1.121±0.044	0.975±0.042
T_z 4	0.550 – 0.700	1.261±0.017	0.414	0.386	1.142±0.036	1.441±0.050
T_z 5	0.700 – 0.800	1.792±0.025	0.402	0.342	1.207±0.041	2.164±0.079
T_z 6	0.800 – 0.900	1.827±0.025	0.531	0.419	1.344±0.041	2.455±0.083
T_z 7	0.900 – 0.980	0.729±0.018	0.526	0.393	1.333±0.065	0.971±0.053
T_z 8	0.980 – 1.000	0.269±0.022	0.250	0.200	1.250±0.331	0.336±0.093
C_p 1	0.000 – 0.050	0.623±0.021	0.110	0.154	0.684±0.069	0.426±0.046
C_p 2	0.050 – 0.250	0.601±0.010	0.438	0.354	1.278±0.047	0.769±0.031
C_p 3	0.250 – 0.450	1.157±0.014	0.483	0.327	1.531±0.042	1.771±0.054
C_p 4	0.450 – 0.650	1.492±0.016	0.439	0.352	1.273±0.032	1.900±0.052
C_p 5	0.650 – 0.900	0.926±0.011	0.375	0.531	0.752±0.023	0.696±0.023
C_p 6	0.900 – 1.000	0.064±0.005	0.053	0.188	0.421±0.121	0.027±0.008
J_m 1	0.000 – 0.013	4.731±0.115	0.152	0.364	0.417±0.034	1.972±0.167
J_m 2	0.013 – 0.050	5.934±0.075	0.369	0.421	0.893±0.028	5.301±0.177
J_m 3	0.050 – 0.087	7.579±0.084	0.399	0.346	1.156±0.031	8.764±0.258
J_m 4	0.087 – 0.125	4.947±0.068	0.366	0.267	1.413±0.046	6.992±0.248
J_m 5	0.125 – 0.162	2.627±0.050	0.325	0.203	1.617±0.070	4.246±0.201
J_m 6	0.162 – 0.200	1.374±0.036	0.345	0.232	1.539±0.093	2.114±0.139
J_m 7	0.200 – 0.250	0.432±0.017	0.320	0.252	1.401±0.132	0.605±0.062
J_b 1	0.000 – 0.075	0.066±0.006	0.263	0.304	1.211±0.328	0.080±0.023
J_b 2	0.075 – 0.150	0.361±0.013	0.491	0.351	1.437±0.098	0.519±0.040
J_b 3	0.150 – 0.225	1.709±0.028	0.549	0.419	1.387±0.048	2.370±0.091
J_b 4	0.225 – 0.300	2.815±0.036	0.495	0.414	1.245±0.036	3.503±0.112
J_b 5	0.300 – 0.375	2.734±0.036	0.442	0.407	1.158±0.035	3.167±0.105
J_b 6	0.375 – 0.475	2.623±0.030	0.525	0.507	1.101±0.027	2.887±0.079
J_b 7	0.475 – 0.500	3.437±0.069	0.285	0.352	0.878±0.044	3.017±0.162

Table C.1: Results of differential event shape distributions in Analysis Bin 1

bin	range	data	eff.	pur.	cor.fac.	corr. data
T_z 1	0.000 – 0.200	0.342±0.008	0.185	0.303	0.697±0.048	0.238±0.017
T_z 2	0.200 – 0.400	0.553±0.010	0.456	0.426	1.033±0.042	0.572±0.026
T_z 3	0.400 – 0.550	0.850±0.014	0.377	0.364	1.035±0.043	0.880±0.039
T_z 4	0.550 – 0.700	1.271±0.017	0.414	0.396	0.971±0.033	1.234±0.045
T_z 5	0.700 – 0.800	1.817±0.025	0.435	0.365	1.187±0.039	2.157±0.078
T_z 6	0.800 – 0.900	1.882±0.026	0.559	0.416	1.338±0.041	2.518±0.085
T_z 7	0.900 – 0.980	0.772±0.018	0.597	0.459	1.371±0.060	1.058±0.053
T_z 8	0.980 – 1.000	0.183±0.018	0.480	0.279	1.720±0.348	0.316±0.071
C_p 1	0.000 – 0.050	0.711±0.022	0.102	0.185	0.634±0.067	0.451±0.049
C_p 2	0.050 – 0.250	0.550±0.010	0.493	0.350	1.369±0.053	0.753±0.032
C_p 3	0.250 – 0.450	1.162±0.014	0.521	0.342	1.526±0.044	1.773±0.055
C_p 4	0.450 – 0.650	1.492±0.016	0.460	0.376	1.194±0.031	1.782±0.050
C_p 5	0.650 – 0.900	0.987±0.012	0.431	0.609	0.656±0.020	0.648±0.021
C_p 6	0.900 – 1.000	0.066±0.005	0.068	0.125	0.364±0.103	0.024±0.007
J_m 1	0.000 – 0.013	4.373±0.111	0.201	0.377	0.524±0.042	2.293±0.193
J_m 2	0.013 – 0.050	5.849±0.074	0.402	0.445	0.886±0.029	5.182±0.179
J_m 3	0.050 – 0.087	7.494±0.084	0.418	0.374	1.123±0.031	8.418±0.252
J_m 4	0.087 – 0.125	5.126±0.069	0.394	0.285	1.298±0.042	6.655±0.231
J_m 5	0.125 – 0.162	2.761±0.051	0.334	0.251	1.320±0.057	3.645±0.170
J_m 6	0.162 – 0.200	1.466±0.037	0.353	0.248	1.353±0.084	1.983±0.134
J_m 7	0.200 – 0.250	0.519±0.019	0.316	0.268	1.246±0.113	0.647±0.063
J_b 1	0.000 – 0.075	0.042±0.004	0.412	0.139	2.118±0.561	0.089±0.025
J_b 2	0.075 – 0.150	0.420±0.014	0.608	0.399	1.545±0.091	0.649±0.044
J_b 3	0.150 – 0.225	1.772±0.029	0.572	0.433	1.333±0.045	2.363±0.088
J_b 4	0.225 – 0.300	2.854±0.036	0.521	0.432	1.174±0.034	3.350±0.107
J_b 5	0.300 – 0.375	2.771±0.036	0.433	0.397	1.017±0.033	2.819±0.099
J_b 6	0.375 – 0.475	2.561±0.030	0.601	0.560	1.039±0.026	2.661±0.075
J_b 7	0.475 – 0.500	3.474±0.070	0.292	0.377	0.797±0.044	2.769±0.163

Table C.2: Results of differential event shape distributions in Analysis Bin 2

bin	range	data	eff.	pur.	cor.fac.	corr. data
T_z 1	0.000 – 0.200	0.370±0.009	0.134	0.304	0.393±0.034	0.145±0.013
T_z 2	0.200 – 0.400	0.648±0.013	0.248	0.344	0.771±0.039	0.500±0.027
T_z 3	0.400 – 0.550	0.933±0.017	0.211	0.273	0.813±0.041	0.759±0.041
T_z 4	0.550 – 0.700	1.289±0.020	0.298	0.294	1.130±0.045	1.457±0.062
T_z 5	0.700 – 0.800	1.725±0.029	0.318	0.237	1.428±0.059	2.463±0.109
T_z 6	0.800 – 0.900	1.623±0.028	0.543	0.302	1.865±0.065	3.026±0.118
T_z 7	0.900 – 0.980	0.620±0.019	0.597	0.297	2.162±0.112	1.341±0.081
T_z 8	0.980 – 1.000	0.094±0.015	0.389	0.149	2.611±0.641	0.246±0.072
C_p 1	0.000 – 0.050	0.437±0.021	0.064	0.078	0.729±0.092	0.318±0.043
C_p 2	0.050 – 0.250	0.501±0.011	0.352	0.252	1.577±0.076	0.790±0.042
C_p 3	0.250 – 0.450	1.028±0.016	0.417	0.263	1.744±0.059	1.793±0.066
C_p 4	0.450 – 0.650	1.507±0.019	0.396	0.304	1.445±0.042	2.178±0.069
C_p 5	0.650 – 0.900	1.129±0.015	0.292	0.514	0.648±0.022	0.732±0.027
C_p 6	0.900 – 1.000	0.102±0.007	0.025	0.200	0.123±0.040	0.013±0.004
J_m 1	0.000 – 0.013	2.889±0.106	0.198	0.297	0.679±0.060	1.962±0.189
J_m 2	0.013 – 0.050	5.032±0.081	0.359	0.353	1.152±0.044	5.796±0.238
J_m 3	0.050 – 0.087	6.988±0.095	0.388	0.327	1.334±0.042	9.325±0.320
J_m 4	0.087 – 0.125	5.560±0.085	0.342	0.267	1.441±0.050	8.010±0.306
J_m 5	0.125 – 0.162	3.232±0.065	0.257	0.219	1.295±0.061	4.186±0.214
J_m 6	0.162 – 0.200	1.924±0.050	0.221	0.257	0.938±0.060	1.804±0.124
J_m 7	0.200 – 0.250	0.685±0.026	0.170	0.221	0.815±0.078	0.558±0.057
J_b 1	0.000 – 0.075	0.021±0.004	0.320	0.160	2.000±0.435	0.041±0.012
J_b 2	0.075 – 0.150	0.334±0.015	0.510	0.249	2.312±0.161	0.772±0.064
J_b 3	0.150 – 0.225	1.496±0.031	0.570	0.293	2.011±0.078	3.008±0.133
J_b 4	0.225 – 0.300	2.600±0.041	0.435	0.303	1.554±0.055	4.040±0.156
J_b 5	0.300 – 0.375	2.802±0.043	0.347	0.337	1.141±0.043	3.198±0.131
J_b 6	0.375 – 0.475	2.912±0.038	0.360	0.487	0.794±0.025	2.311±0.079
J_b 7	0.475 – 0.500	3.526±0.083	0.184	0.340	0.535±0.037	1.888±0.136

Table C.3: Results of differential event shape distributions in Analysis Bin 3

bin	range	data	eff.	pur.	cor.fac.	corr. data
T_z 1	0.000 – 0.200	0.283±0.010	0.281	0.391	0.719±0.068	0.203±0.021
T_z 2	0.200 – 0.400	0.501±0.014	0.493	0.503	0.882±0.052	0.442±0.029
T_z 3	0.400 – 0.550	0.706±0.019	0.384	0.387	0.877±0.058	0.619±0.044
T_z 4	0.550 – 0.700	1.072±0.023	0.405	0.423	0.908±0.046	0.974±0.054
T_z 5	0.700 – 0.800	1.677±0.036	0.446	0.410	1.022±0.048	1.713±0.088
T_z 6	0.800 – 0.900	2.376±0.042	0.600	0.485	1.145±0.041	2.720±0.108
T_z 7	0.900 – 0.980	1.389±0.036	0.679	0.469	1.377±0.063	1.912±0.101
T_z 8	0.980 – 1.000	0.455±0.041	0.500	0.424	1.179±0.223	0.537±0.113
C_p 1	0.000 – 0.050	0.644±0.031	0.133	0.200	0.612±0.092	0.394±0.063
C_p 2	0.050 – 0.250	0.730±0.017	0.519	0.395	1.250±0.056	0.913±0.046
C_p 3	0.250 – 0.450	1.420±0.023	0.527	0.374	1.287±0.045	1.828±0.071
C_p 4	0.450 – 0.650	1.392±0.023	0.470	0.410	1.069±0.038	1.488±0.059
C_p 5	0.650 – 0.900	0.784±0.015	0.389	0.616	0.545±0.027	0.427±0.023
C_p 6	0.900 – 1.000	0.059±0.007	0.231	0.500	0.462±0.188	0.027±0.011
J_m 1	0.000 – 0.013	4.937±0.172	0.163	0.374	0.460±0.050	2.273±0.257
J_m 2	0.013 – 0.050	7.897±0.126	0.487	0.521	0.854±0.030	6.741±0.261
J_m 3	0.050 – 0.087	7.624±0.124	0.491	0.388	1.143±0.040	8.715±0.338
J_m 4	0.087 – 0.125	3.944±0.089	0.434	0.305	1.263±0.060	4.980±0.260
J_m 5	0.125 – 0.162	2.186±0.066	0.361	0.248	1.262±0.091	2.758±0.216
J_m 6	0.162 – 0.200	1.262±0.050	0.286	0.231	1.114±0.114	1.407±0.154
J_m 7	0.200 – 0.250	0.498±0.027	0.394	0.388	0.904±0.110	0.451±0.060
J_b 1	0.000 – 0.075	0.112±0.011	0.536	0.366	1.464±0.270	0.165±0.034
J_b 2	0.075 – 0.150	0.809±0.028	0.652	0.427	1.470±0.086	1.189±0.081
J_b 3	0.150 – 0.225	2.627±0.051	0.602	0.487	1.167±0.044	3.066±0.131
J_b 4	0.225 – 0.300	2.783±0.053	0.499	0.446	1.040±0.043	2.895±0.133
J_b 5	0.300 – 0.375	2.363±0.049	0.479	0.467	0.946±0.044	2.236±0.113
J_b 6	0.375 – 0.475	2.164±0.040	0.606	0.592	0.930±0.036	2.012±0.086
J_b 7	0.475 – 0.500	3.224±0.099	0.350	0.460	0.673±0.050	2.171±0.174

Table C.4: Results of differential event shape distributions in Analysis Bin 4

bin	range	data	eff.	pur.	cor.fac.	corr. data
T_z 1	0.000 – 0.200	0.279±0.011	0.185	0.356	0.412±0.047	0.115±0.014
T_z 2	0.200 – 0.400	0.465±0.014	0.434	0.458	0.823±0.056	0.383±0.028
T_z 3	0.400 – 0.550	0.730±0.020	0.371	0.443	0.800±0.051	0.584±0.041
T_z 4	0.550 – 0.700	1.135±0.024	0.394	0.407	0.828±0.045	0.939±0.055
T_z 5	0.700 – 0.800	1.747±0.037	0.382	0.403	0.933±0.048	1.631±0.091
T_z 6	0.800 – 0.900	2.351±0.043	0.558	0.416	1.274±0.048	2.995±0.127
T_z 7	0.900 – 0.980	1.394±0.037	0.748	0.423	1.673±0.078	2.332±0.125
T_z 8	0.980 – 1.000	0.198±0.028	0.278	0.200	1.389±0.376	0.275±0.084
C_p 1	0.000 – 0.050	0.491±0.028	0.133	0.310	0.429±0.071	0.211±0.037
C_p 2	0.050 – 0.250	0.630±0.016	0.579	0.353	1.464±0.074	0.923±0.052
C_p 3	0.250 – 0.450	1.332±0.023	0.560	0.357	1.411±0.052	1.878±0.077
C_p 4	0.450 – 0.650	1.488±0.024	0.455	0.404	0.992±0.037	1.477±0.060
C_p 5	0.650 – 0.900	0.912±0.017	0.346	0.622	0.520±0.026	0.474±0.026
C_p 6	0.900 – 1.000	0.090±0.008	0.062	0.500	0.125±0.062	0.011±0.006
J_m 1	0.000 – 0.013	3.786±0.155	0.209	0.423	0.436±0.054	1.649±0.215
J_m 2	0.013 – 0.050	7.121±0.123	0.517	0.497	0.971±0.037	6.911±0.287
J_m 3	0.050 – 0.087	7.702±0.128	0.490	0.392	1.150±0.041	8.857±0.350
J_m 4	0.087 – 0.125	4.593±0.099	0.404	0.343	1.167±0.056	5.360±0.283
J_m 5	0.125 – 0.162	2.555±0.073	0.353	0.249	1.179±0.088	3.012±0.240
J_m 6	0.162 – 0.200	1.461±0.056	0.320	0.363	0.773±0.069	1.130±0.109
J_m 7	0.200 – 0.250	0.545±0.029	0.287	0.353	0.723±0.100	0.395±0.059
J_b 1	0.000 – 0.075	0.066±0.008	0.375	0.273	1.375±0.305	0.090±0.023
J_b 2	0.075 – 0.150	0.806±0.029	0.754	0.399	1.758±0.097	1.417±0.093
J_b 3	0.150 – 0.225	2.535±0.052	0.595	0.408	1.348±0.055	3.417±0.157
J_b 4	0.225 – 0.300	2.974±0.056	0.462	0.435	1.026±0.046	3.053±0.148
J_b 5	0.300 – 0.375	2.429±0.051	0.362	0.424	0.755±0.041	1.834±0.107
J_b 6	0.375 – 0.475	2.224±0.042	0.574	0.614	0.839±0.033	1.866±0.082
J_b 7	0.475 – 0.500	2.822±0.095	0.250	0.384	0.579±0.052	1.635±0.158

Table C.5: Results of differential event shape distributions in Analysis Bin 5

bin	range	data	eff.	pur.	cor.fac.	corr. data
T_z 1	0.000 – 0.200	0.361±0.014	0.051	0.273	0.206±0.033	0.074±0.012
T_z 2	0.200 – 0.400	0.660±0.018	0.186	0.449	0.436±0.041	0.288±0.028
T_z 3	0.400 – 0.550	0.909±0.025	0.130	0.267	0.502±0.049	0.456±0.046
T_z 4	0.550 – 0.700	1.171±0.028	0.183	0.339	0.625±0.046	0.732±0.056
T_z 5	0.700 – 0.800	1.623±0.041	0.232	0.245	0.880±0.059	1.428±0.102
T_z 6	0.800 – 0.900	1.831±0.043	0.498	0.287	1.780±0.085	3.259±0.174
T_z 7	0.900 – 0.980	0.855±0.033	0.713	0.255	2.758±0.173	2.359±0.174
T_z 8	0.980 – 1.000	0.152±0.028	0.333	0.148	2.250±0.696	0.342±0.123
C_p 1	0.000 – 0.050	0.347±0.027	0.036	0.074	0.491±0.113	0.170±0.041
C_p 2	0.050 – 0.250	0.602±0.017	0.353	0.277	1.411±0.085	0.849±0.057
C_p 3	0.250 – 0.450	1.193±0.025	0.391	0.253	1.696±0.079	2.023±0.103
C_p 4	0.450 – 0.650	1.413±0.027	0.312	0.344	1.008±0.047	1.424±0.071
C_p 5	0.650 – 0.900	1.030±0.020	0.221	0.560	0.416±0.027	0.428±0.029
C_p 6	0.900 – 1.000	0.145±0.012	0.023	1.000	0.023±0.022	0.003±0.003
J_m 1	0.000 – 0.013	2.838±0.152	0.176	0.434	0.445±0.065	1.264±0.196
J_m 2	0.013 – 0.050	5.547±0.122	0.403	0.370	1.231±0.059	6.826±0.360
J_m 3	0.050 – 0.087	6.958±0.137	0.417	0.309	1.432±0.063	9.966±0.481
J_m 4	0.087 – 0.125	5.212±0.119	0.282	0.276	1.029±0.060	5.364±0.333
J_m 5	0.125 – 0.162	3.206±0.093	0.173	0.294	0.719±0.062	2.306±0.209
J_m 6	0.162 – 0.200	2.063±0.075	0.168	0.383	0.525±0.060	1.083±0.129
J_m 7	0.200 – 0.250	0.708±0.038	0.163	0.378	0.356±0.061	0.252±0.045
J_b 1	0.000 – 0.075	0.064±0.009	0.217	0.143	1.522±0.372	0.097±0.027
J_b 2	0.075 – 0.150	0.551±0.027	0.629	0.198	3.212±0.253	1.771±0.165
J_b 3	0.150 – 0.225	1.711±0.048	0.522	0.271	1.997±0.104	3.418±0.203
J_b 4	0.225 – 0.300	2.494±0.058	0.313	0.262	1.126±0.067	2.809±0.180
J_b 5	0.300 – 0.375	2.540±0.059	0.230	0.383	0.645±0.044	1.638±0.117
J_b 6	0.375 – 0.475	2.981±0.055	0.223	0.554	0.456±0.028	1.360±0.088
J_b 7	0.475 – 0.500	3.325±0.116	0.089	0.324	0.274±0.035	0.911±0.119

Table C.6: Results of differential event shape distributions in Analysis Bin 6

bin	range	data	eff.	pur.	cor.fac.	corr. data
T_z 1	0.000 – 0.350	0.282±0.012	0.391	0.575	0.705±0.029	0.199±0.012
T_z 2	0.350 – 0.600	0.566±0.020	0.484	0.574	0.862±0.029	0.488±0.024
T_z 3	0.600 – 0.750	1.055±0.035	0.407	0.457	0.899±0.032	0.948±0.046
T_z 4	0.750 – 0.850	2.060±0.060	0.470	0.466	0.995±0.029	2.050±0.084
T_z 5	0.850 – 0.925	3.198±0.086	0.580	0.496	1.154±0.026	3.692±0.129
T_z 6	0.925 – 0.980	2.023±0.080	0.698	0.490	1.424±0.038	2.880±0.138
T_z 7	0.980 – 1.000	0.417±0.060	0.490	0.338	1.510±0.154	0.630±0.111
C_p 1	0.000 – 0.050	0.605±0.046	0.112	0.226	0.496±0.051	0.300±0.038
C_p 2	0.050 – 0.200	0.811±0.031	0.575	0.416	1.388±0.042	1.126±0.054
C_p 3	0.200 – 0.350	1.552±0.042	0.545	0.400	1.320±0.031	2.049±0.074
C_p 4	0.350 – 0.550	1.491±0.036	0.481	0.442	1.034±0.023	1.542±0.051
C_p 5	0.550 – 0.750	0.990±0.029	0.349	0.454	0.765±0.026	0.757±0.034
C_p 6	0.750 – 0.900	0.509±0.024	0.230	0.561	0.433±0.030	0.220±0.019
C_p 7	0.900 – 1.000	0.066±0.011	0.054	0.250	0.216±0.080	0.014±0.006
J_m 1	0.000 – 0.013	5.201±0.269	0.237	0.454	0.530±0.032	2.754±0.218
J_m 2	0.013 – 0.038	9.588±0.258	0.476	0.507	0.901±0.022	8.641±0.316
J_m 3	0.038 – 0.062	9.811±0.261	0.450	0.371	1.188±0.030	11.657±0.426
J_m 4	0.062 – 0.087	6.390±0.211	0.391	0.283	1.324±0.044	8.462±0.396
J_m 5	0.087 – 0.112	3.629±0.159	0.305	0.240	1.233±0.059	4.474±0.290
J_m 6	0.112 – 0.150	2.253±0.102	0.287	0.302	0.926±0.049	2.085±0.146
J_m 7	0.150 – 0.200	1.165±0.064	0.407	0.431	0.969±0.055	1.128±0.089
J_m 8	0.200 – 0.250	0.414±0.038	0.380	0.416	0.913±0.073	0.378±0.046
J_b 1	0.000 – 0.050	0.035±0.011	0.429	0.373	1.214±0.198	0.042±0.015
J_b 2	0.050 – 0.100	0.601±0.046	0.573	0.401	1.468±0.071	0.883±0.080
J_b 3	0.100 – 0.150	2.117±0.086	0.586	0.401	1.474±0.044	3.120±0.157
J_b 4	0.150 – 0.200	3.240±0.106	0.470	0.430	1.110±0.032	3.595±0.158
J_b 5	0.200 – 0.275	2.994±0.083	0.466	0.489	0.930±0.026	2.786±0.111
J_b 6	0.275 – 0.350	2.186±0.071	0.440	0.472	0.932±0.033	2.038±0.098
J_b 7	0.350 – 0.450	1.700±0.054	0.559	0.613	0.921±0.027	1.566±0.068
J_b 8	0.450 – 0.500	2.114±0.086	0.423	0.596	0.719±0.028	1.519±0.085

Table C.7: Results of differential event shape distributions in Analysis Bin 7

bin	range	data	eff.	pur.	cor.fac.	corr. data
T_z 1	0.000 – 0.350	0.336±0.014	0.235	0.586	0.416±0.025	0.140±0.010
T_z 2	0.350 – 0.600	0.638±0.023	0.307	0.550	0.581±0.026	0.371±0.021
T_z 3	0.600 – 0.750	1.191±0.041	0.253	0.441	0.616±0.027	0.734±0.040
T_z 4	0.750 – 0.850	2.148±0.067	0.274	0.387	0.790±0.028	1.696±0.080
T_z 5	0.850 – 0.925	2.638±0.085	0.485	0.362	1.471±0.040	3.881±0.164
T_z 6	0.925 – 0.980	1.522±0.076	0.682	0.318	2.282±0.078	3.474±0.210
T_z 7	0.980 – 1.000	0.155±0.040	0.562	0.196	3.109±0.381	0.482±0.138
C_p 1	0.000 – 0.050	0.533±0.047	0.155	0.236	0.746±0.087	0.398±0.058
C_p 2	0.050 – 0.200	0.622±0.029	0.495	0.310	1.730±0.066	1.075±0.065
C_p 3	0.200 – 0.350	1.276±0.042	0.430	0.290	1.670±0.050	2.131±0.095
C_p 4	0.350 – 0.550	1.464±0.039	0.357	0.393	1.053±0.028	1.542±0.058
C_p 5	0.550 – 0.750	1.200±0.035	0.226	0.432	0.563±0.021	0.675±0.032
C_p 6	0.750 – 0.900	0.677±0.031	0.140	0.574	0.247±0.022	0.167±0.016
C_p 7	0.900 – 1.000	0.095±0.014	0.021	0.167	0.125±0.053	0.012±0.005
J_m 1	0.000 – 0.013	3.754±0.249	0.296	0.393	0.801±0.056	3.006±0.289
J_m 2	0.013 – 0.038	7.211±0.244	0.488	0.426	1.276±0.037	9.198±0.411
J_m 3	0.038 – 0.062	9.080±0.274	0.424	0.371	1.257±0.035	11.418±0.469
J_m 4	0.062 – 0.087	6.946±0.240	0.316	0.288	1.201±0.043	8.340±0.412
J_m 5	0.087 – 0.112	4.490±0.193	0.221	0.267	0.911±0.045	4.089±0.266
J_m 6	0.112 – 0.150	2.889±0.126	0.200	0.343	0.648±0.037	1.872±0.135
J_m 7	0.150 – 0.200	1.563±0.080	0.229	0.414	0.570±0.037	0.890±0.074
J_m 8	0.200 – 0.250	0.571±0.049	0.180	0.320	0.629±0.064	0.359±0.048
J_b 1	0.000 – 0.050	0.025±0.010	0.323	0.141	2.065±0.407	0.051±0.023
J_b 2	0.050 – 0.100	0.459±0.044	0.549	0.225	2.545±0.147	1.168±0.130
J_b 3	0.100 – 0.150	1.617±0.082	0.534	0.266	2.139±0.079	3.458±0.216
J_b 4	0.150 – 0.200	2.626±0.104	0.380	0.296	1.383±0.048	3.632±0.192
J_b 5	0.200 – 0.275	2.925±0.090	0.319	0.416	0.856±0.029	2.504±0.114
J_b 6	0.275 – 0.350	2.437±0.082	0.261	0.442	0.622±0.027	1.515±0.084
J_b 7	0.350 – 0.450	1.983±0.064	0.335	0.597	0.598±0.024	1.185±0.060
J_b 8	0.450 – 0.500	2.369±0.099	0.250	0.619	0.439±0.025	1.041±0.074

Table C.8: Results of differential event shape distributions in Analysis Bin 8

bin	range	data	eff.	pur.	cor.fac.	corr. data
T_z 1	0.000 – 0.350	0.244±0.018	0.359	0.618	0.551±0.043	0.135±0.014
T_z 2	0.350 – 0.600	0.477±0.029	0.496	0.575	0.774±0.047	0.369±0.032
T_z 3	0.600 – 0.750	0.915±0.052	0.500	0.497	0.891±0.050	0.816±0.065
T_z 4	0.750 – 0.850	1.562±0.084	0.427	0.500	0.780±0.040	1.219±0.090
T_z 5	0.850 – 0.925	3.372±0.142	0.559	0.516	0.990±0.035	3.340±0.184
T_z 6	0.925 – 0.980	3.789±0.176	0.726	0.526	1.323±0.042	5.014±0.282
T_z 7	0.980 – 1.000	1.080±0.156	0.480	0.448	1.050±0.109	1.134±0.202
C_p 1	0.000 – 0.050	0.801±0.085	0.146	0.302	0.438±0.060	0.350±0.061
C_p 2	0.050 – 0.200	1.149±0.059	0.638	0.447	1.341±0.051	1.541±0.098
C_p 3	0.200 – 0.350	1.875±0.075	0.572	0.448	1.169±0.039	2.193±0.114
C_p 4	0.350 – 0.550	1.310±0.054	0.451	0.479	0.831±0.033	1.088±0.062
C_p 5	0.550 – 0.750	0.722±0.040	0.398	0.540	0.649±0.038	0.469±0.038
C_p 6	0.750 – 0.900	0.483±0.038	0.343	0.636	0.464±0.050	0.224±0.030
C_p 7	0.900 – 1.000	0.086±0.020	0.053	0.250	0.211±0.111	0.018±0.010
J_m 1	0.000 – 0.013	7.741±0.528	0.265	0.491	0.491±0.039	3.800±0.398
J_m 2	0.013 – 0.038	12.493±0.474	0.537	0.527	0.966±0.030	12.070±0.595
J_m 3	0.038 – 0.062	9.379±0.411	0.489	0.362	1.209±0.047	11.339±0.663
J_m 4	0.062 – 0.087	4.752±0.292	0.364	0.333	1.035±0.058	4.920±0.410
J_m 5	0.087 – 0.112	2.664±0.219	0.295	0.275	0.913±0.085	2.431±0.302
J_m 6	0.112 – 0.150	1.944±0.153	0.422	0.391	0.939±0.081	1.825±0.213
J_m 7	0.150 – 0.200	1.143±0.101	0.408	0.475	0.752±0.072	0.859±0.112
J_m 8	0.200 – 0.250	0.441±0.063	0.266	0.267	0.703±0.121	0.310±0.069
J_b 1	0.000 – 0.050	0.153±0.037	0.341	0.350	0.976±0.175	0.149±0.045
J_b 2	0.050 – 0.100	1.431±0.113	0.692	0.466	1.448±0.068	2.073±0.191
J_b 3	0.100 – 0.150	3.546±0.179	0.605	0.473	1.180±0.044	4.185±0.263
J_b 4	0.150 – 0.200	3.393±0.175	0.423	0.423	0.880±0.044	2.987±0.215
J_b 5	0.200 – 0.275	2.388±0.120	0.534	0.580	0.843±0.039	2.013±0.137
J_b 6	0.275 – 0.350	1.800±0.104	0.508	0.551	0.841±0.047	1.514±0.122
J_b 7	0.350 – 0.450	1.467±0.081	0.561	0.619	0.825±0.043	1.211±0.092
J_b 8	0.450 – 0.500	1.881±0.130	0.378	0.605	0.592±0.044	1.114±0.112

Table C.9: Results of differential event shape distributions in Analysis Bin 9

bin	range	data	eff.	pur.	cor.fac.	corr. data
T_z 1	0.000 – 0.350	0.228±0.018	0.293	0.625	0.384±0.040	0.087±0.011
T_z 2	0.350 – 0.600	0.510±0.031	0.276	0.522	0.544±0.048	0.277±0.030
T_z 3	0.600 – 0.750	1.078±0.059	0.251	0.537	0.492±0.037	0.530±0.049
T_z 4	0.750 – 0.850	1.988±0.098	0.239	0.422	0.548±0.034	1.090±0.086
T_z 5	0.850 – 0.925	3.398±0.148	0.436	0.437	1.008±0.040	3.424±0.201
T_z 6	0.925 – 0.980	2.720±0.154	0.776	0.393	2.042±0.074	5.556±0.374
T_z 7	0.980 – 1.000	0.410±0.099	0.616	0.289	2.082±0.235	0.854±0.228
C_p 1	0.000 – 0.050	0.541±0.072	0.244	0.228	1.013±0.142	0.547±0.106
C_p 2	0.050 – 0.200	0.840±0.052	0.632	0.353	1.875±0.083	1.575±0.120
C_p 3	0.200 – 0.350	1.580±0.071	0.486	0.359	1.410±0.054	2.228±0.132
C_p 4	0.350 – 0.550	1.523±0.061	0.283	0.432	0.667±0.030	1.016±0.061
C_p 5	0.550 – 0.750	1.021±0.050	0.195	0.440	0.474±0.032	0.484±0.040
C_p 6	0.750 – 0.900	0.492±0.040	0.158	0.564	0.301±0.041	0.148±0.024
C_p 7	0.900 – 1.000	0.077±0.019	0.000	0.000	0.083±0.087	0.006±0.007
J_m 1	0.000 – 0.013	4.170±0.401	0.348	0.427	0.873±0.072	3.638±0.462
J_m 2	0.013 – 0.038	10.116±0.442	0.606	0.476	1.325±0.045	13.403±0.739
J_m 3	0.038 – 0.062	9.865±0.436	0.464	0.367	1.262±0.051	12.451±0.743
J_m 4	0.062 – 0.087	5.270±0.319	0.245	0.308	0.818±0.051	4.312±0.376
J_m 5	0.087 – 0.112	4.537±0.296	0.179	0.338	0.529±0.049	2.398±0.273
J_m 6	0.112 – 0.150	2.548±0.181	0.187	0.391	0.557±0.054	1.418±0.172
J_m 7	0.150 – 0.200	1.284±0.111	0.171	0.351	0.527±0.067	0.677±0.104
J_m 8	0.200 – 0.250	0.473±0.068	0.288	0.618	0.466±0.077	0.220±0.048
J_b 1	0.000 – 0.050	0.097±0.031	0.289	0.197	1.605±0.293	0.155±0.057
J_b 2	0.050 – 0.100	1.033±0.100	0.690	0.306	2.345±0.128	2.422±0.269
J_b 3	0.100 – 0.150	2.857±0.166	0.546	0.332	1.693±0.072	4.838±0.349
J_b 4	0.150 – 0.200	3.494±0.184	0.261	0.312	0.799±0.046	2.793±0.217
J_b 5	0.200 – 0.275	2.825±0.135	0.278	0.473	0.576±0.033	1.628±0.122
J_b 6	0.275 – 0.350	2.104±0.116	0.271	0.535	0.568±0.043	1.196±0.112
J_b 7	0.350 – 0.450	1.520±0.086	0.325	0.602	0.514±0.040	0.781±0.075
J_b 8	0.450 – 0.500	1.689±0.128	0.328	0.637	0.434±0.042	0.733±0.090

Table C.10: Results of differential event shape distributions in Analysis Bin 10

bin	range	data	eff.	pur.	cor.fac.	corr. data
T_z 1	0.000 – 0.350	0.178±0.024	0.217	0.483	0.483±0.092	0.086±0.020
T_z 2	0.350 – 0.600	0.358±0.040	0.455	0.615	0.591±0.079	0.211±0.037
T_z 3	0.600 – 0.750	0.793±0.077	0.387	0.412	0.731±0.095	0.580±0.094
T_z 4	0.750 – 0.850	1.552±0.133	0.302	0.455	0.553±0.062	0.859±0.120
T_z 5	0.850 – 0.925	3.443±0.228	0.480	0.535	0.835±0.050	2.874±0.257
T_z 6	0.925 – 0.980	5.004±0.321	0.770	0.544	1.345±0.053	6.727±0.506
T_z 7	0.980 – 1.000	1.302±0.272	0.592	0.373	1.447±0.163	1.885±0.447
C_p 1	0.000 – 0.050	0.498±0.106	0.320	0.340	0.940±0.156	0.468±0.127
C_p 2	0.050 – 0.200	1.661±0.112	0.728	0.473	1.430±0.067	2.375±0.195
C_p 3	0.200 – 0.350	1.774±0.116	0.504	0.427	1.142±0.062	2.027±0.172
C_p 4	0.350 – 0.550	1.189±0.082	0.329	0.531	0.495±0.041	0.588±0.064
C_p 5	0.550 – 0.750	0.730±0.064	0.359	0.494	0.618±0.069	0.452±0.064
C_p 6	0.750 – 0.900	0.370±0.053	0.280	0.478	0.460±0.099	0.170±0.044
C_p 7	0.900 – 1.000	0.057±0.025	0.000	0.000	0.111±0.117	0.006±0.007
J_m 1	0.000 – 0.013	7.792±0.840	0.487	0.511	0.867±0.074	6.756±0.931
J_m 2	0.013 – 0.038	13.952±0.795	0.663	0.551	1.124±0.045	15.676±1.091
J_m 3	0.038 – 0.062	8.607±0.624	0.496	0.403	1.158±0.074	9.968±0.964
J_m 4	0.062 – 0.087	4.439±0.448	0.360	0.421	0.685±0.083	3.040±0.479
J_m 5	0.087 – 0.112	3.488±0.398	0.211	0.343	0.493±0.091	1.719±0.372
J_m 6	0.112 – 0.150	1.570±0.218	0.529	0.500	0.824±0.127	1.293±0.268
J_m 7	0.150 – 0.200	0.883±0.141	0.275	0.406	0.627±0.119	0.554±0.138
J_m 8	0.200 – 0.250	0.453±0.101	0.154	0.364	0.423±0.139	0.192±0.076
J_b 1	0.000 – 0.050	0.227±0.072	0.527	0.459	1.109±0.151	0.251±0.086
J_b 2	0.050 – 0.100	2.446±0.235	0.767	0.455	1.584±0.084	3.875±0.426
J_b 3	0.100 – 0.150	4.394±0.315	0.527	0.467	1.078±0.064	4.738±0.442
J_b 4	0.150 – 0.200	3.171±0.268	0.330	0.428	0.714±0.064	2.265±0.278
J_b 5	0.200 – 0.275	2.310±0.187	0.383	0.539	0.639±0.059	1.476±0.181
J_b 6	0.275 – 0.350	1.586±0.155	0.371	0.419	0.697±0.095	1.105±0.185
J_b 7	0.350 – 0.450	1.144±0.114	0.500	0.575	0.745±0.086	0.852±0.130
J_b 8	0.450 – 0.500	1.336±0.174	0.261	0.515	0.478±0.085	0.639±0.141

Table C.11: Results of differential event shape distributions in Analysis Bin 11

bin	range	data	eff.	pur.	cor.fac.	corr. data
T_z 1	0.000 – 0.350	0.213±0.028	0.041	0.500	0.081±0.034	0.017±0.008
T_z 2	0.350 – 0.600	0.351±0.043	0.194	0.708	0.333±0.067	0.117±0.028
T_z 3	0.600 – 0.750	0.891±0.088	0.106	0.543	0.232±0.040	0.207±0.041
T_z 4	0.750 – 0.850	1.900±0.158	0.097	0.323	0.314±0.041	0.597±0.093
T_z 5	0.850 – 0.925	3.180±0.236	0.212	0.326	0.663±0.056	2.108±0.238
T_z 6	0.925 – 0.980	4.075±0.312	0.687	0.370	1.873±0.095	7.632±0.701
T_z 7	0.980 – 1.000	1.573±0.321	0.660	0.213	3.100±0.421	4.875±1.195
C_p 1	0.000 – 0.050	0.419±0.105	0.244	0.182	1.341±0.246	0.563±0.175
C_p 2	0.050 – 0.200	1.389±0.110	0.607	0.311	1.870±0.110	2.598±0.256
C_p 3	0.200 – 0.350	1.713±0.122	0.313	0.292	1.081±0.072	1.852±0.181
C_p 4	0.350 – 0.550	1.232±0.090	0.097	0.381	0.313±0.034	0.385±0.050
C_p 5	0.550 – 0.750	0.904±0.077	0.141	0.377	0.374±0.050	0.338±0.054
C_p 6	0.750 – 0.900	0.411±0.060	0.102	0.500	0.286±0.081	0.117±0.037
C_p 7	0.900 – 1.000	0.052±0.026	0.000	0.000	1.000±1.414	0.052±0.079
J_m 1	0.000 – 0.013	6.186±0.805	0.404	0.367	1.103±0.104	6.823±1.097
J_m 2	0.013 – 0.038	11.848±0.788	0.584	0.408	1.466±0.073	17.375±1.443
J_m 3	0.038 – 0.062	8.440±0.665	0.340	0.337	1.130±0.088	9.540±1.058
J_m 4	0.062 – 0.087	5.400±0.532	0.056	0.233	0.301±0.050	1.624±0.314
J_m 5	0.087 – 0.112	4.142±0.466	0.099	0.378	0.333±0.058	1.381±0.287
J_m 6	0.112 – 0.150	1.887±0.257	0.093	0.308	0.302±0.063	0.571±0.142
J_m 7	0.150 – 0.200	1.101±0.170	0.100	0.312	0.320±0.085	0.352±0.108
J_m 8	0.200 – 0.250	0.629±0.128	0.037	0.667	0.111±0.065	0.070±0.044
J_b 1	0.000 – 0.050	0.419±0.105	0.486	0.189	2.568±0.429	1.077±0.324
J_b 2	0.050 – 0.100	1.835±0.219	0.678	0.251	2.588±0.183	4.748±0.660
J_b 3	0.100 – 0.150	3.303±0.294	0.329	0.302	1.147±0.086	3.789±0.442
J_b 4	0.150 – 0.200	3.748±0.313	0.163	0.276	0.652±0.070	2.443±0.333
J_b 5	0.200 – 0.275	2.656±0.215	0.099	0.373	0.292±0.040	0.776±0.123
J_b 6	0.275 – 0.350	1.608±0.168	0.122	0.421	0.273±0.045	0.440±0.086
J_b 7	0.350 – 0.450	1.166±0.124	0.170	0.679	0.280±0.052	0.327±0.070
J_b 8	0.450 – 0.500	1.573±0.203	0.052	0.500	0.078±0.032	0.123±0.053

Table C.12: Results of differential event shape distributions in Analysis Bin 12

bin	range	data	eff.	pur.	cor.fac.	corr. data
T_z 1	0.000 – 0.350	0.120±0.033	0.050	0.000	0.200±0.110	0.024±0.015
T_z 2	0.350 – 0.600	0.245±0.056	0.348	0.600	0.435±0.131	0.107±0.040
T_z 3	0.600 – 0.750	0.860±0.136	0.320	0.583	0.480±0.133	0.413±0.132
T_z 4	0.750 – 0.850	1.032±0.182	0.196	0.562	0.286±0.070	0.295±0.089
T_z 5	0.850 – 0.925	3.312±0.377	0.320	0.474	0.553±0.074	1.833±0.323
T_z 6	0.925 – 0.980	6.276±0.607	0.754	0.543	1.308±0.073	8.209±0.916
T_z 7	0.980 – 1.000	1.129±0.427	0.732	0.284	2.659±0.377	3.002±1.212
C_p 1	0.000 – 0.050	0.387±0.158	0.458	0.262	1.750±0.366	0.677±0.311
C_p 2	0.050 – 0.150	1.677±0.233	0.712	0.376	1.964±0.165	3.294±0.534
C_p 3	0.150 – 0.250	2.065±0.258	0.380	0.351	1.039±0.104	2.145±0.343
C_p 4	0.250 – 0.400	1.548±0.182	0.189	0.370	0.509±0.074	0.789±0.147
C_p 5	0.400 – 0.600	0.919±0.122	0.250	0.436	0.574±0.096	0.527±0.113
C_p 6	0.600 – 0.850	0.490±0.080	0.250	0.929	0.269±0.063	0.132±0.038
C_p 7	0.850 – 1.000	0.129±0.053	0.000	-1.000	0.000±0.000	0.000±0.000
J_m 1	0.000 – 0.013	8.516±1.482	0.543	0.469	1.210±0.130	10.303±2.106
J_m 2	0.013 – 0.038	14.968±1.390	0.762	0.550	1.345±0.073	20.136±2.168
J_m 3	0.038 – 0.062	7.613±0.991	0.390	0.434	0.688±0.099	5.240±1.015
J_m 4	0.062 – 0.100	3.097±0.516	0.351	0.586	0.509±0.090	1.576±0.383
J_m 5	0.100 – 0.138	2.409±0.455	0.381	0.462	0.619±0.176	1.491±0.508
J_m 6	0.138 – 0.200	0.877±0.213	0.125	0.333	0.375±0.162	0.329±0.163
J_m 7	0.200 – 0.250	0.387±0.158	0.000	0.500	0.118±0.088	0.046±0.039
J_b 1	0.000 – 0.025	0.258±0.182	0.400	0.571	0.700±0.251	0.181±0.143
J_b 2	0.025 – 0.075	1.935±0.353	0.838	0.396	2.162±0.175	4.184±0.836
J_b 3	0.075 – 0.150	4.043±0.417	0.484	0.491	0.920±0.071	3.720±0.479
J_b 4	0.150 – 0.225	3.011±0.360	0.312	0.396	0.663±0.097	1.995±0.377
J_b 5	0.225 – 0.335	1.584±0.215	0.259	0.583	0.414±0.082	0.655±0.157
J_b 6	0.335 – 0.425	1.004±0.190	0.261	0.750	0.348±0.112	0.349±0.130
J_b 7	0.425 – 0.500	0.731±0.177	0.107	0.444	0.321±0.113	0.235±0.100

Table C.13: Results of differential event shape distributions in Analysis Bin 13

bin	range	data	eff.	pur.	cor.fac.	corr. data
T_z 1	0.000 – 0.350	0.000±0.000	0.000	-1.000	0.000±0.000	0.000±0.000
T_z 2	0.350 – 0.600	0.053±0.053	0.333	1.000	0.333±0.272	0.018±0.023
T_z 3	0.600 – 0.750	0.356±0.178	0.000	-1.000	0.000±0.000	0.000±0.000
T_z 4	0.750 – 0.850	2.133±0.533	0.091	0.333	0.273±0.164	0.582±0.380
T_z 5	0.850 – 0.925	3.378±0.775	0.318	0.467	0.682±0.180	2.303±0.805
T_z 6	0.925 – 0.980	5.818±1.188	0.578	0.591	0.978±0.134	5.689±1.398
T_z 7	0.980 – 1.000	4.000±1.633	0.833	0.341	2.444±0.491	9.778±4.449
C_p 1	0.000 – 0.050	1.333±0.596	0.333	0.273	1.222±0.460	1.630±0.952
C_p 2	0.050 – 0.150	2.533±0.581	0.750	0.323	2.321±0.389	5.881±1.670
C_p 3	0.150 – 0.250	1.067±0.377	0.048	0.083	0.571±0.200	0.610±0.304
C_p 4	0.250 – 0.400	1.244±0.333	0.091	0.222	0.409±0.151	0.509±0.232
C_p 5	0.400 – 0.600	1.200±0.283	0.211	0.375	0.421±0.157	0.505±0.222
C_p 6	0.600 – 0.850	0.320±0.131	0.111	0.500	0.222±0.157	0.071±0.058
C_p 7	0.850 – 1.000	0.000±0.000	-1.000	-1.000	0.000±0.000	0.000±0.000
J_m 1	0.000 – 0.013	14.933±3.991	0.607	0.436	1.393±0.242	20.800±6.632
J_m 2	0.013 – 0.038	12.267±2.558	0.564	0.440	1.282±0.195	15.726±4.057
J_m 3	0.038 – 0.062	5.867±1.769	0.312	0.417	0.750±0.230	4.400±1.891
J_m 4	0.062 – 0.100	6.044±1.466	0.077	0.250	0.308±0.165	1.860±1.096
J_m 5	0.100 – 0.138	0.356±0.356	0.000	0.000	0.143±0.153	0.051±0.074
J_m 6	0.138 – 0.200	0.640±0.370	0.500	1.000	0.500±0.354	0.320±0.292
J_m 7	0.200 – 0.250	0.267±0.267	0.333	-1.000	0.000±0.000	0.000±0.000
J_b 1	0.000 – 0.025	0.000±0.000	0.250	0.500	0.500±0.354	0.000±0.000
J_b 2	0.025 – 0.075	3.467±0.961	0.892	0.440	2.027±0.261	7.027±2.149
J_b 3	0.075 – 0.150	3.911±0.834	0.294	0.556	0.529±0.121	2.071±0.647
J_b 4	0.150 – 0.225	3.022±0.733	0.286	0.444	0.643±0.222	1.943±0.819
J_b 5	0.225 – 0.335	1.818±0.469	0.083	0.500	0.167±0.118	0.303±0.228
J_b 6	0.335 – 0.425	0.296±0.210	0.333	1.000	0.333±0.272	0.099±0.107
J_b 7	0.425 – 0.500	0.178±0.178	0.250	-1.000	0.000±0.000	0.000±0.000

Table C.14: Results of differential event shape distributions in Analysis Bin 14

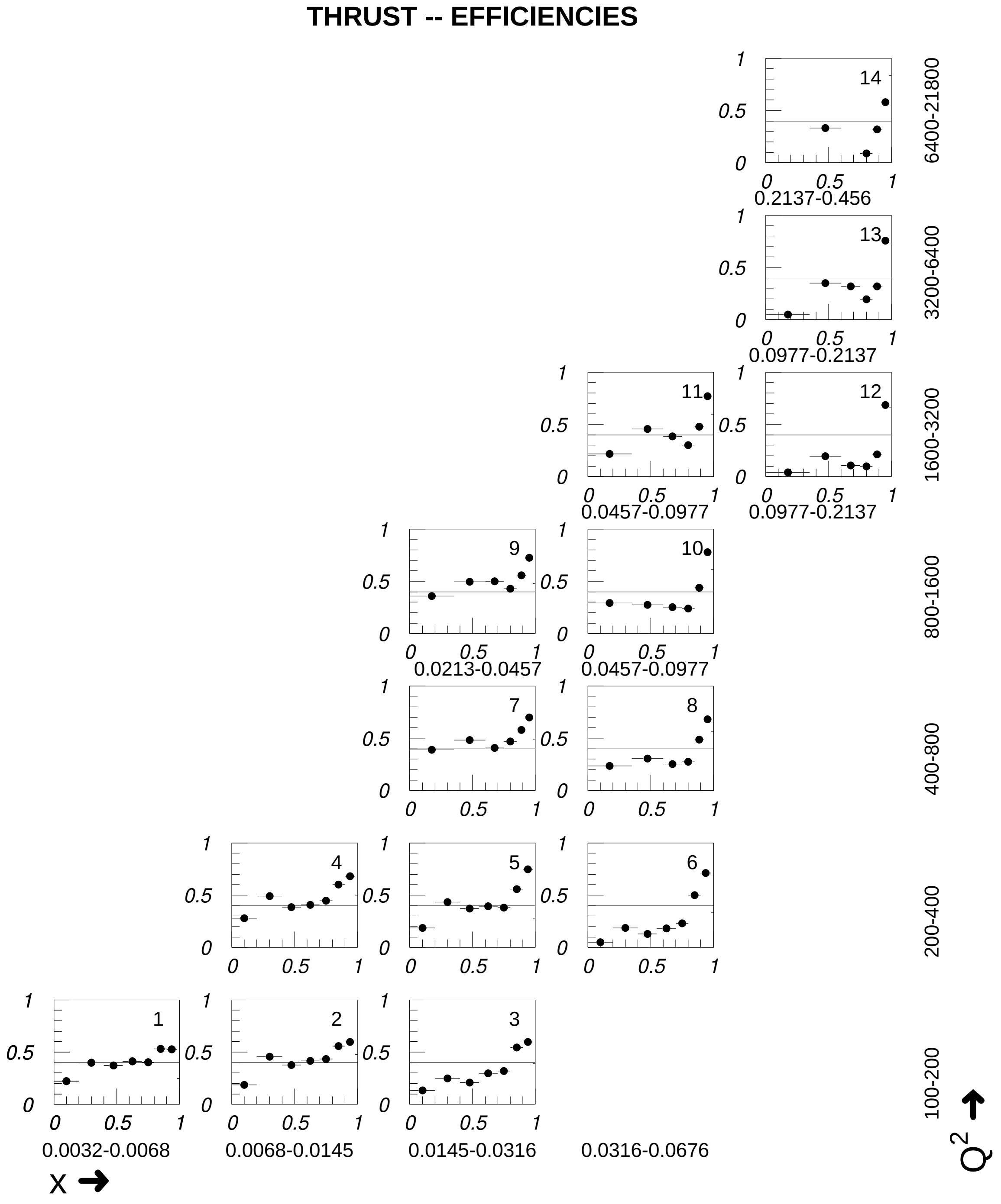

Figure C.9: *Efficiencies of T_z differential distributions.*

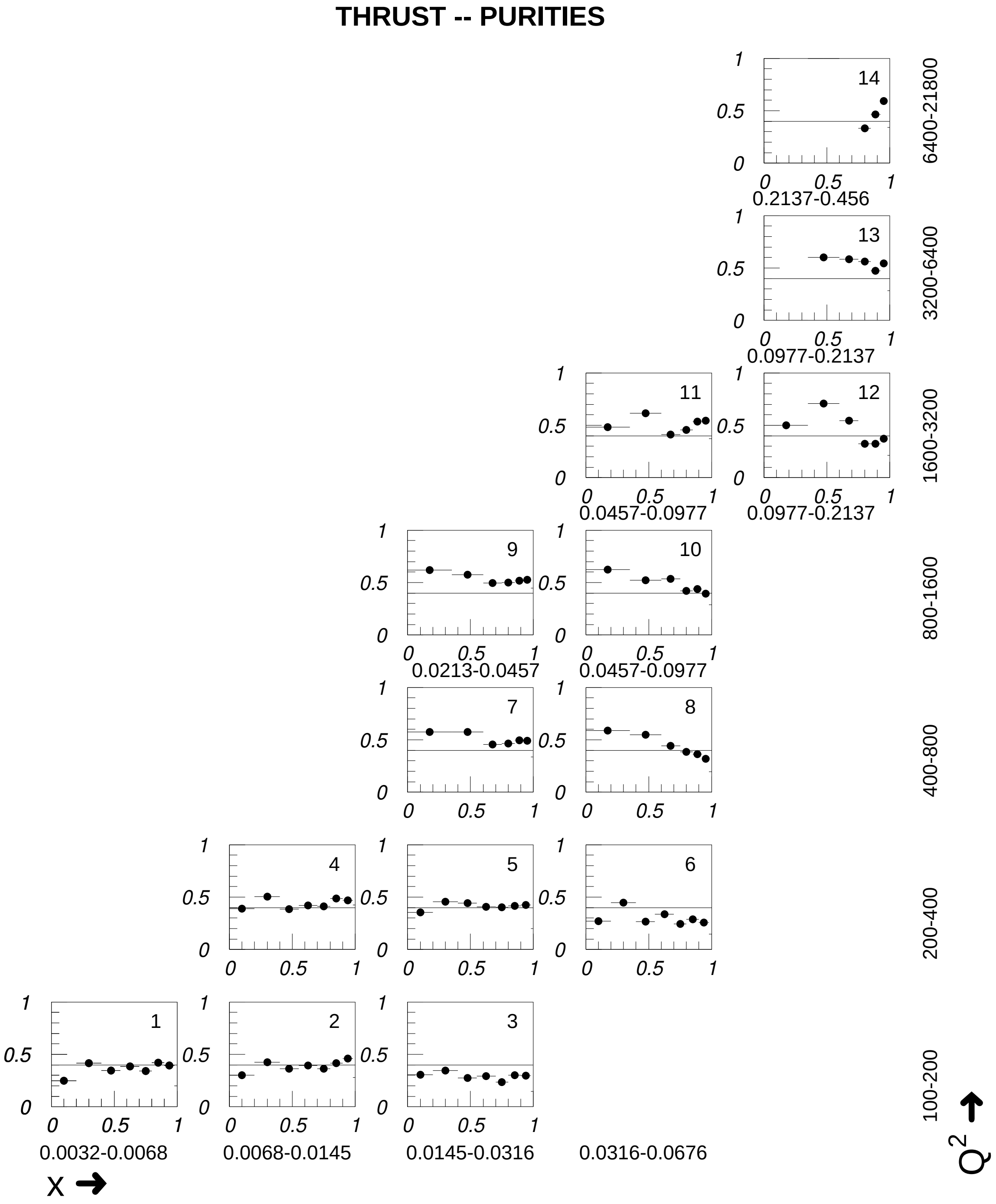

Figure C.10: *Purities of T_z differential distributions.*

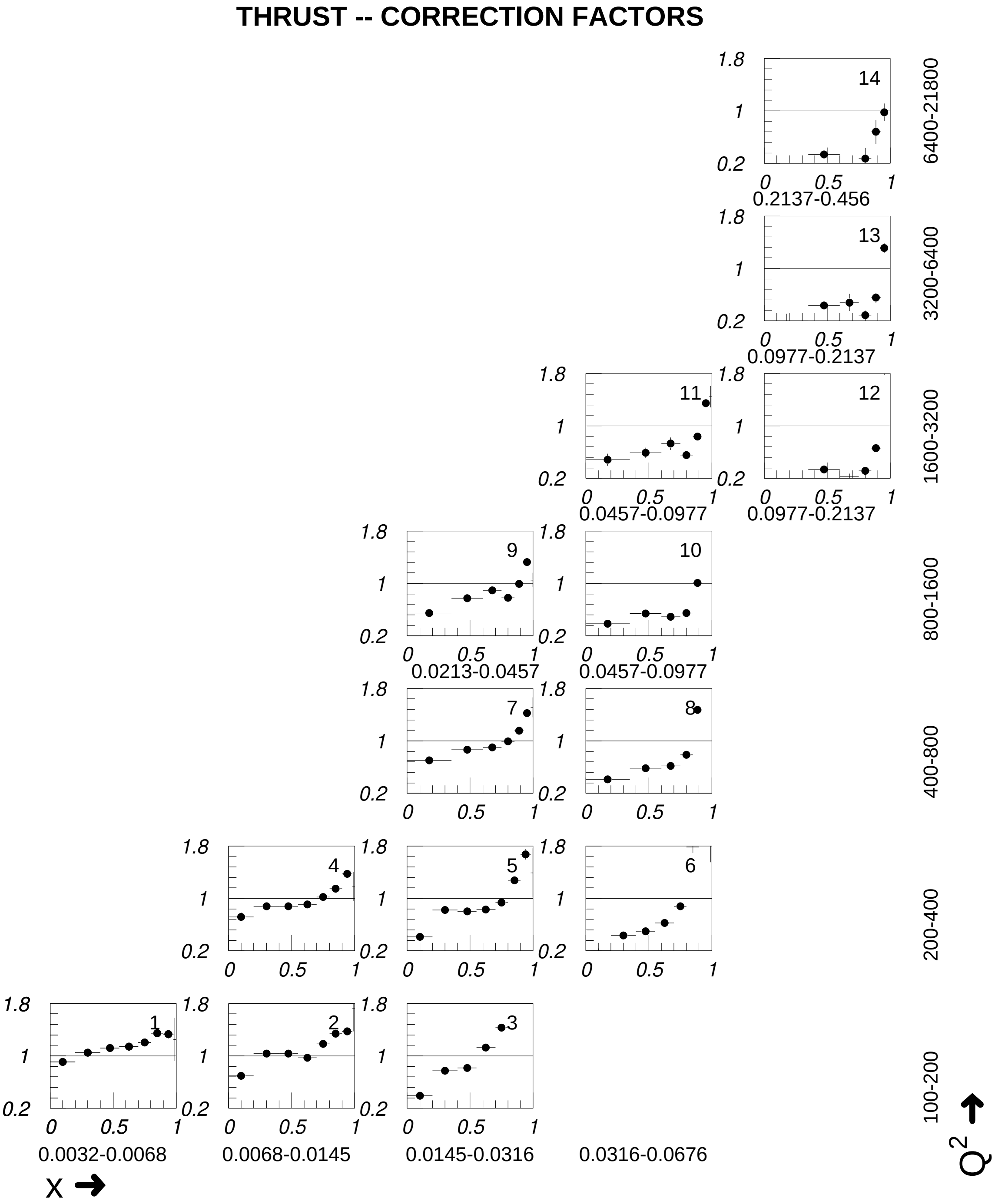

Figure C.11: *Correction factors of T_z differential distributions.*

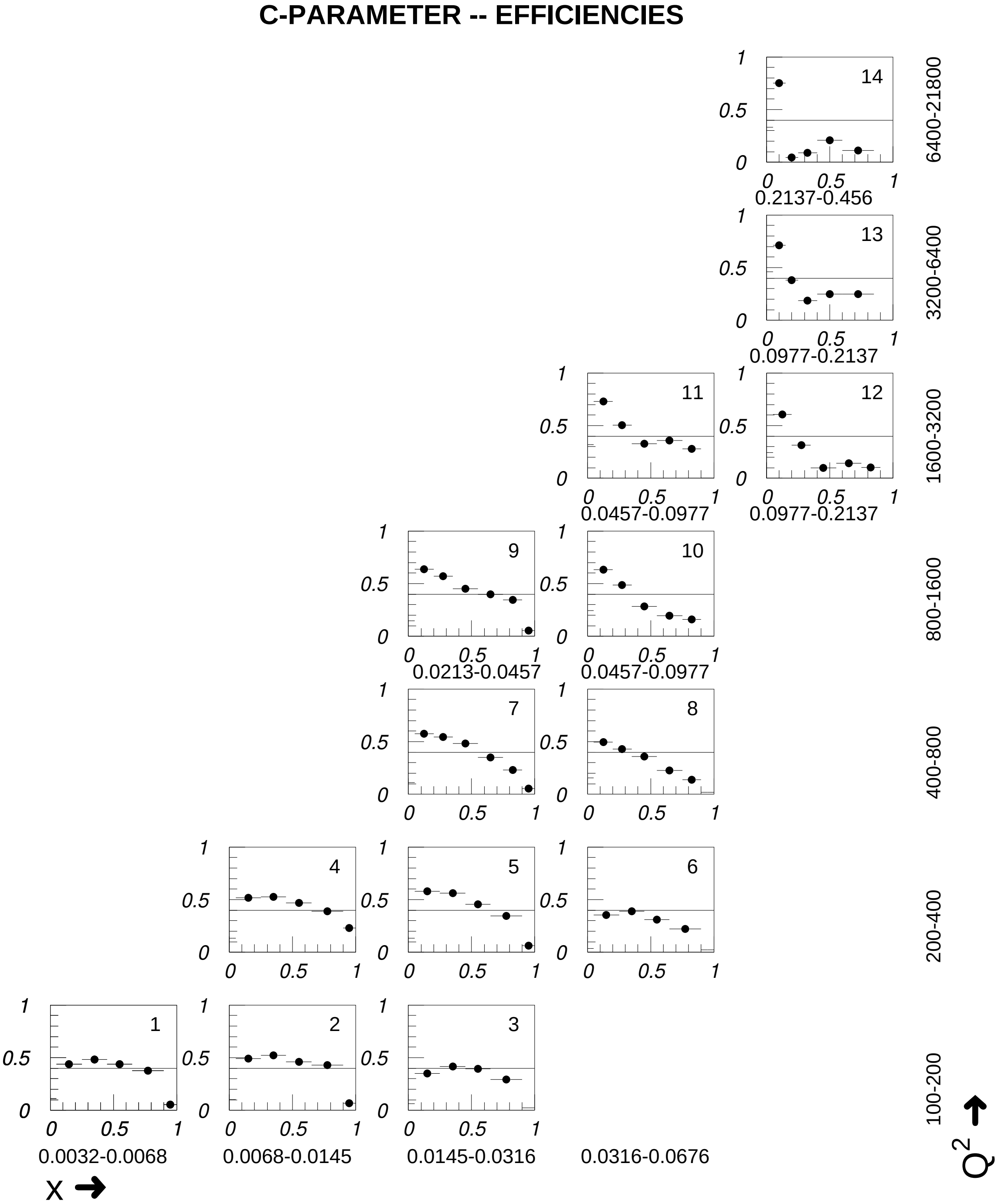

Figure C.12: *Efficiencies of C_p differential distributions.*

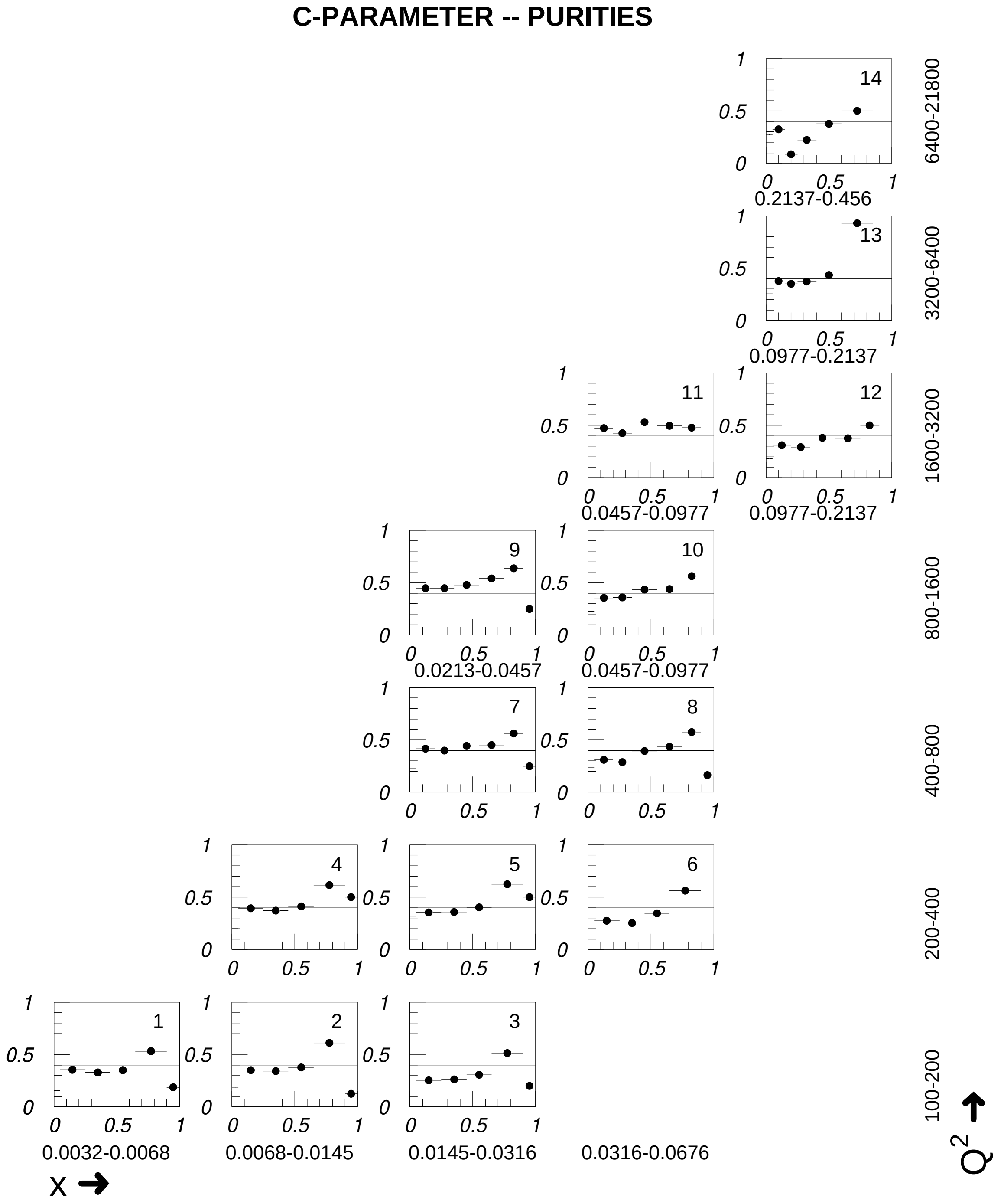

Figure C.13: *Purities of C_p differential distributions.*

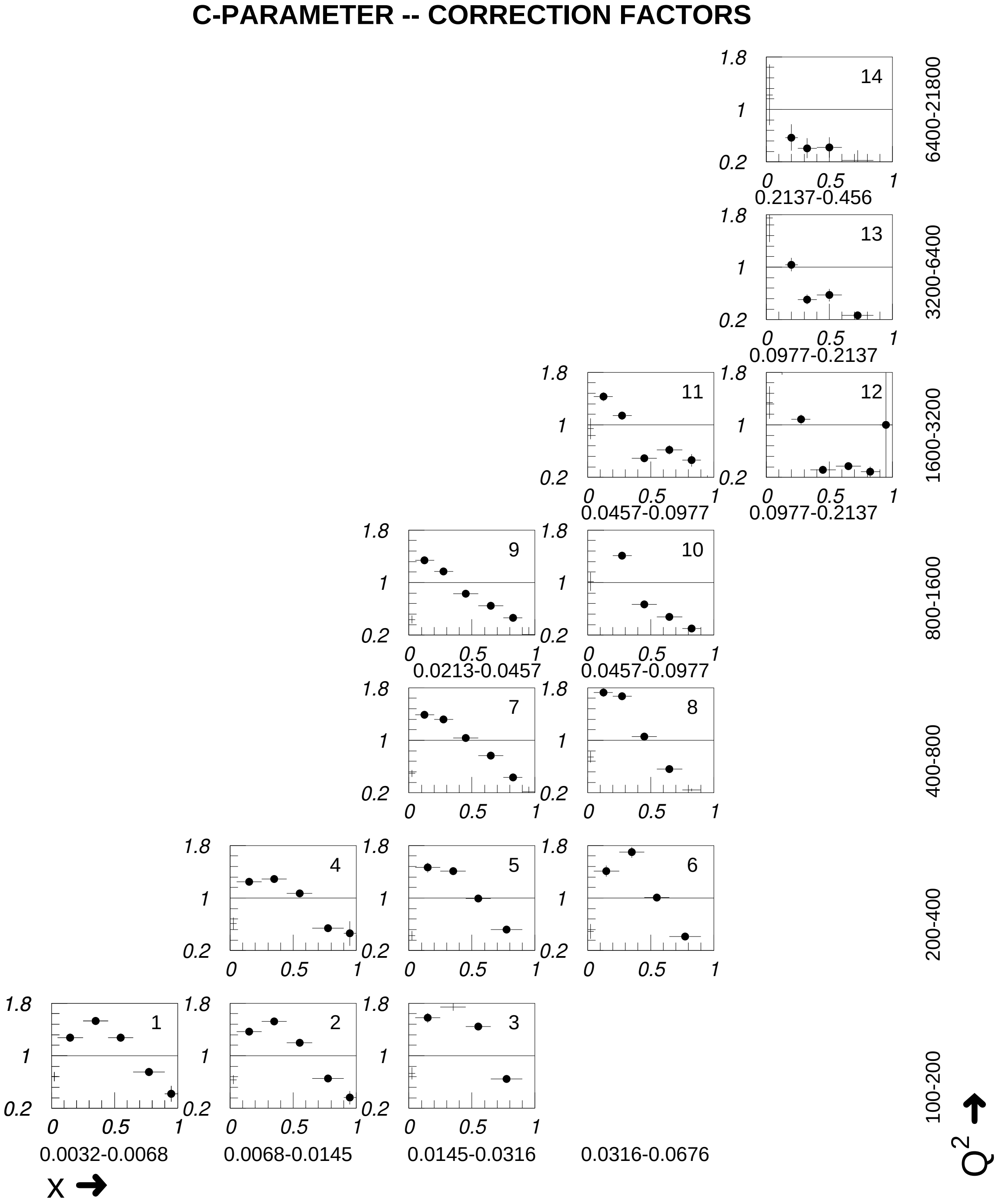

Figure C.14: *Correction factors of C_p differential distributions.*

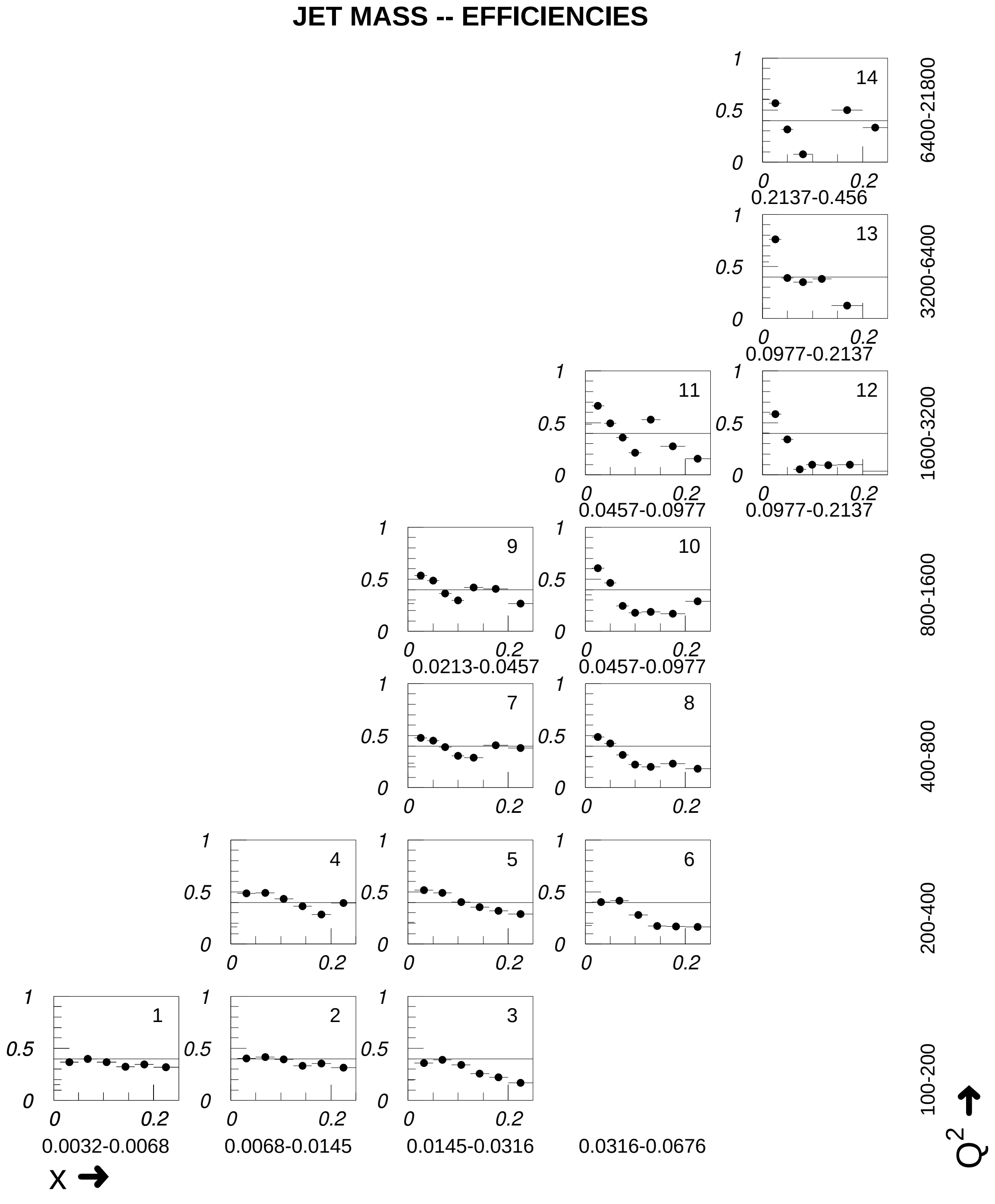

Figure C.15: *Efficiencies of J_m differential distributions.*

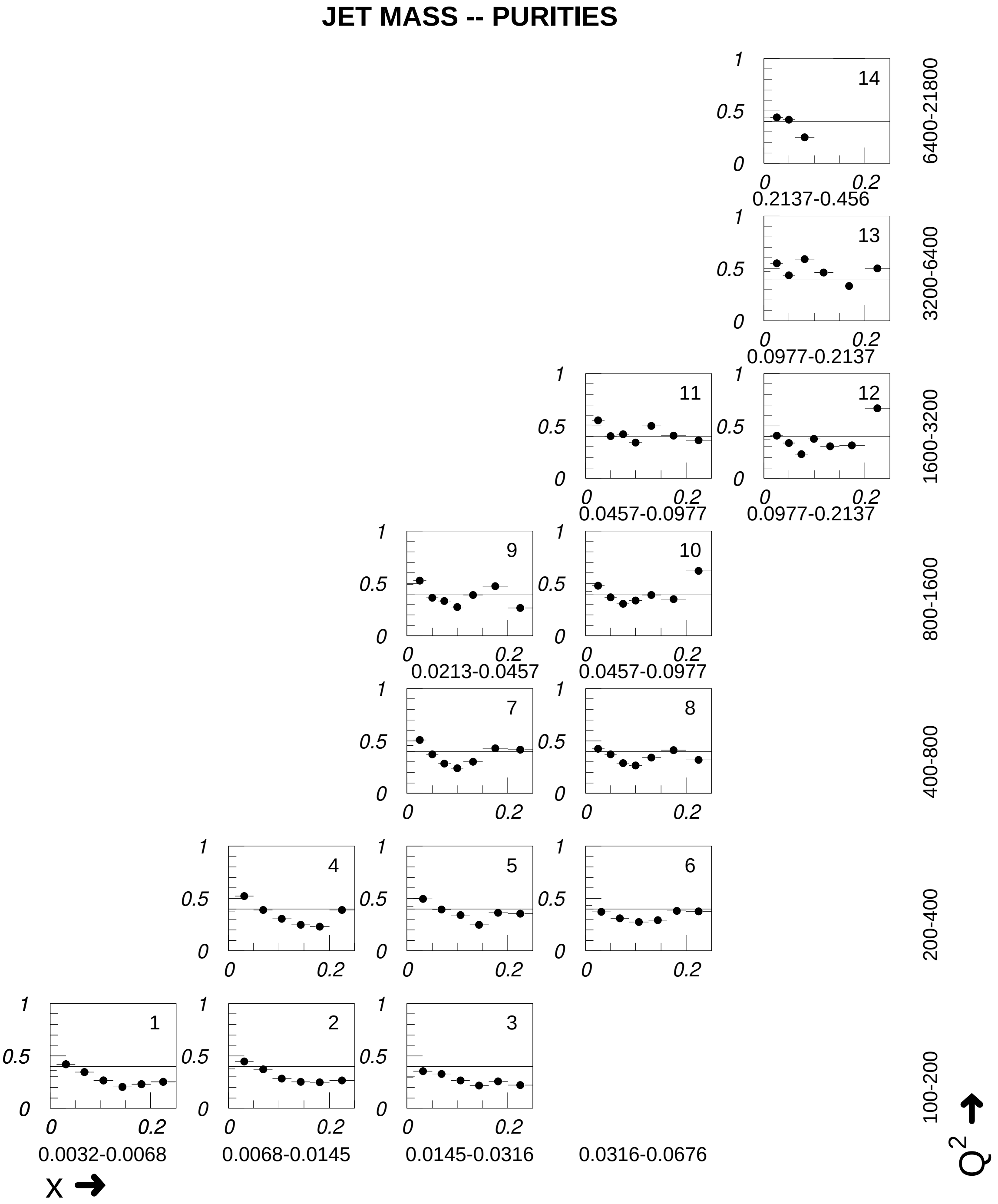

Figure C.16: *Purities of J_m differential distributions.*

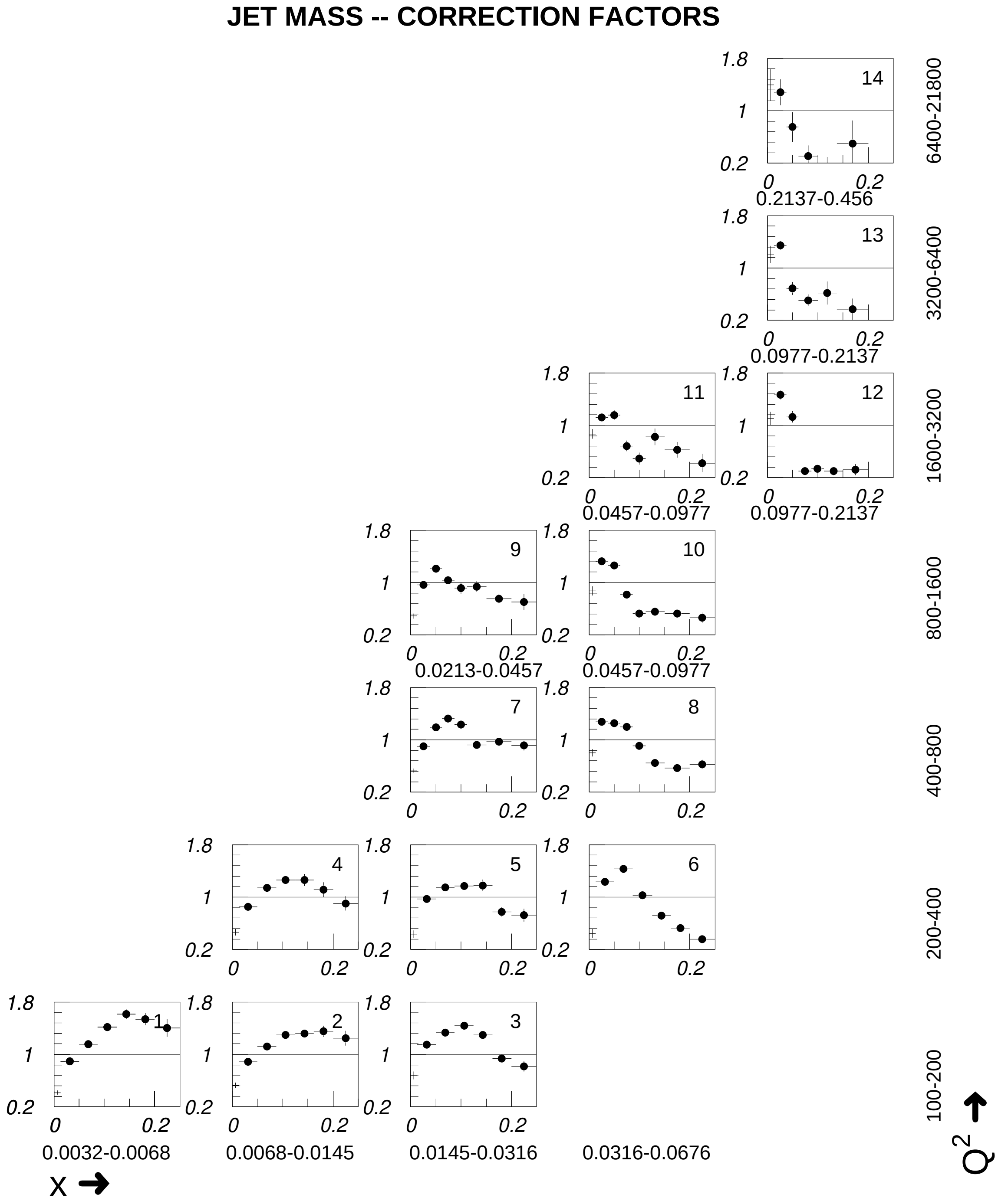

Figure C.17: *Correction factors of J_m differential distributions.*

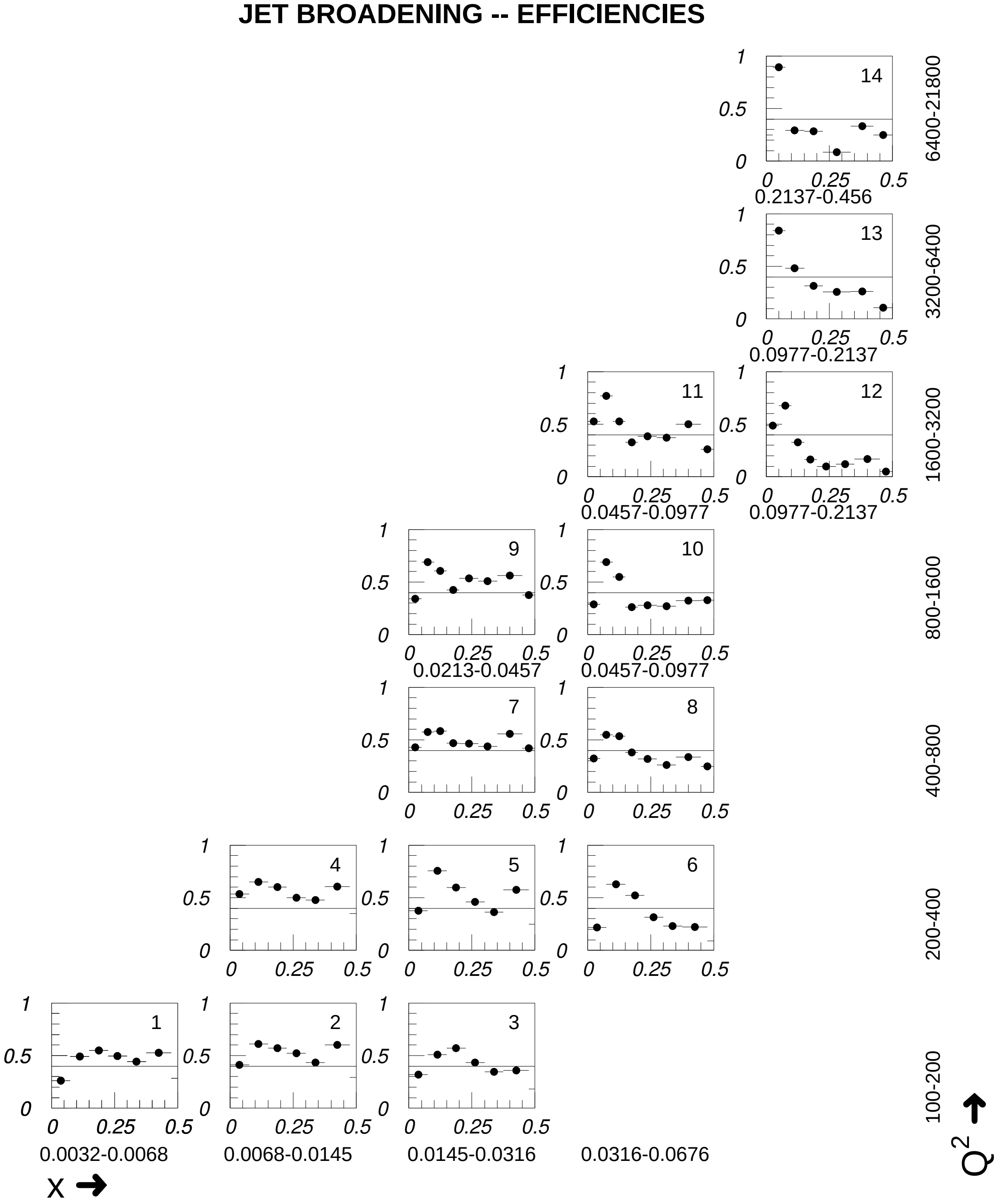

Figure C.18: *Efficiencies of J_b differential distributions.*

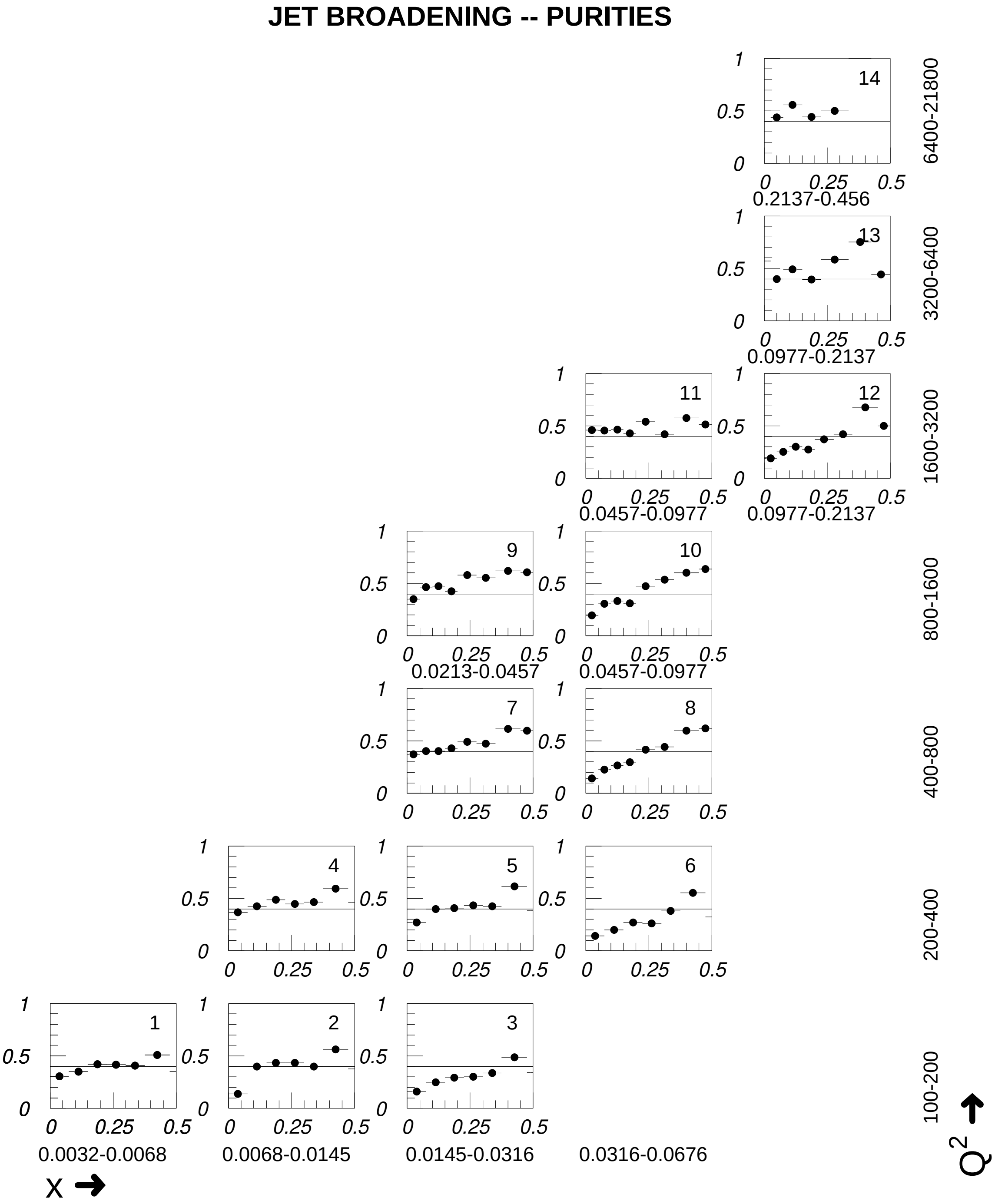

Figure C.19: *Purities of J_b differential distributions.*

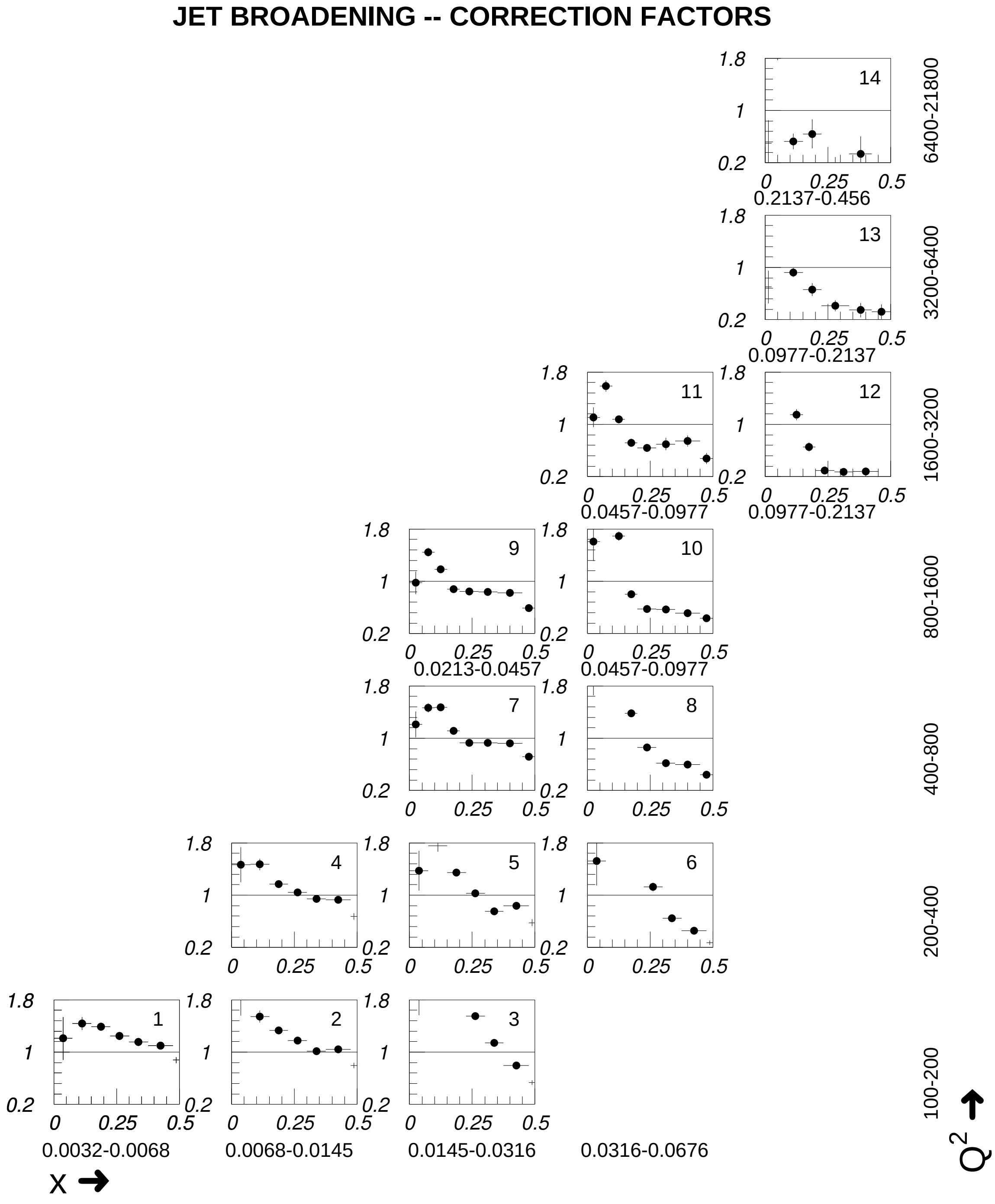

Figure C.20: *Correction factors of J_b differential distributions.*